

Metabolic regulation of *Drosophila* macrophage tissue invasion

by

Shamsi Emtenani

December, 2020

*A thesis presented to the
Graduate School
of the
Institute of Science and Technology Austria, Klosterneuburg, Austria
in partial fulfillment of the requirements
for the degree of
Doctor of Philosophy*



Institute of Science and Technology

The dissertation of Shamsi Emtenani, titled Metabolic Regulation of *Drosophila* macrophage tissue invasion, is approved by:

Supervisor: Dr. Daria Siekhaus, IST Austria

Signature: _____

Committee Member: Dr. Michael Sixt, IST Austria

Signature: _____

Committee Member: Dr. G.V.Shivashankar, ETH Zurich & Paul Scherrer Institute, Switzerland

Signature: _____

Exam Chair: Dr. Bernd Bickel, IST Austria

Signature: _____

signed page is on file

© by Shamsi Emtenani, December 2020

All Rights Reserved

IST Austria Thesis, ISSN: 2663-337X

I hereby declare that this dissertation is my own work and that it does not contain other people's work without this being so stated; this thesis does not contain my previous work without this being stated, and the bibliography contains all the literature that I used in writing the dissertation.

I declare that this is a true copy of my thesis, including any final revisions, as approved by my thesis committee, and that this thesis has not been submitted for a higher degree to any other university or institution.

I certify that any republication of materials presented in this thesis has been approved by the relevant publishers and co-authors.

Signature: _____

Shamsi Emtenani

December 29, 2020

signed page is on file

ABSTRACT

Metabolic adaptation is a critical feature of migrating cells. It tunes the metabolic programs of migrating cells to allow them to efficiently exert their crucial roles in development, inflammatory responses and tumor metastasis. Cell migration through physically challenging contexts requires energy. However, how the metabolic reprogramming that underlies *in vivo* cell invasion is controlled is still unanswered. In my PhD project, I identify a novel conserved metabolic shift in *Drosophila melanogaster* immune cells that by modulating their bioenergetic potential controls developmentally programmed tissue invasion. We show that this regulation requires a novel conserved nuclear protein, named Atossa. Atossa enhances the transcription of a set of proteins, including an RNA helicase Porthos and two metabolic enzymes, each of which increases the tissue invasion of leading *Drosophila* macrophages and can rescue the *atossa* mutant phenotype. Porthos selectively regulates the translational efficiency of a subset of mRNAs containing a 5'-UTR cis-regulatory TOP-like sequence. These 5'TOPL mRNA targets encode mitochondrial-related proteins, including subunits of mitochondrial oxidative phosphorylation (OXPHOS) components III and V and other metabolic-related proteins. Porthos powers up mitochondrial OXPHOS to engender a sufficient ATP supply, which is required for tissue invasion of leading macrophages. Atossa's two vertebrate orthologs rescue the invasion defect. In my PhD project, I elucidate that Atossa displays a conserved developmental metabolic control to modulate metabolic capacities and the cellular energy state, through altered transcription and translation, to aid the tissue infiltration of leading cells into energy demanding barriers.

Acknowledgments

I wish to take this opportunity to give my big thank to many people who provided their invaluable help, support, love, guidance, and mentorship over the years, during which I was carrying out my PhD project at IST Austria.

First and foremost, I would like to express my sincere gratitude to my supervisor, motivator, and leader, Prof. Daria Siekhaus, for giving me the opportunity to accomplish my PhD project in her lab, for her constant support and encouragement during the project and for her wisdom, guidance, and compassion throughout my doctoral journey. I always appreciate her impact on shaping my scientific character and developing my personal horizon.

Besides my advisor, it has also been a great pleasure for me to have Prof. Michael Sixt and Prof. Shivashankar as my committee members. I would like to thank Prof. Rangan and his awesome group, especially Elliot Martin, for all fundamental assistance, insightful comments and encouragement. I would also like to express my sincere thanks to Prof. Thomas Hurd and his group for amiable and fruitful collaboration and advice.

It was the greatest pleasure to work together with so many fabulous colleagues during these years for all their care and help and for being constantly there for me. I would also like to give a big thank to my brilliant and hard working colleagues Julia Bicher and Attila György for their excellent technical assistance. I would like to thank my best PhD buddy and spiritual coach, Stepahnie Wachner. I would offer my deep appreciation to Dr. Ratheesh, Dr. Marko Roblek, and Dr. Maria Akhmanova, from whom I have learned a lot. I also want to give thank to my former colleagues Katarina, Michaela, Vera, and Justine. Thanks to my lovely and caring friends Feyza, Gemma, Laura, and all 2014 PhD students. A special thanks goes to my adorable friend Shayan Shamipour for all his scientific help and invaluable advice. Also, I would like to express my appreciation and thanks to the Bioimaging facility, LSF, GSO, library, and IT people at IST Austria.

Last but not least, I dedicate this work to my lovely family. To my mother Marzieh and my father Mohammad, for their unconditional love, considerable encouragement and wholehearted support, whom I owe everything, and to my brother Peyman who is always a source of pure kindness, trust and compassionate. The last word goes to my best friend, my sweet twin sister Shirin, who has been always with me through all ups and downs of life.

About the Author

Shamsi Emtenani completed a BSc in Molecular Biology-Biochemistry at IAUM and a MSc in Biochemistry at the Ferdowsi University of Mashhad, Mashhad, Iran. She joined IST Austria in September 2014 and afterwards affiliated with the Siekhaus group in the summer 2015. Her main research interests include “metabolic regulation of tissue invasion of the fly immune cells”. During her PhD studies, she has presented her research in different conferences, including the 26th EDRC, Lausanne, Switzerland in 2019, the Development and Stem Cells Regional meeting, IST Austria in 2020, The Crick, London Cell Motility Club Mini-Symposium, London in 2020, and ASCB, USA in 2020. Shamsi has collaborated in the paper ‘A conserved major facilitator superfamily member orchestrates a subset of O-glycosylation to aid macrophage tissue invasion’ published in eLife, 2019.

List of Publications Appearing in Thesis

1. Valoskova K*, Biebl J*, Roblek M, Emtenani S, Gyoergy A, Misova M, Ratheesh A, Reis-Rodrigues P, Shkarina K, Larsen ISB, Vakhrushev SY, Clausen H, Siekhaus DE. 2019. A conserved major facilitator superfamily member orchestrates a subset of O-glycosylation to aid macrophage tissue invasion. *eLife*. 8. pii: e41801. DOI: 10.7554/eLife.41801
2. Vera Belyaeva*, Stephanie Wachner*, Igor Gridchyn, Markus Linder, Shamsi Emtenani, Attila Gyoergy, Maria Sibilia, Daria Siekhaus. 2020. Cortical actin properties controlled by *Drosophila* Fos aid macrophage infiltration against surrounding tissue resistance. bioRxiv. DOI: <https://doi.org/10.1101/2020.09.18.301481> (in review at PLOS Biology).
3. Shamsi Emtenani, Elliott Martin, Attila Gyoergy, Julia Biebl, Jakob-Wendelin Genger, Thomas R. Hurd, Thomas Köcher, Andreas Bergthaler, Prashanth Rangan, Daria Siekhaus. A concerted metabolic program that increases mitochondrial function powers tissue infiltration by macrophage leader cells (under submission).

* These authors contributed equally

Table of Contents

Abstract	v
Acknowledgments	vi
About the Author	vii
List of Publications	viii
List of Figures	xi
List of Tables	xii
List of Symbols/Abbreviations	xiii
Chapter 1: Introduction	1
1.1 WHY DOES CELL MIGRATION MATTER FOR LIFE?	1
1.2 DIFFERENT TYPES OF CELL MIGRATION	1
1.2.1 <i>Single cell migration</i>	1
1.2.2 <i>Models of single cell migration</i>	2
1.2.2.1 <i>Adhesion-dependent cell migration</i>	2
1.2.2.2 <i>Adhesion-independent cell migration</i>	3
1.2.3 <i>Multicellular streaming</i>	4
1.2.4 <i>Collective cell migration</i>	4
1.2.4.1 <i>Fundamental features of collective cell migration</i>	4
1.2.5 <i>Collective chemotaxis</i>	6
1.2.5.1 <i>Models of collective chemotaxis</i>	7
1.2.5.2 <i>Fundamental features of chemotaxis</i>	7
1.3 INVASIVE MIGRATION OF IMMUNE CELLS.....	9
1.3.1 <i>Vertabrate immune cell extravasation</i>	10
1.3.2 <i>Drosophila immune cell extravasation</i>	10
1.4 ENERGETIC REGULATION OF INVASIVE LEADING CELLS	10
1.5 HOW DOES METABOLISM REGULATE CELLULAR ENERGY HEMOSTASIS?.....	11
1.5.1 <i>Mechanistic control of metabolic reprogramming in migrating cells?</i>	13
1.5.2 <i>Metabolic heterogeneity in migrating cells</i>	13
1.5.3 <i>Differential metabolic adaption of immune cells in distinct tissue niches</i>	14
1.6 ENERGY REGULATION THROUGH RNA TRANSLATION MODULATION	17
1.6.1 <i>TOR-mediated control of mRNA translation and bioenergetics</i>	17
1.6.2 <i>mRNA translation</i>	18
1.6.3 <i>Steps of mRNA translation process</i>	18
1.6.4 <i>Regulation of steps of mRNA translation by cis- and trans-acting signals</i>	20
1.6.5 <i>Regulation of 5'TOP mRNA translation by the TOR pathway</i>	20
1.7 <i>DROSOPHILA</i> IMMUNE CELLS AS AN IN VIVO MODEL TO STUDY CELLULAR BIOENERGETICS OF TISSUE INVASION	21
1.8 <i>DROSOPHILA MELANOGASTER</i> IMMUNE SYSTEM.....	21
1.8.1 <i>Origin of Drosophila immune cells</i>	22
1.8.2 <i>Embryonic migration of Drosophila macrophages</i>	22
1.8.3 <i>Functional roles of Drosophila macrophage migration</i>	24
1.8.3.1 <i>Collaboration of Drosophila macrophages with adipose tissue</i>	25
1.8.3.2 <i>Secretion of ECM components and tissue remodeling</i>	25
1.8.3.3 <i>Drosophila macrophages and tumor metastasis</i>	26
1.8.3.4 <i>Maintenance of stem cell niches by Drosophila macrophages</i>	26
	ix
Chapter 2: A concerted metabolic program that increases mitochondrial function powers tissue infiltration by macrophage leader cells	27

1. ABSTRACT	27
2. RESULTS	29
2.1 <i>CG9005 is required in macrophages for their early invasion into the extended germband</i>	29
2.2 <i>Atossa (CG9005) is required for the efficient invasion of pioneer macrophages into the germband tissue</i>	32
2.3 <i>Atossa (CG9005) is a novel nuclear protein whose conserved motifs and TADs are important for macrophage tissue invasion</i>	34
2.4 <i>Atossa's vertebrate orthologs, mFAM214A and mFAM214B, maintain the capacity to promote macrophage tissue invasion</i>	38
2.5 <i>Atossa leads to higher mRNA levels of an RNA helicase and enzymes involved in metabolism, which are each required for germband invasion</i>	38
2.6 <i>The nuclear RNA helicase, Porthos, functions downstream of Atossa in pioneer macrophages to allow their initiation of germband invasion</i>	42
2.7 <i>Loss of Porthos alters translation</i>	47
2.8 <i>Porthos is required for the selective translation of transcripts harboring a conserved Terminal Oligo Pyrimidine Like (TOPL) motif in their 5'UTRs</i>	49
2.9 <i>Porthos is required for mitochondrial oxidative respiration and energy production</i>	51
2.10 <i>Mitochondrial respiration is required for metabolism and energy production in macrophages to initiate invasion into the germband tissue</i>	51
2.11 <i>Atossa and its transcriptional target Porthos are required to shift macrophage bioenergetics for germband tissue invasion</i>	55
2.12 <i>Atossa enhance cellular metabolism and ATP level</i>	56
3. DISCUSSION	60
4. MATERIAL AND METHODS	64
5. REFERENCES	76
Chapter 3: Future direction	95
1. MORE INVESTIGATION ON ATOSSA'S MOLECULAR FUNCTION(S)	95
2. MORE EXPLORATION ON PORTHOS' MECHANISM OF FUNCTION(S)	97
3. FUNCTIONAL CONSERVATION OF ATOSSA AND PORTHOS	102
Chapter 4: Side projects	106
4.1 <i>The effect of the tumor suppressor Merlin, a putative CG9005 (Atossa) interacting protein, on tissue invasion of Drosophila macrophages</i>	106
4.2 <i>How does the alteration in nuclear Lamin levels affect the tissue invasion of macrophages?</i>	110
References	112

List of Figures

Chapter 1: INTRODUCTION

Figure 1: Lead-rear polarization during single cell migration	3
Figure 2: Polarization of a collectively migrating cluster	6
Figure 3: Examples of collective cell migration in response to chemokines	9
Figure 4: The TCA cycle and OXPHOS are tightly coordinated in the mitochondrion	12
Figure 5: Functions of metabolic phenotypes of different vertebrate immune cells	17
Figure 6: Eukaryotic mRNA translation steps	19
Figure 7: Macrophage migration routes and their functional relevance during embryonic development	24

Chapter 2: PAPER DRAFT

Figure 1: CG9005 acts in macrophages to spur pioneer cell infiltration into the germband tissue.....	30
Figure S1: <i>CG9005^{PBG}</i> mutant macrophages migrate normally within the head and along the vnc	33
Figure 2: CG9005/Atossa requires conserved domains linked to transcriptional activation to enhance tissue invasion, a function maintained by its murine orthologs	35
Figure S2: Atossa's TAD domains are essential to enhance macrophages tissue infiltration, a function conserved up to the vertebrates	37
Figure 3: Atossa leads to higher RNA levels of an RNA helicase and metabolic enzymes required for germband invasion.....	39
Figure S3: Macrophage transcriptome analysis reveals that Atossa targets participate in signaling, cell communication and ion transport	41
Figure 4: The nuclear RNA helicase, Porthos, acts as a main downstream target of Atossa to promote pioneer macrophage germband invasion	43
Figure S4: Downregulation of <i>porthos</i> recapitulates the <i>CG9005^{PBG}</i> mutant phenotype	45
Figure 5: Porthos increases the translation of TOPL RNAs, including many involved in mitochondrial OXPHOS and metabolic processes	48
Figure S5: Porthos enhances the translation of TOPL mRNAs, including many involved in gene regulation and transcription, protein synthesis and turnover, signal transduction, and immune responses	50
Figure 6: Mitochondrial respiration is required in macrophages to power their germband tissue invasion.....	52
Figure S6: Depletion of <i>atossa</i> or <i>porthos</i> causes impairment in mitochondrial metabolic activity, reduced ATP production, and a deficiency in macrophage tissue invasion.	54
Figure 7: Mitochondrial metabolism is enhanced by Atossa and Porthos.....	57
Figure S7: Atossa and Porthos enhance ATP production by programming mitochondrial oxidative phosphorylation metabolism.....	59
Figure 8: Nuclear Atossa turns on a metabolic program in <i>Drosophila</i> embryonic macrophages to boost mitochondrial bioenergetics for tissue invasion.....	62

Chapter 3: FUTURE DIRECTION

Figure 1: RNA helicases Aramis and Athos enhance germband tissue invasion of macrophages	98
Figure 2: Increase of proliferation of macrophages attenuates their tissue invasion, while suppressing their cell division promotes tissue invasion	99

Chapter 4: SIDE PROJECTS

Figure 1: Tumor suppressor Merlin is specifically required in macrophages to trigger their invasion into the germband	107
Figure 2: Merlin localizes into the cell membrane in macrophages without interacting with nuclear Atossa (<i>CG9005</i>).	109
Figure 3: Alteration of nuclear stiffness by either overexpressing or downregulation of Lamin in macrophages doesn't affect their germband invasion.....	111

List of Tables

Chapter 2: PAPER DRAFT

Table 1: The enriched expression of FAM214A and FAM214B genes, the vertebrate orthologs of <i>Drosophila</i> Atossa, in vertebrate human immune cells.....	85
Table S1: Fly lines utilized in the paper	86
Table S2: The DNA plasmid constructs utilized in gene construction	88
Table S3: Oligonucleotides utilized in gene construction.....	88
Table S4: List of key resources.....	90
Table S5: List of software tools, analytical packages, and laboratory devices utilized in this paper	93

Chapter 3: FUTURE DIRECTION

Table 1: Fly lines utilized in the thesis	105
--	-----

List of Symbols/Abbreviations

α-KG	alpha-Ketoglutarate
ARE	AU-rich element
AS	amnioserosal tissue
ASAA	alpha-amino adipic semiadldehyde
ATP	Adenosine triphosphate
BCR	blastocoel roof
BDGP	Berkeley Drosophila Genome Project
BLAST	Basic Local Alignment Search Tool
BM	basement membrane
BMDMs	bone marrow-derived macrophages
BMP	bone morphogenetic protein
CIL	contact inhibition of locomotion
CNS	central nervous system
ColIV	Collagen IV DC dendritic cells
Crq	Croquemort
CAGE	Cap analysis gene expression
Cdc4	cell division control protein 4
cDNA	complementary DNA
ChromSeg	Chromosome segregation domain
CR	calorie restriction
CRISPR	clustered regularly interspaced short palindromic repeats
dlg	discs large
DUF4210	domain of unknown function
ECAR	extracellular acidification rate
ECM	extracellular matrix
EcR/USP	ecdysone-regulated hormone receptor
eEF1A	Eukaryotic elongation factor 1A
eIF4F	Eukaryotic initiation factor 4F
e4E-BP	Eukaryotic initiation factor 4E-binding protein
EGF	Epidermal growth factor
EMT	Epithelial to mesenchymal transition
eRF	Eukaryotic release factor
ETC	Electron transport chain
FACS	Fluorescence-activated cell sorting
FAD	Flavin adenine dinucleotide
FAM214A	Family with Sequence Similarity 214 Member A
FAM214B	Family with Sequence Similarity 214 Member B
FOX	Forkhead box
FOG	Friend of GATA
GFP	Green fluorescent protein
Gpo2	Glycerophosphate oxidase 2
GR/HPR	Glyoxylate Reductase/Hydroxypyruvate Reductase
GSC	Germline stem cell
ICAM 1	Intercellular adhesion Molecule 1
ISCs	Intestinal stem cells
LARP1	La-related proteins 1

I(2)gl	lethal (2) giant larvae
LKR/SDH	Lysine α -Ketoglutarate Reductase/Saccharopine Dehydrogenase
LPS	Lipopolysaccharides
MFS	major facilitator superfamily
mRNA	Messenger RNA
mTOR	mechanistic target of rapamycin
NADH	nicotinamide adenine dinucleotide
NES	nuclear export signal
NLS	nuclear localization signals
Non1	Novel Nucleolar protein 1
OCR	Oxygen Consumption Rate
OXPHOS	Oxidative Phosphorylation
Patj	Pals-1-associated tight junction protein
PCP	planar cell polarity
PDGF	platelet-derived growth factor
PDH	Pyruvate dehydrogenase complex
Perl	Perlecan
PIC	pre-initiation complex
PI3K	Phosphoinositide 3-kinases
pLLP	Posterior lateral line primordium
PRTE	pyrimidine-rich translational element
Pvf	Family of growth factors
PVR	PDGF/VEGF-receptor related (Pvr) protein
RNAi	RNA interference
RS6K	ribosomal subunit kinase
scrib	scribbled
Srp	Serpent
TAD	transactivation domain
TC	ternary complex
TCA	Tricarboxylic acid
TE	Translational efficiency
TME	tumor microenvironment
TNF	tumor necrosis factor
TOP	terminal oligopyrimidine motif
TORC	TOR complex
Ush	U-shaped
UTR	Untranslated region
VCAM 1	Vascular cell adhesion molecule 1
VEGF	Vascular endothelial growth factor



این نکته رما کردانی دانی
هر چیزی که در خستن آنی آنی

You are a treasure, if the gems are your aim.
No more than a grain, if a loaf is your claim!

Recall this secret, when you play this game:
Whatever you pursued- is what you became!

Mevlânâ Rumi (1207-1273)

Chapter 1: Introduction

1.1. Why does cell migration matter for life?

Sensing and initiating directional movement in response to external cues is a fundamental property of biological systems from individual cells to entire organisms. Cell migration refers to the process by which a cell alters its location from one position to another. Cell migration is mechanistically a well-orchestrated cyclic process that includes cell polarization, formation of protrusions and focal adhesions at the front edge, nuclear movement, contraction and detachment at the rear, and finally cell body translocation (Wilson et al. 2010). This evolutionarily ancient capability plays crucial roles in various aspects of life. Cell movement is fundamental phenomenon required for establishing and sustaining the proper organization of multicellular organisms (Treat et al., 2012). Alongside general migration, the specialized ability of cells to move through challenging tissue barriers underlies various normal and pathogenic processes, including tissue homeostasis, the protective responses of immune cells, and even the deleterious effects of cancer metastasis (Kurosaka and Kashina, 2008; Nourshargh and Alon, 2014; Friedl et al. 2012). My discovery of a new mechanism that enables such movement into challenging environments is the focus of this thesis.

1.2 Different types of cell migration

Many motile cells, owing to an inherent plasticity, can adopt distinct modes of migration depending on their contexts. Cells can move in amoeboid, mesenchymal or epithelial modes, as individuals or in clusters, strands, streams, sheets or fluid-like masses and can even switch dynamically between different types in response to a changing environment. This diversity in migratory dynamics is accomplished by differential regulation of forces in space and time (Friedl et al., 2012; Nagai et al., 2020). Key forces are integrated and tuned to different magnitudes and subcellular localizations to generate diverse cell migration behaviors, including cell-matrix adhesions, intercellular connections, cortical stiffness, actin polymerization-mediated protrusions and actomyosin contractility. The main modes of cellular movement are generally single or collective cell migrations (Wilson et al. 2010; Nagai et al., 2020).

Here, I will first describe single cell migration, the required molecular events, and the main types of individual cell migration. Afterwards, I will briefly mention the stream/chain mode of cell migration. I will then explain the basic features of collective migration and continue with collective chemotaxis in *in vivo* models.

1.2.1 Single cell migration

Single cell migration, in which cells move solitarily, is important for development, immune surveillance and cancer metastasis *in vivo* (Ridley et al., 2003; Friedl and Weigelin, 2008). Convincing evidence suggests that there is a high plasticity in the mode of single cell migration carried out by different migratory cell types, so that they are able to switch

between adhesion-dependent and adhesion-independent modes in distinct contexts (Treat et al., 2012; Wu et al., 2021).

1.2.2 Models of single cell migration

Single or individual cell migration employs a range of strategies, depending on the stringency of cell-matrix adhesions, external signals and the capability to remodel the extracellular matrix (ECM) during migration (Watanabe and Mitchison, 2002; Friedl and Weigelin, 2008).

1.2.2.1 Adhesion-dependent cell migration

Cell migration can be conceptualized as an integrated multistep process. In this step-wise cyclical process, first cells undergo front-rear polarization, then they form protrusions or blebs, which are stabilized through focal adhesions, and finally contractility mediates rear retraction and forward motion (Watanabe and Mitchison, 2002; Treat et al., 2012):

i. Polarization: a migratory cell should first become polarized along its front-back axis to ensure persistent forward locomotion. Polarity is derived in response to external cues, including chemoattractants, ECM components or stiffness gradients. Front-rear polarity is generated and maintained by preferential localization of Cdc42 and PI3K at the front and Rho at the rear edge of the cell. Cdc42 and PI3K control polarity by activation of the actin polymerization machinery, making the front edge extensions. While at the back, Rho promotes myosin II activity in the actomyosin structure, which contracts the actin cytoskeleton in an ATP-dependent manner (Etienne-Manneville 2008; Ladoux et al., 2016).

ii. Formation of membrane protrusions: In a polarized cell the actin polymerization machinery drives the generation of membrane extensions towards the direction of movement in the form of protrusions (lamellipodia, filopodia, and invadopodia). In some cases a cell makes a small roundish extension, named a bleb, through hydrostatic pressure (Friedl and Weigelin, 2008; Paluch and Raz, 2013).

iii. Stabilization of protrusions by cell-substrate adhesion formation: cell-substrate connections are formed between protrusions and the matrix. These so-called “focal adhesions” are generally large dynamic transmembrane complexes, which interconnect the ECM to the intracellular cytoskeleton that stabilize cellular protrusions (Schmidt and Friedl, 2010).

iv. Rear retraction and forward translocation: Actin flows backwards away from the cell membrane through “retrograde flow”, a process reliant on actin polymerization and myosin motors. Focal adhesions act as “molecular clutches” supporting forward cell locomotion by regulating the forces generated by actin dynamics. They reduce actin retrograde flow to allow actin assembly to form protrusions at the leading edge (Parsons et al., 2010).

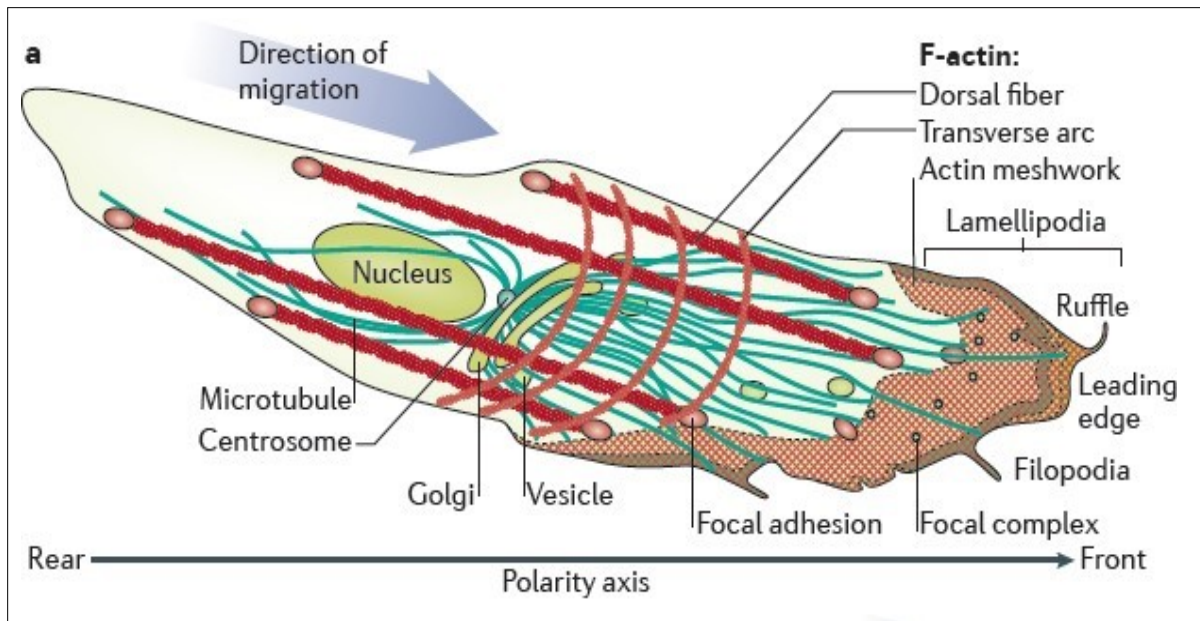


Figure 1: Lead-rear polarization during single cell migration. At the front cell, actin-polymerization based protrusions and cell-ECM adhesions are formed. Force retractions are applied to the focal adhesions to provide forward cell locomotion. At the cell rear, the focal adhesions are disassembled and the cell body is detached from the ECM, leading to contraction. Adapted from (Mayor and Etienne-Manneville, 2016).

1.2.2.2 Adhesion-independent cell migration: amoeboid migration

The social amoeba *D. discoideum* has been used for years as a simple model to study directed single cell migration and chemokine signaling (Stuelten et al., 2018). Through highly orchestrated migration events the amoeba *D. discoideum* is able to navigate in complex environments (Barry et al., 2010). In multicellular organisms, although adhesion-dependent migration is known to be universal especially on 2D substrates, cells within a 3D confined matrix can migrate without requiring adhesions. The same migratory strategy is often employed by amoeboid (shape-changing) types of cells, like leukocytes, which can migrate only under confinement and not on flat surfaces (Lämmermann et al. 2008; Reversat et al. 2020). Amoeboid migration generally refers to the movement of round or ellipsoid cells that do not strongly adhere to the ECM, basically under a condition of enhanced confinement and with reduced or absent substrate adhesions. During migration, they have very transient or no cell-matrix attachment, while dynamically changing their shape to maintain front-rear polarity (Paluch and Raz, 2013). Mechanistically, amoeboid migration is driven by high actomyosin contractility that leads to rapid actin-rich front protrusions and back retractions, which finally drives fast and persistent cell movement in confined contexts (Hawkins et al., 2011; Wu et al., 2021). In some non-adhesive cells, it relies on the formation of actin-devoid protrusions, known as blebs, which are driven by hydrostatic pressure at the rear edge, generating cytoplasmic flows (Friedl et al. 2004; Lämmermann and Sixt, 2009). Many cell types in confinement, like T cells, leukocytes (Reversat et al., 2020), germ layer progenitors and breast cancer cells undergo migration in

an adhesion-independent manner without the need for substrate attachment (Mayor and Theveneau, 2013).

1.2.3 Multicellular streaming

Some cell cohorts migrate in streams or chains. This mode of directed migration occurs when cells are jointly guided by a chemotactic relay and/or oriented extracellular guidance cues in multicellular streams or in small chain-like files. All cells in a stream exert traction forces independently on the matrix, while they are loosely distributed with transient intercellular adhesions and preferentially follow small tracks and tissue discontinuities. Multicellular streaming has been identified in many subpopulations of the neural crest, the mammalian endoderm (Carmona-Fontaine et al., 2008) as well as orthotopic breast cancer and melanoma tumors (Friedl et al. 2012). Likewise, chain migration has been observed in *Drosophila* myoblasts, squamous cell carcinoma (Richardson et al., 2007), neural crest cell populations (Simkin et al., 2013) as well as *Dictyostelium* in restricted food conditions (Barry et al., 2010).

1.2.4 Collective cell migration

Collective cell migration is the coordinated motion of a group of cells that emerges from their chemical, physical and or mechanical interactions across a 2D extracellular matrix or through a complex 3D tissue contexts. Collective cell migration, when connected cells move in cohorts, contributes to numerous developmental processes, including embryogenesis, morphogenesis, wound healing, and tissue remodeling, which can be smartly recapitulated by tumor cells (Friedl et al., 2004; Ilina and Friedl, 2009; Friedl and Alexander, 2011).

In multicellular organisms during development, embryonic cells often travel in numbers, whereas in adults, epithelial cells close wounds collectively. The morphological organization of collectively migrating cells can vary considerably. Migrating cell groups may range from strands of only two cells in diameter to broad masses (Treat et al., 2012; Theveneau and Linker, 2017). Migration of a cohesive multicellular group occurs when the intercellular connections and front-rear polarity of the unit are mainly retained and coordinated over long time periods. Collectively migrating multicellular clusters are also polarized into the “leading or front edge” and the “rear or trailing edge”. The leading edge generates traction force by actomyosin-mediated protrusion and contractility, often together with cells at lateral regions of the group (Friedl and Wolf, 2009).

1.2.4.1 Fundamental features of collective cell migration

i. Preserving mechanical and functional coupling: This is potentially the primary characteristic of collective cell migration. Within the category of collective migration, epithelial cells move cooperatively with stable and preserved cell-cell junctions, while mesenchymal cells have transient intercellular adhesions in a cohesive unit. Cell-cell adhesions, mainly mediated by adherens junction proteins, are essential for maintaining the cohesion and cooperation of migrating multicellular platform. In many cases, the fine-

tuned levels of Cadherin proteins, including E-, N- and VE-Cadherins, are involved in establishing stable cell-cell contacts during collective cell migration (Suffoletto et al., 2018; Wu et al., 2021).

ii. Establishing and maintaining supracellular polarity: Collective polarity promotes the cell cluster to respond and adapt more efficiently to the environment, compared to single cells. Supracellular polarity can be generated either by genetically determined differentiation (e.g. angiogenesis) (Gaggioli et al., 2007), differential expression of ECM-adhering proteins, or gradients of external cues (e.g. chemokines or growth factors) (Vitorino and Meyer, 2008). Cluster polarity can also be provided by the temporary positional or functional state of a cell within the population as an outcome of the phenomenon of “contact inhibition of locomotion” (CIL). CIL is an essential process to secure the inhibition of protrusion formation at intercellular contacts in the middle of the group, while promoting protrusion generation in the leader cells (Theveneau and Mayor, 2013). As a consequence of supracellular polarity, multicellular platforms, by virtue of respective positions, have leader and follower cells, each exerting distinct roles for the efficient organization of the cluster. Due to collective polarity, leader cells are discriminated from follower cells within a multicellular cohort. Leading cells display a highly dynamic cytoskeleton with large protrusions towards the migration direction, which are necessary to explore and respond to the extracellular guidance cues (Vitorino and Meyer, 2008). In many cases, leader cells gain a pseudomesenchymal phenotype with a large lamellipodium at the front edge, attached to the rest of the cluster via actomyosin cables. Follower cells also exert essential roles in a migrating cluster, largely by affecting leader cell polarization and also through gradient sensing or formation and chemotaxis. Generally, Notch lateral inhibition, mechanical signals, and topology are determining factors for leader cell specification within the cohesive unit (Wilson et al., 2013; Wu et al., 2021).

iii. Coordinating supracellular cytoskeletal activity in a cluster: Cellular forces are applied through cytoskeletal rearrangements and protrusions as well as stable intercellular connections. Consequently, cells are coordinated to function as a single unit to enable the persistent synchronized translocation of the entire cluster. Moreover, collective migration relies on leader cell-ECM interactions, mostly through integrin-mediated signaling, to generate the force required for forward movement of the whole population (Friedl et al., 2004; Montell, 2008; Carmona-Fontaine et al., 2008; Mayor and Etienne-Manneville, 2016)

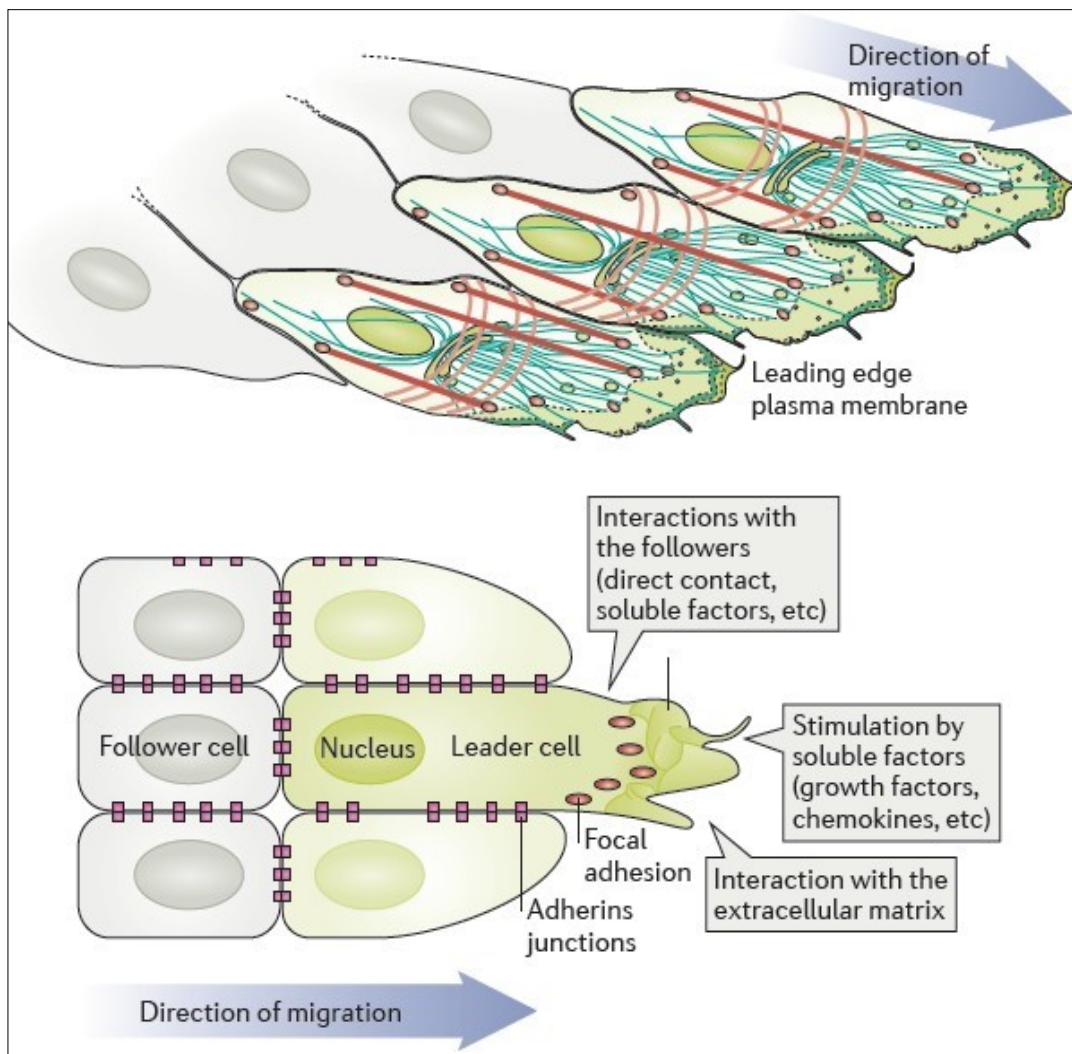


Figure 2: Polarization of a collectively migrating cluster. (A) At the front edge of most migrating cohesive populations, polarized leader cells display an elongated morphology with dynamic actin-based protrusions towards the direction of migration. **(B)** Leader cells are attached to follower ones through cell-cell junctions, which restrict focal adhesions only at the front site. They sense and respond to external cues like chemokine molecules and ECM components. Adapted by (Mayor and Etienne-Manneville, 2016).

1.2.5 Collective chemotaxis

Migrating cells sense and respond to particular signals, including mechanical stimuli, ECM molecules or soluble external cues, which direct long-range migrations. Cell migration relies on a response to detectable gradients of soluble external signals, mostly chemokines and growth factors, known as chemotaxis, which provides a directional persistent migration. The chemotactic response similarly involves supracellular polarization via actin polymerization and protrusion formation at the front edge along with myosin-II-mediated contraction at the trailing edge (Kay et al., 2008; Friedl et al., 2012). Migrating cells fail to reach the target destination in the absence of chemoattractant or its receptors. In a collectively migrating multicellular unit, leader cells are pivotal in sensing soluble guidance

factors to promote the chemotaxis of the entire cohort (Wilson et al., 2013; Riahi et al., 2015; Wu et al., 2021).

1.2.5.1. Models of collective chemotaxis

i. Mammalian vessel sprouting: During angiogenesis, Notch-mediated transcriptional control through lateral inhibition defines and later maintains the identities of endothelial leader and follower cells. In this case, the cell cluster responds and moves towards the chemoattractant vascular endothelial growth factors (VEGF). Within the group, tip leading cells adopt a highly dynamic morphology with large actin-rich protrusions, mechanically connected via Cadherins and actomyosin to their follower counterparts (Fig. 3a,b) (Theveneau and Linker 2017; Nagai et al., 2020).

ii. Branching morphogenesis of *Drosophila* trachea: Similar to the blood vessel sprouting model, directional collective migration of endothelial cells in the *Drosophila* trachea is governed by leader-directed chemotaxis towards the chemokines Bnl and FGF (Pocha and Montell, 2014; Scarpa and Mayor, 2016) (Figure 3a',b').

iii. Caudal migration of zebrafish lateral line primordium: In zebrafish embryos, posterior lateral line primordium (pLLP), derived as an epithelial placode, migrates anteroposteriorly as a cohesive cluster, while it periodically deposits sensory organs called neuromasts during its migration. Front and trailing cells within the polarized pLLP cluster have distinct morphologies and display differential responses towards chemokine CXCL12/SDF1 (Figure 3c,d) (Scarpa and Mayor, 2016). Front cells are mesenchymal with a front-back polarity, whereas rear cells are more organized in an epithelial fashion. CXCL12/SDF1, is initially uniformly expressed, binds receptor CXCR4b on the leading cells to promote actin polymerization and large protrusions. The receptor on the trailing cells CXCR7, responds to the same ligand, as a decoy receptor, Binding of SDF1 to CXCR7 on the rear cells permits the cluster to sense a gradient by acting as a sink. Thereby, the lateral line self-generates an SDF1 gradient across the primordium, which can be followed (Haas and Gilmour, 2006; Donà et al., 2013). The ultimate result of the migration is the assembly of epithelial rosettes, which are deposited as proneuromasts (Hava et al., 2009).

iv. *Drosophila* border cell migration: The collective migration of border cells in ovaries is crucial for normal development and proper fertilization (Figure 3e,f) (Scarpa and Mayor, 2016). The ovary is composed of ovarioles and the egg chamber. Within the egg chamber, a small cluster of about eight border cells is organized around a center of two immobile cells called polar cells. Border cells in the egg chamber first detach from the epithelium before migrating a long distance as a small unit. They move through the surrounding nurse cells towards the oocyte in two distinct migration modes. In the earliest phase they mostly migrate in a 'linear or running mode' towards the oocyte. Cell movement in the absence of detectable ECM is characterized by protrusion formation, restricted to the leading edge

and oriented towards the nurse cells. Border cells, once close to the oocyte, switch to a 'rotating migration mode' (Montell et al., 2012; Pocha and Montell, 2014). One of the border cells expressing the highest receptor tyrosine kinase and Rac1 levels can take on the leader cell duty. The leader cell adopts a pseudomesenchymal phenotype with a distinctive protrusion and also responds better to the oocyte-secreted guidance cues, including PVF (platelet-derived/vascular endothelium-derived growth factor homologue) and EGF (epidermal growth factor) ligands (Montell et al., 2012; Prasad et al., 2015; Stuelten et al. 2018). During the linear migration phase, leader-follower roles are maintained via mechanical coupling, preventing excessive protrusive activity in non-front cells. Occasionally, a follower cell takes over the lead position, resulting in the proposal that the leading cell's identity is not precisely unique and pre-defined (Montell et al., 2012; Theveneau and Linker, 2017; Nagai et al., 2020).

v. Neural crest migration: The *Xenopus* neural crest population is one of the most common models of mesenchymal collective cell migration. Cephalic neural crests are formed in the dorsal part of the neural tube at late gastrula stages and migrate ventrally contributing to many head structures (Figure 3c,d). Cephalic neural crests first delaminate from the neural tube and then undergo an epithelial-to-mesenchymal transition (EMT), while still migrating as a cohesive cluster. In response to the chemoattractant CXCL12/SDF-1, the cohesive unit migrates ventrally across the head of the embryo until they reach their target destinations, where they finally differentiate into a plethora of derivatives. Neural crest cells require transient and loosely connected intercellular adhesions via receptor C3a/C3aR to prevent dispersion as well as CIL-mediated polarization of large protrusions towards the migration direction to be able to migrate as a single unit. The leader-follower identity or position, similar to *Drosophila* border cells, is transient and exchangeable during cluster migration (Theveneau and Linker, 2017; Scarpa and Mayor, 2016).

vi. Collective migration of head mesendoderm: Head mesendoderm is another well-studied model of mesenchymal collective migration. In *Xenopus*, mesendodermal cells migrate as a cohesive sheet. However, zebrafish mesendodermal cells gain a mesenchymal phenotype. *Xenopus* head mesendoderm moves collectively towards the blastocoel roof (BCR) as a source of the chemokine PDGF (Figure. 3 i,j). Mesendodermal cells orient their protrusions in a PDGF and intercellular contact-dependent manner. In both migrating mesendoderm models, the Wnt/planar cell polarity (PCP) pathway via Rac1 determines and coordinates the orientation of protrusions towards the direction of migration (Scarpa and Mayor, 2016; Diz-Muñoz et al., 2010; Damm et al., 2011).

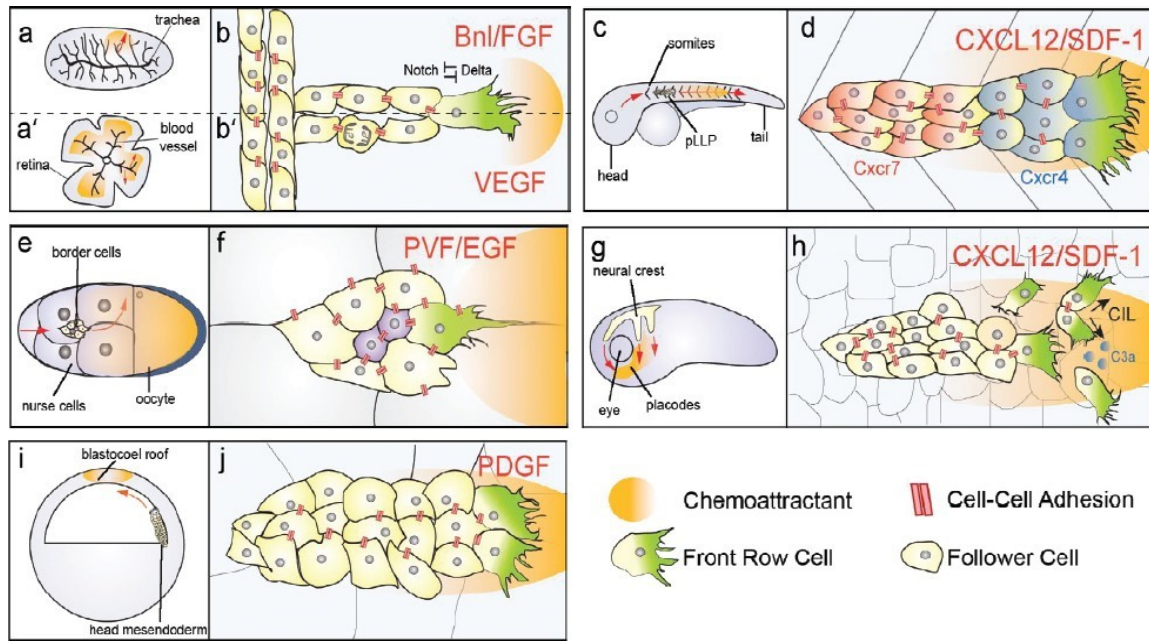


Figure 3: Examples of collective cell migration in response to chemokines, named collective chemotaxis. (a and b) Branching morphogenesis of *Drosophila* trachea in response to Bnl/FGF chemokine. **(a' and b')** During sprouting morphogenesis, one tip cell responds to VEGF and gains a pseudomesenchymal phenotype with large lamellipodial protrusions. **(c and d)** Cohesive migration of the zebrafish lateral line primordium towards the chemokine CXCL12/SDF1. Mesenchymal front cells sense the ligand via CXCR7 and make large protrusions, while epithelial back cells respond to CXCL12/SDF1 via the CXCR4 receptor and engulf this chemokine. **(e and f)** *Drosophila* border cells, while surrounding two polar cells in the center, move dorsally between nurse cells in the egg chamber towards the chemokines PVF and EGF. The most PVF-responsive border cell in the unit adopts a pseudomesenchymal leader phenotype with distinctive large forward-directed protrusions. **(g and h)** Neural crest cells sense chemokine CXCL12/SDF1 via their receptor C3a/C3aR and make transient intercellular connections, but still migrate ventrally as a cohesive file across the *Xenopus* head. CIL drives the polarization of front cells, promotes their protrusive activity, and prevents cell dispersion during collective migration. **(i and j)** *Xenopus* head mesendodermal cells cohesively migrate toward chemokine PDGF, secreted by the blastocoel roof (BCR). Protrusions in front cells are oriented in a PDGF- and intercellular contact-dependent manner. Adapted from Scarpa and Mayor, 2016.

1.3 Invasive migration of immune cells

Immune cells, like other migrating cells, migrate by similar mechanisms, whose perturbation leads to severe developmental and physiological defects (Nourshargh, et al., 2014). For instance, the ability to migrate from non-lymphoid to lymphoid tissue is a fundamental feature of dendritic cells (DCs), by which they can initiate protective pro-inflammatory as well as tolerogenic immune responses (Worbs et al., 2016). As another example, tissue-resident macrophages, potent phagocytic immune cells, should migrate to their final destinations to exert their essential roles in organ development, tissue homeostasis, and pathogenic responses (such as infection, injury and cancer) (Dawson et al., 2020; Eming et al., 2017). Similarly, microglia, known as brain resident macrophages, regulate neuronal cell number, control the early brain wiring via axon outgrowth & fasciculation, control the cortical interneuron migration, and also impact neuronal cell survival. These phagocytosing cells should first migrate to their destinations to exert their

roles, mainly secreting of diffusible factors and phagocytosis (Tanabe et al., 2018; Thion et al., 2018).

1.3.1. Vertebrate immune cell extravasation

Infiltration of leukocytes is central to immune cell development, immunosurveillance and effector function (Friedl, 2008; Nourshargh et al., 2010). Leukocytes first passively flow within the blood stream. Upon receiving proinflammatory and damage signals, immune cells initiate their transmigration through the vascular endothelial layer by binding to the vessel endothelium followed by diapedesis. Immune cell transmigration consists of a sequence of steps:

1. slow rolling of a leukocyte along the vessel wall, mediate by binding to selectins
2. contacting and attaching to the vessel cells, followed by the binding of leukocyte adhesion receptors, “activated integrins”, to their counterpart ligands VCAM-1 and ICAM-1 on the endothelial cells
3. moving across the endothelium border, following the dephosphorylation of the VE-Cadherin and thus opening of endothelial junctions
4. passaging through subendothelial basement membrane
5. penetrating through interstitial tissue, facilitated by the proteolytic cleavage of ECM components, including laminin-10 and collagen IV (Friedl et al., 2008; Muller 2013; Nourshargh et al., 2010).

1.3.2. *Drosophila* immune cell extravasation

The fruit fly, *Drosophila melanogaster*, has been neglected for a long time as a viable model to study immune cell extravasation, due to its open circulatory system without discrete blood vessels. Interestingly, there is a time window during pupal development when beating wing hearts pulse hemolymph (the fly version of blood), containing circulating immune cells through developing wing veins. *Drosophila* immune cells extravasate from wing veins to wounded tissue. Extravasation of *Drosophila* macrophages reveals parallels to vertebrate immune cell diapedesis, including dynamic protrusions at the leading edge towards the direction of migration, an integrin dependent-rear contractility, and Rho-dependent polarization (regulated by the *Drosophila* GPCR Tre1) (Thuma et al. 2018). Nevertheless, there are certainly some differences between *Drosophila* immune cell extravasation and the analogous episodes for mammalian immune cell diapedesis, such as differences at the level of the vessels, the absence of a pericyte layer or lack of any fly orthologs for P- and E-selectins.

1.4 Energetic regulation of invasive leading cells

Cells generally consume energy to grow, proliferate, migrate, and sustain their essential life processes in response to distinct environmental cues. Cell infiltration through physically challenging barriers costs energy (Van Horssen et al., 2009; Caino et al. 2013). Different migrating populations, including immune cells, neurons or tumor cells, adopt distinct

metabolic requirements during migration, development and invasion (Xie et al., 2021; Riera-Domigo et al., 2020). Cells increase their intracellular energy production rate due to the increased consumption caused by increased actin polymerization, protrusion formation, cytoskeletal rearrangement and focal adhesion remodeling during the infiltration of challenging environments (Zanotelli et al., 2018; Zanotelli et al., 2019; Li et al., 2019).

Leading cells apparently need higher energy to overcome these highly energy-demanding obstacles. Pioneer cells are often described as more migratory but less proliferative than follower cells, when migrating cooperatively. Interestingly, when encountering a physically challenging environment, leader and follower cells can occasionally switch their positions to overcome the energy barrier of invasion (Zhang et al., 2019). Moreover, migrating cells within the invasive population can be metabolically heterogeneous. Leader and follower cells have been found to preferentially rely on different metabolic sources to sustain energy demands and fuel the energy pools required for migration (Kim and De Berardinis, 2019; Commander et al., 2020). In a cohesive cluster or stream, the front cells consume more ATP, which may reflect their necessity for more efficient ATP generation to meet the required energy for tissue infiltration (Hoang-Minh et al., 2018; Commander et al., 2020). However, metabolic programs that control the bioenergetics of leading cells to drive their invasion in different physically challenging tissues are not fully understood.

In this section, I will discuss the metabolic regulation of cellular energy homeostasis and afterwards will explain how migrating cells, including immune cells, fine-tune their metabolic state for cell migration in various contexts. In the end, I will focus in more details on the metabolic control of bioenergetics at the translational level.

1.5 How does metabolism regulate cellular energy hemostasis?

Metabolism is an integrated web of cellular processes that coordinates energy production (ATP), the synthesis of biomass (nucleotides, amino acids and lipids) and the balancing of reducing equivalents (NAD(P)H and FADH₂). These aspects of metabolism are linked to each other, to signal transduction and to epigenetic regulation (O'Sullivan et al., 2019). Cellular metabolism has emerged as a critical determinant of the viability and function of migrating cells during development and diseases. Clearly, dynamic metabolic adaptations, not a single metabolic state, signify metabolic plasticity to enable phenotype switching of migrating cells in response to various stimuli in different environments (Lee et al., 2020). Glucose, the major source of energy, is converted to pyruvate in the cytoplasm via glycolysis (Jose et al., 2011; Riera-Domigo et al., 2020). Glycolysis commonly refers to the lactate end-point branch of glycolysis, while when pyruvate goes on for further energy production; the process is referred to as glucose oxidative or mitochondrial metabolism. Under normal conditions, pyruvate is shuttled into mitochondrion, where it is converted to Acetyl-CoA by pyruvate dehydrogenase (PDH) and then is oxidized via the Krebs or tricarboxylic acid (TCA) cycle (Riera-Domigo et al., 2020; Tiku et al., 2020). ATP is generated

through the mitochondrial electron transport chain (ETC) using the electrochemical potential energy generated by the transfer of electrons from donor metabolites (nicotinamide adenine dinucleotide (NADH) or reduced flavin adenine dinucleotide (FADH₂)) to electron acceptors and finally to oxygen, in a process called oxidative phosphorylation (OXPHOS) (Leone and Powell, 2020). Five ETC multiprotein complexes (I-V), located within the inner membrane of mitochondria, constitute the oxidative respiratory system (Figure. 4, Martínez-Reyes and Chandal, 2020; van der Blik et al., 2017). In the OXPHOS process, ETC complex I, NADH dehydrogenase, oxidizes NADH to NAD. Complex II, Succinate dehydrogenase, oxidizes succinate to fumarate to reduce ubiquinone. Reduced ubiquinone is then oxidized by complex III, cytochrome c reductase, which catalyzes the reduction of cytochrome, permitting its oxidation by complex IV, cytochrome oxidase. The resulting proton gradient throughout the mitochondrial inner membrane drives the synthesis of ATP by complex V, the ATP synthase (van der Blik et al., 2017; Martínez-Reyes et al., 2020).

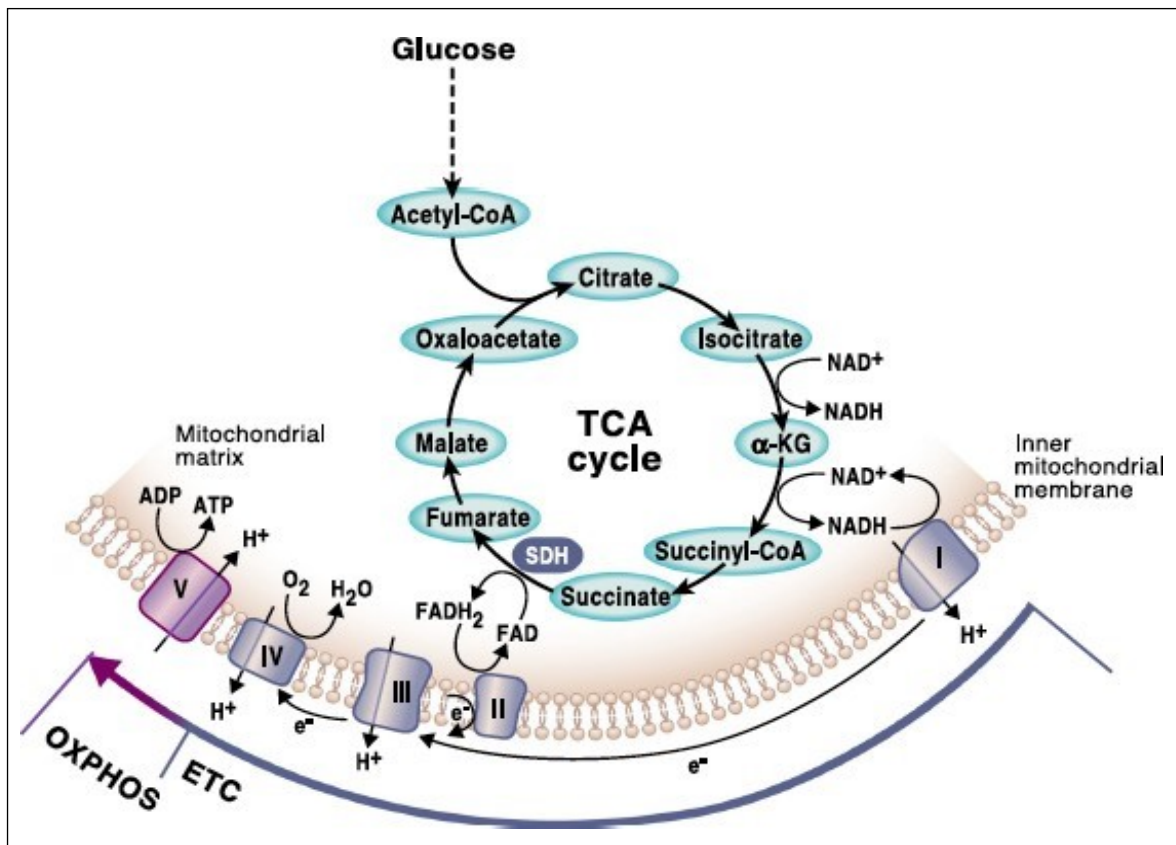


Figure 4: The TCA cycle and OXPHOS are tightly coordinated in the mitochondrion. In a series of enzymatic reactions by glycolysis in cytoplasm, pyruvate is produced from glucose, and then in mitochondrion it is converted to Acetyl-CoA by pyruvate dehydrogenase (PDH). Acetyl-CoA goes to the TCA cycle, which generates the reducing equivalents NADH and FADH₂, required to transfer electrons to the mitochondrial respiratory chain. Mitochondrial ETC consists of five multi-subunit complexes (I-V). As the electrons are funneled through the complexes (I, III, and IV) across the mitochondrial inner membrane, ETC generates a mitochondrial membrane potential being used to produce ATP by complex V. This process requires the presence of oxygen and it is known as OXPHOS. Adapted from Martínez-Reyes and Chandal, 2020.

There is a structural dependency between complexes I and III, in which the assembled complex III is required to stabilize complex I in mitochondria (Acín-Pérez, et al., 2004). On the other hand, the energy-transducing state of mitochondria, determined by the level of ATP synthase activity, can modulate the assembly of complex III (Ostojić, et al., 2013). Complex III as an important site of proton translocation catalyzes ubiquinol oxidation and cytochrome c reduction. Complex III consists of 11 or 10 different subunits in mammals and yeast, respectively: three catalytic subunits of cytochrome b (Cytb), cytochrome c1 (Cyt1) and the Rieske-FeS protein Rip1, core proteins, and small subunits (Qcr8, 9, and 10). Qcr9 is a highly conserved subunit of mitochondrial Complex III (cytochrome bc1 complex), required for formation of the mature dimeric bc1 complex. Cells lacking Qcr9 form a stalled assembly intermediate with only residual bc1 activity (Smith, et al., 2012). Mitochondrial complex V, F₁F₀-ATP synthase, consists of the catalytic F₁ region, which is made up of subunits α , β , γ , δ , and ϵ as well as the F₀ region, which contains subunits a, b, c, d, e, f, g, A6L, and F69. The supernumerary subunits, e and g, play a specific role in crista maintenance by promoting dimerization of ATP synthase complexes (Song et al., 2018).

1.5.1 Metabolic reprogramming in migrating cells

The main challenge to understand metabolic pathways has always been their complexity. Metabolic reprogramming reflects the responses of cells to changes in the environment and is emerging as a critical mechanism to alter cell activation, differentiation and function. Studies in the growing field of metabolism support a paradigm of cellular selectivity or plasticity based on demand.

1.5.2 Metabolic heterogeneity in migrating cells

In order to sustain the prodigious energetic needs underlying proliferation, some activated immune cells and tumor cells gain specialized metabolic states. Most immune cells as well as solid and ascites tumor cells generally rewire their energy sources toward aerobic glycolysis at the expense of mitochondrial respiration, the so-called 'Warburg effect' (Warburg et al., 1926; Dang, 2012; Riera-Domigo et al., 2020). In aerobic glycolysis pyruvate generated from glycolysis is converted to lactate in the cytoplasm, producing two ATP molecules for each glucose molecule, instead of the 36 produced through mitochondrial respiration. The Warburg shift while providing less ATP, leads to a rapid transit of glucose derived carbon through the glycolysis pathway and enhances funneling of glucose-derived intermediates to anabolic pathways that can fuel the proliferation required for tumor growth or immune cell activation (Pavlova et al. 2016; Riera-Domigo et al., 2020; Warburg et al., 1926; Lee et al., 2020). Glycolysis is also the predominant energy pathway in slow-growing solid tumors, or so-called dormant cancer cells due to low oxygen and nutrition availability (Eales et al., 2016). So, such metabolic adaptations through elevated aerobic glycolysis will enable a fast response to emerging high energy demands for anabolic processes during cell propagations and also will aid cells to survive under nutrient

deprivation, stress or hypoxic conditions (Zhang et al., 2014; Riera-Domigo et al., 2020; Eales et al., 2016).

Cell metabolism is heterogeneous with a high degree of plasticity and migrating cells engage in a range of metabolic programs to meet the demands of both growth and invasion (Jose et al., 2011; Walker et al., 2014; Nikolaou and Machesky, 2020). It has become increasingly clear that even when oxygen and nutrients are not limiting, many migrating cell types preferably utilize aerobic glycolysis over OXPHOS in order to generate building blocks essential for anabolic processes (Lehuédé et al., 2016; Riera-Domigo et al., 2020). However, mitochondrial metabolism can also have prominent roles in migrating cells (O'Sullivan et al., 2019). Recently, the new concept of 'reverse Warburg effect' has been evoked in cancer cells under normoxic conditions, which could induce the reprogramming of the tumor microenvironment (TME) to provide OXPHOS-produced high-energy metabolites to anabolic cancer cells (Witkiewicz et al., 2012; Kim and De Berardinis, 2019). According to the paradigm, the metabolism of invasive cancer cells, and in a broader perspective highly motile cells can be metabolically heterogeneous within the migrating population (Commander et al., 2020).

1.5.3 Differential metabolic adaption of immune cells in distinct tissue niches

Similar to other migrating cell types, immune cells require energy for survival, migration, and proper functions (Stienstra et al., 2017). During development or in response to tissue damage or pathogens, various immune cell populations are recruited to their target sites to perform distinct roles. Such immune cells in vertebrates comprise lymphoid-derived cells, including circulating T- and B-lymphocytes, and NK cells, as well as myeloid-derived cells, including bone marrow derived monocytes that can develop into dendritic cells (DCs) and macrophages as well as tissue associated bone marrow-derived mast cells and tissue-specific macrophages. Clearly, the immune responses that these cells carry out, such as phagocytosis, migration, proliferation, and or cytokine release, in which all necessitate a balanced metabolic reprogramming (Stienstra et al., 2017; Riera-Domigo et al., 2020).

The function of immune cells in response to tissue-specific cues (Caputa et al. 2019) can be powerfully defined by their metabolism. Immune cells flexibly reprogram intracellular metabolic pathways that subsequently modify immune functions, altering transcription and posttranscription events in a process called 'immunometabolism' (Bernier et al., 2020; O'Neill and Pearce, 2016; Riera-Domigo et al., 2020). The various alterations in their metabolism that immune cells depend on their nature, and the tissue-specific cues and different tissue-niches surrounding them, which altogether underlie their distinctive tissue-specific functions (Davies et al., 2019; Caputa et al. 2019). The considerable degree of functional heterogeneity among diverse immune cell populations probably dictates diverse metabolic strategies in distinct microenvironments (Orihuela et al., 2016). Inflammation cues or injury signals appear to cause robust metabolic fluctuations in immune cell metabolism. Upon LPS stimulation, activated myeloid cells, DCs and bone marrow-derived macrophages (BMDMs) promote a profound metabolic rewiring towards glycolysis,

resembling the Warburg effect (Stienstra et al., 2017). As another example, highly proliferative short-lived T_H17 cells upregulate glycolytic programs, including aerobic glycolysis and PPP, to allow massive cell division and proper differentiation and functions (Macintyre et al., 2014; Caputa et al., 2019). In contrast, naive and tolerant T cells as well as T_H2 cells (specially upon antigen activation) preferentially rely on mitochondrial OXPHOS (Buck et al., 2017; Walker et al., 2014; Riera-Domigo et al., 2020). Macrophages and DCs favor mitochondrial respiration for long-term responses (e.g. in responses to Interleukin-4), while they can easily switch to glycolytic flux as a rapid response to pathogenic or danger signals (e.g. LPS) (Caputa et al., 2019; Riera-Domigo et al., 2020; Lauro and Limatola, 2020). As an immediate response to pathogen signals or for cell proliferation, immune cells boost their ATP levels via upregulating glycolysis. Conversely, long-lasting responses, like tissue repair or developmental tissue remodeling, would require more constant energy production, which can be provided by enhanced mitochondrial respiration. Nevertheless, it is still not completely clear which molecular mechanisms regulate such a fast or differential impact in diverse immune subsets.

Normoxia (a normal oxygen level) or hypoxia (a low oxygen level) in surrounding tissues also triggers a reprogramming of the metabolic platform in immune cells, with normoxia promoting the TCA cycle and OXPHOS and hypoxia promoting glycolysis, both for ATP production. For instance, classically activated M1 macrophages, key defense players, are mainly found in hypoxic environments. When they are exposed to bacterial infections in such environment, they activate glycolysis to fulfill tissue-specific requirements. Conversely, alternatively activated M2 macrophages upregulate oxidative metabolism as well as FAO to meet their emerging energy demands for long-term functions such as tissue hemostasis and repair (Mantovani, et al., 2013; Rodríguez-Prados et al., 2010; Galvan-Peña and O'Neill, 2014) (Figure 5). In a similar manner, brain-resident macrophages, microglia, can quickly adapt their energy metabolism to maintain essential immune actions in brain tissue. Under normal oxygen supply, microglia, like macrophages, produce energy via mitochondrial OXPHOS (Cherry et al., 2014; Lauro and Limatola, 2020; Bernier et al., 2020). However during neuroinflammation or in hypoxic environments, thanks to metabolic plasticity, microglia undergo a metabolic shift from OXPHOS towards aerobic glycolysis (Bernier et al., 2020) (Figure 5). The mentioned examples above clearly reflect the presence of metabolic plasticity and heterogeneity in at least some subsets of immune cell populations. Commonly, immune cells engaging in potent inflammatory responses, which necessitate rapid proliferation or high-output production of mediators are preferentially rewired for high aerobic glycolysis. Under low oxygen accessibility by favoring aerobic glycolysis, cells are still presumably able to produce sustainable ATP levels and retain functional within the infection-associated hypoxic niches. While some immune cells would fulfill a sustained supply of energy, under normal oxygen availability, through higher oxidative glucose metabolism to properly contribute to the tissue remodeling, repair and healing processes (Bernier et al., 2020; Riera-Domingo et al., 2020). Altogether, such

metabolic plasticity allows the migrating cells to adapt their functions to the biological needs in response to a wide range of activation signals within distinct microenvironments.

Most of current investigations in the field of metabolism of immune cell have been achieved *in vitro*, or obtained from immune cell populations found in the blood or bone marrow rather than on tissue-resident or recruited cells. Thus, they cannot entirely take into account the *in vivo* complexity of immune cell metabolism. Indeed, one of the major current caveats is that the *in vitro* investigations cannot contribute to reproduce immune cell metabolism really faithfully. More studies *in vivo* or in more sophisticated culture systems, like organoids, will greatly improve our current knowledge on how exactly metabolic alterations in immune cells affect the response to their *in vivo* environments. Nevertheless, due to the emerging of novel techniques in the metabolism realm, some of the current paradigms will be likely challenged. The converse studies are also lacking. Addressing this question, of how distinct tissue niches, with divergent metabolic requirements, can influence the nature of metabolic reprogramming inside immune cells will be not only a challenging but also interesting topic for future research. Discovering the nature of the tissue-derived instructional signals that stimulate such adaptive metabolic reprogramming would allow extraneous modulation of immune functions, which could be beneficial in disease states.

Moreover, so far most studied models of immune cell metabolic reprogramming mainly rely on a binary shift between mitochondrial respiration and glycolysis and glutaminolysis. This perspective should be reevaluated. Given the diversity of immune cell types and their metabolic plasticity, investigations should examine if immune cell subsets employ other adaptive metabolic strategies to meet their emerging energy demands. Last but not least, it would be highly intriguing to expand our current prospective on the transcriptional and post-transcriptional regulation of bioenergetics by searching for novel metabolic nodes or shifts, which act as critical coordinators of metabolic adaptations in immune cells.

Cell type	Function	Metabolic phenotype
<i>Immune activation or inflammatory</i>		
 NK cell	MHC-independent cytotoxicity: Perforin, granzymes FASL, TRAIL IFN γ , TNF	Glycolysis and OXPHOS
 Inflammatory TAM	MHC-independent cytotoxicity: TNF, IL-1 β Oxidative burst Antigen presentation	Glycolysis and PPP
 DC	DAMP processing T _{eff} cell activation Antigen presentation	Glycolysis
 T _{eff} cell	Antigen-specific cytotoxicity: Perforin, granzymes FASL IFN γ , TNF	Highly glycolytic and OXPHOS Amino acid metabolism (arginine, tryptophan, serine, leucine, glutamine, cysteine) PPP
 T _{mem} cell	Maintain long-lived response	OXPHOS
<i>Immunosuppression</i>		
 MDSC	IL-10, TGF β Amino acid depletion Polyamines, kynurenine	Glycolysis and OXPHOS
 Immunosuppressive TAM	IL-10 Amino acid depletion Polyamines, kynurenine VEGF	OXPHOS, HBP
 T _{reg} cell	IL-2 sequestration: Dampen APC co-stimulation IL-10, TGF β Adenosine	OXPHOS

Figure 5: Functional of metabolic phenotypes of different vertebrate immune cells, following inflammation or immunosuppression. Adapted from Leone et al. 2020.

1.6 Energy regulation through RNA translation modulation

An inability to maintain energy homeostasis is a common factor in metabolic disorders such as obesity, diabetes, and cancer (Albert and Hall, 2015). Normally cells possess central signaling pathways by which they sense their nutrient and/or energy status and adjust their metabolic states. mRNA translation is tightly linked to energy metabolism, which acts as key node of metabolic control. Motile cells face the challenge of producing sufficient ATP to meet the energy demands of both an elevated mRNA translation rate and motility itself (Leibovitch and Topisirovic, 2018; Roux and Topisirovic, 2018).

1.6.1 TOR-mediated control of mRNA translation and bioenergetics

The highly conserved Target of Rapamycin (TOR) signaling pathway is a central regulator of growth and metabolism in all eukaryotes, which coordinates energy consumption by modulating the general translational apparatus as well as ATP production in mitochondria (Albert and Hall, 2015; Leibovitch and Topisirovic, 2018).

The mammalian mechanistic target of rapamycin (mTOR) is a serine/threonine kinase that plays a critical role in regulating cell growth, proliferation and migration (Saxton and Sabatini, 2017). TOR exists in mainly two different complexes: TOR complex 1 (TORC1) and TOR complex 2 (TORC2) (Liu and Parent, 2011, Saxton and Sabatini, 2017; Carson et al., 2012; Zou et al., 2020). The mTORC1 stimulates mRNA translation and other anabolic processes in response to a variety of extracellular/intracellular signals, thereby promoting cell growth, proliferation, and homeostasis. The mTORC2 controls cell survival, cytoskeletal organization, lipogenesis, and gluconeogenesis (Sarbasov et al., 2004). Mechanistically, mTORC1 accelerates cellular bioenergetics by enhancing the translation of mRNAs, which encode proteins with mitochondrial function and ETC components, and therefore boosting mitochondrial respiration capacity and ATP production (Morita et al., 2013). mTOR inhibition reduces mitochondrial energy production, which is highly needed for energy demanding processes like translation and cell migration. A body of studies in *Drosophila* has shown that TOR signaling specifically promotes fly longevity, which is mediated by TORC1 of the TOR pathway, through alteration of autophagy and the reprogramming of protein translation (Bjedov et al., 2010; Robida-Stubbs et al., 2012; Carvalho et al., 2017). In fly larvae, dTOR inhibition causes a similar phenotype to amino acid deprivation, developmental arrest and lipid vesicle aggregation (Beauchamp and Plataniias, 2013). Conclusively, the conserved TOR pathway, via translational regulation, plays a pivotal function in cellular energy hemostasis in response to metabolic shifts.

I will briefly explain the steps of mRNA translation and its regulation. Afterwards, I will talk about the mechanisms by which the TOR pathway applies its controlling role to the translation of its target mRNAs, specifically 5'TOP mRNAs, thus affecting cellular biogenetics as a metabolic response.

1.6.2. mRNA translation

Cell migration is tightly regulated at multiple levels, including transcriptional, post-transcriptional (mRNA splicing, mRNA stability and localization, mRNA translation and efficiency) as well as post-translational stages (Roux and Topisirovic, 2018). Intracellularly, it is coordinated through the regulation of the general transcriptome and translatoome, post-translational modifications, cytoskeleton organization, and signaling pathways. Post-transcriptional control of mRNA metabolism plays a critical role in the fine-tuning of the cellular genetic and metabolic programs.

1.6.3. Steps of mRNA translation process

Protein synthesis in eukaryotes occurs in four major steps: initiation, elongation, termination and ribosome recycling (Hershey et al., 2012, Leibovitch and Topisirovic, 2018) (Figure 6):

(A) Initiation: the first step requires the ATP-dependent activation of 5'-capped mRNA by initiation factor 4F (eIF4F), the assembly of the 43S pre-initiation complex (PIC) and eIF4F (1), 48S PIC assembly (2), ATP-dependent unwinding of 5'UTR by eIF4A and RNA scanning

(3), and recognition of the translational initiation codon, followed by GTP-dependent release of the ternary complex (TC) and finally joining of the 60S ribosomal subunit (4).

(B) Elongation: Aminoacyl-tRNAs (aa-tRNA) are recruited by elongation factor 1A (eEF1A). The anticodon of the incoming aa-tRNA is matched against the mRNA codon in the A site, resulting in the release of eEF1A by eIF1B (1). The polypeptide chain is growing with an empty tRNA in the P site (2). As the mRNA moves one codon forward, tRNAs are aminoacylated through ATP hydrolysis by aminoacyl tRNA synthetase (3). These steps are repeated until the ribosome encounters an in-frame stop codon.

(C) Termination: An in-frame stop codon is positioned in the A site and release factors 1, 2 and 3 (eRFs) form a complex near the A site (1). Upon recognition of the stop codon by eRF1 and eRF2, the polypeptide chain is released following GTP hydrolysis by eRF3 (2). The 40S, 60S ribosomal subunits and mRNA are dissociated, followed by releasing of eRFs (3).

(D) Ribosome recycling: The ribosomal subunits are again recycled (Figure 6).

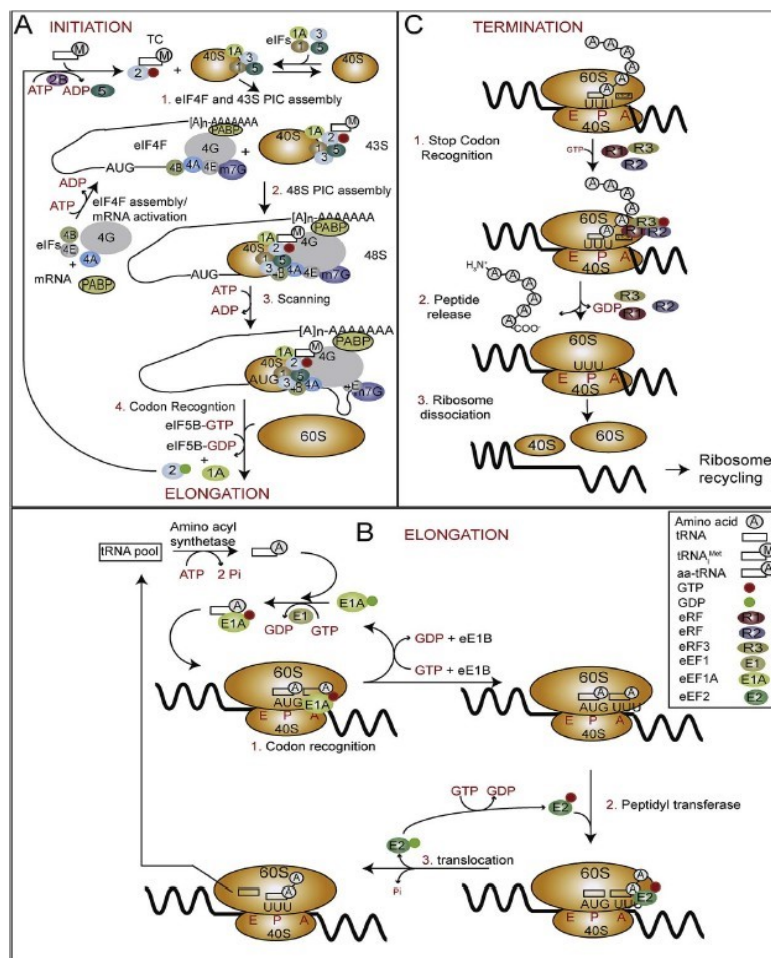


Figure 6: The eukaryotic mRNA translation occurs in four major steps: initiation, elongation, termination and ribosome recycling. Abbreviations: eIF, eukaryotic initiation factor; eRF, eukaryotic release factor; eEF, eukaryotic elongation factor; PIC, preinitiation complex; TC, ternary complex; PABP, poly(A) binding protein; tRNAⁱ Met, initiator tRNA; M7G, 7-methylguanylate cap. Adapted from Leibovitch and Topisirovic, 2018.

1.6.4 Regulation of mRNA translation by cis- and trans-acting signals

Regulation of mRNA translation partially relies on the activity of trans-acting factors, including RNA-binding proteins (RBPs) and/or non-coding RNAs (ncRNAs) that recognize cis-acting signals residing in the 5'- and 3'-untranslated regions (5'- and 3'-UTRs) or in the RNA coding sequence. The most common RNA-binding proteins cooperating in RNA translation include RNA chaperones, DEAD-box RNA helicases, and tertiary structure-binding proteins, which stabilize the 'correctly' folded RNAs. Translational regulation of most mRNAs occurs mainly at the initial stage (Liao et al., 2015; Di Liegro et al., 2014).

i. 3'-UTR cis-regulatory elements

Two common cis-acting sequences within the 3'-UTR of mRNAs are the AU-rich elements (ARE) and the stem-loop structure, which are critical elements in controlling gene expression at the post-transcriptional level and mRNA degradation (Spriggs et al. 2010).

ii. 5'-UTR cis-regulatory elements

For protein synthesis process, the 5'-UTR acts as an internal ribosome entry site (IRES) and can recruit ribosomes directly in combination with IRES transacting factors (ITAFs) to initiate translation in a cap-dependent manner (Liao et al., 2015; Di Liegro et al., 2014). The eukaryotic 5'-UTR region is critical for ribosome recruitment to the mRNA and start codon choice and plays a major role in the control of translational efficiency and shaping of the cellular proteome (Hinnebusch et al., 2016).

The 5' terminal oligopyrimidine motif (5'TOP) is a 5'UTR cis-regulatory RNA element, which is located immediately downstream of the 7-methylguanosine (m7G) cap of TOP mRNAs. It consists of a cytosine at the cap site, followed by a stretch of 4-15 pyrimidines. Besides the 5'TOP tract, recent studies have identified similar conserved 5'-UTR cis-acting elements, including 5'TOP-like (5'TOPL) and pyrimidine-rich translational element (PRTE) sequences in other mRNAs. Interestingly, such subsets of mRNAs mainly encode proteins of the translation machinery, mitochondrial proteins and proteins involved in cell cycle progression as well as invasion and metastasis (Albert and Hall, 2015; Morita et al., 2015; Thoreen et al., 2012; Meyuhas and Kahan 2015; Zou et al., 2020).

1.6.5 Regulation of 5'TOPL mRNA translation by TOR pathway

The conserved 5'TOP(L) sequence, and potentially other similar 5'UTR tracts, function as a potent metabolic sensor that sensitize the translation of respective mRNAs in response to alterations in metabolic circumstances. Translational control of 5'TOP(L) mRNAs seems to be conserved in metazoans. Interestingly, most TOR-responsive genes contain either 5'TOP, 5'TOP-like or PRTE. In response to metabolic alterations, TOR affects the translation of this set of mRNAs, many of them are associated with RNA translation, metabolism, mitochondrial function and bioenergetics, and invasion (Hsieh et al, 2012; Thoreen et al., 2012).

Two key downstream targets of TOR in RNA translation process are the ribosomal subunit kinase (S6K) and the eukaryotic initiation factor 4E-binding protein (4E-BP).

Mechanistically, TORC1 positively regulates translation elongation rates via phosphorylation/inactivation of eEF2K through ribosomal S6Ks, which has shown to consequently support tumor initiation and early carcinogenesis (Kenney et al., 2014). Simultaneously, TORC1 phosphorylates and inactivates translational suppressors of 4E-BPs, leading to a selective increase in the translation of 5'TOP mRNAs, which mainly encode ribosomal and mitochondrial proteins, as well as long 5'UTR mRNAs, commonly encoding for proteins involved in mitochondrial integrity (Gandin et al., 2016; Lee et al., 2020). Moreover, activated AMPK, another member of the TOR pathway, acts as a central sensor of energy status in cells to speed down catabolic processes, including protein synthesis and mitochondrial OXPHOS by TORC1 inactivation (Morita et al., 2013). As a conserved regulatory pathway in flies, under calorie restriction (CR) condition 4E-BP, the TOR translational repressor, suppresses the translation of 5'dPRTE mRNAs, whose proteins function in protein synthesis and mitochondrial OXPHOS (complexes I and IV) (Zid et al., 2009).

1.7 *Drosophila* immune cells as an in vivo model to study cellular bioenergetics of tissue invasion

Invasive migration plays a crucial role not only during development and homeostasis, but also in pathological states such as immunopathology and tumor metastasis (Blumberg et al., 2019). *Drosophila* macrophage tissue infiltration is an interesting system to study invasive migration. It carries striking similarities to mammalian immune cell infiltration and cancer cell invasion. Therefore studying this process could also bring new understanding of invasion in higher organisms (Siekhaus et al., 2010; Ratheesh, et al., 2015).

As with any active biological process, cell migration costs energy. Despite the importance of cellular bioenergetics for migration, little is known about the contributions of metabolic programs that maintain energy in an *in vivo* context (Li et al., 2019, Nagai et al., 2020; Zanotelli et al., 2018; Zhang et al., 2019). Since most major metabolic regulators and pathways are evolutionarily well conserved, *Drosophila melanogaster* has emerged as a model system for bioenergetics and metabolism studies (Zid et al., 2009).

To explore possible metabolic shifts that link cell bioenergetics to cellular movement, in my PhD project I have employed the tissue invasion of *Drosophila* immune cells. In this part I will describe *Drosophila* immune system and discuss the different functions of macrophages that could depend on distinct bioenergetics.

1.8 *Drosophila melanogaster* immune system

For proper development and defense, the fruit fly *Drosophila melanogaster* relies on multiple innate compartments, many of which are shared with higher organisms (Lemaitre & Hoffmann, 2007). The two main components are the humoral and cellular systems. The humoral response is mainly induced in the fat body, which is thought of as the insect equivalent to the liver. The activated fat body can secrete antimicrobial peptides into the hemolymph. The cellular immune system involves phagocytosis, nodule formation, and

encapsulation of pathogens. The mammalian innate cellular immune response comes from both the lymphoid and myeloid lineages, in which neutrophils, macrophages, and dendritic cells (DCs) act as professional phagocytes. As a comparison, three morphologically distinct types of immune cells, called hemocytes, have been identified in *Drosophila*. Macrophages, also referred to as plasmatocytes, are professional phagocytes that eliminate both apoptotic cells and invading particles, secrete extracellular matrix (ECM) components and signaling molecules, as well as participate in wound healing and developmental tissue patterning. Macrophages make up ~95% of circulating hemocytes and most resemble the mammalian monocyte/macrophage lineage (Franc et al. 1996, Evans and Wood, 2011). *Drosophila* macrophages display striking similarities with their vertebrate orthologs in ontogeny, functionality, and migratory behavior. The second cell type, crystal cells are involved in the melanization of invading organisms and also facilitate wound repair and the hypoxic response. The third type, lamellocytes, rarely seen in healthy larvae, primarily respond to wasp parasitization and the encapsulation of invading pathogens. (Banerjee et al., 2017; Williams et al., 2007).

1.8.1 Origin of *Drosophila* immune cells

Drosophila hematopoiesis much like in vertebrates occurs in two waves:

1. Primitive hematopoiesis, as a first wave, occurs in the early embryonic stage from head mesoderm. The hematopoietic precursors proliferate and give rise to both mature macrophages and crystal cells and constitute the larval circulatory and sessile pools of immune cells and later in adult stages. Similar transcription factors, including the GATA factor Serpent (Srp), the friend of GATA (FOG) transcription factor, RUNX, and U-shaped (Ush) regulate the specification and fate in macrophages during both *Drosophila* and vertebrate hematopoiesis. Moreover, the proliferation and survival of macrophages is later controlled by fly orthologs of the vertebrate platelet-derived growth factor/vascular endothelial growth factor (PDGF/VEGF), named family of growth factors (Pvf) (Brückner et al., 2004; Gold and Brückner, et al. 2015)
2. Definitive hematopoiesis, as a second wave, initiates post-embryonically in a larval hematopoietic organ, called the lymph gland, which supplies all three differentiated and mature immune cell types from multipotent undifferentiated progenitor cells. By the early pupal stage, the lymph gland releases the differentiated macrophages into circulation contributing to immune cells in the adult fly (Gold and Brückner, 2015; Banerjee et al., 2017).

1.8.2 Embryonic migration of *Drosophila* macrophages

The embryonic migration of *Drosophila* macrophages occurs mostly along paths where their function is required for further developmental purposes. After their birth, embryonic macrophages have to disperse from the head mesoderm throughout the embryo by the end of embryogenesis (Tepass et al., 1994). Meanwhile they can actively engulf cell debris as well as pathogens upon infection.

Embryonic macrophages are specified in the head mesoderm at embryonic stages 4-6. At stage 9, macrophages start dispersing along three developmentally hardwired paths following chemotactic signals from the fly orthologs of chemokines PDGF and VEGF, named (Pvf) 2 and 3, to populate the entire embryo (Figure 7). In migratory route 1, macrophages move from the head mesoderm across the yolk sac and into the extended germband. T-antigen, a common feature of human cancer cells, is upregulated in *Drosophila* macrophages and tunes the developmentally programmed tissue infiltration of these immune cells. Higher macrophage T-antigen levels require Minerva, an atypical major facilitator superfamily (MFS) member, which enables macrophage dissemination and invasion and is highly maintained up to the vertebrates (Valoskova and Biebl et al., 2018). The amnioserosal tissue (AS), laying adjacent to the germband, expresses *Drosophila* tumor necrosis factor (TNF), Eiger. Eiger acts via its receptor Grindelwald on the macrophages to facilitate invasive germband entry of immune cells and their initial extravasation between the apposing ectoderm and mesoderm. Mechanistically, fly TNF enables macrophage invasion by lowering active Myosin levels in the germband ectodermal cortex and thus apical tension in the ectoderm through enhanced localization of Patj (Pals-1-associated tight junction protein) (Ratheesh et al. 2018). Once in the germband, macrophages secrete collagen IV, which facilitates the bone morphogenetic protein (BMP) signaling required for the proper positioning of the kidney-like organs called the renal tubules. The extended germband undergoes retraction to the posterior of the embryo by late stage 12. Based on previous studies, migration along the extended germband requires macrophage tissue infiltration and shares molecular similarities to vertebrate immune cell transmigration in its requirement for modulation of Integrin affinity through small GTPases in macrophages (Siekhaus et al., 2010, Ratheesh et al. 2015; Weavers et al., 2016).

Embryonic macrophages also migrate along the posterior ventral nerve cord (vnc) and the developing central nervous system (CNS) (1c), eventually joining other set of cells moving out of their birthplace towards the posterior along the vnc in route 2. Once populated the entire length of the developing CNS, they spread laterally in series of “rib-like” migration, which are partially patterned by the process of contact inhibition (Evan and Wood, 2011; Wood and Martin, 2017). Embryonic macrophages moving along the vnc engulf apoptotic midline glia and facilitate vnc condensation. The final route, number 3, moving along the forming heart, is required for dispersal of macrophages to exert their larval immune functions.

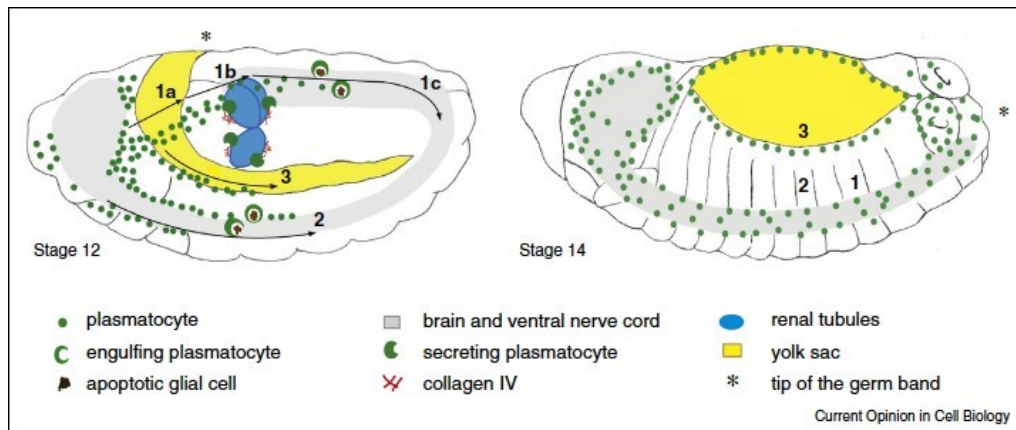


Figure 7: Macrophage migration routes and their functional relevance during embryonic development. Schematic of two embryos (early Stage 12 on the left and Stage 14 on the right) illustrate that macrophages derived from the head mesoderm move along three main predetermined routes during embryonic development. At early Stage 12, a group of immune cells move over the yolk sac to the tip of the extended germband (route 1a). They then invade into the germband epithelium and reach the renal tubules where they secrete collagen IV to remodel them (route 1b). Macrophages in the germband continue along the posterior ventral nerve cord (vnc, route 1c in left embryo, route 1 in right embryo). While another set move out from the head mesoderm (route 2 in both embryos) along the anterior vnc, where they phagocytose apoptotic midline glia. The third group migrates along the developing heart also towards the posterior of the embryo (route 3 in both embryos). Arrows indicate the migration routes Adapted from Ratheesh et al., 2015.

1.8.3 Functional roles of *Drosophila* macrophage migration

Fly macrophages share striking parallels with their vertebrate counterparts, both in their embryonic migrations and their developmental functions (Weavers et al., 2016; Ratheesh et al., 2015). Macrophages are highly motile phagocytic cells that are actively recruited to clear infections and debris from developmental tissue homeostasis or tissue damage. Such professional phagocytosis requires a high degree of morphological and therefore plasticity of the actin cytoskeleton. Blocking phagocytosis either by depleting macrophages or Croquemort (Crq), leads to failed condensation of the vnc, indicating the important role of phagocytosis for proper embryonic development (Buchon et al., 2014; Guillou et al. 2016; Banerjee et al., 2017). Macrophages employ two distinct modes of phagocytosis *in vivo* to fulfill their critical clearance function. The Arp2/3-complex-dependent ‘lamellipodial phagocytosis’ allows highly motile macrophages to migrate toward and engulf apoptotic corpses. Alternatively, Diaphanous/Ena derived ‘filopodial phagocytosis’ allows macrophages to overcome spatial constraint and reach out to apoptotic debris (Davidson and Wood, 2020).

These immune cells might also generate an immunological memory, a trait previously linked to the adaptive system. Apoptotic corpse phagocytosis is an essential step to prime *Drosophila* macrophages for a robust inflammatory recruitment to tissue damage and infection. Priming is triggered via calcium-induced JNK signaling, which leads to upregulation of the damage receptor Draper. This thus provides a molecular memory within macrophages that allows them to rapidly boost the innate inflammatory response to subsequent injury or infection that is associated with extensive apoptotic cell death (Weaver et al., 2016).

1.8.3.1 Collaboration of *Drosophila* macrophages with adipose tissue

Macrophages have also been shown to exert a physiological impact on fly homeostasis. A lipid-rich diet reduced insulin sensitivity and life span in flies, both of which are mediated by macrophages (Woodcock et al., 2015). Parallel to what occurs in flies, vertebrate macrophages are also critical for controlling insulin signaling in adipocytes, where a lipid-rich diet activates macrophages and therefore disturbs organism homeostasis (Odegaard and Chawla, 2013).

Pupal macrophages can synergize with fat body cells (FBCs), *Drosophila* adipocytes, during the wound healing process. At the wound site, fat body cells in collaboration with macrophages tightly seal the epithelial wound gap and locally release antimicrobial peptides to combat wound infection (Franz et al., 2018). *Drosophila* macrophages in fat tissue can also act as professional fat storing cells, through sensing the organism's nutritional state (Remmerie and Scott, 2018). The conserved PDGF family of growth factors promotes lipid storage in fat tissue (Hoch and Soriano, 2003). A recent study investigated the role of tissue resident macrophages in adipose tissue of *Drosophila* larva, and found that, similar to adipocytes, these immune cells are critical for establishment and regulation of fat storage in fat tissue in response to dietary alterations. Macrophages produce PDGF ortholog (Pvf3) to support the storage of excess lipids by Pvr-expressing adipocytes in condition of excess nutrient intake, in an evolutionary conservation process (Cox et al., 2020).

1.8.3.2 Secretion of ECM components and tissue remodeling: renal tubule formation and vnc condensation

Macrophages as motile phagocytic cells play crucial developmental patterning roles, which require their correct distribution with the embryo. *Drosophila* has an evolutionarily conserved source of ECM proteins such as Laminin, Collagen IV (ColIV), Nidogen, and Perlecan (Perl). During embryogenesis, macrophages secrete ECM components at precise stages of development for proper basement membrane (BM) maturation and tissue remodeling (Matsubayashi et al., 2017; Banerjee et al., 2017; Olofsson and Page 2005; Bunt et al. 2010).

Regulated macrophage migration is essential for the uniform delivery of ECM proteins such as Collagen IV, Perlecan, and Laminin A (Matsubayashi et al., 2017; Sánchez-Sánchez et al. 2017). One example of this occurs during the deposition of these BM components by macrophages on renal (Malpighian) tubules, which is crucial for their embryonic morphogenesis and path finding. Collagen IV sensitizes tubule cells to localized BMP guidance cues (Bunt et al. 2010) and VEGF/PDGF ligands from the tubules attract macrophages, bringing them close enough to secrete such ECM components for ensheathment. Furthermore, embryonic vnc condensation requires the deposition of ECM components around tissues and corpse engulfment by macrophages as well as the initiation of neural activity in the CNS. When Pvr is missing, macrophage migration along

vnc route fails, which leads to the disruption of ECM deposition around the vnc and thus inhibition of its condensation (Olofsson et al., 2005; Parsons et al., 2016).

1.8.3.3 *Drosophila* macrophages and tumor metastasis

Drosophila melanogaster can also serve as a more direct model for tumor metastasis and can be investigated as a powerful model for identifying molecular pathways and intercellular interactions associated with metastasis (Parsons et al., 2016). In developing *D. melanogaster* larvae, genes, including lethal (2) giant larvae (l(2)gl), discs large (dlg), and scribbled (scrib) have emerged due to their phenotypes in a systematic screen for metastatic cell behavior.

Similar to vertebrate tissues, fly macrophages are recruited to abnormally growing clones of cells to exert different effects. In polarity gene mutation-mediated tumors, macrophages inhibit tumor growth via the production of the *Drosophila* TNF ortholog, Eiger. In contrast, in RasV12 expressing tumors similar to analogous to vertebrate tumor associated macrophages, macrophages produce TNF to trigger tumor overgrowth and invasion (Ostuni et al., 2015; Ratheesh et al., 2015).

1.8.3.4 Maintenance of stem cell niches by *Drosophila* macrophages

Recent studies show that fly macrophages are also required for maintaining and regulating the microenvironment of various stem cell niches. BM deposition by these immune cells is likewise important for later stages of development (Banerjee et al., 2017). Macrophages deposit ECM components like collagen IV to form the basement membrane around the ovarian germline stem cell niche, while loss of macrophages causes the abnormal proliferation of stem cells in adult niches (Van De Bor et al., 2015). Furthermore, macrophages regulate intestinal stem cells (ISCs) during the early phase of intestinal regeneration in the fly. Following injury in the intestinal epithelium, macrophages are recruited to the site of damage to secrete BMP, activating ISC proliferation (Ayyaz et al., 2015). Macrophages can also remotely trigger intestinal stem cell proliferation upon septic damage by secreting the cytokine-like secreted proteins, Unpaired 2 (Upd2) and Unpaired 3 (Upd3) (Cox et al., 2016).

Taken together, *Drosophila* macrophages, as professional phagocytic cells, should sustain their energy sources to be able to migrate to target destinations during development and defense. Which metabolic pathways are utilized by *Drosophila* macrophages to provide their emerging energy demands for their functions? Do macrophages undergo the same or distinct metabolic programming in responses to distinct signals in different tissues over multiple life phases? Certainly, such unanswered questions inspired me to search more in the realm of *Drosophila* immune cell metabolism to see how far their migration ability is all actually dictated by their underlying metabolic states.

Chapter 3

A concerted metabolic program that increases mitochondrial function powers tissue infiltration by macrophage leader cells

Shamsi Emtenani¹, Elliott Martin², Attila Gyoergy¹, Julia Biebl¹, Jakob-Wendelin Genger⁴, Thomas R. Hurd³, Thomas Köcher⁵, Andreas Bergthaler⁴, Prashanth Rangan², Daria Siekhaus^{1*}

*Corresponding author, daria.siekhaus@ist.ac.at

1) Institute of Science and Technology Austria, Am Campus 1, 3400 Klosterneuburg, Austria

2) University at Albany, Department of Biological Sciences, RNA Institute; 1400 Washington 6 Avenue, LSRB 2033D, Albany, NY 12222

3) Department of Molecular Genetics, University of Toronto, Toronto, Ontario, Canada.

4) CeMM Research Center for Molecular Medicine of the Austrian Academy of Sciences, 1090 Vienna, Austria

5) Vienna Biocenter Core Facilities, 1030 Vienna, Austria

ABSTRACT

Metabolic adaptation is a critical feature of migrating cells. It tunes the metabolic programs of migrating cells to allow them to efficiently exert their crucial roles in development, inflammatory responses and tumor metastasis. Cell migration through physically challenging contexts requires energy. However, how the metabolic reprogramming that underlies *in vivo* cell invasion is controlled is still unanswered. Here, we identify a novel conserved metabolic shift in *Drosophila melanogaster* immune cells that by modulating their bioenergetic potential controls developmentally programmed tissue invasion. We show that this regulation requires a novel conserved nuclear protein, named Atossa. Atossa enhances the transcription of a set of proteins, including an RNA helicase Porthos and two metabolic enzymes, each of which increases the tissue invasion of leading *Drosophila* macrophages and can rescue the *atossa* mutant phenotype. Porthos selectively regulates the translational efficiency of a subset of mRNAs containing a 5'-UTR cis-regulatory TOP-like sequence. These 5'TOPL mRNA targets encode mitochondrial-related proteins, including subunits of mitochondrial oxidation phosphorylation (OXPHOS) components III and VI and other metabolic-related proteins. Porthos powers up mitochondrial OXPHOS to engender a sufficient ATP supply, which is required for the tissue invasion of leading macrophages. Atossa's two vertebrate orthologs rescue the invasion defect. We thus elucidate that Atossa displays a conserved developmental metabolic capacity control to modulate metabolic capacities and the cellular energy state, through altered transcription and translation, to aid the tissue infiltration of leading cells into energy demanding barriers.

INTRODUCTION

Multicellular organisms require cell migration during a diverse range of physiological and pathophysiological processes, including development, wound repair, immune responses, tissue homeostasis, and cancer metastasis (Kurosaka and Kashina, 2008; Nourshargh and Alon, 2014; Friedl, et al. 2012). Cell motility is characterized by the coordinated movement of individual or multiple cells in a specific direction through 2-D and 3-D environments (Friedl and Brocker, 2000; Montell, 2008; Petrie and Yamada, 2012; Yamada and Sixt, 2019; Bodor et al., 2020).

Cell migration is an active biological process that costs energy. Cells consume the common energy budget, ATP, to convert it into mechanical power. During migration, cells remodel their shapes, expending energy to restructure the actin cytoskeleton, activate myosin ATPase, spread more widely and reorganize the cell membrane, particularly at the leading edge (Bernstein et al., 2003; Cunniff et al., 2016; Cuvelier et al., 2009; Rottner et al., 2019; Li et. al, 2019). To move inside tissues, cells dynamically adapt their internal machinery to generate forces, remodeling their own shapes and sometimes also that of the surrounding cells, both of which are energy-demanding processes (Van Horsen et al., 2009; Zanotelli et al., 2018; Kelley et al., 2019). Thus in order to advance, migrating cells boost their energy sources in response to physically challenging environments (Xie et al., 2021). When coordinated groups of cells move into through physically constrained environments, the pioneer or leading cells bear the majority of the energetic costs to forge an initial path (Khalil et al., 2010; Zhang, et al., 2019, Commander et al., 2020). However previous *in vitro* studies have produced contradictory results as to the metabolic pathways leader cells utilize; some studies have shown a greater dependence on glucose uptake in leader, others in follower cells (Zhang, et al., 2019; Commander et al., 2020). Nevertheless, the question remained, as to what concerted metabolic programs tune the energy state of pioneer cells *in vivo* towards invasion.

To identify novel mechanisms governing *in vivo* migration, we study *Drosophila* macrophages, also called plasmotocytes. Macrophages are the primary phagocytic and innate immune cell in the *Drosophila* embryo and share remarkable similarities with vertebrate macrophages in ontogeny, functional properties, and migratory behavior (Brückner et al. 2004; Nourshargh et al., 2010; Ratheesh et al. 2015; Weavers et al., 2016; Wood et al. 2017; Weavers et al., 2020). Phagocytic macrophages are credited with exerting essential roles not only for a fast resolution of inflammation, but also by an active engagement in long-lasting developmental and physiological processes, such as tissue homeostasis and remodeling (Caputa et al. 2019; Riera-Domigo et al., 2020; Buck et al., 2017; Bunt et al., 2010). *Drosophila* macrophages are first specified in the head mesoderm of the embryo and later follow guidance cues from the platelet-derived growth factor- and vascular endothelial growth factor-related factors (Pvf) 2 and 3 to disseminate along predetermined routes (Brückner et al. 2004). We have previously found that in late Stage 11 to Stage 12 of embryogenesis a dynamic chain of macrophages penetrates into the extended germband between the closely apposed

ectoderm and mesodermal tissues (Siekhaus et al., 2010; Ratheesh et al., 2018), moving against the resistance of surrounding tissues (Siekhaus et al., 2010; Ratheesh et al., 2018; Valoskova et al., 2019). The rate limiting step for tissue invasion is the infiltration of the pioneer macrophage, a process affected both by the properties of the surrounding tissues (Ratheesh et al., 2018) as well as macrophages themselves (Valoskova et al., 2019).

Here we identify a program that orchestrates cellular bioenergetics to power the invasive capability of pioneer macrophages. We characterize a metabolic shift orchestrated in these immune cells by a single previously uncharacterized nuclear factor that we name Atossa. We show that Atossa governs transcriptional and translational changes that increase OXPHOS through a diverse set of proteins affecting mitochondrial function. Our work thus reveals a cellular mechanism to easily induce a concerted metabolic and mitochondrial reprogramming that supports higher energy levels, here utilized for tissue invasion in an *in vivo* context. Given that we find that Atossa's mammalian orthologs maintain its regulatory capacity, our data lays the foundation for studies in mammalian cells that can impact both normal physiological and pathological conditions. Understanding how invading cells are metabolically rewired to meet the bioenergetics needs evoked during movement into distinct complex tissue niches would expand the current knowledge aimed at developing novel tissue-specific therapeutic tactics against diverse pathological conditions, from autoimmunity to cancer.

RESULTS

CG9005 is required in macrophages for their early invasion into the extended germband

To identify novel molecular pathways mediating macrophage germband invasion, we searched for previously unstudied genes enriched in macrophages prior to and during germband tissue entry. In macrophages CG9005 is highly expressed from Stage 7 through Stage 10-12, the period in which macrophages move towards and invade into the germband. CG9005 is also expressed ubiquitously at low levels through Stage 12 and in salivary glands (<https://insitu.fruitfly.org/>). CG9005 is uncharacterized, but is predicted to contain a conserved domain of unknown function 4210 (DUF4210) and a Chromosome segregation domain (Chr_Seg) (Fig. 1A). CG9005 also displays two trans-activating domains (TADs) common among transcription factors as well as nuclear localization signals (NLS) and a nuclear export signal (NES), potentially indicating shuttling between the nucleus and cytoplasm. We examined a P element insertion allele, *CG9005^{BG02278}*, henceforth abbreviated to *CG9005^{PBG}*, visualizing macrophages through expression of a nuclear fluorescent marker. We quantified the number of macrophages within the germband in fixed embryos at Stage 12 and observed a 36% decrease in *CG9005^{PBG}* mutant embryos compared to the control (Figs. 1B-C and 1E). We also saw a similar decrease when the *CG9005^{PBG}* mutant was placed over either *Df(2R)ED2222* or

D. melanogaster CG9005

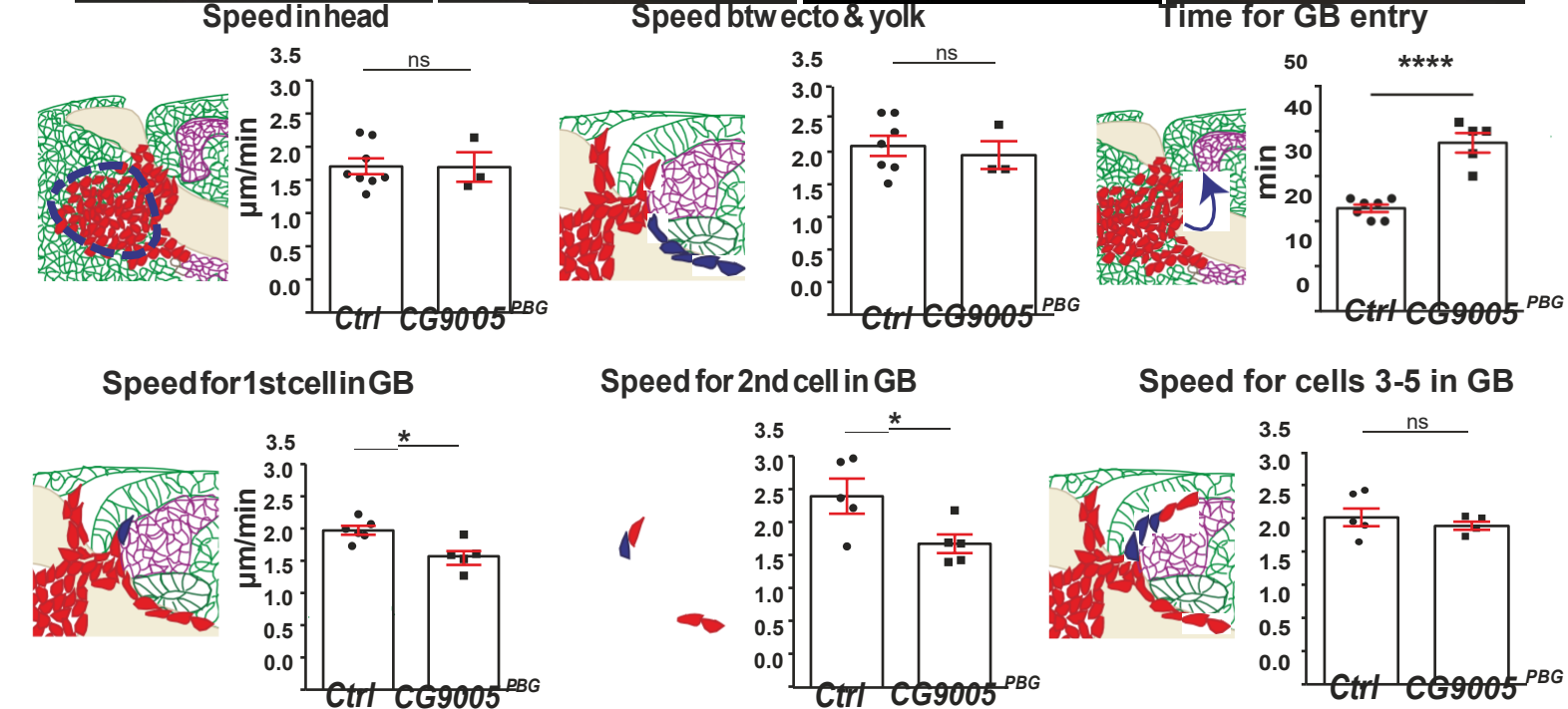
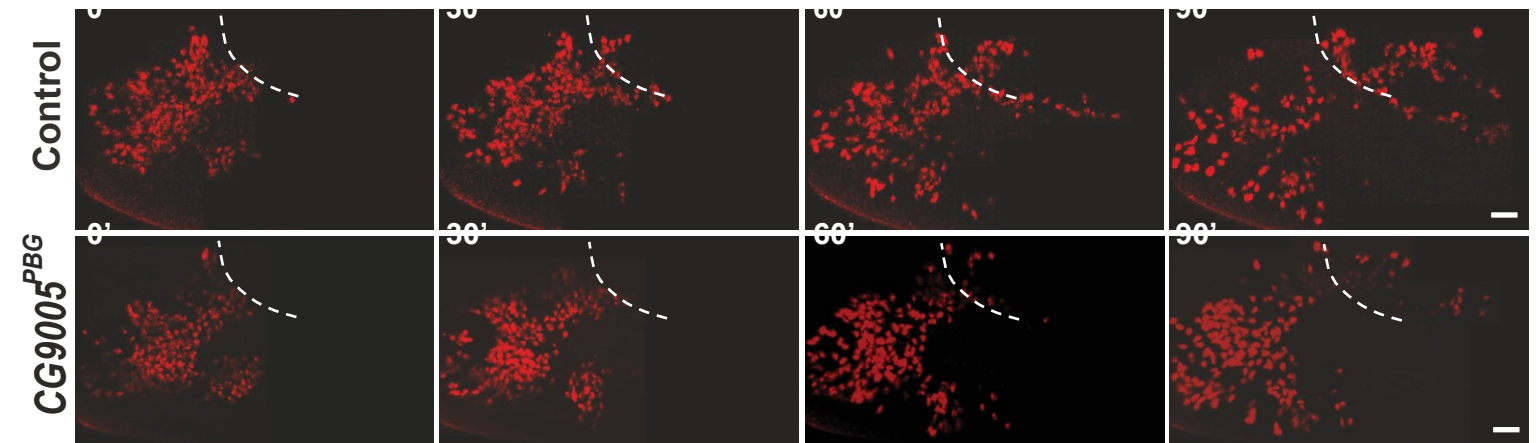
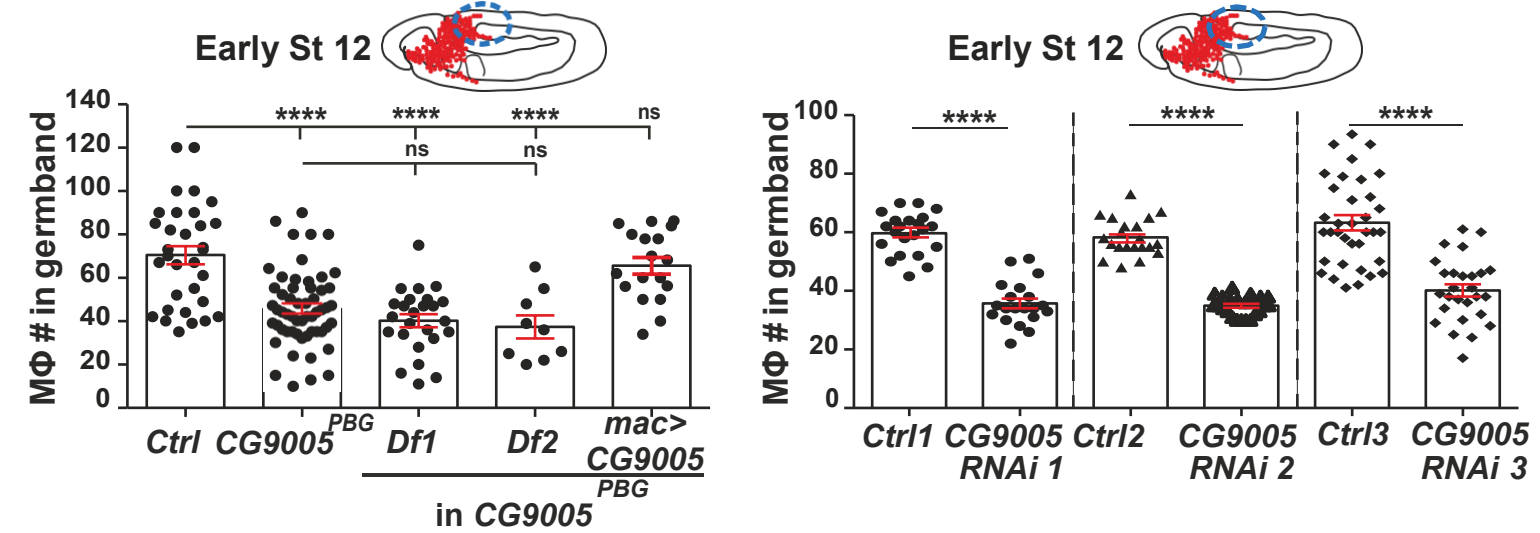
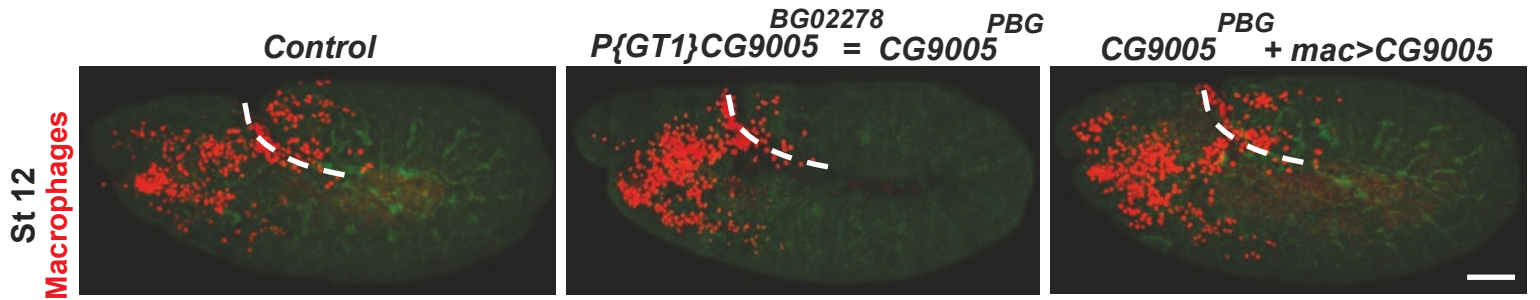
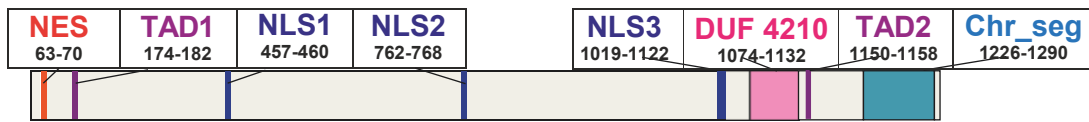


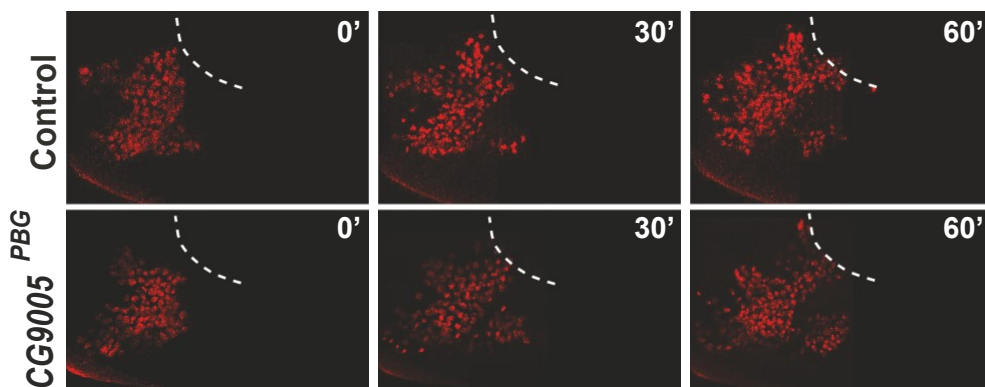
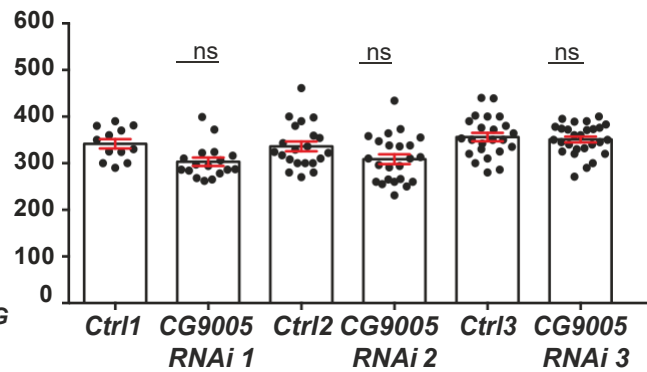
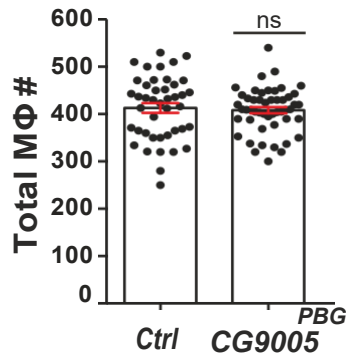
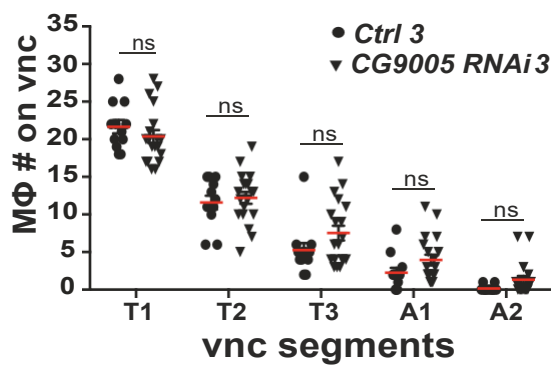
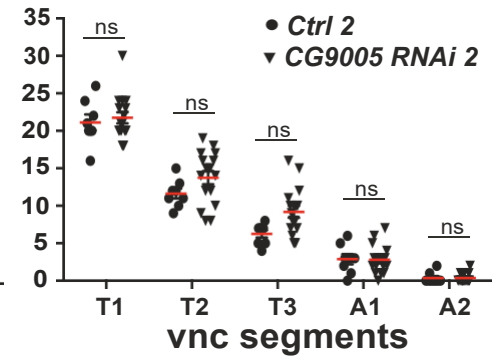
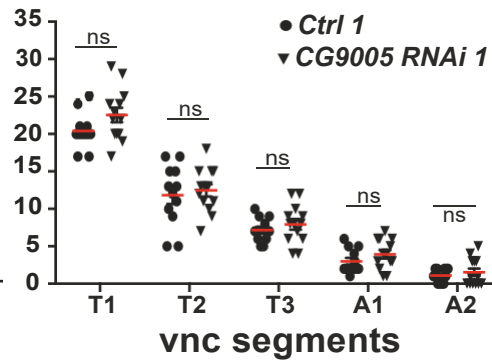
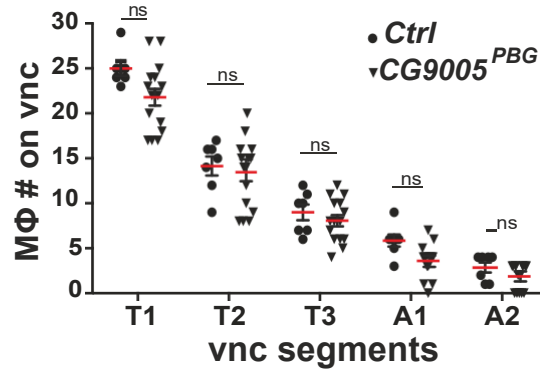
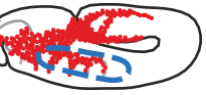
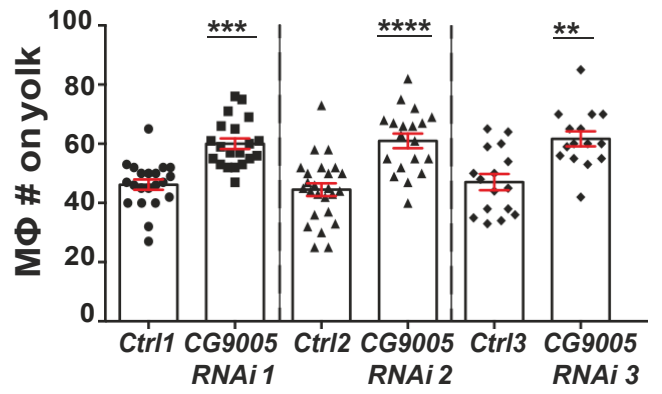
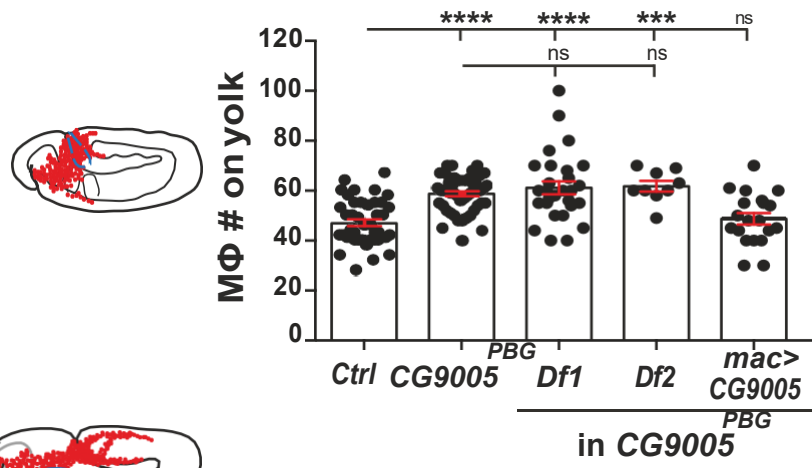
Figure 1. CG9005 acts in macrophages to spur pioneer cell infiltration into the germband tissue. Fig 1A. Deduced protein structure of CG9005. CG9005 contains two conserved motifs, a domain of unknown function (DUF4210) and a chromosome segregation domain (Chr_Seg), as well as a predicted nuclear localization signal (NLS), a nuclear export signal (NES), and two transactivation domains (TAD). **Figs. 1B-D.** Representative confocal images of Stage 12 embryos from the control, the $P\{GT1\}CG9005^{BG02278}$ P element mutant (henceforth called $CG9005^{PBG}$), and $CG9005^{PBG}$ with $CG9005$ expression restored in macrophages. Macrophages (red) are visualized by $srpHemo-H2A::3xmCherry$ expression and Phalloidin by antibody staining green). “*mac*” represents the $srpHemo-Gal4$ driver. Germband edge indicated by dotted white line. **Fig 1E.** Quantification reveals a significant decrease in the number of macrophages that have penetrated the germband in Stage 12 embryos from the $CG9005^{PBG}$ mutant (n=56), and from embryos containing this mutation over two different deficiencies (Df) that completely remove the gene ($CG9005^{PBG}/Df1(2R)$ n=25 and $CG9005^{PBG}/Df2(2R)$ n=9), compared to the control (n=35). Expression of $CG9005$ in macrophages rescues the $CG9005^{PBG}$ mutant phenotype arguing that $CG9005$ is required in macrophages for germband penetration (n=18 for rescue, p<0.0001 for control vs mutant, p=0.98 for control vs rescue, p=0.001 for mutant vs rescue). $Df1(2R)=BL8911$, $Df(2R)ED2222$. $Df2(2R)=BL23159$, $Df(2R)BSC259$. **Fig 1F.** Macrophage specific knockdown of $CG9005$ by UAS RNAi lines under the control of $srpHemo-GAL4$ can recapitulate the mutant phenotype (RNAi 1= $vdr106589$, n=20; control 1, n=22, p<0.0001. RNAi 2= $vdr36080$, n=23; control 2 n=21, p<0.0001. RNAi 3= $BL33362$, n=28; control 3 n=35, p<0.0001). **Fig 1G.** Stills from two-photon movies of control and $CG9005^{PBG}$ mutant embryos, showing macrophage nuclei labeled with $srpHemo-H2A::3xmCherry$ migrating starting at Stage 10 from the head towards the germband and while invading into the germband tissue. Elapsed time indicated in minutes. The germband edge (white dotted line) was detected by yolk autofluorescence. **Figs. 1H-I.** Quantification shows no change in macrophage migration speed (H) in the head or (I) between the yolk sac and the germband mesoderm in the $CG9005^{PBG}$ mutant compared to the control. Head speed: control=2.2 $\mu\text{m}/\text{min}$, mutant=2.2 $\mu\text{m}/\text{min}$; movie #: control=8, mutant=3; track #: control=360, mutant=450, p=0.65. Between yolk sac and germband speed: control=2.6 $\mu\text{m}/\text{min}$, mutant=2.4 $\mu\text{m}/\text{min}$; # movies: control=7, mutant=3; # tracks: control=46, mutant=19, p=0.62. **Fig 1J.** The time required for the first macrophage nucleus to enter into the extended germband is increased by 65% in the $CG9005^{PBG}$ mutant compared to the control (control=22.8 min, n=7, mutant=37.4 min, n=5, p<0.0001). Blue arrow in schematic indicates the route analyzed. **Fig 1K.** The migration speed of the first and second macrophage into the germband between the mesoderm and ectoderm is significantly slower respectively in the $CG9005^{PBG}$ mutant compared to the control. First macrophage speed: control=2.5 $\mu\text{m}/\text{min}$, mutant=2.1 $\mu\text{m}/\text{min}$, movie #: control=6, mutant=5, p=0.012. Second macrophage speed: control=2.9 $\mu\text{m}/\text{min}$, mutant=2.2 $\mu\text{m}/\text{min}$, movie #: control=5, mutant=5, p=0.03. **Fig 1M.** The migration speed of the third to fifth macrophage nuclei along the first 25-30 μm of the path between the germband mesoderm and ectoderm is similar in the $CG9005^{PBG}$ mutant and the control (speed: control=2.5 $\mu\text{m}/\text{min}$, mutant=2.4 $\mu\text{m}/\text{min}$, movie #: control=5, mutant=4, p=0.17). Throughout this work, embryos were staged for imaging and quantification based on germband retraction away from the anterior of less than 29% for stage 10, 29%-31% for stage 11, and 35%-40% for stage 12. In all figures histograms show mean \pm SEM and ns=p>0.05, *p<0.05, **p<0.01, ***p<0.001, ****p<0.0001. One-way ANOVA with Tukey for (E-F), and unpaired t test for (H-M). Scale bars: 5 μm in (A), 30 μm in (B), and 50 μm in (I).

$Df(2R)BSC259$ that remove the $CG9005$ gene entirely (Fig. 1E), arguing that $CG9005^{PBG}$ is a genetic null for macrophage germband invasion. Expressing wild type $CG9005$ in macrophages in the $CG9005^{PBG}$ mutant completely restored their capacity to invade the germband (Figs. 1D-E). To further validate $CG9005$'s specific requirement in macrophages for their germband invasion, we depleted $CG9005$ in these cells by separately driving one of three independent RNA interference (RNAi) lines in macrophages. Fixed embryos from $CG9005$ RNAi 1, RNAi 2, and RNAi 3 displayed a 40%, 40%, and 37% decrease in macrophages within the germband compared with their controls (Fig. 1F). We concomitantly observed a significant increase in the number of macrophages sitting on the yolk next to the germband in the $CG9005^{PBG}$ mutant (22%, Fig. S1A) and the RNAi lines (25% for RNAi 1, 27% for RNAi 2, and 24% for RNAi 3, Fig. S1B) compared to their controls,

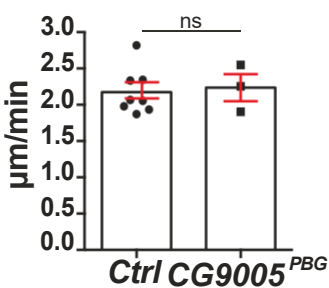
supporting the conclusion that macrophages in these backgrounds migrate normally up to the germband but then are less able to enter. To determine if the absence of *CG9005* could be causing general migratory defects, we counted macrophages migrating along the ventral nerve cord (vnc) in late Stage 12 embryos, a route guided by the same Pvf factors that lead into the germband (Brückner et al., 2004; Cho et al., 2002) but one that does not require tissue invasion (Siekhaus et al., 2010; Weavers et al., 2016). There was no significant difference in the numbers of macrophages on the vnc in both the *CG9005^{PBG}* mutant (Fig. 1SC) and the *CG9005* RNAi-expressing macrophages (Fig. 1SD-F), compared to their controls in late Stage 12, arguing that basic migratory processes and recognition of chemotactic signals are unperturbed. Moreover, we detected no significant change in the total number of macrophages for any of these genotypes (Fig. 1SG and 1SH). Taken together, these results from fixed embryos clearly suggest that *CG9005* is specifically required for the early steps of germband invasion.

Atossa (*CG9005*) is required for the efficient invasion of pioneer macrophages into the germband tissue

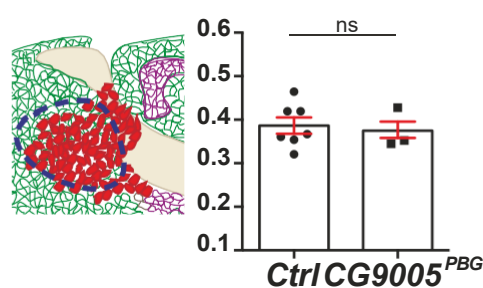
We sought to assess how the *CG9005^{PBG}* mutant altered the dynamics of macrophage migration, and what precise step of germband invasion was affected. We therefore conducted two-photon live imaging of macrophages labeled with the nuclear marker *srpHemo-H2A::3xmCherry* in the *CG9005^{PBG}* mutant and control embryos (Figs. 1G and 1SJ, Videos 1 and 2). We observed no significant change in speed during macrophage migration from their initial position at Stage 9 in the head mesoderm up to the yolk neighboring the germband entry point (Fig. 1H, Fig. 1SK-M) (speed in the head and yolk: 2.2 $\mu\text{m}/\text{min}$ for both the control and the *CG9005^{PBG}* mutant; $p=0.65$, $p=0.78$ respectively). We also did not detect any change in their directionality within these regions (directionality: 0.39 in control and 0.37 in mutant, $p=0.74$ for head, $p=0.86$ for yolk). We therefore conclude that the *CG9005^{PBG}* mutation does not affect the initial migratory steps in the head prior to germband entry. We also observed no significant change in migration speed for macrophages moving between the yolk and ectoderm (2.6 or 2.5 $\mu\text{m}/\text{min}$ for the control or *CG9005^{PBG}* mutant, respectively, $p=0.62$) (Fig.1I). However, *CG9005^{PBG}* mutant macrophages entering the germband paused longer at the tissue edge, with the first macrophage nucleus requiring 65% more time than the control to enter into the germband (time to entry: 23 min for the control and 38 min *CG9005^{PBG}* mutant, respectively, $p<0.0001$) (Figs. 1J). This delay in germband entry is consistent with our initial observation in fixed embryos that *CG9005^{PBG}* mutant macrophages accumulated at the edge of the germband. We also found that the speed of the first two pioneering macrophages invading along the path between the mesoderm and ectoderm is significantly slower in *CG9005^{PBG}* mutant embryos compared to the control (1st cell: 2.5 or 2 $\mu\text{m}/\text{min}$ for the control or *CG9005^{PBG}* mutant, respectively $p=0.012$; 2nd cell: 2.9 or



Speed on yolk



Directionality in head



Directionality on yolk

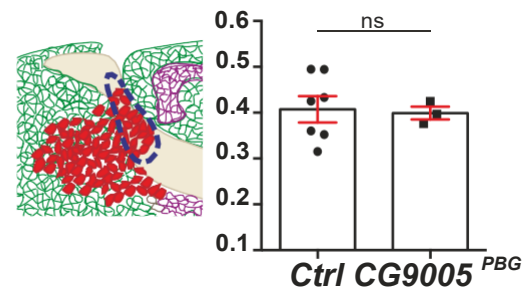


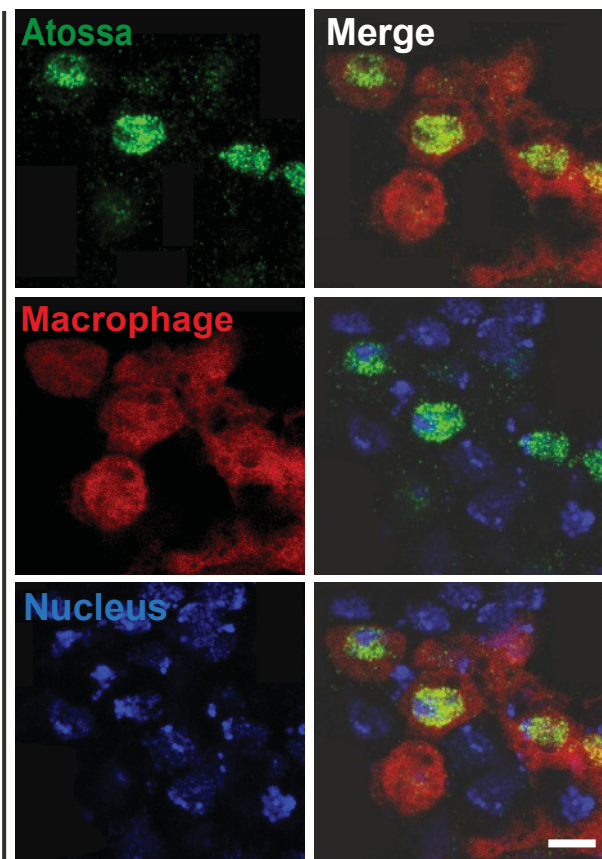
Figure S1: *CG9005^{PBG}* mutant macrophages migrate normally within the head and along the vnc. Fig S1A. Quantification of macrophages on the yolk in fixed early Stage 12 embryos shows a significant increase in the *P{GT1}CG9005^{BG02278}* P element mutant (*CG9005^{BG}*) compared to the control (n for control=43, mutant=50, mutant/*Df1*=28, mutant/*Df2*=9, rescue=20; p<0.0001 for control vs mutant, p=0.99 for control vs rescue, p=0.001 for mutant vs rescue. **Fig S1B.** Quantification reveals a significant increase in macrophage numbers on the yolk compared to the controls in fixed early Stage 12 embryos upon the expression of each of the *CG9005* RNAis in macrophages (control 1 n=21, RNAi 1 n=20, p=0.0002; control 2 n=25, RNAi 2 n=19, p<0.0001; control 3 n=16, RNAi 3 n=15, p=0.001). **Fig S1C.** Macrophage quantification in ventral nerve cord (vnc) segments reveals no significant difference in macrophage migration along the vnc between *CG9005^{PBG}* mutant (n=15) and control embryos (n=7, p>0.05). **Figs. S1D-F.** Quantification of macrophage numbers in vnc segments reveals no significant change in general migration in *srpHemo>CG9005* RNAi embryos compared to the controls (control 1 n=8, RNAi 1 n=13, p=0.25; control 2 n=8, RNAi 2 n=16, p=0.5; control 3 n=8, RNAi 3 n=16, p>0.99). **Fig S1G.** Quantification of the total macrophage number reveals no significant difference between the control (n=43) and *CG9005^{PBG}* mutant embryos (n=50, p=0.69). **Fig S1H.** Quantification of the total macrophage number reveals no significant difference between the control and *srpHemo>CG9005* RNAi embryos (control 1 n=12, RNAi 1 n=17, p>0.05; control 2 n=27, RNAi 2 n=19, p>0.05; and control 3=23, RNAi 3=27, p>0.05). **Fig S1I.** Stills from two-photon movies of control and *CG9005^{PBG}* mutant embryos, showing macrophage nuclei labeled with *srpHemo-H2A::3xmCherry* migrating starting at Stage 10 from the head towards the germband. Elapsed time indicated in minutes. The germband edge (white dotted line) was detected by yolk autofluorescence. **Figs. S1J-L.** Quantification of migration parameters from two-photon live imaging of macrophages. **(J)** Macrophages on the yolk sac in the *CG9005^{PBG}* mutant reach the germband with a similar speed to control macrophages. Speed: control=2.2 $\mu\text{m}/\text{min}$, mutant=2.2 $\mu\text{m}/\text{min}$; movie #: control=8, mutant=3; track #: control=373, mutant=124, p=0.78. **(K)** Macrophage directionality in the head shows no change in the *CG9005^{PBG}* mutant compared to the control. Directionality: control=0.39, mutant=0.37; # movies: control=7, mutant=3, p=0.74). **(L)** Macrophage directionality on the yolk sac shows no change in the *CG9005^{PBG}* mutant compared to the control. Directionality: control=0.40, mutant=0.39, p=0.86; movie #: control=7, mutant=3. Macrophages analyzed in **A-L** were labeled with *srpHemo-H2A::3xmCherry* to visualize nuclei. Throughout this work embryos were staged for imaging and quantification based on germband retraction away from the anterior of less than 29% for stage 10, 29%–31% for stage 11, and 35%–40% for stage 12. In all figures histograms show mean \pm SEM, ns=p>0.05, *p<0.05, **p<0.01, ***p<0.001, ****p<0.0001. One-way ANOVA with Tukey for (B) and unpaired t test for (C-M).

2.1 $\mu\text{m}/\text{min}$ for the control or *CG9005^{PBG}* mutant, respectively p=0.03) (Figs. 1K-L). However, the speed of the next few cells migrating along this path was not affected (3rd-5th cells: 2.5 or 2.4 $\mu\text{m}/\text{min}$ for the control or *CG9005^{PBG}* mutant, respectively p=0.17) (Fig.1M). We therefore conclude that *CG9005* regulates tissue invasion by facilitating the initial entry into and subsequent movement within the germband tissue of the first two pioneer macrophages. Since in the *CG9005^{PBG}* mutant the stream of macrophages invading the germband becomes like a trickle with fewer cells moving at a lower speed we named the *CG9005* gene *atossa* (*atos*), for the powerful Persian queen whose name literally means trickling.

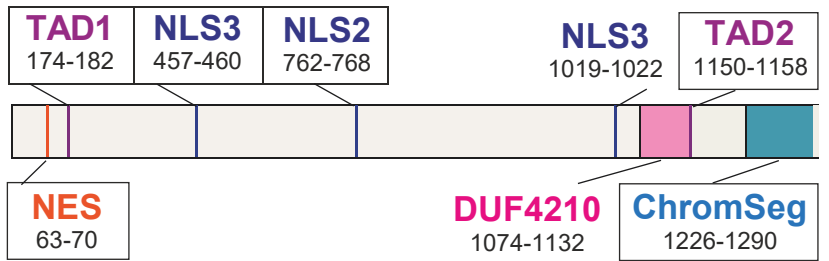
Atossa (*CG9005*) is a novel nuclear protein whose conserved motifs and TADs are important for macrophage tissue invasion

We wished to determine how *Atossa* (*CG9005*) aids initial macrophage invasion. We therefore first tested the subcellular distribution of the *Atossa* protein. We transfected the macrophage-like S2R+ cell line with a *FLAG::HA* tagged form of *atossa* under the control of the *srpHemo* (macrophage: *mac*>) driver. As expected from our bioinformatic analysis which predicts three NLSs and two TADs within the *Atossa* protein sequence, in

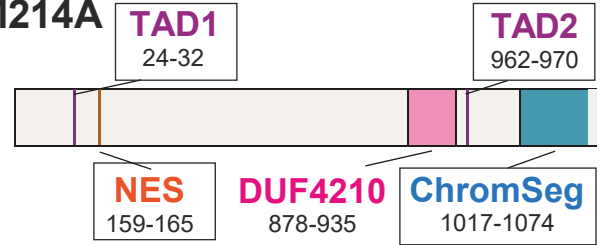
Stage 12 (GB entry)



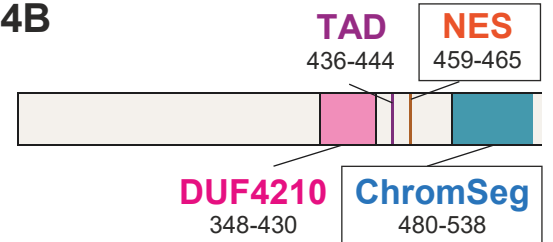
CG9005 = Atossa



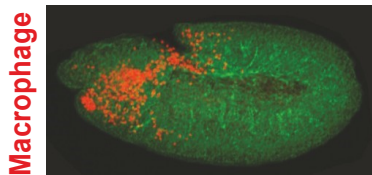
Murine FAM214A



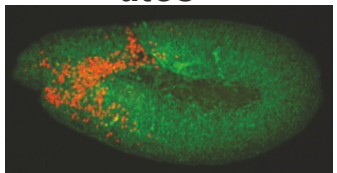
Murine FAM214B



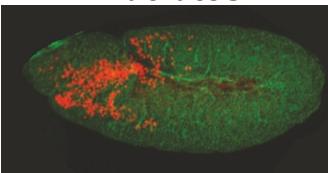
Control



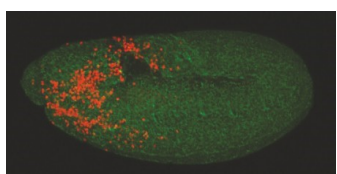
atos^{BG}



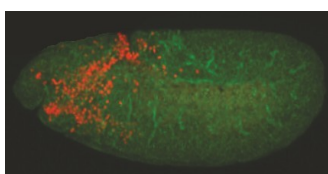
+ mac-atos



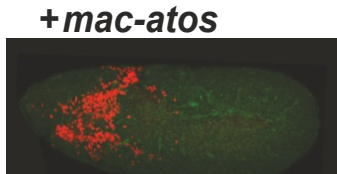
+ mac-atos^{DUF-}



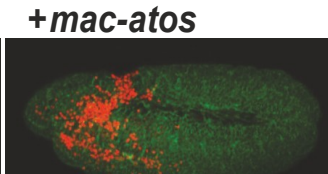
ChrSeg-



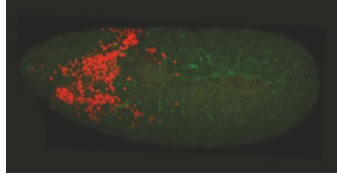
DUF-/ChrSeg-



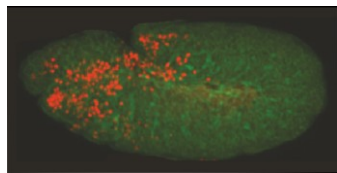
TAD1-/TAD2-



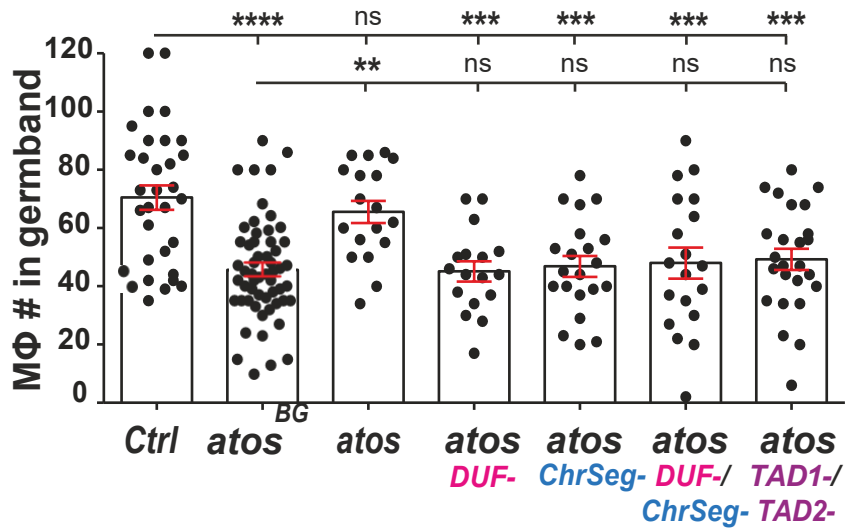
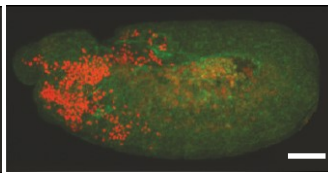
+ mac-atos



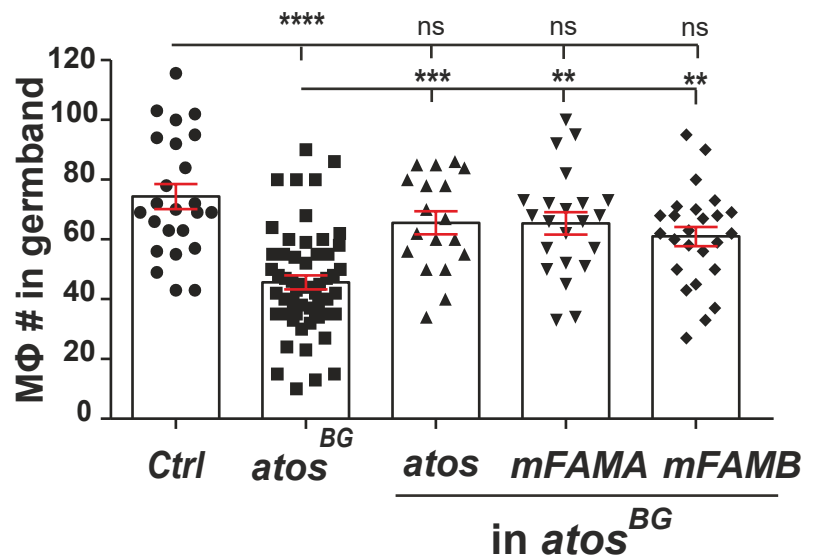
+ mac-mFAM214A



+ mac-mFAM214B



in *atos*^{BG}



in *atos*^{BG}

Figure 2. CG9005/Atossa requires conserved domains linked to transcriptional activation to enhance tissue invasion, a function maintained by its murine orthologs. **Fig 2A.** Macrophages (red) near the germband in Stage 11/12 embryos display colocalization of Atossa tagged with HA (HA antibody, green) with the nucleus stained by DAPI (blue). Line utilized: *srpHemo-atossa::H2A*. **Fig 2B.** Deduced protein structure of *Drosophila* CG9005/Atossa and its mammalian orthologs, mFAM214A and B. These proteins all contain the same conserved motifs: a domain of unknown function (DUF4210), a domain associated with Chromosome segregation (ChromSeg), at least one transcriptional activation domain (TAD), nuclear localization signals NLS and a nuclear export signal (NES). Atossa contains three identifiable NLSs. FAM214A and B are 44% identical to their *Drosophila* counterpart and are predicted to localize into the nucleus. **Fig 2C.** Representative confocal images of Stage 12 embryos from the control, the *atos^{PBG}* mutant, and the *atos^{PBG}* mutant expressing Atossa itself or variants lacking particular domains in macrophages. **Fig 2D.** Germband macrophage quantification in embryos from the control, the *atos^{PBG}* mutant, and the *atos^{PBG}* mutant expressing Atossa or its altered forms in macrophages. The tissue invasion defect in the *atos^{PBG}* mutant can be fully rescued by Atossa expression in macrophages unless Atossa lacks the conserved DUF4210, the chromosome segregation domain (ChrSeg), or the transcriptional activation domains (TAD1 and 2). control n=32, mutant n=56, WT rescue n=18, DUF4210⁻ rescue n=17, ChrSeg⁻ rescue n=21, DUF4210⁻/ChrSeg⁻ rescue n=19, TAD1⁻/TAD2⁻ rescue n=25. p<0.0001 for control vs mutant. p=0.99 for control vs rescue. p=0.0014 for mutant vs rescue. **Fig 2E.** Representative confocal images of the *atos^{PBG}* mutant rescued with a murine ortholog, *mFAM214A* or *mFAM214B*, expressed in macrophages. **Fig 2F.** Quantification of macrophages in the germband in St 12 embryos from the control, the *atos^{PBG}* mutant, and the *atos^{PBG}* mutant embryos expressing *mFAM214A* or *mFAM214B* in macrophages shows that Atossa's mammalian orthologs can rescue *atos*'s macrophage tissue invasion defect. Control n=25, *atos^{PBG}* mutant n=56, rescue with *atos* n=18, with *mFAM214A* n=22, with *mFAM214B* n=25. p>0.05 for control vs *mFAM214A* and *mFAM214B* rescues. p<0.005 for *atos^{PBG}* mutant vs *mFAM214A* and *mFAM214B* rescues. *mFAM214A* or *B* are expressed under the direct control of the *srpHemo* promoter. Throughout paper > indicates *GAL4 UAS* regulation. In C and E macrophages (red) are visualized by *srpHemo-H2A::3xmCherry* expression and actin by Phalloidin staining (green). One-way ANOVA with Tukey for (D) and (F). Scale bars are 5 μm in (B) and 50 μm in (C) and (E).

S2R+ cells we found Atossa mainly in the nucleus, colocalized with the nuclear marker DAPI, and also partially in the cytoplasm (Fig. 2SA). When expressed *in vivo* in embryonic macrophages under the *srpHemo* promoter Atossa is also predominantly a nuclear factor (Fig. 2A). To assess if the conserved domains and TADs are important for Atossa's function in macrophage tissue invasion, we made versions of Atossa lacking these regions. All mutant forms localized similarly to wild-type Atossa, mainly in the nucleus and partially in the cytoplasm of S2R+ cells (Fig. 2SA). While macrophage-specific expression of wild-type Atossa in *atossa* mutant embryos completely rescues germband invasion (Figs. 2C-D), such expression of mutant Atossa lacking either the conserved DUF2140 or the Chr_Seg domain failed to do so. Moreover, forms of Atossa missing either or both of the two TAD motifs (Figs. 2SB and 2SC) were also unable to rescue germband invasion (Figs. 2C-D). Consistent with a germband invasion defect, expression of mutant versions of Atossa led to a higher number of macrophages sitting on the yolk at the germband entry site than in the rescue with wild-type Atossa (Fig. 2SD). These data clearly show that the conserved domains and TADs are critical for the primarily nuclear protein, Atossa, to facilitate macrophage invasion.

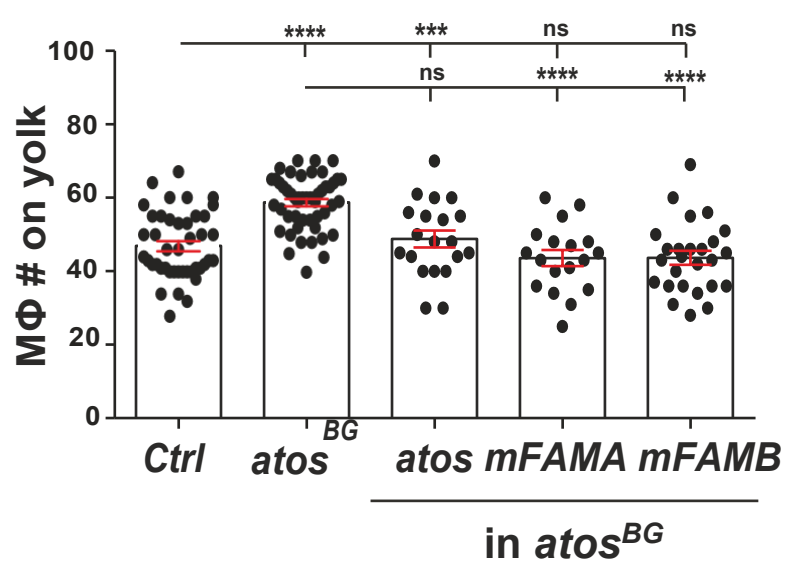
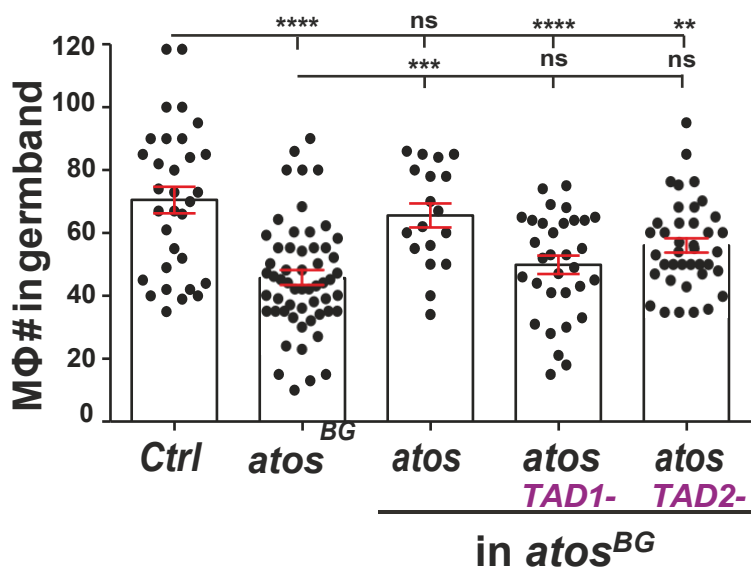
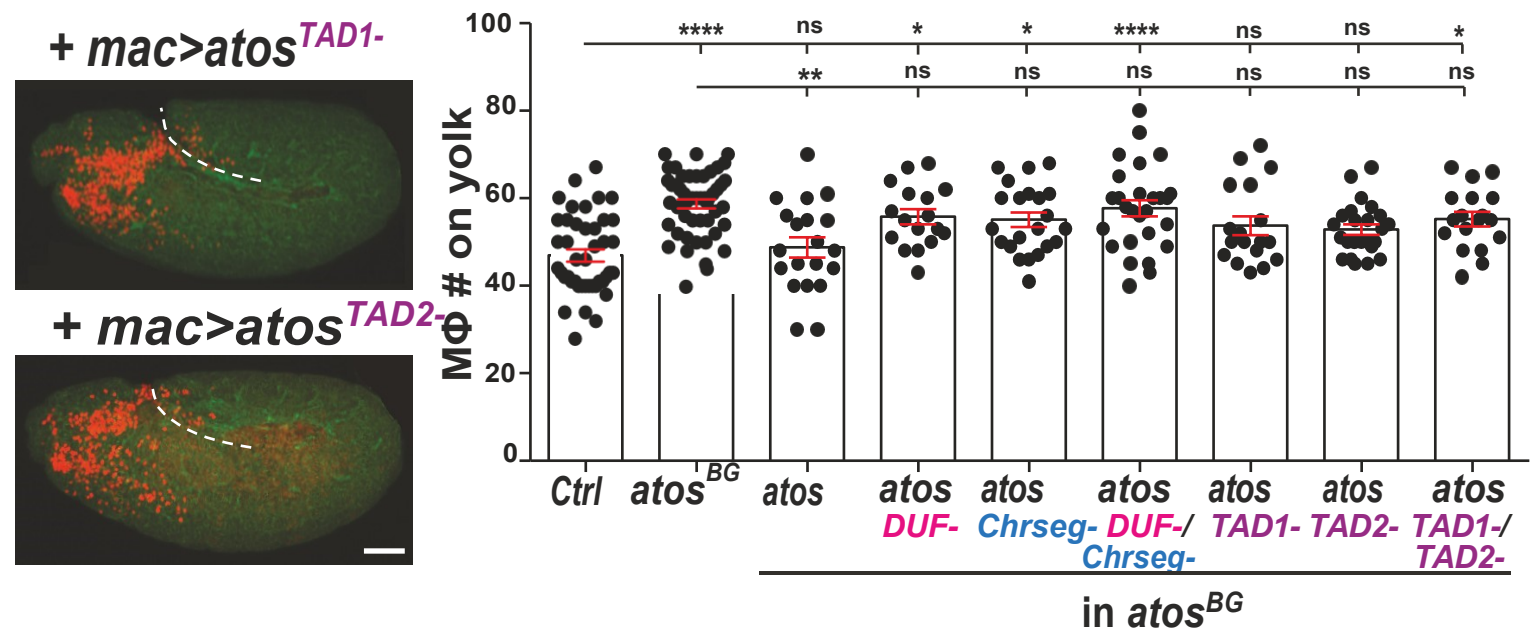
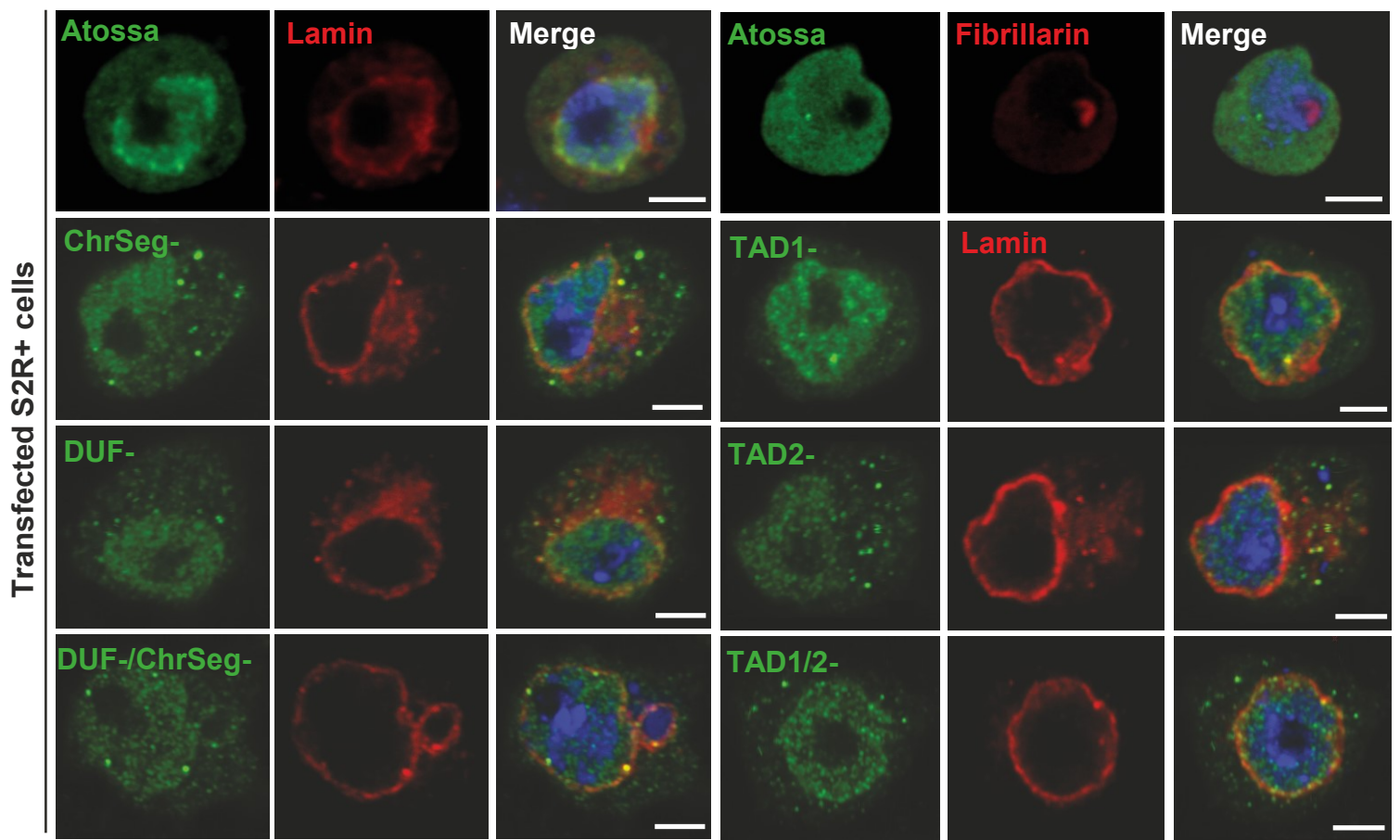


Figure S2. Atossa's TAD domains are essential to enhance macrophages tissue infiltration, a function conserved up to the vertebrates. Fig S2A. S2R+ cells were transfected with wild type Atossa or forms lacking the indicated domains. HA tagged Atossa (green), the nuclear membrane marker Lamin (red) and the nucleolar marker Fibrillarin (red) were visualized with antibodies, and the nucleus with DAPI (blue). All forms of Atossa are expressed under direct control of the *srpHemo* promoter. **Fig S2B.** Representative confocal images of Stage 12 embryos from *atos^{PBG}* mutants expressing Atossa lacking either TAD1 or 2 in macrophages from the *srpHemo* promoter. Macrophages (red) were visualized with *srpHemo-H2A::3xmCherry* expression and the embryo outlines with phalloidin staining to detect actin (green). **Fig S2C.** Quantification shows that deletion of TAD1 or 2 blocks Atossa's ability to rescue the germband migration defect of St 12 *atos^{PBG}* mutant embryos upon expression in macrophages. Control n=32, mutant n=56, WT rescue n=18, TAD1⁻ n=32, TAD2⁻ n=39, p=0.2 for WT rescue vs NLS1⁻ rescue, p<0.0001 for WT rescue vs TAD1⁻ or TAD2⁻ rescues. **Fig S2D.** Quantification shows a similar number of macrophages on the yolk in fixed early Stage 12 *atos^{PBG}* mutant embryos which express *mFAM214A* or *mFAM214B* in macrophages compared to the control. Control n=43, mutant n=50, WT rescue n=20, *mFAM214A* rescue n=18, *mFAM214B* rescue n=26. p=0.93 for control vs *atos^{PBG}*, p=0.65 for control vs *mFAM214A* rescue and p=0.56 for control vs *mFAM214B* rescue. p<0.0001 for *atos^{PBG}* mutant vs *atos^{PBG}*, *mFAM214A* and *mFAM214B* rescues. One-way ANOVA with Tukey for (D-E). Scale bars are 3 μ m in (A) and 50 μ m in (B).

Atossa's vertebrate orthologs, mFAM214A and mFAM214B, maintain the capacity to promote macrophage tissue invasion

These domains are also found in Atossa's uncharacterized murine orthologs, mFAM214A and mFAM214B, which display 40% identity to their *Drosophila* counterpart and are enriched in vertebrate immune cells (Fig. 2B) (Table 1). Expression in macrophages of either mFAM214A or B in *atossa^{PBG}* mutant embryos rescued the germband invasion defect as efficiently as the *Drosophila* protein itself (Fig. 2F) and restored the normal number of macrophages on the yolk next to the extended germband (Fig. 2SF). Therefore we conclude that the molecular functions that enable Atossa to promote macrophage tissue invasion are maintained in vertebrates.

Atossa leads to higher mRNA levels of an RNA helicase and enzymes involved in metabolism, which are each required for germband invasion

Given Atossa's nuclear localization and requirement for TADs, we hypothesized that Atossa might modulate transcription in macrophages to aid their initiation of germband invasion. To identify potential targets, we performed RNA-sequencing analysis on FACS isolated fluorescently labeled macrophages from wild type and *atossa^{PBG}* mutant embryos during germband invasion in early Stages 11-12 (Fig. S3A) (Supp. Data 1). Transcriptome analysis revealed 25 genes that were downregulated and 39 genes whose levels were enhanced in the absence of Atossa across all four replicates with a P value less than 0.05 and a log₁₀FC (fold change) in expression of more than 1.5 (Fig. S3B). We further focused on genes with at least a >5-fold change in expression, and either embryonic expression in macrophages and or an identified molecular function (Fig. 3A and Fig. 3SC). Gene ontology analysis (GO term) indicates that the 24 significantly downregulated genes are involved in oxidation-reduction (redox) processes, metabolic pathways, stress responses as well as signal transduction (Fig. S3D). The 27 genes that are upregulated are involved in signaling, cell communication and ion transport (Fig. S3E). We

Gene name	Expression			Biological & molecular functions
	wt	mut	Fold	
<i>CG9253</i> (<i>porthos</i>)	144	14	-10	ATP-dependent RNA helicase
<i>CG2137</i> (<i>Gpo2</i>)	31	0.95	-33	Glycerophosphate oxidase 2
<i>CG11061</i> (<i>GM130</i>)	27.5	3.4	-8	Connects distinct Golgi compartments in dendritic branch points
<i>CG9331</i> (<i>dGR/HPR</i>)	20.7	3.2	-6.5	Glyoxylate reductase/hydroxypyruvate reductase Oxidation/reduction activities
<i>CG7144</i> (<i>LKR/SDH</i>)	16.4	0.64	-25	Lysine ketoglutarate reductase/ saccharopine dehydrogenase

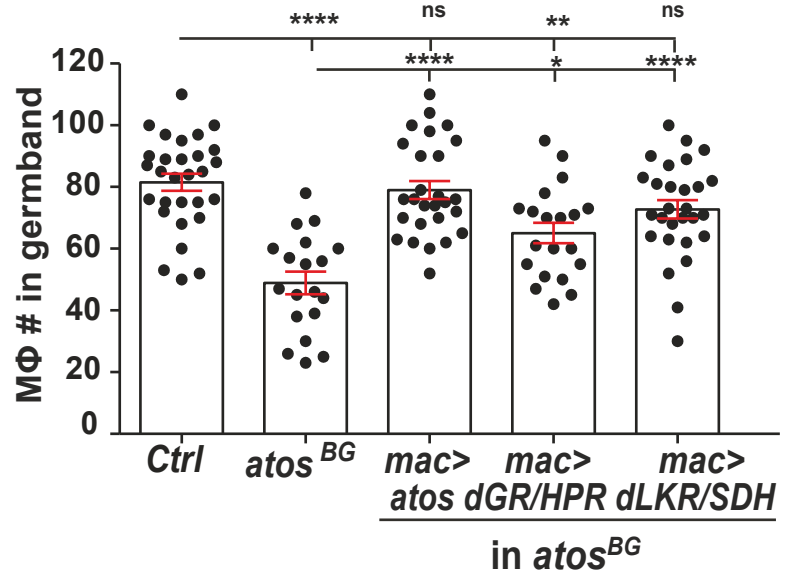
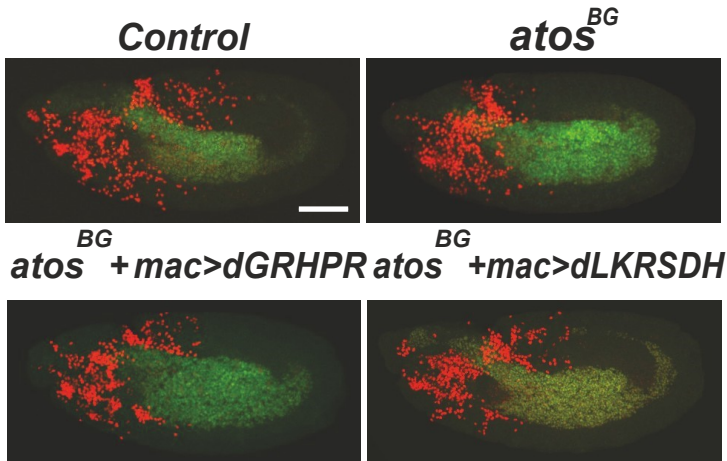
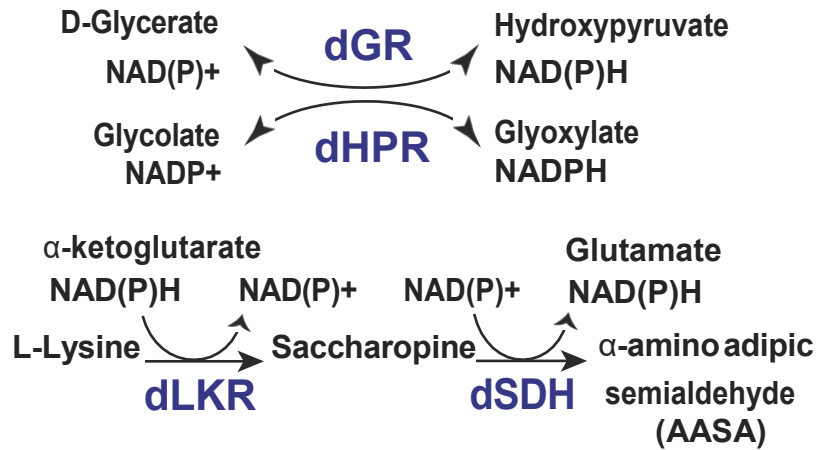
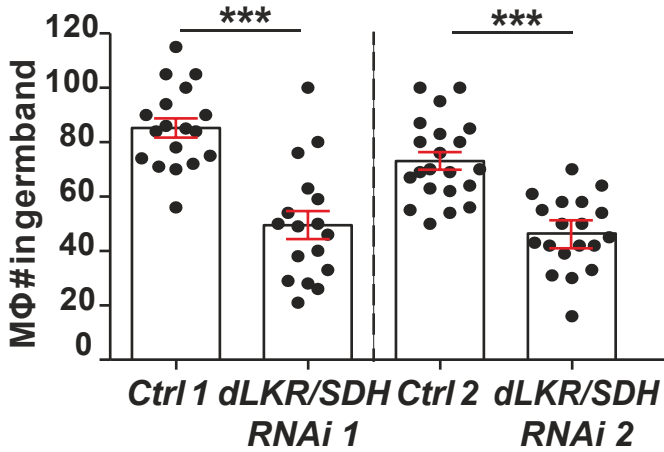
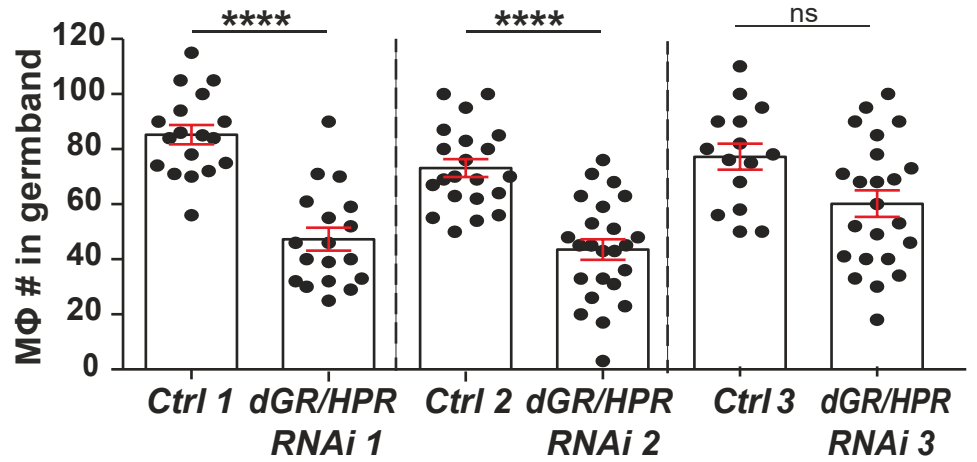
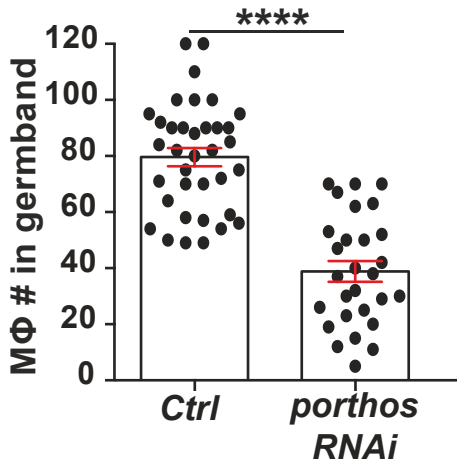
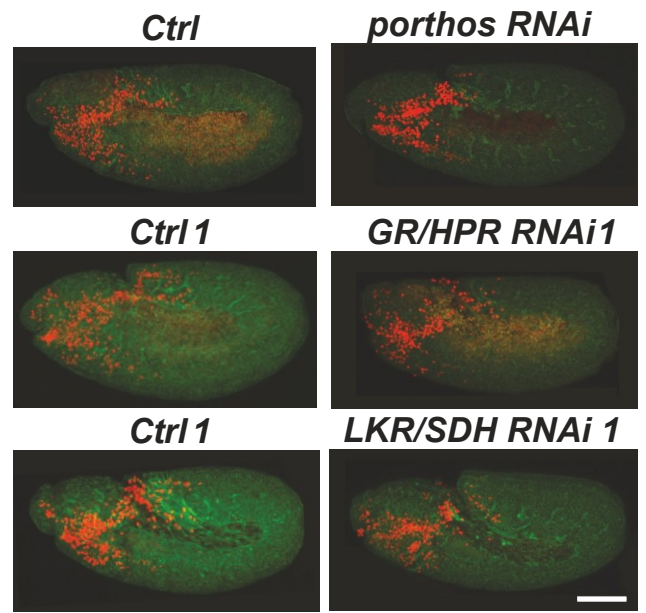
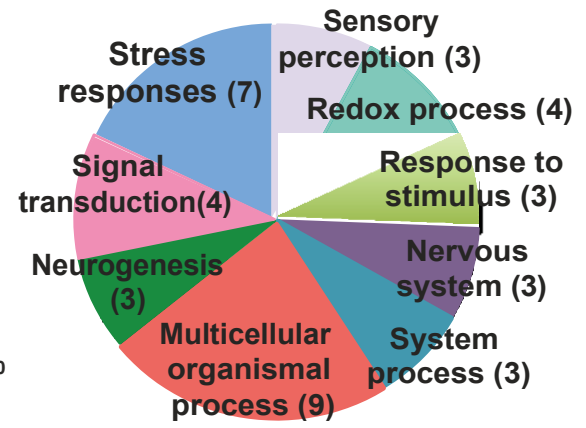
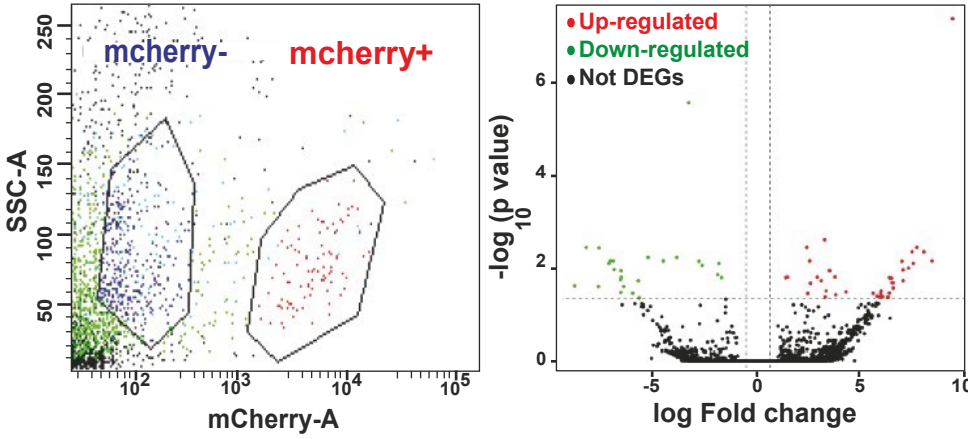


Figure 3. Atossa leads to higher RNA levels of an RNA helicase and metabolic enzymes required for germband invasion. Fig 3A. A selection of genes down-regulated in *atos^{PBG}* mutant macrophages compared to the control, chosen for having a >5 fold change in expression as well as an identified biological function. **Figs. 3B-D.** Representative confocal images of early Stage 12 embryos from the control, and lines expressing an RNAi against **(B)** *porthos*, **(C)** *dGR/HPR* or **(D)** *dLKR/SDH* specifically in macrophages (red). *srpHemo-H2A::3XmCherry* labels macrophages. **Fig 3E.** Quantification of Stage 12 embryos reveals that expression of a *porthos RNAi* in macrophages decreases their number in the germband by 48%. Control n=36, *RNAi BL36589* n=28, p<0.0001. **Figs. 3F-G.** Quantification of Stage 12 embryos indicates that fewer macrophages have moved into the germband upon the expression in macrophages of either of **(F)** three different RNAis against *dGR/HPR* or **(G)** two different RNAis against *dLKR/SDH*, arguing that these metabolic enzymes are required in macrophages for tissue invasion. Control 1 n=18, *dGR/HPR RNAi 1* (VDRC 44653) n=18, p<0.0001, *dGR/HPR RNAi 2* (VDRC 107680) n=24, p<0.0001, *dGR/HPR RNAi 3* (VDRC 64652) n=23, p=0.08. *dLKR/SDH RNAi 1* (VDRC 51346) n=17, control 2 n=21, *dLKR/SDH RNAi 2* (VDRC 109650) control 3 n=15, p<0.0001. **Fig 3H.** Schematic illustrates how the bifunctional enzyme dGR/HPR can catalyze the reduction of glyoxylate into glycolate and convert hydroxypyruvate into D-glycerate by oxidation of the cofactor NAD(P)H. **Fig 3I.** Schematic shows the metabolic pathway in which *Drosophila* Lysine α -Ketoglutarate Reductase/Saccharopine Dehydrogenase (*dLKR/SDH*) catalyzes the first two steps of the Lysine catabolism pathway, resulting in the production of Glutamate and Acetyl-CoA, a TCA substrate, through several downstream enzymatic reactions. Glu: Glutamate, α -KG: α -Ketoglutarate, AASA: α -Amino adipate δ -semialdehyde. **Fig 3J.** Representative confocal images of early Stage 12 embryos from the control, the *atossa^{BG02278}* (*atos^{PBG}*) mutant, and the *atos^{PBG}* mutant with Atossa, dGR/HPR, or dLKR/SDH expressed in macrophages. *srpHemo-Gal4* drives macrophage expression of *UAS-atossa::FLAG::HA*, *UAS-dGR/HPR::FLAG::HA*, or *UAS-dLKR/SDH::FLAG::HA*. Macrophages (red) are visualized by *srpHemo-H2A::3xmCherry* and the embryo by phalloidin staining (green). **Fig 3K.** Quantification reveals that expressing dGR/HPR or dLKR/SDH in macrophages can partially rescue the germband invasion defect seen in the *atos^{PBG}* mutant, as compared to the rescue with Atossa itself. Control n=29, *atos^{PBG}* n=19, *atos^{PBG}* with *srpHemo>atossa::FLAG::HA* n=27, *srpHemo>dGR/HPR::FLAG::HA* n=20, and *srpHemo>dLKR/SDH::FLAG::HA* n=28. p<0.0001 for control vs *atos^{PBG}* mutant; p>0.99 for control vs *atos^{PBG}* with *atossa* rescue; p=0.004 for control vs *atos^{PBG}* rescued with *GR/HPR*; p=0.3 for control vs *atos^{PBG}* rescued with *dLKR/SDH*; p<0.0001 for *atos^{PBG}* vs *atos^{PBG}* rescued with *atossa*; p=0.01 for *atos^{PBG}* vs *atos^{PBG}* rescued with *dGR/HPR*; p<0.0001 for *atos^{PBG}* vs *atos^{PBG}* rescued with *dLKR/SDH*. Unpaired t-test for (E-G) and one-way ANOVA with Tukey for (K). Scale bars are 50 μ m in (B-D), and (J).

therefore conclude that the presence of Atossa in macrophages results in both higher and lower mRNA levels of a discrete set of proteins. We tested the hypothesis that the *atossa^{PBG}* macrophage germband invasion defect is caused by the lower levels of these downregulated genes (Fig 3A). We drove *srp-Hemo>UAS-RNAi* in macrophages and observed a significant reduction in germband macrophage numbers for three of these 5 candidates: a predicted ATP-dependent RNA helicase named Porthos (CG9253) (Figs. 3B and 3E), and two metabolic enzymes, Glyoxylate Reductase/Hydroxypyruvate Reductase (*dGR/HPR*, CG9331) (Figs. 3C and 3F) and Lysine α -Ketoglutarate Reductase/Saccharopine Dehydrogenase (*dLKR/SDH*, CG7144) (Figs. 3D and 3G). Downregulation of *Glycerophosphate oxidase 2* (*Gpo2*, CG2137) (Fig. S3F) and *Golgi matrix protein 130 kD* (*GM130*, CG11061) (Fig. S3G) did not produce any invasion defect. GR/HPR is highly conserved from bacteria to mammals and the *Drosophila* form shows 48% identity to its human ortholog (identified by NCBI BLAST). GR/HPR is the linchpin of the glyoxylate cycle, catalyzing the reduction of glyoxylate into glycolate and the conversion of hydroxypyruvate into D-glycerate through the cofactor NAD(P)H (Fig. 3H) (Booth et al., 2006). This contributes to glucose and urea synthesis.

MΦ downregulated genes



Gene name	Expression			Biological & molecular functions
	wt	mut	Fold	
<i>CG12505 (Arc1)</i>	41.3	107.6	2.6	Activity-regulated cytoskeleton associated protein 1
<i>CG3752 (Aldh)</i>	12.3	59	4.4	Aldehyde dehydrogenase
<i>CG8780 (tey)</i>	5.3	46.8	9	E3 ubiquitin protein ligase
<i>CG5005 (HLH54F)</i>	3	42	14	Transcription factor, positive control of transcription

MΦ upregulated genes

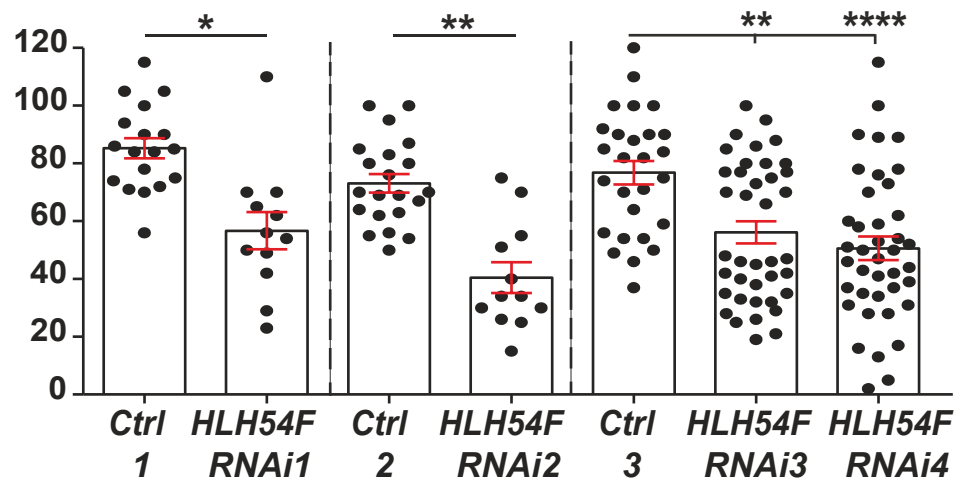
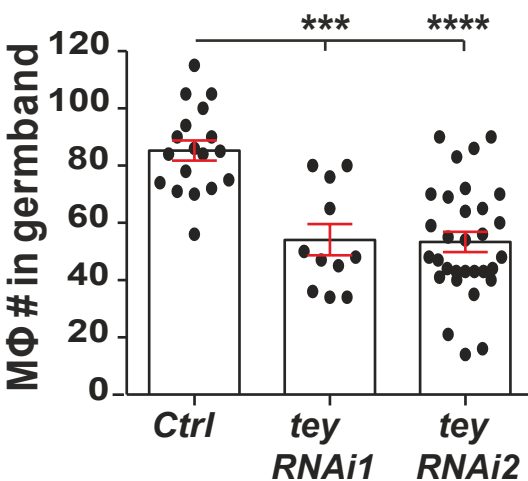
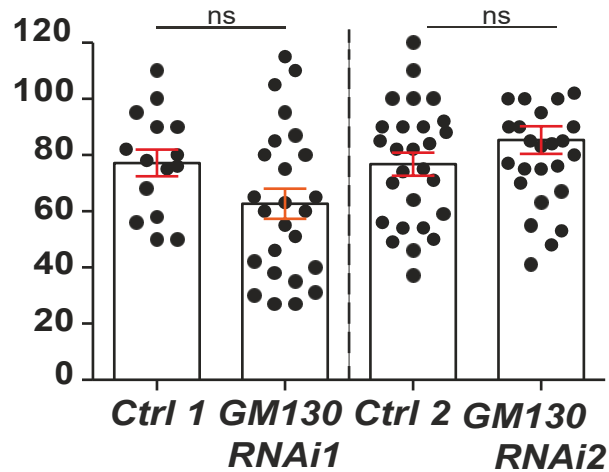
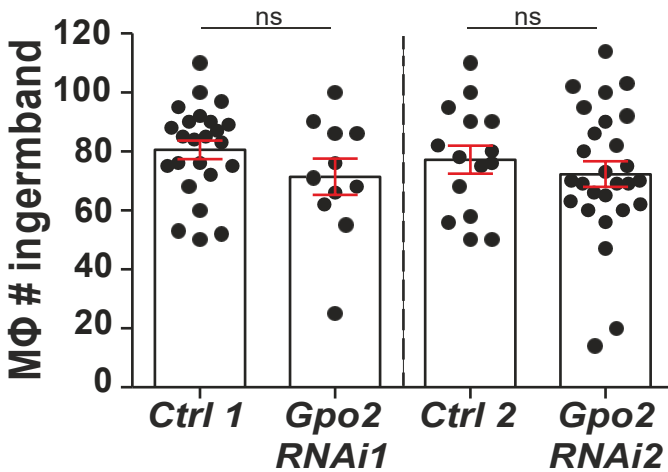
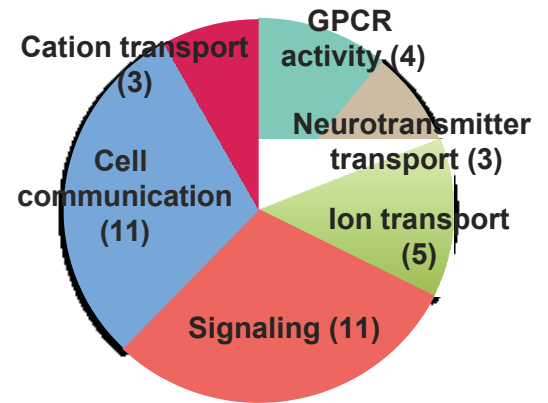


Figure S3. Macrophage transcriptome analysis reveals that Atossa targets participate in signaling, cell communication and ion transport. **Fig S3A.** FACS plot of Side Scatter (SSC) vs. mCherry fluorescence signal in macrophages obtained from embryos expressing *srpHemo-3xmCherry*. The two populations are sorted as mCherry marker + (red) and - (blue) cells. **Fig S3B.** Genes expressed differentially in analysis of RNA sequencing data from macrophages from the *atos^{PBG}* mutant compared to the control are shown in a volcano plot graphing the log base 10 of the P value against the log fold change (FC) of the mean normalized expression levels. Each point represents the average value of one gene's expression from four replicate experiments. A \log_{10} fold change ≥ 1 is indicated by the dotted vertical lines and a P value of ≤ 0.05 by the dotted horizontal line. Statistically significantly up- and down-regulated genes are reported as red and green dots, respectively. **Fig S3C.** A selection of the genes upregulated in *atos^{PBG}* mutant macrophages compared to the control, chosen for a >5 fold change in expression level and a potential biological function. **Figs. S3D-E.** Gene ontology (GO) analysis of (C) down- and (D) up-regulated genes from *atos^{PBG}* mutant macrophages compared to the control. The upregulated genes encode proteins involved in signaling, cell communication and ion transport; the downregulated genes are involved in transcription, oxidation-reduction processes, stress responses as well as signal transduction. **Figs. S3H-I.** Quantification in fixed early Stage 12 embryos shows that expression in macrophages of any of (H) two RNAis against *teyrha-meyrha* (*tyr*) or (I) four RNAis against *HLHF54F* results in a significant decrease in the number of macrophages within the germband compared to the control. Control 1 n=18, *tyr RNAi* 1 (VDRC 28947) n=11, p=0.0001; *tyr RNAi* 2 (24067) n=31, p<0.0001. Control 1 n=18, *HLHF54F RNAi* 1 (VDRC 13725) n=12, p=0.01; Control 2 n=21, *HLHF54F RNAi* 2 (VDRC 103965) n=12, p=0.001; *Arc1 RNAi* 1: (VDRC 31123) n=10, p=0.9; *Arc1 RNAi* 2 (VDRC 109141) n=10 p=0.03. Control 3 n=27, *HLHF54F RNAi* 3 (VDRC 28698) n=39, p=0.004; *HLHF54F RNAi* 4 (VDRC 65244) n=40, p<0.001. Unpaired t test for (F-I), and (K), one-way ANOVA with Tukey for (H), and (K).

The bifunctional enzyme dLKR/SDH is also highly conserved, with 71% identity to its human counterpart (identified by NCBI BLAST). The N-terminal dLKR domain converts L-lysine to saccharopine in the presence of α -ketoglutarate (α -KG), and the C-terminal SDH domain catalyzes the NAD⁺-dependent oxidation of saccharopine to AASA (α -Aminoadipate δ -semialdehyde) and glutamate (Fig. 3I) It thus catalyzes the first two steps of lysine catabolism and participates in the metabolism of Glutamate and Histidine molecules (Bhattacharjee et al., 1985). We then examined the capacity of each of these metabolic enzymes to substitute for the absence of Atossa by forcing expression of dGR/HPR or LKR/SDH in *atossa^{PBG}* mutant macrophages through GAL4/UAS control (Figure 3J, 3K). Forced expression of either enzyme in *atossa^{PBG}* mutant macrophages produced a substantial rescue of invasion compared to that produced by exogenous Atossa (80% and 85% rescue respectively, Fig. 3K). We therefore conclude that Atossa regulates macrophage metabolism by increasing the levels of dLKR/SDH and dGR/HPR to enhance macrophage germband invasion.

The nuclear RNA helicase, Porthos, functions downstream of Atossa in pioneer macrophages to allow their initiation of germband invasion

The third gene requiring Atossa for higher expression, *porthos* (*CG9253*), displayed the strongest invasion defect upon RNAi knockdown (Fig 3E). Porthos is a conserved DEAD-box RNA helicase (Fig. 4SA) sharing 87% similarity with its human ortholog, the helicase DDX47, including the conserved DEAD motif and helicase C terminal domain, with which DDX47 interacts with RNA structures (Jarmoskaite and Russell, 2011). (<https://blast.ncbi.nlm.nih.gov/Blast.cgi?PAGE=Proteins>).

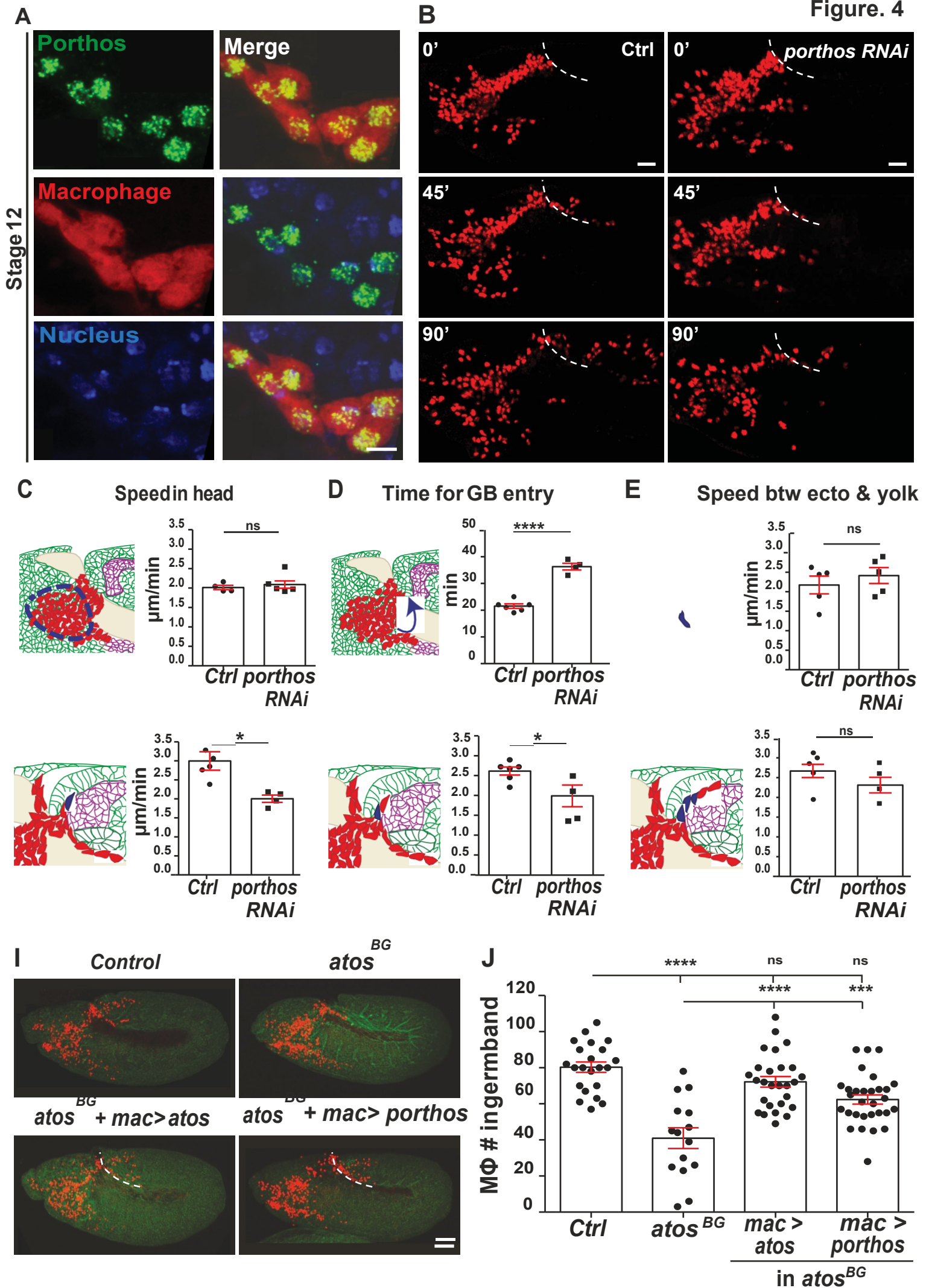
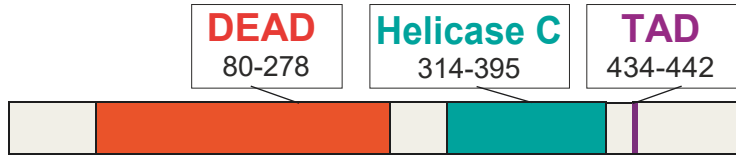


Fig. 4. The nuclear RNA helicase, Porthos, acts as a main downstream target of Atossa to promote pioneer macrophage germband invasion. **Fig 4A.** Macrophages (red) near the germband in Stage 11/12 embryos show partial colocalization of the HA antibody labeling Porthos (green) with the nucleus stained by DAPI (blue). Embryo expressing *srpHemo-porthos::HA*. **Fig 4B.** Stills starting at Stage 10 from two-photon movies of control embryos and those expressing *porthos RNAi* in macrophages; stills show macrophage migration from the head mesoderm towards and into the germband at the indicated time points. White dotted line indicates the germband edge. Macrophage nuclei labeled by *srpHemo-H2A::3xmCherry*. *UAS-porthos RNAi* (BL36589) expressed by *srpHemo-GAL4*. **Figs. 4C-H.** Quantification of macrophage migration parameters from two-photon movies. **(C,E)** Macrophages expressing *porthos RNAi* migrate with a similar speed in the head and between the yolk sac and the germband mesoderm compared to the control. Speed in head: control=2.01 $\mu\text{m}/\text{min}$, *porthos RNAi*=2.09 $\mu\text{m}/\text{min}$; movie #: control=4, *porthos RNAi*=6; track #: control=507, *porthos RNAi*=859, $p=0.56$. Speed between yolk sac and germband mesoderm: control=2.17 $\mu\text{m}/\text{min}$, *porthos RNAi*=2.41 $\mu\text{m}/\text{min}$, $p=0.45$; movie #: control n=5, *porthos RNAi* n=5, track #: control n=40, *porthos RNAi* n=51. **Fig 4E.** The time required for the first macrophage nucleus to enter into the germband is significantly increased in embryos expressing *porthos RNAi* compared to the control. Control=21.5 min, n=6, *porthos RNAi*=36.2 min, n=4, $p<0.0001$. Blue arrow in schematic indicates route analyzed. **Figs. 4F-G.** The speed of the first and second macrophage invading into the germband along the path between the mesoderm and ectoderm is significantly slower in embryos expressing *porthos RNAi* compared to the control. First macrophage speed: control=2.99 $\mu\text{m}/\text{min}$, *porthos RNAi*=2.0 $\mu\text{m}/\text{min}$; $p=0.009$; # movies: control n=4, *porthos RNAi* n=4. Second macrophage speed: control=2.61 $\mu\text{m}/\text{min}$, *porthos RNAi*=1.98 $\mu\text{m}/\text{min}$; $p=0.037$; # movies: control n=6, *porthos RNAi* n=4. **Fig 4H.** The speed of the third to fifth macrophages invading the germband is similar in macrophages downregulated for *porthos* and the control (speed: control=2.66 $\mu\text{m}/\text{min}$, *porthos RNAi*=2.31 $\mu\text{m}/\text{min}$; $p=0.21$; # movies: control n=5, *porthos RNAi* n=4). **Fig 4I.** Representative confocal images of early Stage 12 embryos from the control, the *atos^{PBG}* mutant, and the *atos^{PBG}* mutant expressing *atos::FLAG::HA* or *porthos::FLAG::HA* in macrophages (red) through *srpHemo-GAL4* control of *UAS* constructs. Embryo detected by phalloidin staining (green). **Fig 4J.** Quantification of macrophages in the germband shows that the *atos^{PBG}* mutant phenotype can be substantially rescued by expressing *porthos::FLAG::HA* in macrophages. Control (n=15), *atos^{PBG}* mutant (n=22), *atos^{PBG}* mutant with *srpHemo>CG9005::FLAG::HA* (n=27), *srpHemo>porthos::FLAG::HA* (n=30). $p<0.0001$ for control vs *atos^{PBG}* mutant, $p<0.0001$ for control vs *atos* rescue, $p=0.0007$ for control vs *atos^{PBG}* mutant rescued with *porthos*. Macrophages detected by *srpHemo-3xmCherry* in A and *srpHemo-H2A::3xmCherry* in movies and in I. Unpaired t test for (C-H), and one-way ANOVA with Tukey for (J). Scale bars: 50 μm in (A) and 30 μm in (E).

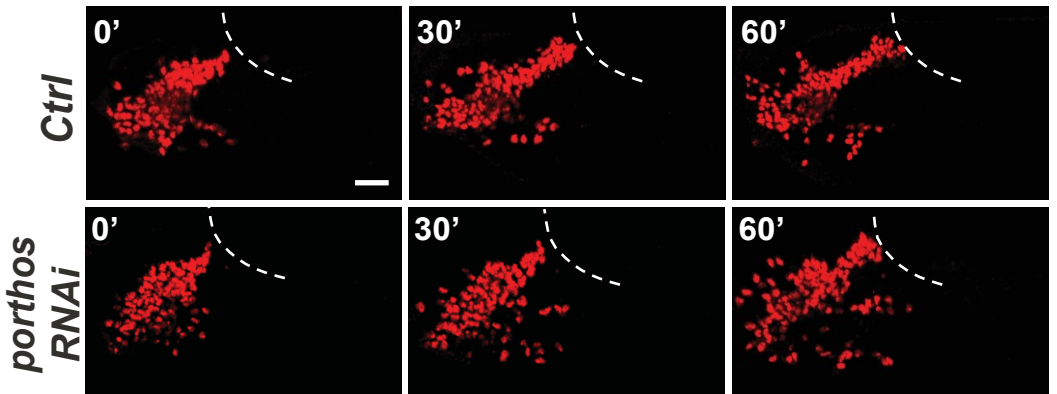
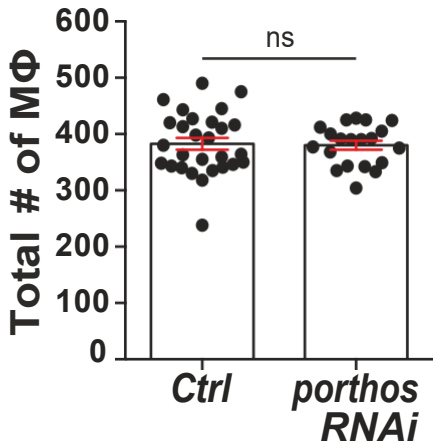
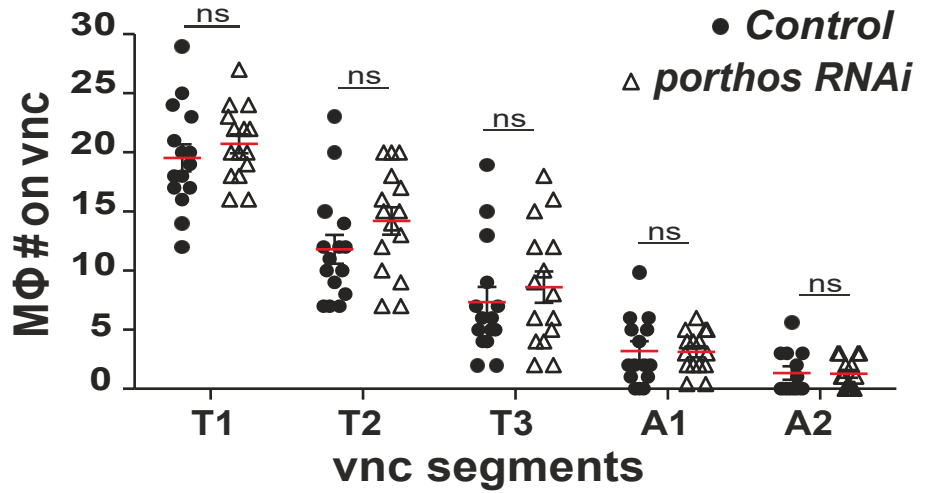
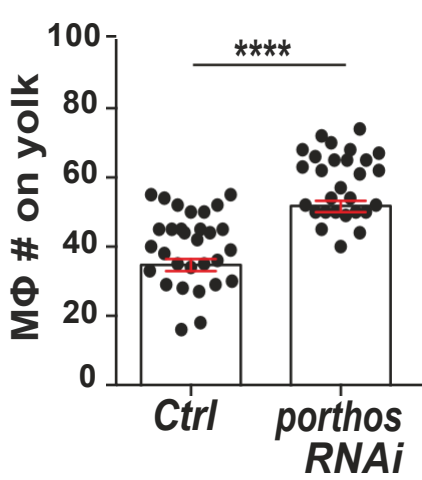
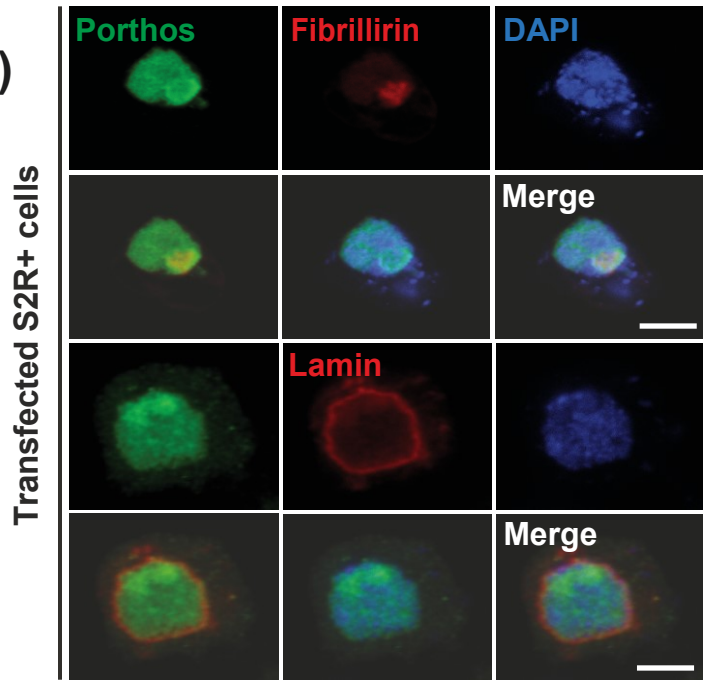
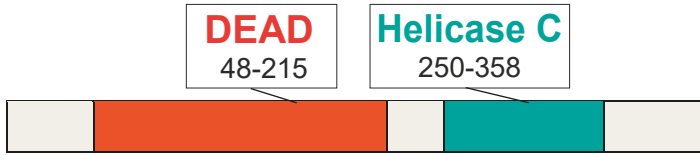
Porthos has an overlapping *in situ* expression pattern with *atossa* in *Drosophila* embryos, being highly enriched in macrophages in the head region during Stages 9-12 (<https://insitu.fruitfly.org/>). In S2R+ cells, HA-tagged Porthos colocalizes with markers for the nucleus (DAPI) and the nucleolus (Fibrillarin), where protein synthesis and rRNA processing occur (Fig. 4SB). In embryonic macrophages HA-tagged Porthos also localizes to the nucleus, detected by DAPI (Fig. 4A). As we had observed for the *atossa^{PBG}* mutant, in *porthos RNAi*-expressing embryos we found 30% more macrophages sitting on the yolk, neighboring the germband (Fig. 4SC) with no change in later *vnc* migration (Fig. 4SD) or in the total number of macrophages compared to the control (Fig. 4SE). This data from fixed embryos clearly argues that Porthos, like Atossa, is a nuclear protein specifically needed in macrophages for germband invasion.

To determine where and how *porthos* depletion causes a defect in macrophage migration, we performed live imaging on *porthos RNAi*-KD and wild type embryos (Movies 3 and 4). We tracked macrophages labeled with the nuclear marker *srpHemo-H2A::3xmCherry* as they migrated from their initial position within the head towards the germband and then during their infiltration into this tissue (Figs. 4B and 4SF). We observed no significant change in speed or in directionality in the head or on the yolk

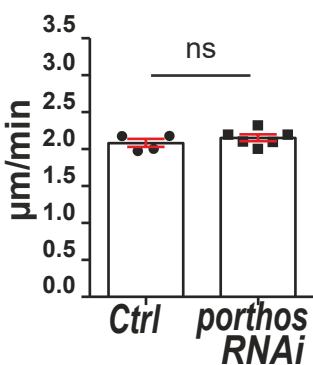
D. melanogaster Porthos (CG9253)



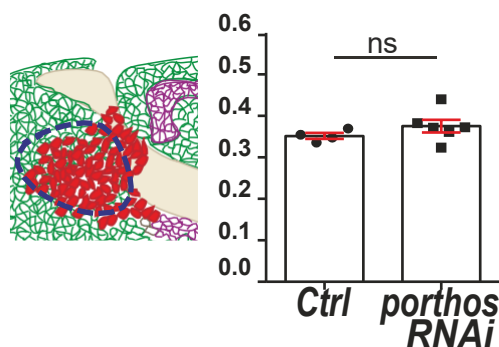
H. sapiens DDX47 (84% similarity)



Speed on yolk



Directionality in head



Directionality on yolk

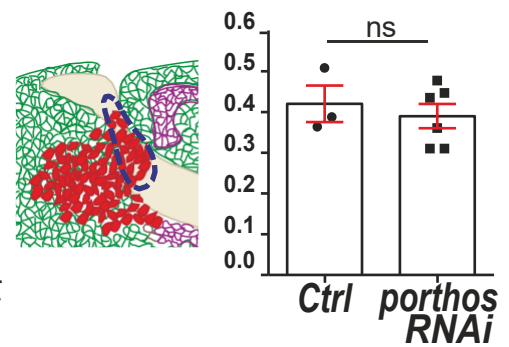


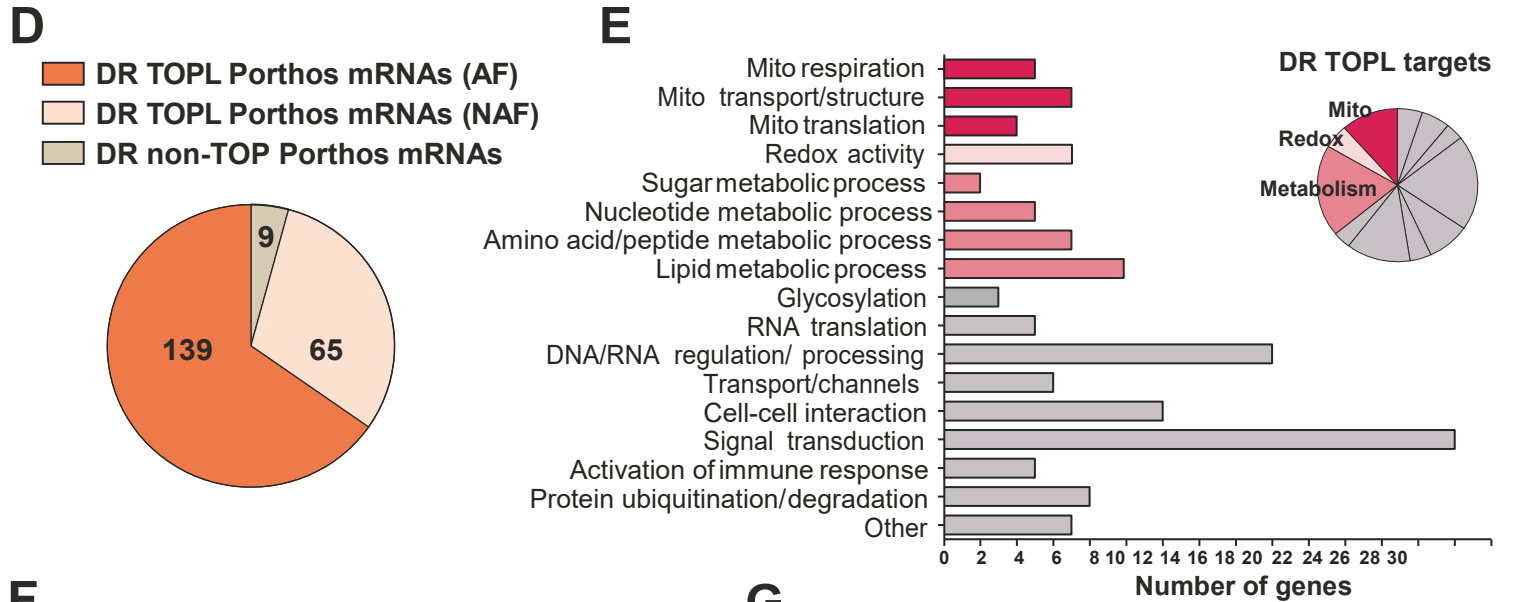
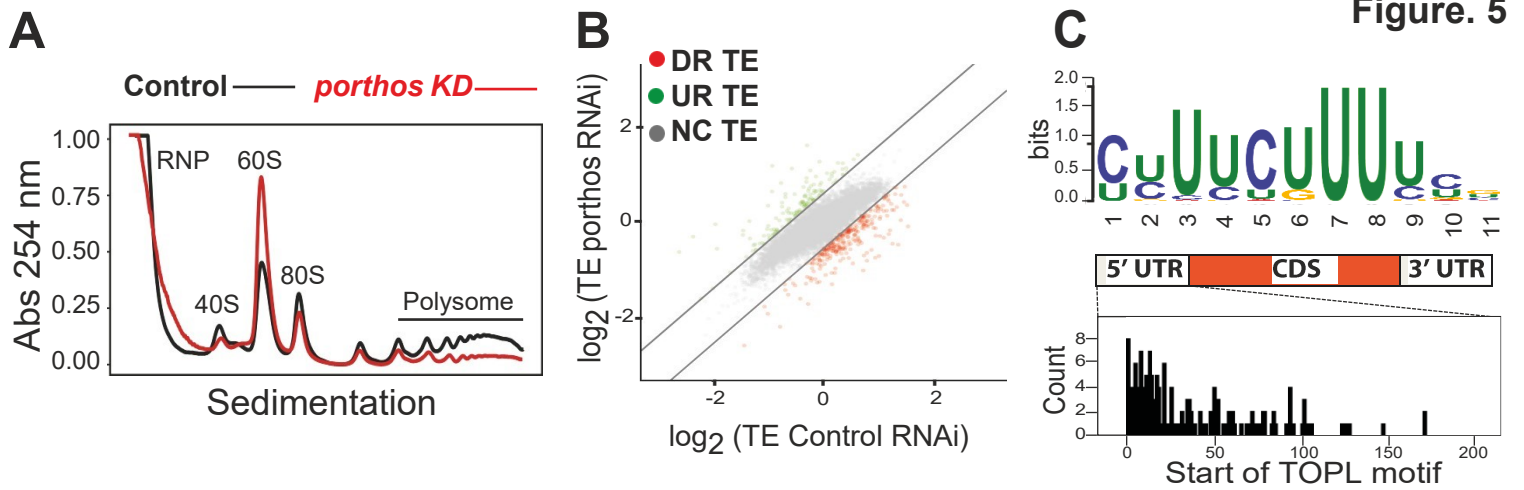
Fig. S4. Downregulation of *porthos* recapitulates the *CG9005^{PBG}* mutant phenotype. Fig S4A. Deduced protein structure of Porthos (CG9253). Porthos contains two conserved motifs, a DEAD motif (Asp-Glu-Ala-Asp) and a Helicase C domain, as well as a predicted transactivation domain (TAD). *Drosophila* Porthos shows 71% identity and 84% similarity to its human ortholog, DDX47. **Fig S4B.** Porthos (green) in S2R+ cells transfected with *UAS-porthos::HA* and *srpHemo-Gal4*, and stained for the nuclear membrane marker Lamin (red), colocalizes with the staining for the nucleolar marker Fibrillarin (red), and DAPI (blue). **Figs. S4C-E.** Quantification of macrophage numbers in fixed Stage 12 embryos. **(C)** Expression of the *porthos* RNAi in macrophages leads to a significant increase in their numbers on the yolk compared to the control without affecting their numbers on **(D)** the vnc or **(E)** in the whole embryo. Yolk: control n=30, *porthos* RNAi n=28, p<0.0001; vnc: n=15 for both, p=0.85; whole embryo: control n=28, *porthos* RNAi n=20, p=0.4 for T1, p=0.16 for T2, p=0.5 for T3, p=0.94 for A1, p=0.92 for A2 for control vs. *porthos* RNAi. **Figs. S4F-H.** **(F)** Stills from two-photon movies of the migration of macrophages labeled with *srpHemo-H2A::3xmCherry* in control embryos and in those expressing *porthos* RNAi in macrophages. Macrophages from both genotypes have a similar **(G)** directionality in the head, and **(H)** speed and **(I)** directionality on the yolk sac, to control macrophages. Speed on yolk sac: control=2.10 $\mu\text{m}/\text{min}$, *porthos* RNAi=2.15 $\mu\text{m}/\text{min}$; p=0.35; movie #: control n=4, *porthos* RNAi n=6; track #: control n=104, *porthos* RNAi n=168. Directionality in head: control n=0.35, *porthos* RNAi n=0.37; p=0.27; movie #: control n=4, *porthos* RNAi n=6. Directionality on yolk: control=0.42, *porthos* RNAi=0.39; p=0.58; movie #: control n=3, *porthos* RNAi n=6. Unpaired t-test for (C-D) and one-way ANOVA with Tukey for (F). Scale bar is 5 μm in (B).

(Fig. 4C, Figs. S4G-I). (Speed: in head, 2 $\mu\text{m}/\text{min}$ for control and *porthos* RNAi (p=0.56); on yolk, 2.1 or 2.2 $\mu\text{m}/\text{min}$ for control or *porthos* RNAi respectively (p=0.35). Directionality: in head, control=0.35 and *porthos* RNAi=0.37 (p=0.27); on yolk, control=0.42 and *porthos* RNAi=0.39 (p=0.58)). Moreover, we detected no significant change in the speed of macrophages moving on the yolk and beneath the germband on their way to the germband entry point and beyond (2.2 $\mu\text{m}/\text{min}$ for the control and 2.4 $\mu\text{m}/\text{min}$ the *porthos* RNAi, p=0.45) (Fig. 4D). However, *porthos* KD macrophages delayed entering the germband tissue, waiting 69% longer than the control (21.5 or 36.3 min for control or *porthos* RNAi, respectively p<0.0001) (Fig. 4E). Once within the germband, the first and second macrophages invading between the mesoderm and ectoderm progressed significantly slower than the control (1st cell: 3.0 or 2.0 $\mu\text{m}/\text{min}$ in the control or *porthos* RNAi, respectively, p=0.009, 2nd cell: 2.6 or 2.0 $\mu\text{m}/\text{min}$ in the control or *porthos* RNAi, respectively, p=0.037) (Figs. 4F-G). In contrast, the speed of the macrophages following these pioneers was not significantly altered by *porthos* KD (3rd-5th cells: 2.7 or 2.3 $\mu\text{m}/\text{min}$ for the control or *porthos* RNAi, respectively, p=0.21) (Fig. 4H). Thus, *porthos* phenocopies *atossa*'s migration defect. Finally, we expressed Porthos in the *atossa* mutant under *srpHemo-GAL4* *UAS* control to restore its higher levels in macrophages. Excitingly, this nearly completely reverses the *atossa* mutant phenotype (87% rescue) (Figs. 4J-K). Thus we conclude that Porthos is a main downstream transcriptional target of Atossa, exerting an essential role in pioneer macrophages to specifically allow their initiation of germband invasion.

Loss of Porthos alters translation

Given that ATP-dependent DEAD-box RNA helicases are involved in RNA metabolism, RNA remodeling, ribosome biogenesis, and efficient mRNA translation (Bourgeois et al. 2016; Jarmoskaite and Russell, 2011), we speculated that the helicase Porthos might rewire the translational status of macrophages by modulating target mRNA structures. To assess translation, we purified ribosomes and polysomes by sucrose density gradient fractionation of the control and S2R+ cells treated with *porthos* RNAi (Fig. S5A). We observed a reduction in polysomes, the 40S small subunit, and 80S ribosome fraction (Fig. 5A) along with an increase in the large 60S subunit peak in the *porthos* KD. This data suggests that Porthos is required for normal levels of 40S biogenesis, ribosome and polysome assembly, and supports a role for Porthos in the translational regulation of mRNAs.

Figure 5. Porthos increases the translation of TOPL RNAs including many involved in mitochondrial OXPHOS and metabolic processes. **Fig 5A.** Sedimentation analysis showing the relative abundance of 40S, 60S, and 80S ribosomes indicates that *porthos* depletion by shRNA markedly reduces the ratio of polysomes to monosomes. Scrambled was used as a control. Profiles were aligned on the basis of the 40S ribosome peak's position and labeled with distinct colors, black for control and red for *porthos* KD, n=3 biological replicates. **Fig 5B.** Scatter plot of Transcripts per Kilobase Million (TPM) from Polysome profiling analysis versus RNA sequencing analysis in *porthos* shRNA S2R+ cells. Red (down-regulated, DR) and green (up-regulated, UP) dots represent genes with significant \log_2 translational efficiency (TE) changes and grey dots (not-changed, NC) indicate genes with no TE significant change. **Fig. 5C.** The consensus sequence, which we call the TOPL motif, is enriched in the 5' UTR of mRNAs that displayed significantly reduced translation in *porthos* shRNA treated S2R+ cells. Hypergeometric $p < 0.00001$. 1 represents the 5' end. **Fig 5D.** The majority of the mRNAs with decreased polysome occupancy (204 transcripts) bear a 5' TOPL motif, with only 9 nonTOPL mRNAs. DR mRNAs with assigned functions (AF) and non-assigned function (NAF) were included. **Fig 5E.** Gene ontology (GO) analysis of downregulated TOPL mRNAs in *porthos* RNAi-treated versus Control-RNAi treated S2R+ cells. The number of genes corresponding to a category of their predicted function is shown. A significant fraction of the mRNAs that require Porthos for enhanced TE encode proteins involved in mitochondrial-related functions, metabolic processes, and redox processes **Fig 5F.** Porthos modulates the TOPL-dependent translation of various mitochondrial proteins. These RNAs consist of the components of mitochondrial OXPHOS, including subunits of mitochondrial complexes I, III, IV and the ATP synthase complex V. Porthos also enhances the translation efficiency of mitochondrial transporting channels, structural proteins as well as those involved in mitochondrial translation. **Fig 5G.** TOPL mRNAs that are downregulated in *porthos* RNAi-treated S2R+ cells are involved in metabolic pathways, including sugar, nucleotide, amino acid/peptide, nucleotide pathways as well as glycolysis.



F

Cellular function	Gene symbol	Description (DR TOPL targets)	Vertebrate ortholog
Mito respiration	CG3270	Complex I, NADH:ubiquinone oxidoreductase, predicted assembly factor	Foxred1
	CG8764	Complex III, ubiquinol-cytochrome c reductase, Oxen Qcr9	Uqcr10
	CG34242	Complex IV, mitochondrial cytochrome c oxidase predicted assembly factor	Smim20
	CG6105	Complex V, ATP synthase, Fo portion, subunit G (ATPsynG)	Atp5l
	CG10731	Complex V, ATP synthase, coupling factor B	Dmac2l
Mito transport/structure	CG1158	Tim17b1, Mito protein-transportingATPase	Timm17a
	CG8860	Mitochondrial protein-transporting ATPase	Sec61g
	CG9090	Mpcp1, Mitochondrial phosphate carrier protein 1	Slc25a3
	CG5646	SLC25A47, acyl carnitine transmembrane transporter	Slc25a45
	CG1287	Mics1, Mitochondrial morphology/ cristae structure 1	Ghitm
	CG34132	Protein localization into MIM	Timm13
	CG11110	Serine peptidase, protein targeting to mitochondrion	Immp2l
CG2854	Predicted mitochondrial T cell activation inhibitor	Tcaim	
Mito translation	CG32531	mRpS14, mitochondrial ribosomal small protein S14	Mrps14
	CG13608	mRpS24, mitochondrial ribosomal small protein S24	Mrps24
	CG34147	mRpL34, mitochondrial ribosomal large protein L34	Mrpl34
	CG11679	Predicted positive regulator of mito translation	Rmnd1
Redox	CG9363	GstZ2, glutathione metabolic process	Gstz1
	CG11512	Mitochondrial GstD4, glutathione metabolic process	Gstt1
	CG6461	Ggt-1, glutathione metabolic process	Ggt1
	CG14221	Glutathione metabolic process	Nme8
	CG6762	Sulfiredoxin, response to oxidative stress	Srxn1
CG7460	Polyamine oxidase, redox process	Paox	
CG5653	Redox process	Paox	

G

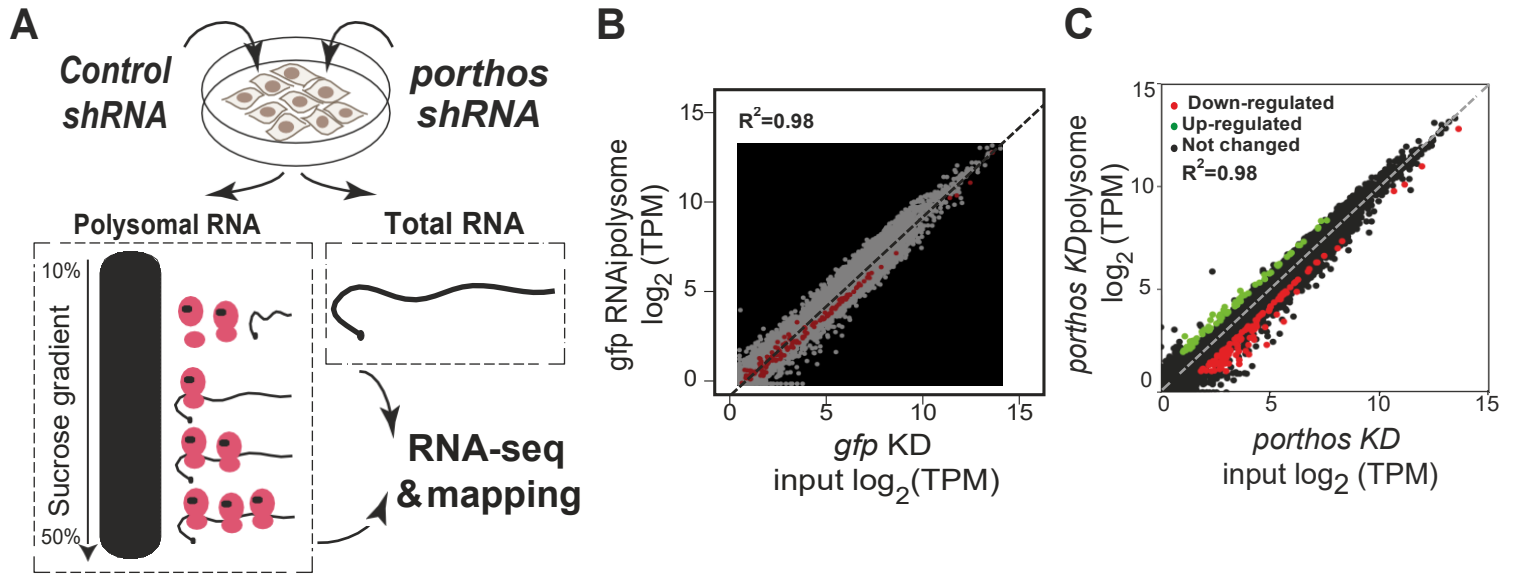
Cellular function	Gene symbol	Description (DR TOPL targets)	Vertebrate ortholog
Sugar metabolism	CG42814	UDP-sugar diphosphatase	Nudt14
	CG14212	Haloacid dehalogenase, sugar dephosphorylation	Phospho1
Nucleotide metabolism	CG30016	Hydroxyisourate hydrolase, purine metabolism	Urah
	CG3788	Uridine phosphorylase	Upp1
	CG5828	Pantothenate kinase	Pank4
	CG7735	ADP ribosylation factor-like 6	Arl6
	CG33514	Phosphatidylinositol bisphosphate binding	Civs1
	CG5840	P5cr-2, Pyrroline-5-carboxylate reductase-like 2	Pycl1
Amino acid/peptide metabolism	CG7768	Peptidylprolyl isomerase	Ppif
	CG11843	Acylaminoacyl-peptidase	F12
	CG34041	Methylation of glycine to generate sarcosine	P4ha2
	CG6188	Gnmt, Glycine N-methyltransferase	Gnmt
	CG14990	SPH97, serine-type endopeptidase	Tpsab1
	CG10764	Acylaminoacyl-peptidase	NF
	CG7367	Carboxylesterase	Liph
	CG17562	Fatty-acyl-CoA reductase	Far2
	CG11052	Acylphosphatase	Acyp2
	CG8303	Fatty-acyl-CoA reductase (alcohol-forming)	Far1
	CG13091	Sgroppino, fatty-acyl-CoA reductase	Far2
Lipid metabolism	CG9709	Acox57D-d, acyl-Coenzyme A oxidase	Acox1
	CG2985	Yolk protein 1, carboxylesterase	Lipi
	CG11129	Yolk protein 3, carboxylesterase	Lipi
	CG8498	Acbp1, Acyl-CoA binding protein 1	Acbd7
Glycosylation	CG31956	N-Acetylgalactosaminyltransferase 4	Galnt10
	CG33774	Protein N-linked glycosylation	Ost4
	CG3253	Glucuronosyltransferase, O-linked mannosylation	B4GAT1

We then examined which mRNA transcripts depend on Porthos for their efficient translation. We performed polysome-profiling, sequencing transcripts associated with translationally active ribosomes as well as all the transcripts in the S2R+ cells, and plotted this ratio for the control and *porthos RNAi KD* cells (Fig. 5B). We calculated the translational efficiency (TE) for each gene by comparing the normalized sequencing counts from polysomes and the total mRNA fractions from control (GFP KD) and *porthos* KD replicates (Fig. S5B). We found that upon *porthos* depletion 282 transcripts are less efficiently translated, whereas 149 transcripts are more prevalent on polysomes in *porthos* KD cells.

Porthos is required for the selective translation of transcripts harboring a conserved Terminal Oligo Pyrimidine Like (TOPL) motif in their 5'-UTRs

To determine if Porthos' target transcripts share any common features in the 5' UTR, we carried out bioinformatic analysis (Cap analysis gene expression; CAGE). We first excluded RNAs from the analysis that do not contain a polyA. We identified that the majority of mRNAs dependent on Porthos for their enhanced translational efficiency share a conserved pyrimidine rich sequence element in their 5'-UTR, (95%, 204 of the 213 target mRNAs) (Fig. 5D). We name this the TOPL motif as it is very similar to the TOP sequence identified in mammals (Albert et al., 2015; Morita et al., 2013; Thoreen et al., 2012; Meyuhas and Kahan 2015), but not previously in *Drosophila* (see also Martin et al., unpublished). The TOPL-containing mRNA targets that require Porthos for enhanced TE are mainly involved in mitochondrial respiration, mitochondrial transport and translation, metabolic processes, transcription, translation, signal transduction, immune responses as well as redox processes (Fig. 5E, Figs. S5D,E). The targets include several components of the mitochondrial OXPHOS, including ubiquinol cytochrome C reductase (complex III, UQCR-Q), ATP synthase subunit G and coupling factor F(o) (complex V) mitochondrial translation and transport (Fig. 5F) as well as the metabolic pathways (Fig. 5G). Thus, our data support the hypothesis that Porthos controls the initiation of macrophage invasion by initially modulating the translational efficiency of a distinct group of mRNAs, which share the conserved TOPL motif in their 5'-UTRs.

Figure S5. Porthos enhances the translation of TOPL mRNAs, including many involved in gene regulation and transcription, protein synthesis and turnover, signal transduction, and immune responses. Fig 5SA. Schematic shows the approach employed to study the translational status of S2R+ cells transfected with control or *porthos* shRNAs. Total or polysomal RNA fractions were pooled following shRNA treatment and RNAseq libraries were prepared. **Figs. 5SB-C.** A bi-plot shows the TE of expressed mRNAs in *porthos RNAi*-treated versus Control-RNAi treated S2R+ cells. The lines represent the cutoffs one standard deviation above and below the median ratio. Red (down-regulated) and green (up-regulated) dots represent genes with significant TE changes. **Figs. 5SD-E.** Other TOPL RNAs downregulated in *porthos KD* cells are mainly involved in gene regulation, RNA processing, mRNA translation, cellular transport, cell signaling, cell-cell interactions, immune response, and protein.



D

Biological function	Gene symbol	Description (DR TOPL mRNAs)	Vertebrate ortholog
DNA regulation, Transcription,	CG11403	DNA DEAD/H box helicase 11	Ddx11
	CG12659	Chromatin remodeling	Ino80c
	CG11335	Lysyl oxidase-like 1 (Loxl1), euchromatinization	Loxl2
	CG10694	nucleotide-excision repair	Rad23a
	CG5441	taxi, transcription factor	Atoh1
	CG13005	Zinc finger protein 839, transcription factor	Zfp839
	CG7963	Zinc finger C2H2 transcription factor	Gm14322
	CG8159	Regulation of transcription	Plag1
	CG11456	Regulation of transcription by RNA polymerase II	Plag2
	CG10654	Regulation of transcription by RNA polymerase II	J23Rik
	CG31626	Regulation of transcription by RNA polymerase II	Pou2af1
	CG12442	wuc, regulation of transcription by RNA polymerase II	Lin52
	CG8021	SLIRP2, mRNA processing	Slirp
	CG12320	A1 cistron-splicing factor, AAR2	Aar2
	CG12938	U7 snRNA-associated Sm-like protein LSm10	Lsm10
CG7637	snRNA/rRNA pseudouridine synthesis	Nop10	
RNA translation	CG15693	RpS20, ribosomal small protein S20	Rps20
	CG3997	RpL39, ribosomal large protein L39	Rpl39l
	CG30425	RpL41, ribosomal large protein L41	NF
	CG4061	Rtca, RNA 3'-terminal phosphate cyclase	Rtca
	CG18643	Dtd, D-aminoacyl-tRNA deacylase, tRNA metabolic process	Dtd1
Protein degradation	CG8272	SCF-dependent proteasomal ubiquitin-dependent proteolysis	Lrrc29
	CG14260	Proteasomal ubiquitin-dependent proteolysis	NF
	CG31807	Ubiquitin-protein transferase	Rfwd3
	CG8419	Ubiquitin-protein transferase	Trim45
	CG32847	Ubiquitin-protein ligase	Rnf185
	CG5001	Chaperone/unfolded protein binding	Dnajb5
	CG2046	Proteasome assembly chaperone 1	Psmg1
CG6972	Desumoylating isopeptidase 1	Desi1	
Immune cell response	CG2723	ImpE3, Ecdysone-inducible gene E3	NF
	CG1367	Cecropin A2, activity against Gram-negative bacteria	NF
	CG10794	Diptericin B, activity against Gram-negative bacteria	NF
	CG16712	IM33 peptide against systemic microbial infection	Eppin
	CG33493	Antibacterial humoral response	Ndufa5

E

Biological function	Gene symbol	Description (DR TOPL mRNAs)	Vertebrate ortholog
Signal transduction	CG1279	reticulum 2, ER organization and function	Rtn1
	CG5417	Srp14, protein targeting to ER	Srp14
	CG12843	Tetraspanin 42Ei, Integrin signaling	Cd63
	CG5657	Sarcoglycan β , negative regulator of EGFR pathway	Sgcb
	CG3302	Corazonin, a G-protein-coupled receptor	NF
	CG42366	Mitogen-activated protein kinase	NF
	CG8767	Mos oncogeneactivates the MAPK cascade	Mos
	CG18188	Damm, caspase family of cysteine proteases	Casp6
	CG9336	positive regulation of voltage-gated K ⁺ channel	NF
	CG3504	inaD, fast light-induced signaling	Lnx1
	CG7916	Haemolymph juvenile hormone binding	NF
	CG9470	Metallothionein A, metal ion homeostasis	Mt1
	CG3227	insensitive, corepressor for the product of Su(H)	NF
	CG10861	Autophagy-related 12	Atg12
	CG14937	G2/M transition of mitotic cell cycle	NF
C17479	Sphingosine kinase 1, regulates cell division/trafficking	NF	
CG17962	Z600, a mitotic inhibitor	NF	
CG32812	negative regulation of phosphatase activity	Chp1	
CG31391	negative regulation of phosphatase activity	Ppp1r36	
Transport	CG17137	Porin2, voltage-dependent anion channel 1	Vdac1
	CG7912	Sulfate transport and transmembrane transport	Slc26a11
	CG18345	Trpl, transient receptor potential-like	Trpc5
	CG32069	ER to Golgi vesicle-mediated transport	Ier3ip1
	CG11703	Sodium:potassium-exchanging ATPase	Atp1b1
CG5421	H(+)-transporting two-sector ATPase	Atp6ap1l	
Cell-cell interaction	CG13664	Cadherin 96Cb, control of cell adhesion	Cdh6
	CG16719	Regulation of cytoskeleton organization	Spef1
	CG5987	TTL6B, microtubule cytoskeleton organization	Ttl6
	CG4537	Cytoplasmic microtubule organization	Cript
	CG7802	Neyo, regulation of cell shape/apical constriction	NF
	CG12408	Troponin C isoform 4, control of muscle contraction	Calm4
	CG8121	Pasiflora 2 (pasi2), endothelial barrier function	NF
	CG5458	Radial spoke head protein 1, axoneme assembly	Rsph1
	CG31020	Sanpodo, cell division/cell fate determination	NF
	CG31801	Mst36Fa, spermatogenesis	NF

Porthos is required for mitochondrial oxidative respiration and energy production

We were struck by the number of mitochondrial proteins in the set of TOPL targets that depend on Porthos for their higher levels of translation in S2R+ cells. Mitochondria are central metabolism hubs crucial for immune cell survival, proliferation, and migration; they generate ATP through mitochondrial OXPHOS frequently from the pyruvate formed by the glycolytic pathway (Pavlova and Thompson, 2016; Vander Heiden et al., 2009) (Fig. S6A). To directly investigate if Porthos regulates mitochondrial energy production, we first employed a CRISPR/Cas9-mediated mutagenesis strategy to generate stable *porthos* KD S2R+ cells producing only 43% of normal mRNA levels for *porthos* (Fig. 5SB); we were unable to stably knockdown *atossa*. Using S2R+ cells we analyzed mitochondrial function via a Seahorse XFp assay in which sequential treatment with compounds that block different steps of mitochondrial respiration permit the calculation of distinct metabolic parameters (Fig. S6B). We calculated oxygen consumption rates (OCR) as an index of mitochondrial oxidative metabolism (Fig. 6A) (Llufrio et al., 2018) and identified a clearly impaired respiration capacity of *porthos* KD cells compared to the control (Fig. 6A). We also observed a significant reduction in the basal oxygen OCR (36%), maximum mitochondrial respiration (36%), non-mitochondrial respiration (58%), spare respiration capacity (28%), as well as ATP turnover (37%) (see Methods for calculations) (Fig. 6B). S2R+ cells utilize primarily mitochondrial OXPHOS rather than glycolysis for ATP production (Freijie et al., 2012); this does not appear to change even in the *porthos* KD cells (Fig. S6D), as we also observed a reduction in measures of lactate production through complete glycolysis, the basal extracellular acidification rate (ECAR; 40%) and the proton production rate (PPR; 40%), compared to control cells (Fig. S6E). In totality, ATP production is reduced by 60% upon *porthos* depletion (Fig. 6B). In sum, *porthos* depletion induces a highly significant decrease in mitochondrial respiration, resulting in a bioenergetic defect and reduced ATP generation capacity. Given that Porthos modulates the TOPL-dependent translation of subunits of mitochondrial complex III and the ATP synthase complex V, our data argues that Porthos induces a shift in metabolic flux that contributes to the upregulation of the OXPHOS pathway and higher levels of energy production.

Mitochondrial respiration is required for metabolism and energy production in macrophages to initiate invasion into the germband tissue

We sought to directly assess the importance of OXPHOS and the complexes whose components are Porthos translation targets for macrophage germband invasion in the embryo. We tested the effect of a dominant negative form of *complex V* also known as ATP synthase (*CV-DN*) (Figs. 6C-F). We also expressed multiple independent RNAis against *complex III* (catalytic subunits *Cyt-c1*, *UQCR-cp1*, and subunit *UQCR-cp2*) and *complex V* (*FOF1*, *CG3612*) in macrophages (Figs. 6G, H). Consistent with the polysome-profiling results from *porthos-KD* S2R+ cells, each of these treatments significantly reduced macrophage numbers within the germband (Figs. 6C-H) and increased them on

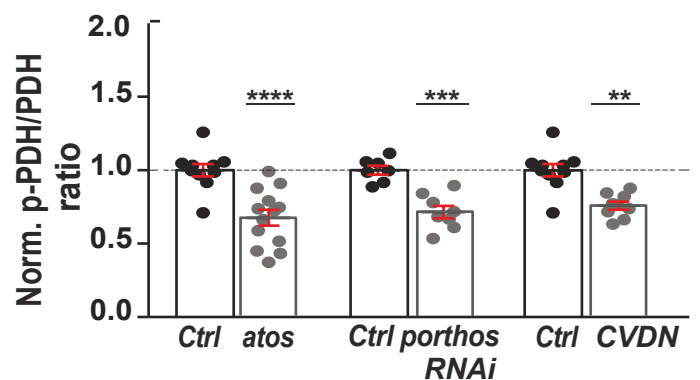
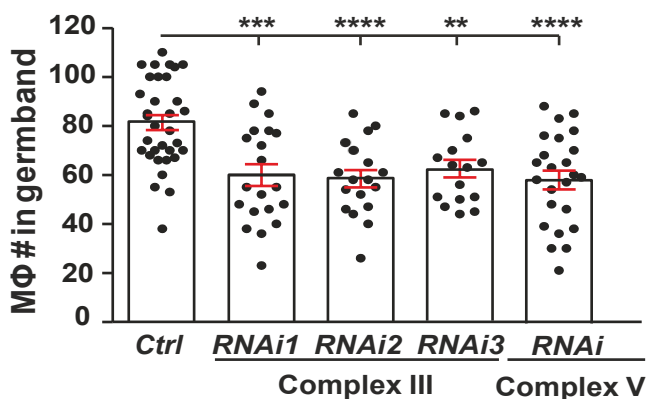
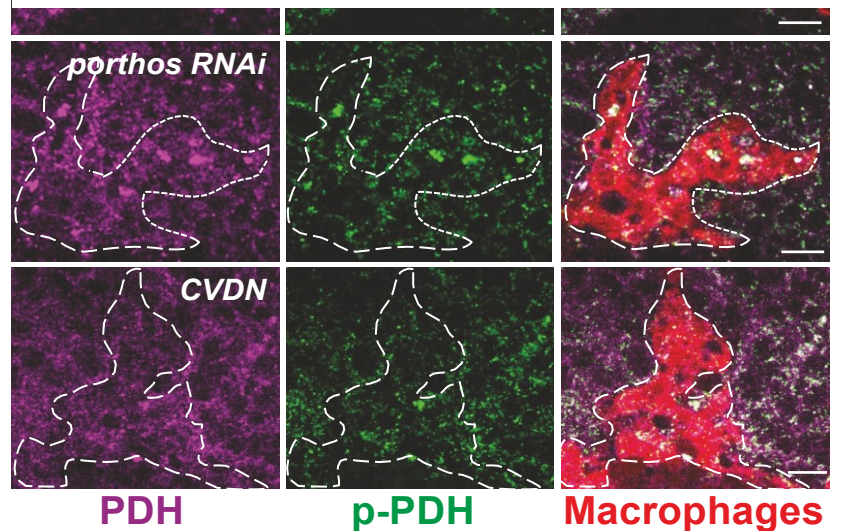
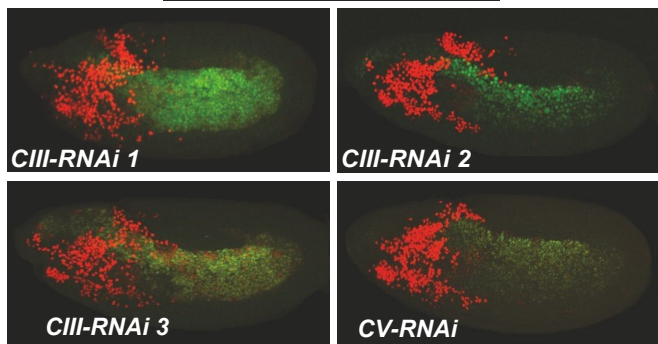
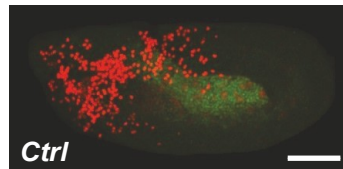
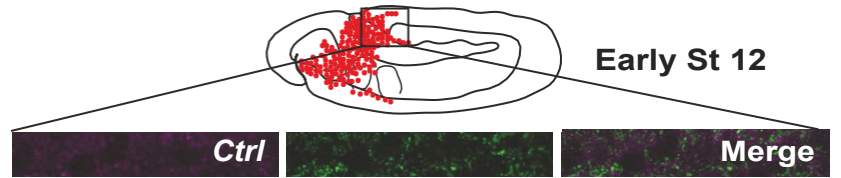
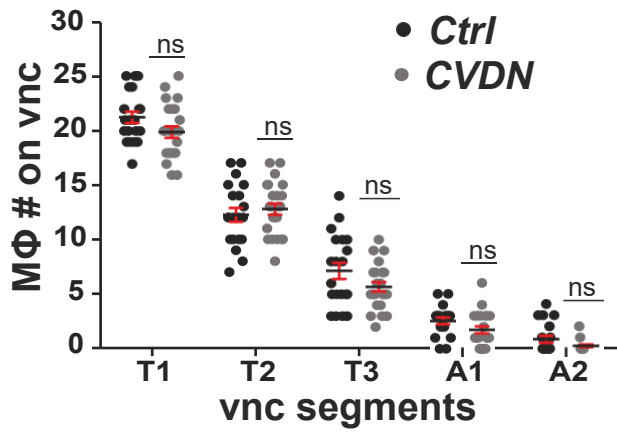
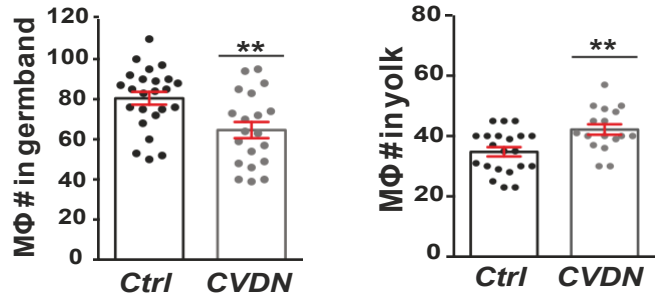
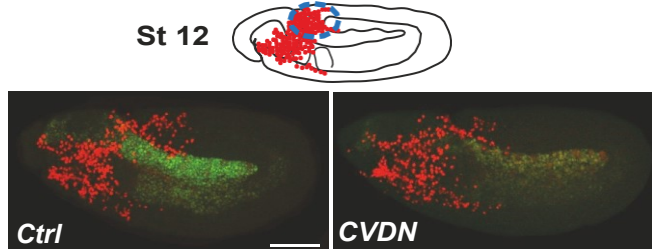
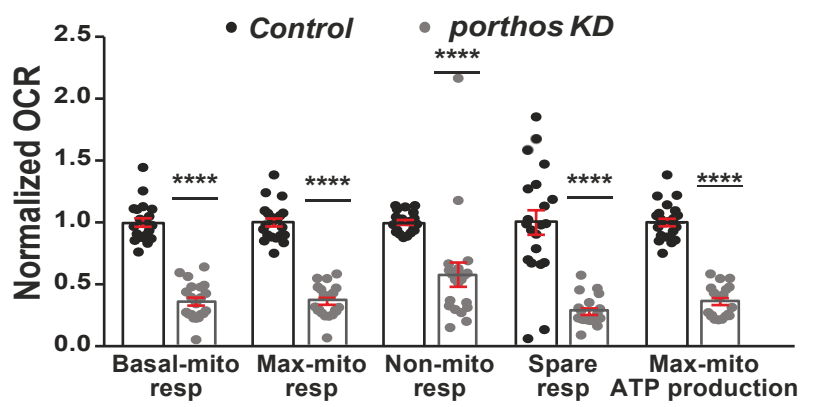
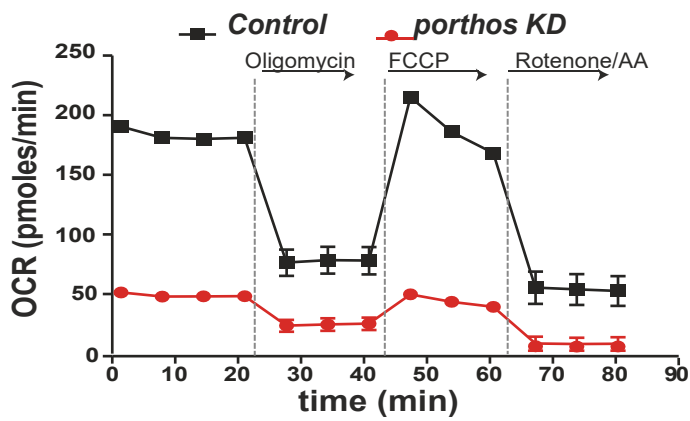


Figure 6. Mitochondrial respiration is required in macrophages to power their germband tissue invasion.

Fig 6A. *porthos*-KD S2R+ cells are less metabolically active than wild-type cells. The Oxygen Consumption Rate (OCR, pmols O₂/min) was assessed as a representative parameter of mitochondrial bioenergetics in control and *porthos*-KD S2R+ cells by a Seahorse Bioscience XF96 Extracellular Flux Analyzer. The ATP synthase inhibitor oligomycin (2μM), the uncoupler FCCP (2μM), and the mitochondrial complex I inhibitor Rotenone (1μM) with Antimycin A (1μM) were injected sequentially (see S7A). **Fig 6B.** Calculation of the relative OCR values at different stages to assess basal respiration, maximum respiration, non-mitochondrial respiration, spare respiratory capacity, and mitochondrial ATP turnover rates. Independent biological experiments were repeated at least three times (n>6 technical replicates in each repeat). Data are represented as the mean ± SEM. **Fig 6C.** Representative confocal images of Stage 12 embryos from the control and lines expressing a dominant negative c-ring of the complex V ATP synthase (CV-DN) in macrophages (red). **Fig 6D.** Quantification reveals that the number of macrophages that penetrated into the germband in Stage 12 embryos is significantly decreased upon the expression of CV-DN, ATP synthase, compared to the control, indicating that Complex V (ATP synthase) is needed for macrophage germband invasion. Control n=24, *CV-DN* n=20, p=0.003. **Fig 6E.** Quantification of macrophages on the yolk in fixed early Stage 12 embryos shows a significant increase in the *CV-DN* embryos compared to the control. Control n=21, *CV-DN* n=17, p=0.003. **Fig 6F.** Quantification of the number of macrophages in vnc segments does not show a significant change in general migration along the vnc in *CV-DN* embryos compared to the control. Control n=20, *CV-DN* n=23. **Fig 6G.** Representative confocal images of Stage 12 embryos from the control and lines expressing RNAis against either *Complex III*, or *Complex V* in macrophages (red). *Complex III RNAi 1*, VDRC 109809; *RNAi 2*, VDRC 101350; *RNAi 3*, VDRC 100818. *Complex V RNAi* VDRC 34664. **Fig 6H.** Quantification of Stage 12 embryos indicates that fewer macrophages move into the germband upon the expression in macrophages of any of three different RNAis against mitochondrial OXPHOS *Complex III (Ubiquinol-cytochrome c reductase, UQCR)*, or an RNAi against *Complex V (FOF1, CG3612)*, arguing that these two components are required in macrophages for germband tissue invasion. Control n=34; *Complex III (Cyt-c1, CG4769) RNAi 1* (VDRC 109809) n=20, p=0.0001. *Complex III (UQCR-cp1, CG3731) RNAi 2* (VDRC 101350) n=18, p<0.0001. *Complex III (UQCR-cp2, CG4169): RNAi 3* (VDRC 100818) n=16, p=0.0027. *Complex V (FOF1, CG3612): RNAi* (VDRC 34664) n=24, p<0.0001. **Fig 6I.** Confocal microscopy images of a single plane from control (Ctrl), *atos* mutant embryos, and embryos expressing *porthos* RNAi or *CV-DN* in macrophages during germband entry in early Stage 12. Embryos were stained with antibodies to the phosphorylated and thus inactivated Pyruvate Dehydrogenase (pPDH, in green) and Pyruvate Dehydrogenase (PDH, in magenta) in macrophages (red). Higher levels of pPDH are usually found when ATP/ADP levels are high and input into the TCA cycle is being downregulated (Patel et al., 2014). **Fig 6J.** Quantification of normalized values for pPDH/PDH levels calculated from fluorescence intensities in macrophages during initial germband invasion in early Stage 12. Values were obtained from control (Ctrl), *atos* mutant embryos, and those expressing either *porthos* RNAi or *CV-DN* in macrophages. The pPDH/PDH ratio is significantly reduced in all compared to the control, arguing that the loss of function of *atos*, *porthos* or expression of *CV-DN* in macrophages results in lower cellular ATP/ADP ratios compared to those in control macrophages. Control n=10, *atos* mutant n=13, level p=0.0002. Control n=7, *macro>porthos* RNAi n=8, p=0.0002. Control n=10, *CV-DN* n=9, p=0.0002. Three independent experiments. Macrophages visualized in C and G with nuclear *srpHemo-H2A::3xmCherry* expression and I with cytoplasmic *srpHemo-3xmCherry*. Unpaired t-test for (A), (B), (D), (E), (F), (H) and (J). Scale bars are 50 μm in (C) and (G), and 10 μm in (I).

the yolk at the germband entry site (Figs. 6C and S6F), phenocopying the defect in germband invasion seen in the *atossa*^{PBG} or *porthos* knockdown in macrophages. We observed no significant difference in macrophage numbers on the vnc upon *CV-DN*-expression as compared to the control in late Stage 12, indicating normal general migration (Fig. 6F). This data strongly supports the conclusion that Complex III and V of the mitochondrial respiratory chain are required specifically for macrophage tissue invasion.

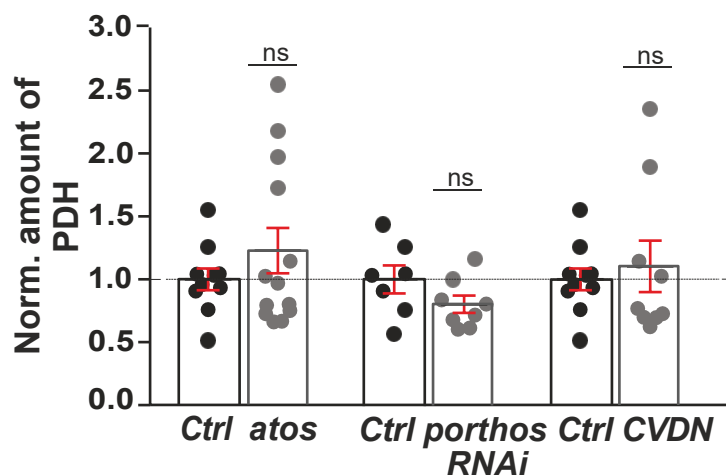
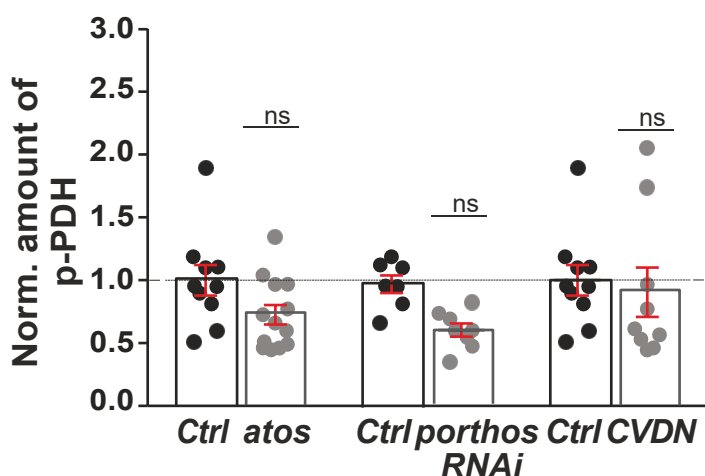
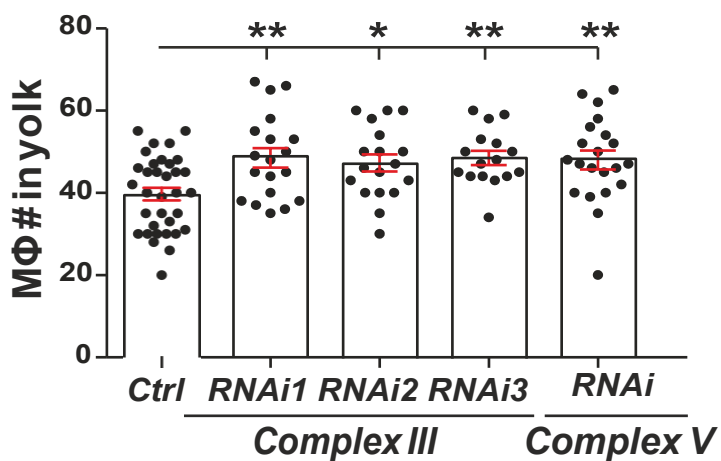
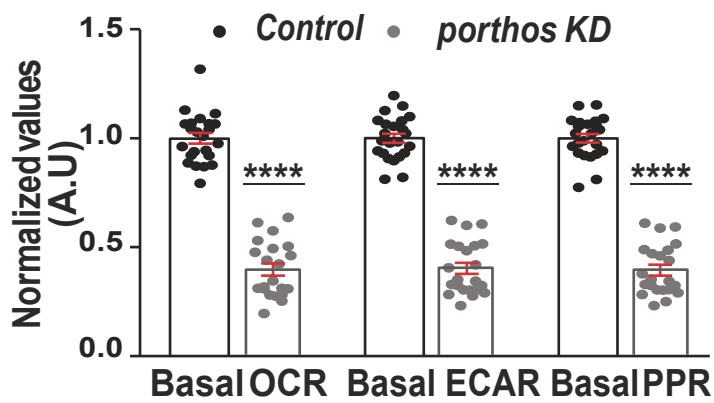
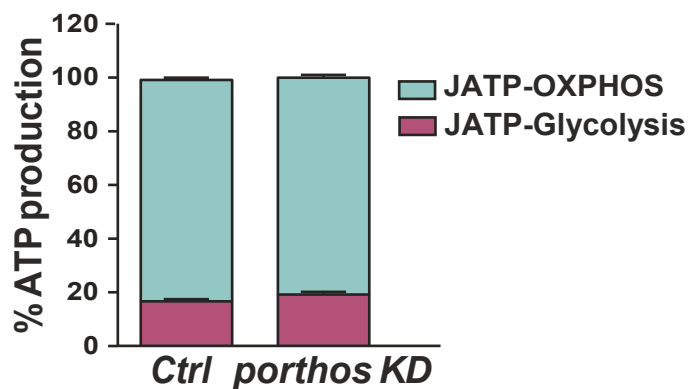
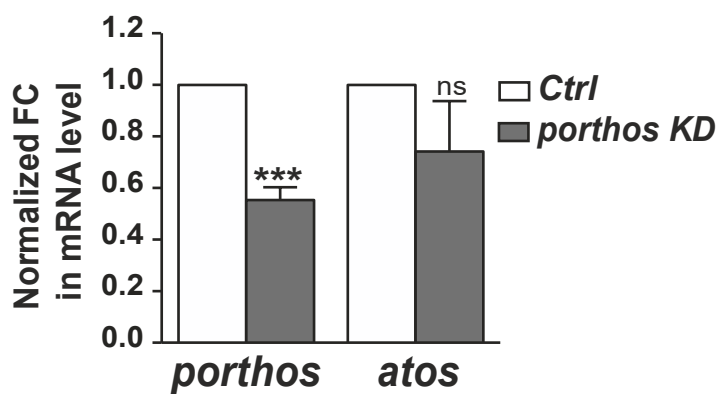
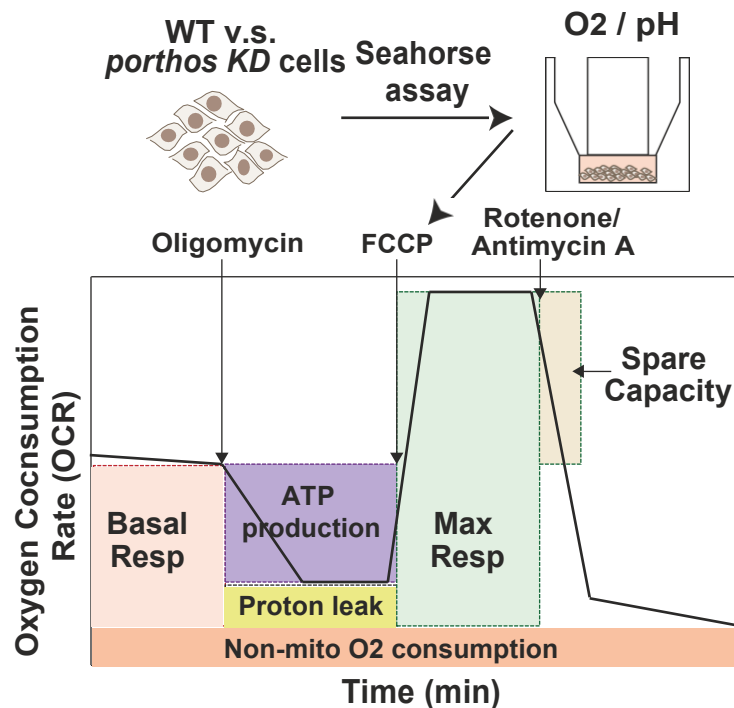
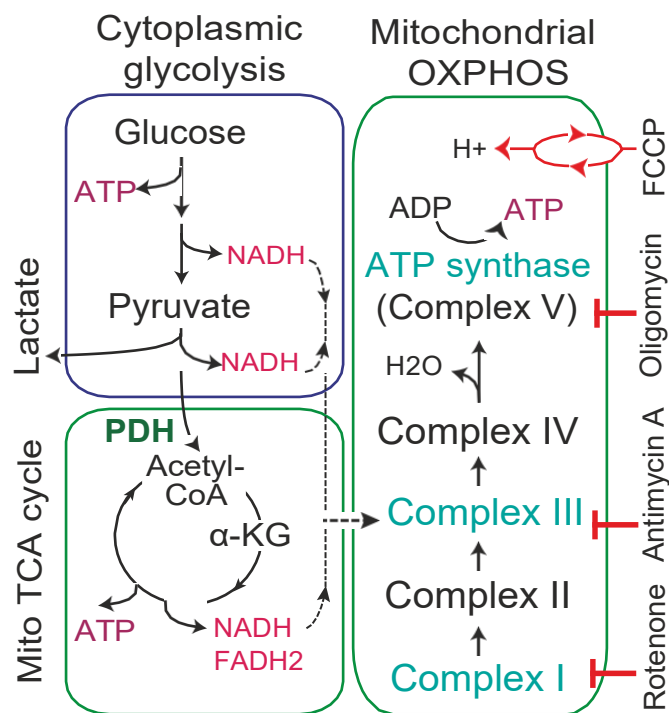


Figure S6. Depletion of *atossa* or *porthos* causes impairment in mitochondrial metabolic activity, reduced ATP production, and a deficiency in macrophage tissue invasion. **Fig S6A.** Schematic depicting the glycolysis, Krebs cycle (TCA cycle), and mitochondrial respiratory chain in eukaryotic cells. Cytoplasmic glycolysis and mitochondrial respiration are the major means to produce ATP, the energy currency of cells. Specific inhibitors are used block the function of mitochondrial OXPHOS components. **Figs. S6A,B.** Graph shows relative *porthos* and *atossa* mRNA levels (\pm SEM) in *porthos*-KD S2R+ cells measured by qPCR from at least three independent experiments. The data are normalized to results for the internal control gene RpS20. *porthos*-KD S2R+ cells contain 56% of normal *porthos* mRNA levels and display a slight statistically insignificant decrease in *atossa* mRNA levels. t-test was used followed by Sidak's correction. Control n=6, *porthos* KD n=6, p= 0.0002, *atos* KD n=3, p=0.09. **Fig S6C.** Schematic shows the procedure for mitochondrial energetic profiling in wild-type and *porthos* KD S2 cells with a Seahorse efflux assay. **Fig S6D.** The contribution of mitochondrial ATP production rate and glycolytic ATP production rate were calculated. The plot shows that both wild-type and *porthos*-KD and S2 cells utilize mitochondrial respiration as the predominant bioenergetic pathway to produce ATP in these cells. Porthos depletion produced no increase in the relative utilization of glycolysis. **Fig S6E.** The relative basal values of OCR as a marker of OXPHOS, Extracellular Acidification Rate (ECAR) as an indication of glycolysis, and Proton Production Rate (PPR) in control and *porthos*-KD S2 cells are plotted. Basal respiration rate is calculated before the addition of Antimycin. Porthos depletion leads to a reduction in basal rates of OCR, ECAR as well as PPR. **Fig S6F.** Quantification in fixed early Stage 12 embryos shows a significant increase of macrophages on the yolk upon the expression in macrophages of any of three different RNAis against mitochondrial OXPHOS *Complex III (UQCR)* or an RNAi against *Complex V (FOF1, CG3612)*. Control n=34, *Complex III (Cyt-c1, CG4769): RNAi 1* (VDRC 109809) n=19, p=0.0049, *Complex III (UQCR-cp1, CG3731): RNAi 2* (VDRC 101350) n=18, p=0.024, *Complex III (UQCR-cp2, CG4169): RNAi 3* (VDRC 100818) n=16, p=0.009. *Complex V (FOF1, CG3612): RNAi* (VDRC 34664) n=21, p=0.0068. **Fig S6G-H.** Scatter plots illustrate the normalized values measured for pPDH and PDH levels, in macrophages at germband entry from control, *atos* mutant, *macro>porthos* RNAi, and *CV-DN* at early Stage 12 embryos. The pPDH and PDH levels did not show a significant change in *atos* mutant macrophages or those expressing *porthos* RNAi or *CV-DN* compared to the control. Control (*Ctrl*) n=10, *atos* mutant n=13; pPDH level p=0.6; PDH level p=0.31. Control n=7, *mac>porthos* RNAi n=8; pPDH level p=0.01; PDH level p=0.14. Control n=10, *CV-DN* n=9; pPDH level p=0.68; PDH level p=0.63. Data are expressed as mean \pm SEM of triplicate experiments. Unpaired t-test for (B), and (D-H).

Atossa and its transcriptional target Porthos are required to shift macrophage bioenergetics for germband tissue invasion

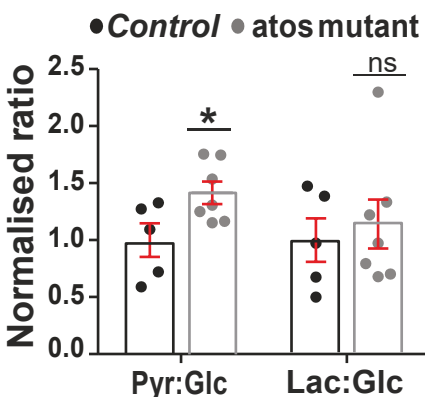
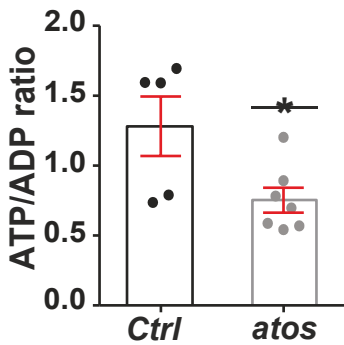
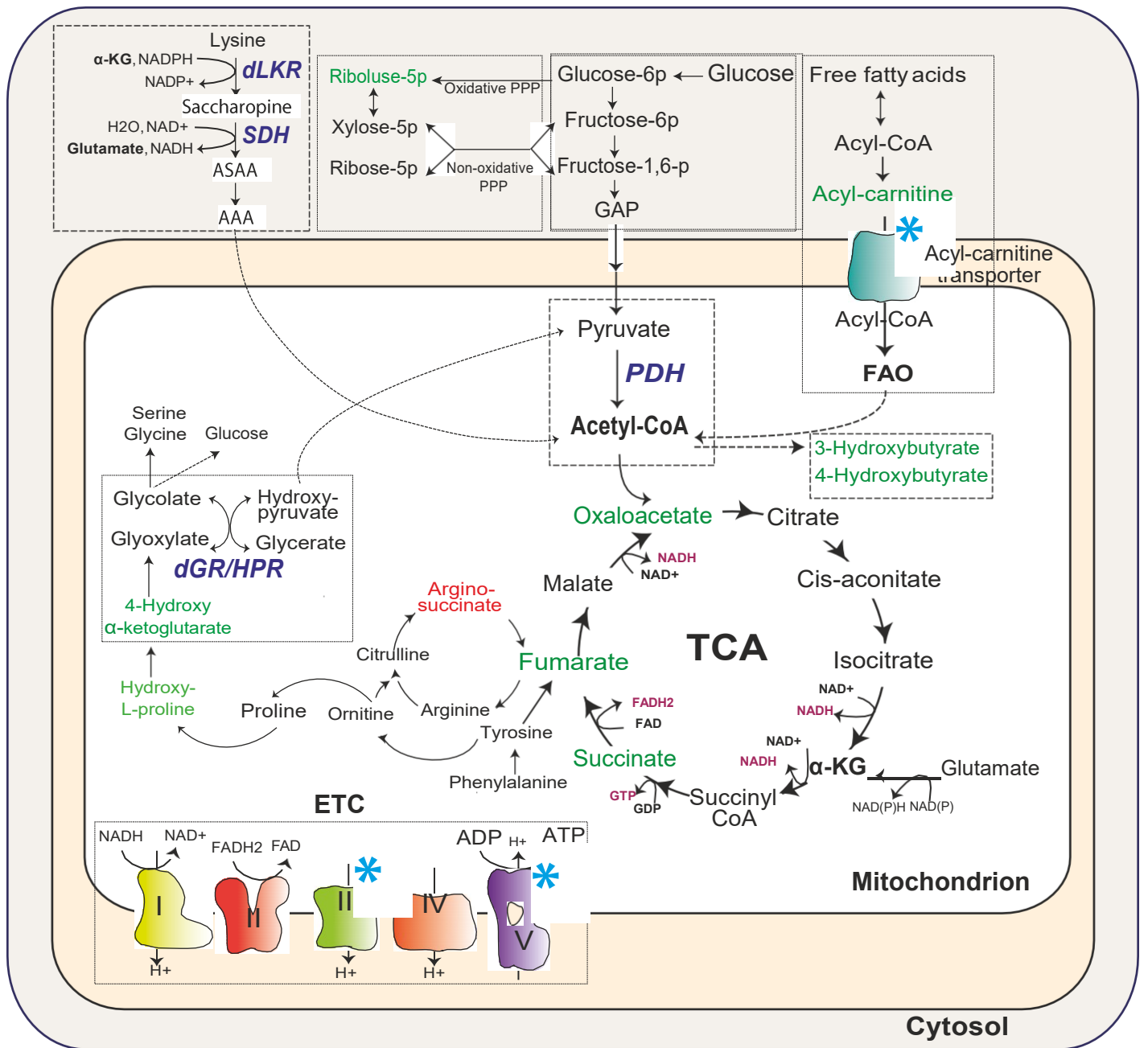
To examine the bioenergetic state of embryonic macrophages *in vivo* in the absence of Porthos or Atossa, we first assessed the activation state of the Pyruvate dehydrogenase complex (PDH), a gatekeeper that bridges glycolysis to the citric acid cycle (TCA or Krebs cycle) in the mitochondria and acts as a key node point for metabolic regulation (Patel et al. 2014). PDH is phosphorylated and thus inactivated by Pyruvate dehydrogenase kinase (PDK), which is itself stimulated or inhibited by numerous metabolites including NAD/NADH, acetyl-CoA/CoA, pyruvate, and ADP. Importantly, PDK is inhibited and PDH is not phosphorylated, remaining active to feed pyruvate into the TCA cycle when mitochondrial ADP levels increase, for example upon reduced ATP synthesis (Patel et al., 2014). Through antibody staining we determined levels of active PDH and inactive phosphorylated PDH (pPDH, targeting p-S293 phosphorylation) (Lieber et al. 2019). We compared macrophages invading the germband in *atos* mutant embryos as well as macrophages expressing *porthos* RNAi or a dominant negative inhibitor of complex V (*CV-DN*) compared to the control at early Stage 12 (Fig. 6I). We found a significantly reduced ratio of pPDH/PDH (Fig. 6J) indicating higher activity of the PDK enzyme in invading macrophages in both the *atos* mutant embryos and those expressing *porthos* RNAi. We found a similar result in our positive control, macrophages expressing *CV-DN*, which should

have reduced ATP/ADP ratios due to a nonfunctional mitochondrial ATP synthase (Fig. 6J, Figs. S6E,F). Our results support the conclusion that in the absence of Atossa or Porthos, macrophages *in vivo* have reduced ATP/ADP ratios, leading the cells to keep PDH in its active form to try to generate more energy as fuel by running the TCA cycle.

Atossa enhances the cellular metabolism and ATP levels

We have shown that Atossa is required both for the upregulation of Porthos, which increases mitochondrial energy production, and the enzymes GR/HPR and LKR/SDH. To investigate the full complement of metabolic changes that Atossa enables, we performed untargeted comparative metabolite profiling by capillary electrophoresis-mass spectrometry (CE-MS) (Figs. S7A, 7A) characterizing extracts from control and *atossa* mutant embryos. As we would expect given Atossa's role in regulating GR/HPR levels, we found lower levels of glycolate, the product of this enzyme's reaction with glyoxylate (Figs. 7A,SB), which can contribute to gluconeogenesis. Atossa also regulates LKR/SDH; we observed a reduced amount of its product alpha-amino adipic semialdehyde (AASA), by targeted-metabolomics profiling (Fig. 7A). This potentially could be part of Glutamate and Lysine catabolism to produce Acetyl CoA as fuel to enter the TCA cycle. Consistent with the results we had observed in the mitochondrial efflux assay on *porthos* KD S2R+ cells and the p-PDH/PDH ratio measurement in *atossa* and *porthos* embryos, we observed a decreased ATP/ADP ratio in the absence of Atossa (Fig. 7B). Thus our metabolic data supports that Atossa regulates a set of targets that shift metabolism to enhance ATP production.

As our metabolomics was conducted on embryos constitutively defective in Atossa, we expected to see some compensatory changes as well. However, matching the data from the Seahorse assay on *porthos* KD S2R+ cells, we did not observe a metabolic shift from mitochondrial OXPHOS towards aerobic glycolysis even in the absence of Atossa (Fig. 7C). Instead the cells in the *atossa* mutant embryos appeared to try to compensate for the reduced efficiency of the electron transport chain by increasing the running of the TCA cycle. We observed slightly higher levels of the metabolic intermediates of glycolysis (Fig. 7D) along with even higher levels of key intermediates of the Krebs (TCA) cycle, including succinate, fumarate, and oxaloacetate in the *atossa* mutant (Fig. 7E). Some of the glycolytic pathway intermediates appear to be diverted into the oxidative branch of Pentose Phosphate Pathway (PPP), as we observed an increase in some PPP intermediates, such as ribulose-1p or sedoheptulose-7p in *atossa* mutant embryos (Fig. 7F). The higher levels of TCA cycle components in the *atossa* mutant could also come from the upregulation we observed of the fatty acid oxidation pathway (FAO), which can also produce acetyl-CoA.



Avg FC

0.90	Glc-6p
0.97	Fru-6p
0.52	Fru-1,6bp
0.96	DHAP
0.23	Glycerol-3p
-0.02	3-phosphoglycerate
0.67	Lactate
0.87	Pyruvate

TCA

0.33	Citrate
0.55	Isocitrate
0.55	α-ketoglutarate
0.65	Succinic semialdehyde
1.09	Succinate
1.29	Fumarate
0.46	Malate
1.57	Oxaloacetate

PPP

1.61	D-Ribulose-5p
0.25	D-Xylose-5p
0.85	D-erythrose-4p
0.85	D-sedoheptulose-7p

Avg FC

0.50	Carnitine
-0.10	Acetyl-carnitine (C2)
1.0	Propionyl-carnitine (C3)
0.04	3-hydroxybutyryl-carnitine (C4)
0.52	Hexanoyl-carnitine (C6)
1.08	Lauryl-carnitine (C12)
1.60	Myristoyl-carnitine (C14)
1.16	Pentadecanoyl-carnitine (C15)
0.92	Palmitoyl-carnitine (C16)
0.20	Stearoyl-carnitine (C18)
0.18	Behenoyl-carnitine (C22)
2.94	3-Hydroxybutyric acid

Phenylalanine metabolism

2.94	3-Hydroxybutyric acid
2.18	4-Hydroxybutyric acid

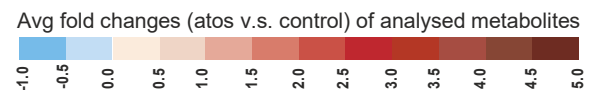
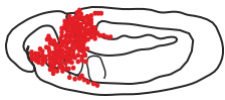


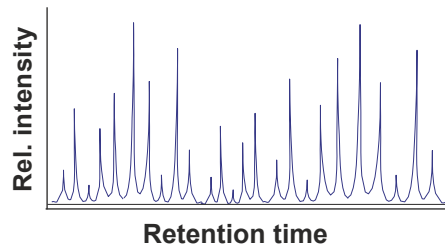
Fig 7. Mitochondrial metabolism is enhanced by Atossa and Porthos. Fig 7A. Schematic depicting the ATP-generating pathways, including glycolysis, the Pentose Phosphate Pathway (PPP), β -oxidation or fatty acid oxidation (FAO), TCA cycle, and mitochondrial respiratory chain in eukaryotic cells. Electron transport chain (ETC) components are also shown. Metabolomics profiling on *atossa* mutant embryos reveals the activation of PPP and FAO pathways, and accumulation of TCA intermediates and increased levels of ketone bodies, but a decreased Argino-succinate metabolite. ASAA as a product of dLKR/SDH is decreased. Increased and reduced metabolites in the *atos* mutant are shown in green and red colors, respectively. *Porthos* targets are marked with blue star. **Fig 7B.** Normalized ATP/ADP ratio values show ATP levels are decreased in *atos* mutant compared to control embryos. (Control n=5, *atos* mutant n=7, p-value= 0.028). Values are obtained from metabolomic analysis. **Fig 7C.** Quantification of metabolite-to-glucose ratios in the *atossa* mutant compared to wild-type embryos shows an increase in the Pyruvate/Glucose ratio (p-value=0.035), but none for the Lactate/Glucose ratio (p-value=0.65). Values are obtained from metabolomics analysis. Control n=5, *atos* mutant n=7. **Fig 7D-H.** Heatmap of non-targeted metabolites in *atossa* mutant embryos compared to wild-type embryos shown with average fold change (FC) (2-times) Cellular metabolites were measured by LC-MS-based metabolomics from extracts of Stage 11 embryos (Control n=5, *atos* mutant n=7). **Figs. 7D-F.** Global metabolite screening reveals less than 1 fold increases for most **(D)** glycolytic intermediates and up to 3 fold increases for metabolites from the, **(E)** TCA cycle, and **(F)** the Pentose Pathway (PPP) in the *atossa* mutant compared to the control. **Fig 7G.** An increase in intermediates of mitochondrial fatty acid β -oxidation (FAO), including different carnitine-conjugated lipids. **Fig 7H.** The *atossa* mutant shows an increase in intermediates of Phenylalanine metabolism compared to the control. Unpaired t-test for **(B)** and **(C)**.

atossa mutant embryos also display accumulations of carnitine-conjugated lipids, which are involved in fatty acid import into mitochondria (Fig. 7G). Potentially as a consequence of enhanced FAO activity, we also observed higher generation of ketone bodies (KBs: β -hydroxybutarates) in the absence of *atossa* (Figs. 7 H,I). We also find enhanced levels of hydroxybutyric acid (Fig. 7I), as well as purine and pyrimidine metabolites in *atossa* mutant embryos (Figs. 7J,K and Figs. S7D,E). There was a slight, but not significant increase, in most amino acids in the *atossa* mutant (Fig. S7F) and a significant increase in some dipeptides (Fig. S7G). Interestingly, we saw that the glycine-related metabolite sarcosine (N-methylglycine) was significantly reduced in the *atossa* embryos (p-value =0.003) (Figs. S7F-H). An elevated level of sarcosine is known to be a biomarker of highly metastatic prostate cancer (Sreekumar et al. 2009; Zhang et al. 2012). In sum, our metabolomics profiling data in combination with our other findings strongly supports the conclusion that Atossa increases the efficiency and amount of ATP production through OXPHOS by inducing a metabolic shift that affects the ETC and the TCA cycle.

WT v.s. atos mutant embryos



CE-MS
Metabolomics analysis

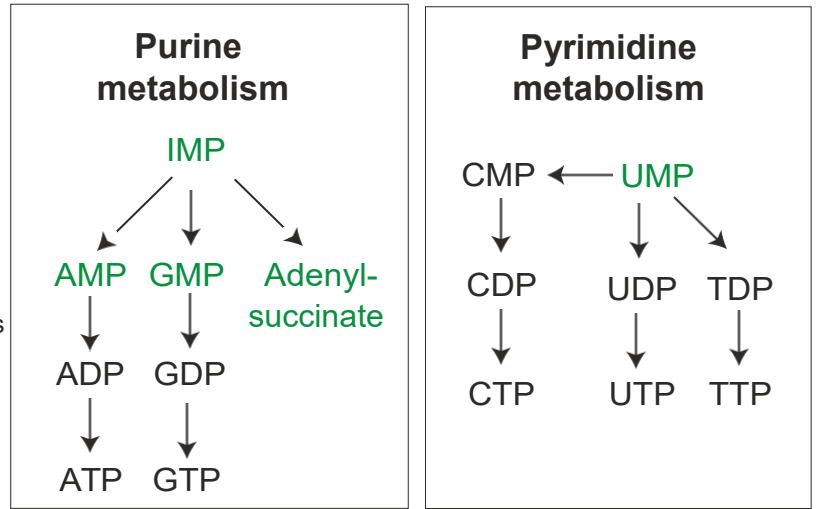


Metabolic pathway analysis

Avg FC

dGR/HPR	0.62	4-hydroxyproline
	1.02	4-hydroxy-alpha-KG
	-0.33	Glycolate
	-0.12	Glycerate

Avg fold changes (atos v.s. control) of analysed metabolites



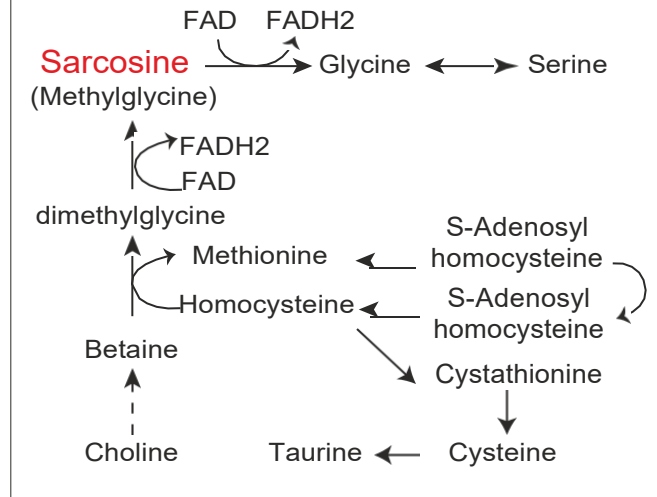
Avg FC

Pyrimidine metabolism	3.29	Deoxyuridine
	0.71	UMP
	0.27	UDP
	0.03	UTP
	0.16	CMP
	0.94	CDP
	0.16	CTP
	1.04	TMP
	1.06	TDP
	4.35	Thymidine

Avg FC

Purine metabolism	1.12	Xanthosine
	0.98	Methylinoine
	1.61	Adenosine
	0.96	Deoxyadenosine
	0.75	IMP
	2.06	AMP
	0.76	ADP
	0.19	ATP
	1.06	Adenylysuccinic acid
	0.83	Deoxyguanosine
	1.58	GMP
	0.51	GDP
	0.58	GTP
1.90	Methylguanosine	

Folate metabolism



Avg FC

Amino acids	-0.63	Methylglycine
	-0.04	Alanine
	0.30	Serine
	0.44	Proline
	0.47	Valine
	0.10	Threonine
	0.49	Leucine
	0.58	Isoleucine
	0.24	Asparagine
	0.40	Aspartate
	-0.11	Glutamine
	0.38	Glutamate
	0.40	Methionine
	0.16	Histidine
	0.43	Phenylalanine
	0.62	Arginine
	0.31	Tyrosine
0.70	Tryptophan	
0.50	Lysine	

Avg FC

Dipeptides	3.04	Val-HydroxyPro
	3.02	Met-Glu
	1.20	Ser-Tyr
	1.17	Arg-HydroxyPro
	0.89	Cys-Asp
	0.88	Ala-Pro
	0.80	Arg-Glu
	0.68	Leu-Gln
0.63	His-Pro	

Fig S7. Atossa and Porthos enhance ATP production by programming mitochondrial oxidative phosphorylation metabolism. **Fig. S7A.** Schematic illustrates the metabolic profiling procedure in wild-type and *atossa* mutant embryos at Stage 12. **Figs. S7B.** Heatmap of non-targeted metabolites in *atossa* mutant embryos reveals an increase in substrates of the dGR/HPR enzyme, including 4-hydroxyketoglutarate and hydroxyproline and a smaller decrease in its products, Glycolate and Glycerate. **Figs. S7C-D.** Schematics show *de novo* nucleotide synthesis, including **(C)** purine and **(D)** pyrimidine metabolism. Depletion of Atossa leads to the accumulation of purine metabolites, including IMP, AMP, GMP, and adenylyl-succinate as well pyrimidine metabolites, including UMP in embryos. **Figs. 7E-F.** The accumulation of cellular nucleotide precursors, and **(E)** purine and **(F)** pyrimidine metabolites. **Fig. S7G.** Schematic shows a link between Folate metabolism and Glycine/Serine metabolism, in which the glycine-related metabolite sarcosine (N-methylglycine) was significantly reduced in the *atossa* mutant. **Figs. S7H-I.** Heatmap of non-targeted metabolites in *atossa* mutant embryos reveals **(H)** a small increase in most amino acids in the *atossa* mutant and **(I)** a significant increase in some dipeptides including those containing hydroxyproline.

DISCUSSION

Metabolic adaptation is a fundamental feature of migrating cells. However, how metabolic reprogramming contributes to *in vivo* cell invasion is not well understood. Here we discover a novel conserved metabolic shift in *Drosophila* immune cells, which modulates their metabolic capacities and cellular bioenergetics to facilitate tissue invasion. We find that a conserved nuclear protein, named Atossa, tunes this developmental metabolic program in *Drosophila* macrophages through its downstream targets, including the RNA helicase Porthos and the metabolic enzymes dGR/HPR and dLKR/SDH (Fig. 3).

Porthos belongs to the ATP-dependent DEAD-box RNA helicases, which influence various aspects of RNA metabolism (Fuller-Pace et al., 2013; Chen et al., 2015; Martin et al., unpublished 2020; Bourgeois et al., 2016; Jarmoskaite et al., 2011; Jin et al., 2020). The mammalian ortholog of *Drosophila* Porthos, the DEAD-box RNA helicase DDX47, and its yeast homolog, Rrp3a, contribute to RNA metabolism, pre-rRNA processing, and ribosome biogenesis (Sekiguchi et al., 2006). In our system, Porthos selectively enhances the translational efficiency (TE) of a subset of mRNAs containing a cis-regulatory 5'UTR TOP-like (TOPL) sequence (Fig. 5). Among Porthos' mRNA targets a sizable portion are involved in mitochondrial and metabolic functions, including mitochondrial complex V, while only three are ribosomal proteins. Consistent with this finding, we demonstrate that in our system Porthos boosts mitochondrial OXPHOS activity for ATP production. Porthos is also required for proper germline stem cell (GSC) differentiation in the *Drosophila* ovary (Martin et al., unpublished 2020), where mitochondrial complex V or ATP synthase (Teixeira et al., 2015) has been shown to be required (Fig. 6). Thus Porthos enhances ribosome biogenesis and TOPL containing mRNA translation, and can potentially act in multiple cell types as a regulator to power up mitochondrial function.

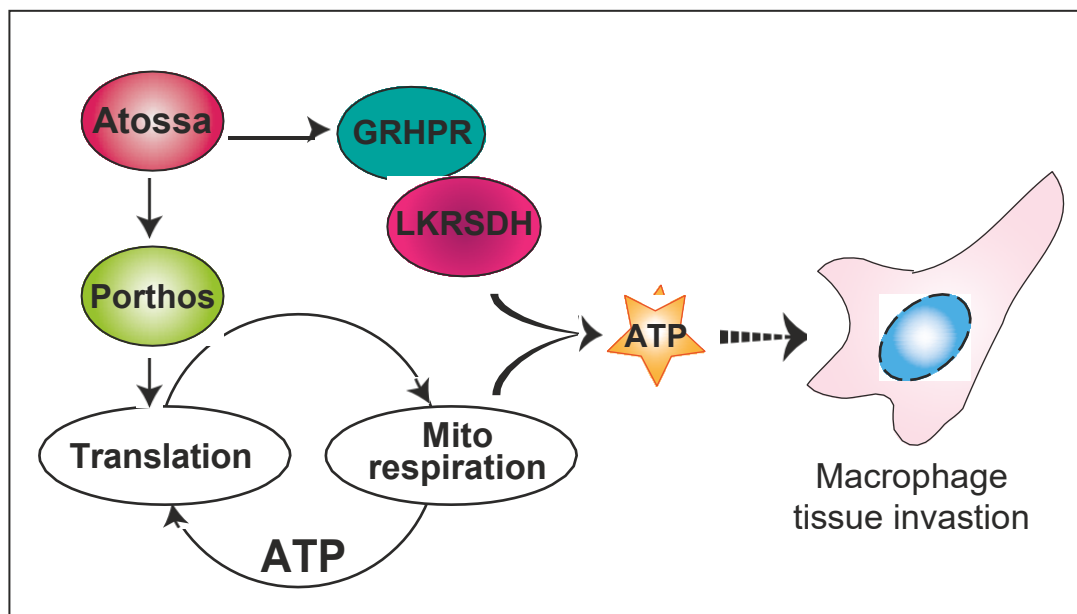
In mammals the translation of TOP containing mRNAs is promoted by the mammalian target of rapamycin (mTOR) in response to higher energy conditions to maintain cellular bioenergetics and promote cell division and growth (Xie et al., 2021). (Robida-Stubbs et al., 2012; Beauchamp and Plataniias, 2013; Thoreen et al., 2012;

Carvalho et al., 2015; Saxton and Sabatini, 2017; Zou et al., 2020). TORC1 phosphorylates and inactivates translational suppressors, the eukaryotic initiation factor 4E-binding proteins (4E-BPs) or LARP1 (Fonseca et al., 2015; Lahr et al., 2017), to selectively stimulate the translation of 5'TOP mRNAs which mainly encode ribosomal and mitochondrial proteins (Gandin et al., 2016; Lee et al., 2020; Zid et al., 2009; Hsieh et al., 2012; Albert et al., 2015; Kahan et al., 2015; Xie et al., 2021). On the other hand, TORC1 inhibition activates eEF2K, a kinase known to be active in times of lower energy levels, which can support cell invasion and early tumor carcinogenesis and recruit ribosomes to weaker mRNAs (Kenney et al., 2014). Surprisingly we only find three ribosomal proteins as Porthos' 5'TOPL mRNA targets. Interestingly, some of Porthos' 5'TOPL mRNA targets, including subunits of mitochondrial complexes III and V and a mitochondrial transporter, have also been identified in another study in *Drosophila* as TOR-regulated mRNAs (Zid et al., 2009). It would be intriguing to examine if the TOR or EF2K pathway acts through Porthos to regulate the translation of 5'TOPL mRNAs involved in cellular bioenergetics and macrophage invasion.

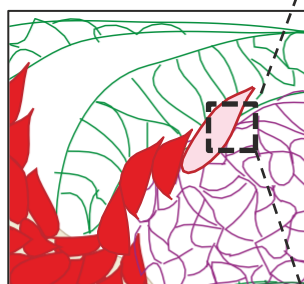
The metabolic states of many migrating cells can be orchestrated by the modulation of mitochondrial dynamics, including fission and fusion, crista formation, mitochondrial biogenesis and repositioning (Beckervordersandforth, 2017; Buck et al., 2016; Seo et al., 2018; Denisenko et al., 2019; Schuler et al., 2017; Cunniff et al., 2016; Senft et al., 2016; LeBleu et al., 2014; Porporato et al., 2018, Kelley, et. al, 2019; Commander; et al., 2020). Porthos' 5'TOPL mRNA targets such as complex V and Mics1 (Teixeira et al., 2015) are linked to crista maturation, and others to mitochondrial transport and mitochondrial mRNA translation. It would be interesting to see if Porthos acts also to modulate mitochondrial biogenesis and distribution to aid macrophage invasion.

Cell infiltration through physically challenging barriers costs energy. Recent *in vitro* studies show that leading cells need higher ATP levels to overcome energy-demanding obstacles during invasion (Van Horsen et al., 2009; Ciano et al., 2015; Zanutelli et al., 2018; Zanutelli et al., 2018; Zhang et al., 2019). Nevertheless, how invasive leading cells obtain these higher energy levels, especially in *in vivo* contexts, is still a challenging topic of research. Our findings provide clear evidence that invading pioneer macrophages are highly reliant on a program governed by Atossa to enhance mitochondrial bioenergetics to produce the energy needed to initiate tissue infiltration (Figs. 6 and 7). Our results show that embryonic macrophages and leading edge invading cancer cells share metabolic states, both having an enhanced mitochondrial energy flux (Schuler et al., 2017; Hoang-Minh et al., 2018; Commander et al., 2020; Vats et al., 2013; Vander Heiden et al., 2009; Morita et al., 2013). Atossa depletion induces metabolic consequences in macrophages, characterized by reduced ATP/ADP levels, an accumulation of TCA cycle intermediates and carnitine-conjugated lipid variants, along with reduced catabolic products of Atossa's target enzymes, LKR/SDH and GR/HPR (Fig. 7).

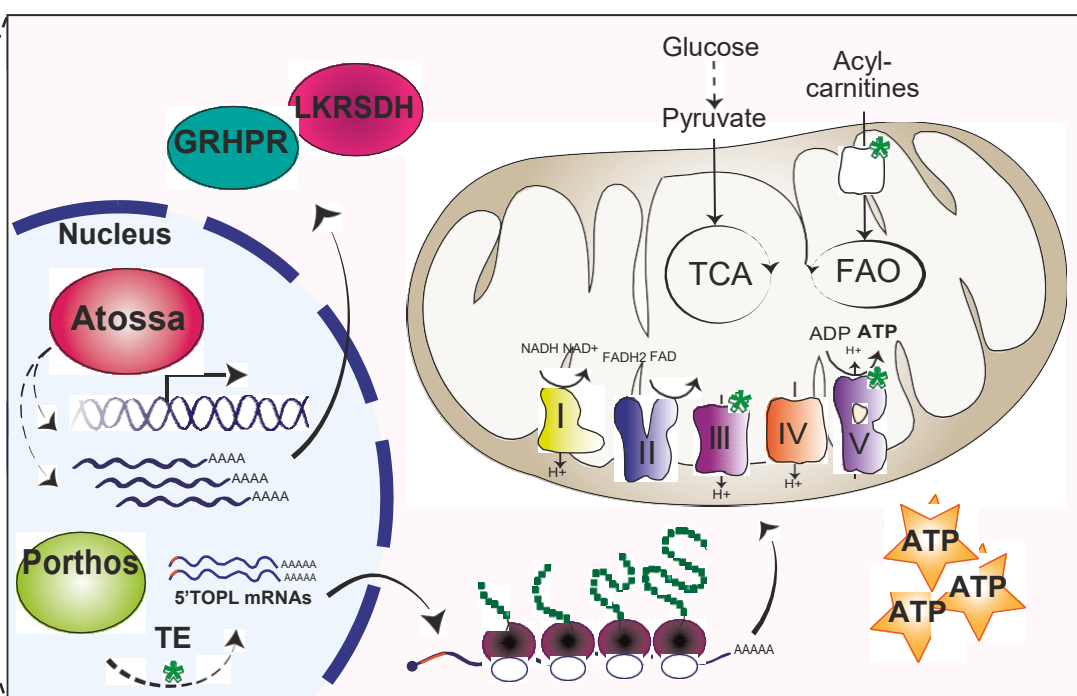
Figure 8



Wildtype



Leading macrophage
Macrophage
Ecto
Meso



atos^{-/-}

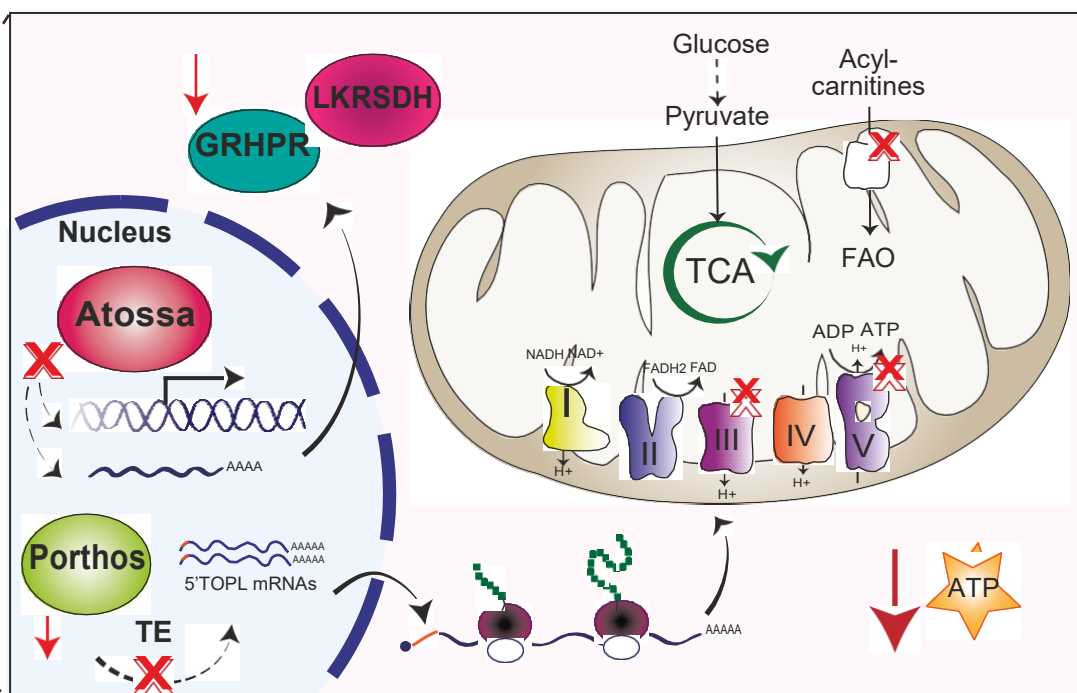
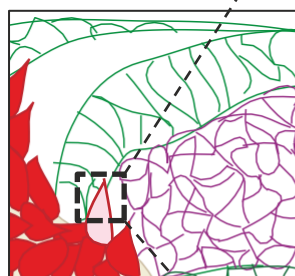


Figure 8. Nuclear Atossa turns on a metabolic program in *Drosophila* embryonic macrophages to boost mitochondrial bioenergetics for tissue invasion. (A) We propose a model for how nuclear Atossa reprograms the metabolism and bioenergetics of pioneering macrophages to aid their tissue entry and infiltration. (B) Atossa increases the mRNA transcript levels of the helicase Porthos and the metabolic enzymes GR/HPR and LKR/SDH in macrophages. Porthos enhances the translational efficiency of mRNAs containing a 5'TOPL motif, including those encoding mitochondrial ETC components (complex III and complex V or ATP synthase) and a mitochondrial carnitine transporter. Macrophages with elevated mitochondrial OXPHOS can meet their emerging energy demands for tissue invasion. (B') However, in *atossa* mutant macrophages, the absence of Atossa leads to a reduced OXPHOS-generated ATP supply, but an accumulation of TCA intermediates, leading to defective tissue infiltration of the pioneering macrophages. through Atossa with the ability to stimulate mitochondrial OXPHOS to secure sufficient energy production in challenging situations such as during tissue invasion. Our novel metabolic program in immune cell invasion also raises the potential of conserved parallels between flies and mammals (Figs. 2,4). Atossa's mammalian orthologs, mFAM214A and B are highly enriched in vertebrate immune cells and can to a large extent rescue the tissue invasion of *Drosophila* macrophages, substituting for the function of Atossa in its absence. Nonetheless, future research needs to determine if Atossa's vertebrate orthologs also serve as key metabolic regulators of tissue invasion or other immune functions in more sophisticated contexts. Atossa's target, the helicase Porthos is also highly conserved throughout vertebrates (Sekiguchi et al., 2006) and though its orthologs are enriched in immune cells, they are also expressed in many tissues. We thus anticipate that this helicase family affects a broader range of functions, extending beyond immune cell invasion in more complex organisms.

In summary, we speculate that during embryonic development Atossa is preprogrammed to be upregulated in macrophages prior to their germband entry. Atossa through altered transcription and translation turns on a bioenergetic shift, which modulates metabolic capacities and the cellular energy state of macrophages. This developmental metabolic program controls the timing and speed of leading macrophages for germband penetration and drives their subsequent invasion through constrained germband tissue (Fig. 8). Our findings can shed light on how migrating cells shape their metabolic states to coordinate long-lasting and energy-demanding cellular performances. This novel metabolic shift modulated by Atossa, and possibly its vertebrate orthologs, may have a potential role as a therapeutic target in metabolism-related malignancies. Blocking Atossa orthologs' functions in cells that express them would be predicted to decrease but not block mitochondrial bioenergetics, decreasing the likelihood of the severe cellular consequences that would result from therapies that target mitochondria directly. In a broader realm, our novel outcomes offer more insights to pave the way toward targeting cellular metabolic adaptations in various physiological aspects, such as development, tissue homeostasis and regeneration, immunological challenges as well as tumor metastasis.

MATERIALS AND METHODS

Fly work

Flies were raised on food bought from IMBA (Vienna, Austria) which was prepared according to the standard recipe of agar, cornmeal, and molasses with the addition of 1.5% Nipagin. Adults were placed in cages in a Percival DR36VL incubator maintained at 29°C and 65% humidity; embryos were collected on standard plates prepared in house from apple juice, sugar, agar and Nipagin supplemented with yeast from Lesaffre (Marcq, France) on the plate surface. Embryo collections for fixation (7-8 hour collection) as well as live imaging (4-5 hour collection) were conducted at 29°C.

Fly lines obtained used in this work

srpHemo-GAL4 was provided by K. Brückner (Brückner et al., 2004). The RNA lines tested in this paper (Table S1) were obtained from the Bloomington *Drosophila* Stock Centre (Bloomington, USA) and the Vienna *Drosophila* Resource Center (VDRC, Vienna, Austria). Lines *w*; *P*{*w*[+*mC*]; *srpHemo-3xmCherry*}, *w*; *P*{*w*[+*mC*]; *srpHemo-H2A::3xmCherry*} were published previously (Gyoergy et al., 2018).

Embryo fixation and immunohistochemistry

Embryos were collected on apple juice plates from between 6-8.5 hours at 29°C. Embryos were incubated in 50% Chlorox (DanClorix) for 5 min and washed. Embryos were fixed with 17% formaldehyde/heptane for 20 min followed by methanol or ethanol devitellinization. Fixed embryos were blocked in BBT (0.1M PBS + 0.1% TritonX-100 + 0.1% BSA) for 2 hours at RT and then incubated overnight at 4°C. Antibodies were used at the following dilutions: Mouse anti α -GFP (Aves Labs Inc., Tigard, Oregon, 1:500) and Rat anti-HA (Roche, Basel, Switzerland, 1:100). Afterwards, embryos were washed in BBT for 2 hours, and incubated with secondary antibodies at RT for 2 hours, and washed again for 2 hours. Secondary antibodies and Phalloidin were used at the following dilutions: anti-rat 488 1:300, anti-chicken 488 1:500, anti-mouse 488 1:500 or anti-mouse 633 1:200, and Phalloidin 1:300 (all from ThermoFisher Scientific, Waltham, Massachusetts, USA). The embryos were mounted overnight at 4°C in Vectashield mounting medium (Vector Laboratories, Burlingame, USA), which contains DAPI. Embryos were placed on a slide and imaged with a Zeiss Inverted LSM800 Confocal Microscope using a Plain-Apochromat 20X/0.8 Air Objective or a Plain-Apochromat 63X/1.4 Oil Objective.

S2R+ cell work and immunostaining

S2R+ cells (a gift from Frederico Mauri of the Knöblich laboratory at IMBA, Vienna) were grown in Schneider's medium (Gibco) supplemented with 10% FBS (Gibco) and transfected with the *srpHemo-HA::CG9005* (*atossa*), and *UAS-CG9005::FLAG::HA*, *UAS-CG9253::FLAG::HA* (*porthos*) and *srpHemo-GAL4* constructs using Effectene Transfection Reagent (Qiagen, Hilden, Germany) following the manufacturer's protocol (Table S3).

Transfected S2R+ cells were grown on Poly-L-Lysine coated coverslips (ThermoFisher Scientific, Waltham, Massachusetts, USA) in complete Schneider's medium (Gibco) supplemented with 10% FBS (Sigma-Aldrich, Saint Louis, Missouri, USA) and 1% Pen/Strep (Gibco) to a confluency of 60%. For antibody staining, cells were fixed with 4% formaldehyde (ThermoFisher Scientific, Waltham, Massachusetts, USA) in PBS for 15 minutes at room temperature (RT). Then cells were washed three times with PBS followed by blocking and permeabilization with 1% BSA (Sigma-Aldrich, Saint Louis, Missouri, USA)/0.3% Triton X-100 in PBS for 1 hour. Antibodies were diluted in blocking/permeabilization buffer and incubated for 2 hours at RT. Primary antibodies were used at the following working dilutions: Chicken anti-GFP (clone 5G4, Ogris lab, MFPL, 1:100), Rat anti-HA (Roche, Basel, Switzerland, 1:50), Mouse anti-Lamin (DSHB, lamin Dm0, ADL1010, 1:50), and Mouse anti-fibrillarin (gift from Rangan's lab, 1:50). Cells were subsequently washed three times with PBS-Tween20 (0.05%) for 5 minutes each, followed by secondary antibody incubation in blocking/permeabilization buffer for 1 hour at RT. Secondary antibodies were used at the following working dilutions: anti-rat Alexa Flour 488 (1:50), anti-mouse Alexa Flour 488 (1:200), and anti-mouse Alexa Flour 633 (1:100) (all from ThermoFisher Scientific, Waltham, Massachusetts, USA). Cells were counterstained with DAPI (ThermoFisher Scientific, Waltham, Massachusetts, USA) for 10 minutes in PBS-Tween 20%. After immunoblotting, cells were mounted with ProLong Gold Antifade Mountant (ThermoFisher Scientific, Waltham, Massachusetts, USA, #P36930). Images were acquired using the Zeiss inverted LSM-800 confocal microscope. Pictures were processed with ImageJ.

DNA isolation from single flies

Single male flies were frozen overnight before being grounded with a pellet homogenizer (VWR, Radnor, USA) and plastic pestles (VWR, Radnor, USA) in 50 μ l of homogenizing buffer (100 mM Tris-HCl, 100 mM EDTA, 100 mM NaCl, and 0.5% SDS). Lysates were incubated at 65°C for 30 minutes. Then 5M KAc and 6M LiCl were added at a ratio of 1:2.5 and lysates were incubated on ice for 10 min. Lysates were centrifuged for 15 minutes at 20,000xg, supernatant was isolated and mixed with Isopropanol. Lysates were centrifuged again for 15 minutes at 20,000xg, the supernatant was discarded and the DNA pellet was washed in 70% ethanol and subsequently dissolved in distilled water.

Fixed embryo image analysis for colocalization

Embryos were imaged with a 63x Objective on a Zeiss LSM800 inverted. 10 μ m stacks (0.5 μ m intervals) were taken for properly staged and oriented embryos, starting 10 μ m deep in the tissue. These images were converted into Z-stacks in Fiji. ROIs were drawn around macrophages (signal), copied to tissue close by without macrophages (background) and the average intensity in the green channel of each ROI was measured. For each pair of ROIs the background for each particular slice was subtracted from each corresponding signal individually. The average signal from control ROIs from one imaging day and staining

was calculated and all data point from control, mutant and rescue from the same set was divided by this value. This way we introduced an artificial value called Arbitrary Unit (AU) that makes it possible to compare all the data with each other, even if they come from different imaging days when the imaging laser may have a different strength or from different sets of stainings. Analysis was done on anonymized samples.

FACS sorting of macrophages

For embryo collections, adult flies of either *w⁺; srpHemo-3xmCherry* or *w⁺; CG9005^{BG02278}; srpHemo-3xmCherry* genotypes were placed into plastic cages topped with apple juice plates with yeast for egg laying. Collections were performed at 29°C at 8h-20h light-dark cycle. Macrophages were collected from Stage 11- early Stage 12, when macrophages initiate invasive migration into the extended germband. Briefly, adult flies laid eggs for 1 hour, then the isolated plates with embryos were kept at 29°C for an additional 4 hours 45 minutes to reach the desired age. Embryos were collected for 2 days with about 6-7 collections per day and stored meanwhile at +4°C to slow down development. Collected embryos were dissociated and the macrophages were sorted according to the procedure described in (Gyoergy et al., 2018). The cells were sorted using a FACS Aria III (BD) flow cytometer. Emission filters were 600LP, 610/20 and 502 LP, 510/50. Data was analyzed with FloJo software (Tree Star). The cells from the negative control embryos were sorted to set a baseline plot. Approximately $1-1.5 \times 10^5$ macrophages were sorted within 30 minutes.

Sequencing of the macrophage transcriptome

Total RNA was isolated from the FACS-sorted macrophages using the Qiagen RNeasy Mini kit (Cat No. 74104). The quality and concentration of RNA was determined using the Agilent 6000 Pico kit (Cat No. 5067-1513) on the Agilent 2100 Bioanalyzer: about 100 ng of total RNA was extracted from 1.5×10^5 macrophages. RNA sequencing was performed by the CSF facility of the Vienna Biocenter according to their standard procedures (<https://www.vbcf.ac.at/facilities/next-generation-sequencing/>). Briefly, a cDNA library was synthesized using the QuantSeq 3' mRNA-seq Library Prep kit and 4 replicates of each of the genotypes (*w⁺; +; srpHemo::3xmCherry* or *w⁺; CG9005^{BG02278}; srpHemo-3xmCherry*) were sequenced on the Illumina HiSeq 2500 platform.

The reads were mapped to the *Drosophila melanogaster* Ensembl BDGP6 reference genome with STAR (version 2.5.1b). The read counts for each gene were detected using HTSeq (version 0.5.4p3). The Flybase annotation (r6.19) was used in both mapping and read counting. The counts were normalised using the TMM normalization from the edgeR package in R (Anders and Huber, 2015; Dobin et al., 2013). (Prior to statistical testing the data was transformed and then the differential expression between the sample groups was calculated with the limma package in R. The functional analyses were done using the topGO and gage packages in R.

Time-lapse imaging

Embryos were dechorionated in 50% bleach for 4 min, washed with water, and mounted in halocarbon oil 27 (Sigma) between a coverslip and an oxygen permeable membrane (YSI). The anterior dorsolateral region of the embryo was imaged on an inverted multiphoton microscope (TrimScope, LaVision) equipped with a W Plan-Apochromat 40X/1.4 oil immersion objective (Olympus). mCherry was imaged at an 820 nm excitation wavelength, using an optical parametric oscillator technology (Coherent Chameleon Compact OPO). Excitation intensity profiles were adjusted to tissue penetration depth and Z-sectioning for imaging was set at 1 μ m for tracking. For long-term imaging, movies were acquired for 180-200 minutes with a frame rate of 40 seconds. Embryos were imaged with a temperature control unit set to 29°C.

Image Analysis

Macrophage cell counts

Autofluorescence of the embryo was used to measure the position of the germband to determine the stages for analysis of fixed samples. Germband retraction away from the anterior was used to classify embryos into Stage 11 or Stage 12. Embryos with germband retraction of between 29-31% were assigned to Stage 11. Embryos with the tip of the germband with 35-40% retraction (Stage 12) were analysed for the number of macrophages that had entered the germband. Embryos with above 50-75% retraction were used for the number along the ventral nerve cord (vnc) and in the whole embryo. Macrophages were visualized using confocal microscopy with a Z-resolution of 2 μ m and the number of macrophages within the germband or the segments of the vnc was calculated in individual slices (and then aggregated) using the Cell Counter plugin in FIJI. Total macrophage numbers were obtained using Imaris (Bitplane) by detecting all the macrophage nuclei as spots.

Macrophage tracking, speed, directionality and time for macrophage entry analysis

Embryos in which the macrophage nuclei were labeled with *srpHemo-H2A::3XmCherry* were imaged and 250X130X36 μ m³ 3D-stacks were typically acquired with a constant 0.5X0.5X1 μ m³ voxel size at every 40-41 seconds for approximately 3 hours. Images acquired from multiphoton microscopy were initially processed with InSpector software (LaVision Bio Tec) to compile channels from the imaging data (Table 3). Afterwards, the exported files were further processed using Imaris software (Bitplane) to visualize the recorded channels in 3D and the movie from each imaged embryo was rotated and aligned along the AP axis for further tracking analysis.

To analyze the movies by Imaris, the following analysis were applied:

- i. To calculate the migration parameters while macrophages migrate from the head mesoderm to the yolk zone, movies were cropped in time to that period (typically 60 minutes from the original movie was used for analysis).

- ii. To calculate the migration parameters of the macrophage moving on the yolk zone into the edge of germband, movies were acquired from the time point of the first macrophage appearing in the yolk zone and recorded until the onset of germband retraction.
- iii. Macrophage nuclei were extracted using the spot detection function and tracks generated in 3D over time. We could not detect all macrophages in the head mesoderm as spots because of limitations in our imaging parameters. Tracks of macrophages, which migrate towards the dorsal vessel, ventral nerve cord (vnc) and to the anterior of the head were omitted. The edge of the germband was detected using autofluorescence from the yolk and the mean position of the tracks in X- and Y-axis was used to restrict analysis to before macrophages reach the edge of the germband.
- iv. Nuclei positions in XYZ-dimensions were determined for each time point and used for further quantitative analysis.
- v. The time point when the first macrophage nuclei reached the germband was defined as T0 and the time point when the macrophage nuclei was within the germband and moved forward along the route between the ectoderm and mesoderm was taken as T1 and T1-T0 was defined as time for macrophage entry. T0 and T1 were determined by precisely examining macrophage position in xy and z dimensions (examination of individual 2 micron slices) over time.
- vi. To measure the speed along the route between the germband mesoderm and the yolk, tracks generated from macrophages from the time when the first macrophages started to move along the mentioned path until the germband retraction onset were utilized.
- vii. To calculate the speed of migration of the first or second macrophages in the germband the track generated for the first or second macrophages alone was used to obtain the nuclei position in XYZ-dimensions. Moreover, the average speed of first five macrophages moving along the same route was also measured. Speed was calculated within the first 30-35 μm of the path between the germband ectoderm and mesoderm. The mean position of the tracks in X- and Y-axis was used to restrict analysis to either of the migratory zones (head, yolk, germband entry, route along the germband ectoderm and mesoderm, route along the germband mesoderm and the yolk).

Macrophage migratory parameters, including cell speed and directionality (persistence), were calculated in Matlab (The MathWorks Inc.) from single cell positions in 3D for each time frame measured in Imaris (Bitplane), as described elsewhere (Smutny et al., 2017). Briefly, instantaneous velocities from single cell trajectories were averaged to obtain a mean instantaneous velocity value over the course of the measurement. To calculate directionality values, single cell trajectories were split into segments of equal length (l ; $l = 10$ frames) and calculated via a sliding window as the ratio of the distance between the macrophage start-to-end distance ($d_{\text{start-to-end}}$) over the entire summed distance covered by the macrophage between each successive frame (d_{summed}) in a segment. Calculated directionality values were averaged over all segments in a single trajectory and all trajectories were averaged to obtain a directionality index (D) for the duration of measurement (with 0 being the lowest and 1 the maximum directionality) as follows:

$$\langle l \rangle = \sum_{l=1}^{\infty} \frac{\left(\frac{\langle l \rangle}{\sum_{l=1}^{\infty} \langle l \rangle} \right)}{l - 1}$$

where $\langle l \rangle$ defines the total number of frames, $\langle l \rangle$ the sum of frame-to-frame distances over one segment and $\langle l \rangle$ the sum over all segments of a trajectory.

Embryos from the control ($w^+; +; srpHemo::3xmCherry$) and the CG9005 mutant ($w^+; CG9005^{BG02278}; srpHemo::3xmCherry$) were used for calculating the time for macrophage entry. Briefly, $100 \times 130 \times 34 \mu\text{m}^3$ 3D-stacks were typically acquired with a constant $0.28 \times 0.28 \times 2 \mu\text{m}^3$ voxel size at every 40-41 seconds for approximately 3 hours.

Cloning of constructs

Standard molecular biology methods were used and all constructs were sequenced by the Mycosynth company (Vienna, Austria) before injection into flies. The enzymes *NotI*, T4 Polynucleotide Kinase (*PNK*) and *DpnI* were obtained from New England Biolabs, Ipswich, Massachusetts, USA (Frankfurt, Germany). PCR amplifications were performed with GoTaq G2 DNA polymerase (Promega, Madison, USA) using a peqSTAR 2X PCR machine from PEQLAB, (Erlangen, Germany). All Infusion cloning was conducted using an Infusion HD Cloning kit (Clontech's European distributor). The relevant oligo sequences were chosen using the Infusion primer Tool at the Clontech website (<http://bioinfo.clontech.com/infusion/convertPcrSlnit.do>).

Construction of *srpHemo*-CG9005

A 3894 bp fragment containing the CG9005 ORF was amplified from the *UAS-CG9005::FLAG::HA* construct (*Drosophila* Genomics Resource Centre, DGRC) using relevant primers (Table S2). The fragment was cloned into the *srpHemo* plasmid (a gift from Katja Brückner (Brückner et al., 2004) after its linearization with *NotI*, using an Infusion HD cloning kit (Clontech's European distributor).

Construction of *srpHemo*-FAM214A and *srpHemo*-FAMB214B

Fragments of 3225 bp and 1615 bp containing the FAM214A and FAMB214B ORFs, respectively, were amplified from cDNA prepared from dendritic cells (a gift from M. Sixt's lab) with FAM214A Fwd and Rev primers, and with FAM214B Fwd and FAM214B Rev primers (Table S2). The fragments were cloned into the *srpHemo* plasmid using an Infusion HD cloning kit after its linearization with *NotI* (NEB).

Construction of mutant forms of *srpHemo*-*atossa*

Mutant forms of *atossa* (CG9005) were generated by removing the desired region from the CG9005 cDNA sequence by using inverse PCR followed by blunt end ligation and related primers ((Table S2). Afterwards, *atossa* mutant constructs in the Bluescript vector were amplified and cloned into the *srpHemo* plasmid after its linearization with *NotI*, using an Infusion HD cloning kit.

Transgenic fly line production

The *sprHemo* and *UAS* constructs ((Table S2) was injected into syncytial blastoderm stage embryos of M{3xP3-RFP.attP}ZH-86Fb (BL 24749) line (obtained from Peter Duchek of IMBA) to generate inserts on third chromosome by C31-mediated integration ((Table S1) (Bischof et al., 2007; Gyoergy et al., 2018).

CRISPR sgRNA production and cloning

sgRNA target sequences for CRISPR-Cas9 based gene knocking down for *CG9005* (*atossa*) and *CG9253* (*porthos*) were designed as 20 nt sequences upstream of an NGG PAM motif in the *Drosophila* genome (<https://www.flyrnai.org/crispr/>) (Basset et al., 2014). The targeting oligonucleotides incorporated into *atossa* or *porthos* sgRNAs are given in (Table S2, The annealed oligo inserts were cloned into BspQ1-digested pAC-sgRNA-Cas9 vector (Addgene, plasmid # 49330) before transformation. Positive clones were confirmed by sequencing with pAC-sgRNA-Cas9-U6F primer ((Table S2). All CRISPR-Cas9 constructs contain three distinct cassettes for expression of Cas9, an sgRNA (against *atossa* or *porthos*), and a puromycin resistance marker.

Generation of *atossa* and *porthos* depleted S2R+ cells

To make the stable depleted S2 cell lines, S2R+ Cells (2×10^5) were seeded in Schneider medium plus 10% FCS (Gibco 21720024, Sigma F9665) in a 24-well plate. Plasmids sgRNA CRISPR *porthos* or sgRNA *atossa* CRISPR were co-transfected (1 μ g of total DNA per well) with the HilyMax Kit (ratio 1:5) according to manufacturer's protocol. 4 hours after transfection the medium was changed and the cells were incubated for 72 hours at 25°C. Cells were then transferred to a 6-well plate before addition of 5 μ g/ml Puromycin. Selection with Puromycin took place for 7 days. Surviving cells were incubated without selection medium for 24 hours, after that they were added to 96-well cell culture plates in conditioned medium at a density of 1 cell/well. After 7 days we checked the wells for growing colonies to rule out of more than 1 colony being present per well. When cells were dense enough we first transferred them to a 24-, then a 12- and finally a 6-well plate. Once the cells reached confluency, we extracted the genomic DNAs using DNeasy Blood & Tissue Kit (Qiagen, Hilden, Germany) to perform a PCR-based prescreening of *atossa*- and *porthos*-depleted cells for effective CRISPR (Table S2).

Quantitative Real Time-PCR (qRT-PCR) analysis

To verify the effective knockdown of genes, we first isolated RNA from S2R+ cells (1×10^7 for the control and KD cells) according to the manufacturer's protocol (Qiagen RNeas Mini Kit Cat No./ID: 74104). We used 500 ng of isolated RNA for cDNA synthesis, according to the manufacturer's protocol (Qiagen Omniscript RT, Cat No./ID: 205111). Afterwards we performed qPCR to assess the mRNA expression of *atossa* and *porthos*, using *Rps20* as an internal control. Primer sequences for *Drosophila atossa* (*CG9005*) and *porthos* (*CG9253*)

transcripts were designed using NCBI's primer design tool (<https://www.ncbi.nlm.nih.gov/tools/primer-blast/>) and primer sequences for RpS20 gene, as an internal control gene, were obtained from the FlyPrimerBank (<http://www.flyrnai.org/FlyPrimerBank>) (Table S3). We amplified 4 μ L cDNA (50 ng) using 10 μ L of Takyon™ No Rox SYBR MasterMix Blue dTTP (Eurogentec, Liege, Belgium), 2 μ L of each reverse and forward primers (10 mM). The thermal cycling conditions were as follows: 40 cycles of amplification each consisting of 10 s at 95°C, 15 s at 60°C and 10 s at 72°C, and cooling at 4°C. The experiments were carried out in technical triplicates and three biological replicates for each data point. The qPCR experiment was run on a LightCycler 480 (Roche, Basel, Switzerland) and data were analyzed in the LightCycler 480 Software and Prism (GraphPad Software). To calculate the fold change in *atossa* and *porthos* mRNA levels compared to the house-keeping gene mRNA levels, we averaged the Ct values of the technical replicates of each trial. We measured Δ ct by subtracting the housekeeping gene Ct average from the Ct average of *atossa* or *porthos*. Afterwards, the $2^{-\Delta$ ct} was calculated for each trial.

Polysome profiling in *porthos*-KD S2 cells

RNAi treatment of S2 cells

dsRNA for *porthos* gene was prepared as described by the SnapDragon manual (<https://www.flyrnai.org/snapdragon>). Briefly, template was prepared from S2 cell cDNA using the following primers designed using SnapDragon 5'-TAATACGACTCACTATAGGATAAG GAAGGGGACAGCGAG-3' and the reverse primer: 5'-TAATACGACTCACTATAGGTTTGAATGCCAGTTCCTC-3' both of which contain a T7 polymerase promoter. As a negative control, we made non-targeting dsRNA against GFP using the following primers: 5'-TAATACGACTCACTATAGGGGAGCGCACCATCTTCTTCAA-3' and 5'-TAATACGACTCACTATAGGGCTGCTTGTCGCCATGATATAG-3'. We performed *in vitro* transcription overnight at 37°C using the T7 Megascript kit (AM1334) following manufacturer's instructions ((Table S2). The RNA was treated with DNase and purified using acid-phenol chloroform extraction and ethanol precipitated. The resulting RNA was annealed by heating at 65°C for 5 minutes and slow cooling to 37°C for an hour. Knocking down of S2 cell was performed using 1 μ g of dsRNA as previously described (<https://www.ncbi.nlm.nih.gov/pmc/articles/PMC4465107/>). 0.5-1.0 $\times 10^6$ cells were seeded 30 minutes prior to transfection to adhere. Prior to transfection, the media was changed for 500 μ L of fresh media. The seeded cells were treated with 500 μ L of transfection complexes per well of a 6-well plate. After 48 hours post transfection, cells were passaged to 10 cm dishes. Following more 3 days cells were harvested for further analysis.

Polysome profiling and polysome sequencing

Polysome sequencing was performed as described by Flora et al. with minor modifications (Flora et al., 2018). Cells were incubated with fresh medium 2-4 hours before harvesting. Cycloheximide (100 µg/ml) was first added to the medium for 3 min at RT, and the cells were subsequently centrifuged at 800 xg for 3 min. The cell pellet was afterwards washed two times with ice-cold phosphate-buffered saline (1X PBS, pH 7.4). The supernatant was discarded and the pellet was gently resuspended in 300 µl of lysis buffer A (300 mM NaCl, 15 mM Tris-HCl, pH 7.5, 15 mM EDTA, 1 mg/ml heparin, 1% Triton-X100, and 100 µg/ml cycloheximide) and lysed for 15 min on ice. The lysate was clarified by centrifugation at 8500 xg for 5 min at 4°C. 20% of the lysate was kept aside as an input. The clarified lysate was loaded onto 10%-50% sucrose gradient in Buffer B (300 mM NaCl, 15 mM Tris-HCl, pH 7.5, 15 mM MgCl₂, supplemented with 100 µg/ml cycloheximide) and centrifuged for 3 hours at 35,000 rpm in an SW41 rotor in a Beckman L7 ultracentrifuge (Beckman Coulter, Krefeld, Germany). The gradients were simultaneously fractionated on a Density Gradient Fractionation System (#621140007) at 0.75 ml/min. We added 20 µl of 20% SDS, 8 µl of 0.5 M pH 8 EDTA, and 16 µl of proteinase K (#P8107S) to each polysome fraction and incubated them for 30 min at 37°C. The RNA from each fraction was extracted by standard acid phenol: chloroform purification followed by 80% ethanol precipitation. The polysome fractions were then measured for RNA content and RNAseq libraries were prepared.

Library preparation and mRNA sequencing

The RNA was first treated with Turbo DNase (TURBO DNA-free Kit, Life Technologies, AM1907) and then purified using DNase Inactivation buffer. The RNA was then centrifuged for 1.5 min at 1000 xg and the supernatant was collected and centrifuged once more at the same condition. The RNA quantity was determined by measuring the absorbance at 260 nm (NanoDrop 1000 spectrophotometer; Peqlab).

Poly-A selection was performed according to manufacturer's instructions (Bioo Scientific Corp., 710 NOVA-512991). Following Poly-A selection mRNA libraries were prepared according to manufacturer's instructions (Bioo Scientific Corp., NOVA-5138-08), except that the RNA was incubated at 95°C for 13 min to generate optimal fragment sizes. The sequencing library quantity was determined using Qubit (Thermo Fisher Scientific). The library integrity was assessed with a Bioanalyzer 2100 system (RNA 6000 Pico kit, Agilent Technologies). The libraries on biological duplicates from each genotype were subjected to a 75 base-pair single-end sequencing on Illumina NextSeq500 at the Center for Functional Genomics (CFG).

Data analysis of S2 cell polysome sequencing

First the reads were assessed for their quality using FastQC. Mapping of the reads was performed against *Drosophila* Genome (dm6.01, www.fruitfly.org) using Hisat version 2.1.0. Mapped reads were then assigned to feature using featureCount version v1.6.4. To measure Translation efficiency (TE), CPMs (counts per million) values for polysome-libraries were calculated (Flora et al., 2018). All transcripts with zero reads were discarded from

libraries for further analysis. The log₂ ratio of CPMs between the polysome fraction and total mRNA was measured and averaged between replicates. This ratio represents TE. The TE value of each replicate was averaged and delta TE (Δ TE) was calculated as (*porthos* RNAi TE)/(GFP RNAi TE). Targets were defined as transcripts falling greater or less than one standard deviation (SD) from the median of Δ TE.

Motif enrichment analysis

To perform motif enrichment analysis on targets versus non-targets from polysome sequencing, the deduplicated fasta files of the 5'UTRs, CDSs, and 3'UTRs were used as input into Homer (v4.10.4, <http://homer.ucsd.edu/homer/>). The initial motif discovery was first performed and to identify the most significant motif resembled a TOPL motif within the first 200 base pair (<http://alternate.meme-suite.org/tools/meme>, Bailey et al., 1994). The analysis was repeated with sequences from the refined Transcription start sites (TSSs) as described in CAGE-seq analysis (Table S3).

CAGE-seq analysis

We employed *Drosophila* CAGE sequencing data from the modENCODE project SRR488282 to map TSSs at 5'UTRs. (CAGE-seq data for ovaries was obtained from the modENCODE project SRR488282.) Mapping of the reads were performed against the *Drosophila* genome (dm6.01) using HISAT version 2.1.0 (Kim et al., 2015). TSSs were annotated using the CAGER package and used to obtain the first 200 base pairs after the TSS, which were assessed for motif enrichment analysis by MEME suite (v5.1.1.) (Bailey et al., 2009) (Table S3).

Western Blots

30 μ g of protein samples were loaded on a 4-15% Mini-PROTEAN TGX Precast Protein Gel (Bio-Rad, Hercules, USA) and run at 100V for 80 min in 1x running buffer (25 mM Tris Base, 190 mM glycine and 0.1% SDS) followed by transfer onto Amersham Protran Premium 0.45 μ m NC (GE Healthcare Lifescience, Little Chalfont, UK) or Amersham Hybond Low Fluorescence 0.2 μ m PVDF (GE Healthcare Lifescience, Little Chalfont, UK) membrane using a wet transfer protocol with 25 mM Tris Base, 190 mM Glycine + 20% MeOH at either 100 Volts for 60 min or 200 mA for 90 min at Mini Trans-Blot Cell Module (Bio-Rad, Hercules, USA). Membranes were blocked in PBS-T (0.1% Triton X-100 in PBS) containing 2% BSA or Pierce Clear Milk Blocking Buffer (ThermoFisher Scientific) for 60 min at RT. Primary antibodies were incubated overnight at 4°C at the following concentrations: α -profilin (Verheyen and Cooley, 1994, DSHB) 73 1:50, anti-GFP (clone 2B6, Ogris lab, MFPL), anti-GAPDH (ab181603, Abcam, Cambridge, UK). Then, we washed blots 3x for 5 min in blocking solution and incubated with Goat anti Mouse IgG (H/L):HRP (Bio-Rad, Hercules, USA) or goat-anti-rabbit IgG (H+L)-HRP (Bio-Rad, Hercules, USA) at 1:5 000 - 10,000 for 1-2 hours at RT. Blots were washed 2x 5 min in blocking solution and 1x 5 min with PBS-T. Blots were developed using SuperSignal West Femto Maximum Sensitivity Substrate (ThermoFisher Scientific, Waltham, Massachusetts, USA) according to manufacturer's instructions.

Chemiluminescent signal was detected using the Amersham Imager 600 (GE Healthcare Lifescience) or VersaDoc (Bio-Rad). Finally we processed images with ImageJ.

Cellular respiration measurement

The cellular respiration was assessed using Seahorse XF96 extracellular flux analyzer (Seahorse Bioscience Europe, Copenhagen, Denmark). The oxygen consumption rate (OCR) as a measure of oxygen utilization of cells is an important indicator of mitochondrial function. The extracellular acidification rate (ECAR) is a measure of lactic acid levels, formed during the conversion of glucose to lactate during glycolysis. Prior to measurement, wild-type and *porthos* KD cells were seeded at 10×10^5 cells per well in Seahorse XF96 polystyrene tissue culture plates (Seahorse Bioscience Europe) and incubated in unbuffered Seahorse RPMI assay medium (Sigma-Aldrich) supplemented with glucose (25 mM; Sigma-Aldrich), sodium pyruvate (1 mM; Gibco), and glutamine (2 mM; Gibco) in a non-CO₂ incubator at 25 °C and pH 7.4 for 1 h before the experiment. Cellular oxygen consumption was assessed in basal condition (prior to any addition) and after addition of oligomycin (2 μM; Sigma-Aldrich), Carbonyl cyanide-4 (trifluoromethoxy) phenylhydrazone (FCCP, 2 μM; Sigma-Aldrich), antimycin A (1 μM; Sigma-Aldrich) and rotenone (1 μM; Sigma-Aldrich). The three drugs were injected into the XF24 sequentially. This allowed for calculation of OCR linked to ATP production, maximal respiration capacity and spare respiratory capacity. Basal respiration was measured prior to injection of oligomycin A. Both OCR and ECAR were measured every 4 min with a mixing of 2 min in each cycle, with 4 cycles in total.

Different parameters from the OCR graph were measured as follows. ATP turnover was calculated by subtracting the “last rate measurement before oligomycin” from the “minimum rate measurement after oligomycin injection”. Maximal respiration was defined as (maximum rate measurement after adding FCCP) - (non-mitochondrial respiration). Spare respiratory capacity (SRC) was measured by subtracting basal respiration from maximal respiration.

Metabolomics profiling analysis

Samples for metabolomics were assessed by VBC according to Rao et al. with slight modifications (<https://www.viennabiocenter.org/facilities/metabolomics/>) (Rao et al., 2019). Cell pellets (1 gr for wild-type and *atos* macrophages embryos) or embryos were extracted using an ice-cold MeOH:ACN:H₂O (2:2:1, v/v) solvent mixture. A volume of 1mL of cold solvent was added to each pellet, vortexed for 30 s, and incubated in liquid nitrogen for 1 min. The samples were thawed at room temperature and sonicated for 10 min. This cycle of cell lysis in liquid nitrogen combined with sonication was repeated three times. To precipitate proteins, the samples were incubated for 1 h at -20 °C, followed by centrifugation at 13,000 rpm for 15 min at 4 °C. The supernatant was removed and evaporated. The dry extracts were reconstituted in 100 μL of ACN:H₂O (1:1, v/v), sonicated for 10 min, and centrifuged at 13,000 rpm for 15 min at 4 °C to remove insoluble debris.

The supernatants were transferred to Eppendorf tubes, shock frozen and stored at -80 °C prior to LC/MS analysis. A volume of 1 µL of the metabolite extract was injected on a ZIC-pHILIC HPLC column operated at a flow rate of 100 µL/min, directly coupled to a TSQ Quantiva mass spectrometer (Thermo Fisher Scientific).

We used the following transitions for quantitation in the negative ion mode: AMP 346 m/z to 79 m/z, ADP 426 m/z to 134 m/z, ATP 506 m/z to 159 m/z, IMP 347 m/z to 79 m/z, GMP 362 m/z to 211 m/z, GDP 442 m/z to 344 m/z, GTP 522 m/z to 424 m/z, taurine 124 m/z to 80 m/z, malate 133 m/z to 115 m/z, citrate 191 m/z to 111 m/z, pyruvate 87 m/z to 43 m/z, lactate 89 m/z to 43 m/z, NADH 664 m/z to 408 m/z, NAD 662 m/z to 540 m/z, hexose phosphates 259 m/z to 97 m/z, Acetyl CoA 808 m/z to 408 m/z, CoA 766 m/z to 408 m/z, succinate 117 m/z to 73 m/z. Glutamine 147 m/z to 130 m/z, glutamate 148 m/z to 84 m/z, serine 106 m/z to 60 m/z were calculated in the positive ion mode. For all transitions, the optimal collision energy was defined by analyzing pure metabolite standards. Chromatograms were manually interpreted using trace finder (Thermo Fisher Scientific), validating experimental retention times with the respective quality controls. All measurements were within the linear range of detection.

For the metabolomics analysis, the metabolite concentration was normalized using a Z-score normalization method with the formula of $y = (x-\alpha)/\lambda$, in which x refers to the real concentration, α indicates the mean value of all samples, and λ is the variance of all samples. The normalized concentrations of metabolites were applied to generate a heatmap, which showed the concentration difference of all metabolites. For KEGG (<http://www.kegg.jp>, Tokyo, Japan) pathway analysis, the clusterProfiler R package was employed.

Statistics and repeatability

Statistical tests as well as the number of embryos/ cells assessed are listed in the figure legends. All statistical analyses were performed using GraphPad Prism and significance was determined using a 95% confidence interval. Data points from individual experiments/ embryos were pooled to estimate mean and SEM. No statistical method was used to predetermine sample size and the experiments were not randomized. Unpaired t-test or Mann-Whitney was used to calculate the significance in differences between two groups and One-way Anova followed by Tukey post-test followed by Conover or Dunn's post-test for multiple comparisons. All measurements were performed in 3-50 embryos. Representative images illustrated in Figures 1B,C,D, Figures 2A,C,E, Figures S2A,B, Figures 3B,C,D,G, Figure 4A,B,E,I, Figure S4B, and Figure 6C,G,I were from separate experiments that were repeated at least 3 and up to 7 times. Stills shown in Figure 1G, Figure S1I, Figure 4I, and Figure S4F are representative images from two-photon movies, which were repeated at least 3 times.

REFERENCES

- Anders S, Huber W. 2010. Differential expression analysis for sequence count data. *Genome Biol.* 11:R106. doi:10.1186/gb-2010-11-10-r106.
- Bassett A, Liu JL. 2014. CRISPR/Cas9 mediated genome engineering in *Drosophila*. *Methods* 69: 128-136. (doi:10.1016/j.ymeth.2014.02.019).
- Beckervordersandforth R. 2017. Mitochondrial metabolism-mediated regulation of adult neurogenesis. *Brain Plast.* 3: 73–87.
- Bernstein BW, Bamberg JR. 2003. Actin-ATP hydrolysis is a major energy drain for neurons. *J. Neurosci.* 23: 1-6.
- Bailey TL, Elkan C. 1994. "Fitting a mixture model by expectation maximization to discover motifs in biopolymers". *Proceedings of the Second International Conference on Intelligent Systems for Molecular Biology: 28-36.*
- Bailey TL, Boden M, Buske FA, Frith M, Grant CE, Clementi L, Ren J, Li WW, Noble WS. MEME SUITE: tools for motif discovery and searching. *Nucleic Acids Res.* 2009 Jul;37(Web Server issue):W202-8. doi: 10.1093/nar/gkp335. Epub 2009 May 20. PMID: 19458158; PMCID: PMC2703892.
- Bischof J, Maeda RK, Hediger M, Karch F, Basler K. 2007. An optimized transgenesis system for *Drosophila* using germ-line-specific uC31 integrases. *Proc. Natl. Acad. Sci. USA* 104: 3312–3317.
- Bhattacharjee JK. 1985. α -Amino-adipate pathway for the biosynthesis of lysine in lower eukaryotes. *Crit. Rev. Microbiol.* 12: 131-151.
- Bodor DL, Pönisch W, Endres RG, Paluch EK. 2020. Of cell shapes and motion: The physical basis of animal cell migration. *Developmental Cell* 52(5): 550-562. doi: 10.1016/j.devcel.2020.02.013.
- Booth MPS, Connors R, Rumsby G, Brady RL. 2006. Structural basis of substrate specificity in human Glyoxylate Reductase/Hydroxypyruvate Reductase. *J. Mol. Biol.* 360: 178–189.
- Bourgeois CF, Mortreux F, Auboeuf D. 2016. The multiple functions of RNA helicases as drivers and regulators of gene expression. *Mol. Cell. Bio.* 17: 426-438.
- Brückner K, Kockel L, Duchek P, Luque CM, Rørth P, Perrimon N. 2004. The PDGF/VEGF receptor controls blood cell survival in *Drosophila*. *Dev. Cell* 7: 73–84.
- Buck MD, O'Sullivan D, Klein Geltink RI, Curtis JD, Chang CH, Sanin DE, Qiu J, Kretz O, Braas D, van der Windt GJW, et al. 2016. Mitochondrial dynamics controls T cell fate through metabolic programming. *Cell* 166: 63–76.
- Bunt, S., Hooley, C., Hu, N., Scahill, C., Weavers, H., and Skaer, H. 2010. Hemocyte-eecreted Type IV collagen enhances BMP signaling to guide renal tubule morphogenesis in *Drosophila*. *Dev. Cell* 19:296-306.
- Caputa G, Castoldi A, Pearce EJ. 2019. Metabolic adaptations of tissue-resident immune cells. *Nat. Immunol.* 20: 793-801.
- Cho NK, Keyes L, Johnson E, Heller J, Ryner L, Karim F, Krasnow MA. 2002. Developmental control of blood cell migration by the *Drosophila* VEGF pathway. *Cell* 108: 865-876.
- Commander R, Wei C, Sharma A, Mouw JK, Burton LJ, Summerbell E, Mahboubi D, RJ Peterson, Konen J, Zhou W, Du Y, Fu H, Shanmugam M, Marcus AI. 2020. Subpopulation targeting of pyruvate dehydrogenase

and GLUT1 decouples metabolic heterogeneity during collective cancer cell invasion. *Nat. Commun.* 11:1.

Chen HH, Yu, HI, Cho WC, Tarn, WY. 2015. DDX3 modulates cell adhesion and motility and cancer cell metastasis via Rac1-mediated signaling pathway. *Oncogene* 34:2790-2800.

Cunniff B, McKenzie AJ, Heintz NH, Howe AK. 2016. AMPK activity regulates trafficking of mitochondria to the leading edge during cell migration and matrix invasion. *Mol. Biol. Cell* 17:2662-74. doi: 10.1091/mbc.E16-05-0286.

Cuvelier D, Thery M, Chu YS, Dufour S, Thiery JP, Bornens M, Nassoy P, Mahadevan, L. 2007. The universal dynamics of cell spreading. *Curr. Biol.* 17: 694-699.

Dobin A, Davis CA, Schlesinger F, Drenkow J, Zaleski C, Jha S, Batut P, Chaisson M, Gingeras TR. 2013. STAR: ultrafast universal RNA-seq aligner. *Bioinformatics* 29 15-21.

Flora P, Wong-Deyrup SW, Martin ET, Palumbo RJ, Nasrallah, M, Oligney A, Blatt P, Patel D, Fuchs G, Rangan, P. 2018. Sequential regulation of maternal mRNAs through a conserved cis-acting element in their 3' UTRs. *Cell. Rep.* 25: 3828–3843. e9. doi:10.1016/j.celrep.2018.12.007.

Fonseca BD, Zakaria C, Jia JJ, Graber TE, Svitkin Y, Tahmasebi S, Healy D, Hoang HD, Jensen JM, Diao IT, Lussier A, Dajadian C, Padmanabhan N, Wang W, Matta-Camacho E, Hearnden J, Smith EM, Tsukumo Y, Yanagiya A, Morita M, Petroulakis E, González JL, Hernández G, Alain T, Damgaard CK. 2015.

La-related protein 1 (LARP1) represses terminal oligopyrimidine (TOP) mRNA translation downstream of mTOR complex 1 (mTORC1). *J Biol Chem.* 290(26): 15996-6020. doi: 10.1074/jbc.M114.621730. Epub May 4. PMID: 25940091; PMCID: PMC4481205.

Freije WA, Mandal S, Banerjee U. 2012. Expression profiling of attenuated mitochondrial function identifies retrograde signals in *Drosophila*. *G3: Genes- Genomes-Genetics* 2: 843–851.

Friedl P, Brocker EB. 2000. The biology of cell locomotion within three-dimensional extracellular matrix. *Cellular and Molecular Life Sciences* 57: 41–64. <https://doi.org/10.1007/s000180050498>.

Friedl P, Locker J, Sahai E, & Segall JE. 2012. Classifying collective cancer cell invasion. *Nat. Cell Bio.* 14(8): 777–783. <https://doi.org/10.1038/ncb2548>.

Llufrio EM, Wang L, Naser FJ, Patti GJ. 2018. Sorting cells alters their redox state and cellular metabolome. *Redox Biol.* 16:381-387. doi: 10.1016/j.redox.2018.03.004. Epub 2018 Mar 9. PMID: 29627745; PMCID: PMC5952879.

Gyoergy A, Roblek M, Ratheesh A, Valoskova K, Belyaeva V, Wachner S, Matsubayashi Y, Sa´ nchez-Sa´ nchez BJ, Stramer B, Siekhaus DE. 2018. Tools allowing independent visualization and genetic manipulation of *Drosophila melanogaster* macrophages and surrounding tissues. *G3: Genes|Genomes|Genetics* 8:845–857.
DOI: <https://doi.org/10.1534/g3.117.300452>

Hoang-Minh LB, Siebzehnrubl FA, Yang C, Suzuki-Hatano S, Dajac, K, Loche T, Andrews N, Massari MS, Patel J, Amin K, et al. 2018. Infiltrative and drug-resistant slow-cycling cells support metabolic heterogeneity in glioblastoma. *EMBO* 37: e98772.

Hsieh AC, Liu Y, Edlind MP, Ingolia, NT, Janes MR, Sher A, Shi EY, Stumpf, CR, Christensen C, Bonham MJ, et al. 2012. The translational landscape of mTOR signalling steers cancer initiation and metastasis. *Nature* 485: 55-61.

Hurd TR, Herrmann B, Sauerwald J, Sanny J, Grosch M, Lehmann R. 2016. Long Oskar controls mitochondrial inheritance in *Drosophila melanogaster*. *Dev. Cell* 39(5): 560-571. PMID: 27923120.

- Jarmoskaite I, Russell R. 2011. DEAD-box proteins as RNA helicases and chaperones. *Wiley Interdiscip. Rev. RNA* 2(1): 135-152.
- Kelley LC, Chi Q, Ca'ceres R, Hastie E, Schindler AJ, Jiang Y, Matus DQ, Plastino, J, Sherwood DR. 2019. Adaptive F-actin polymerization and localized ATP production drive basement membrane invasion in the absence of MMPs. *Dev. Cell* 48: 313-328.
- Khalil, AA, Friedl P. 2010. Determinants of leader cells in collective cell migration. *Integr. Biol. (Camb.)* 2: 568-574.
- Kim D, Langmead B, Salzberg SL. 2015. HISAT: a fast spliced aligner with low memory requirements. *Nat Methods*. 12:357–360.
- Kurosaka S, Kashina A . 2008. Cell biology of embryonic migration. *Birth Defects Res C: Embryo Today* 84: 102-122.
- Lahr RM, Fonseca BD, Ciotti GE, Al-Ashtal HA, Jia JJ, Niklaus MR, Blagden SP, Alain T, Berman AJ. 2017. Lar-related protein 1 (LARP1) binds the mRNA cap, blocking eIF4F assembly on TOP mRNAs. *Elife* 6:e24146.
- LeBleu VS, O'Connell JT, Gonzalez Herrera KN, Wikman H, Pantel K, Haigis MC, de Carvalho FM, Damascena A, Domingos Chinen LT, Rocha RM, Asara JM, Kalluri R. 2014. PGC-1 α mediates mitochondrial biogenesis and oxidative phosphorylation in cancer cells to promote metastasis. *Nat Cell Biol.* 16(10): 992-1003, 1-15. doi: 10.1038/ncb3039.
- Li Y, Yao L, Morie Y, Sun SX. 2019. On the energy efficiency of cell migration in diverse physical environments. *PNAS* 116: 23894-23900.
- Lieber T, Jeedigunta SP, Palozzi JM, Lehmann R, Hurd TR. 2019. Mitochondrial fragmentation drives selective removal of deleterious mtDNA in the germline. *Nature* 570: 380-384.
- Montell DJ. 2008. Morphogenetic cell movements: diversity from mechanical properties. *Science* 322: 1502-1505.
- Morita M, Gravel SP, Chénard V, Sikström K, Zheng L, Alain T, Gandin V, Avizonis D, Arguello M, Zakaria C, McLaughlan S, Nouet Y, Pause A, Pollak M, Gottlieb E, Larsson O, St-Pierre J, Topisirovic I, Sonenberg N. 2013. mTORC1 controls mitochondrial activity and biogenesis through 4E-BP-dependent translational regulation. *Cell Metab.* 18(5):698-711. doi: 10.1016/j.cmet.2013.10.001. PMID: 24206664.
- Nourshargh S, Alon R. 2014. Immune cell invasion and function leukocyte migration into inflamed tissues. *Immunity* 41: 694-707.
- Patel MS, Nemeria NS, Furey W, Jordan F. 2014. The pyruvate dehydrogenase complexes: structure-based function and regulation. *J. Biol. Chem.* 289: 16615–16623.
- Pavlova NN, Thompson CB. 2016. The emerging hallmarks of cancer metabolism. *Cell Metab* 23(1):27-47. doi: 10.1016/j.cmet.2015.12.006. PMID: 26771115; PMCID: PMC4715268.
- Petrie RJ , Yamada KM . 2012. At the leading edge of three-dimensional cell migration. *J. Cell Sci.* 125: 5917-5926.
- Rao S, Mondragón L, Pranjić B, Hanada T, Stoll G, Köcher T, Zhang P, Jais A, Lercher A, Bergthaler A, Schramek D, Haigh K, Sica V, Leduc M, Modjtahedi N, Pai TP, Onji M, Uribealag I, R Hanada, Kozieradzki I, Kogelgruber R, Cronin SJ, She Z, uehenberger FQ. 2019. AIF-regulated oxidative phosphorylation supports lung cancer development. *Cell Res.* 29: 579-591.
- Ratheesh, A., Belyaeva, V., and Siekhaus, D.E. 2015. *Drosophila* immune cell migration and adhesion during embryonic development and larval immune responses. *Curr. Opin. Cell Biol.* 36: 71–79.

- Ratheesh A, Biebl J, Vesela J, Smutny M, Papusheva E, Krens SFG, Kaufmann W, Gyoergy A, Casano AM, Siekhaus DE. 2018. *Drosophila* TNF modulates tissue tension in the embryo to facilitate macrophage invasive migration. *Dev Cell*. 45(3): 331-346.e7. doi: 10.1016/j.devcel.2018.04.002. PMID: 29738712.
- Riera-Domingo C, Audigé A, Granja S, Cheng WC, Ho PC, Baltazar F, Stockmann C, Mazzone M. 2020. Immunity, hypoxia, and metabolism- the ménage a trois of cancer: implications for immunotherapy. *Physiol Rev* 100: 1–102.
- Rottner K, Schaks M. 2019. Assembling actin filaments for protrusion. *Curr Opin Cell Biol*. 56:53-63. doi: 10.1016/j.ceb.2018.09.004.
- Saxton RA, Sabatini DM. 2017. mTOR signaling in growth, metabolism, and disease. *Cell* 168(6):960-976. doi: 10.1016/j.cell.2017.02.004.
- Seiguchi T, Hayano T, Yanagida M, Takahashi N, Nishimoto T. 2006. NOP132 is required for proper nucleolus localization of DEAD-box RNA helicase DDX47. *Nucleic Acids Research* 16: 4593-4608.
- Siekhaus D, Haesemeyer M, Moffitt O, Lehmann R. 2010. RhoL controls invasion and Rap1 localization during immune cell transmigration in *Drosophila*. *Nat. Cell Biol* 12: 605–610.
- Smutny M, A'kos Z, Grigolon S, Shamipour S, Ruprecht V, Capek D, Behrndt M, Papusheva E, Tada M, Hof B, et al. (2017). Friction forces position the neural anlage. *Nat. Cell Biol*. 19: 306-317.
- Sreekumar A, Poisson LM, Rajendiran TM, Khan AP, Cao Q, Yu J, Laxman B, Mehra R, Lonigro RJ, Li Y, Nyati MK, Ahsan A, Kalyana-Sundaram S, Han B, Cao X, Byun J, Omenn GS, Ghosh D, Pennathur S, Alexander DC, Berger A, Shuster JR, Wei JT, Varambally S, Beecher C, Chinnaiyan AM. 2009. Metabolomic profiles delineate potential role for sarcosine in prostate cancer progression. *Nature* 457(7231):910-4. doi: 10.1038/nature07762. Erratum in: *Nature*. 2013 Jul 25;499(7459):504. PMID: 19212411; PMCID: PMC2724746.
- Teixeira FK, Sanchez CG, Hurd TR, Seifert JRK, Czech B., Preall J.B., Hannon G. J, Lehmann R. 2015. ATP synthase promotes germ cell differentiation independent of oxidative phosphorylation. *Nature Cell Biology* 17: 689–696. DOI: 10.1038/ncb3165.
- Thoreen CC, Chantranupong L, Keys HR, Wang T, Gray NS, Sabatini DM. 2012. A unifying model for mTORC1-mediated regulation of mRNA translation. *Nature* 485: 109–113.
- Valoskova K, Biebl J, Roblek M, Emtenani S, Gyoergy A, Misova M, Ratheesh A, Reis-Rodrigues P, Shkarina K, Larsen ISB, Vakhrushev SY, Clausen H, Siekhaus DE. 2019. A conserved major facilitator superfamily member orchestrates a subset of O-glycosylation to aid macrophage tissue invasion. *eLife*. 8. pii: e41801.
- Vander Heiden MG, Cantley LC, Thompson CB. 2009. Understanding the Warburg effect: the metabolic requirements of cell proliferation. *Science* 324: 1029–1033.
- Van Horsen R, Janssen E, Peters W, Van de Pasch L, Te Lindert MM, Van Dommelen MMT, Linssen PC, Ten Hagen TLM, Franssen JAM, Wieringa B. 2009. Modulation of cell motility by spatial repositioning of enzymatic ATP/ADP Exchange capacity. *J Biol Chem* 284: 1620–1627.
- Vats D, Mukundan L, Odegaard J I, Zhang L, Smith K L, Morel CR, Greaves DR, Murray PJ, Chawla A. 2006. Oxidative metabolism and PGC-1 β attenuate macrophage mediated inflammation. *Cell Metabolism* 4: 13–24.
- Verheyen E. M., Cooley L. (1994). Profilin mutations disrupt multiple actin-dependent processes during *Drosophila* development. *Development* 120, 717–728
- Weavers H, Martin P. 2020. The cell biology of inflammation: From common traits to remarkable

immunological adaptations. *J. Cell Biol.* 219 (7): e202004003.

Weavers H, Evans IR, Martin P, and Wood W. 2016. Corpse engulfment generates a molecular memory that primes the macrophage inflammatory response. *Cell* 165: 1658–1671.

Wood W, Martin P. 2017. Macrophage functions in tissue patterning and disease: new insights from the fly. *Dev. Cell.* 40: 221–233.

Yamada KM, Sixt M. 2019. Mechanisms of 3D cell migration. *Nat. Rev. Mol. Cell Biol.* 20: 738-752.

Zanotelli MR, Goldblatta ZE, Millera JP, F Bordeleaub, Lia J, VanderBurgha JA, Lampia MC, Kinga MR, Reinhart-Kinga A. 2018. Regulation of ATP utilization during metastatic cell migration by collagen architecture. *Molecular Biology of the Cell*: 29.

Zanotelli MR, Rahman-Zaman A, Vander Burgh JA, Taufalele PV, Jain A, Erickson D, Bordeleau F, Reinhart-King CA. 2019. Energetic costs regulated by cell mechanics and confinement are predictive of migration path during decision-making. *Nat. Commun* 10: 4185.

Zhang J, Goliwas KF, Wang W, Taufalele PV, Bordeleau F, and Reinhart-King, CA. 2019. Energetic regulation of coordinated leader-follower dynamics during collective invasion of breast cancer cells. *Proc. Natl. Acad. Sci. USA* 116: 7867–7872.

Zhang WC, Shyh-Chang N, Yang H, Rai A, Umashankar S, Ma S, Soh BS, Sun LL, Tai BC, Nga ME, Bhakoo KK, Jayapal SR, Nichane M, Yu Q, Ahmed DA, Tan C, Sing WP, J Tam, Thirugananam A, Soroush Noghabi M, Pang YH, Ang HS, Mitchell W, Robson P, Kaldis P, RA Soo, Swarup S, Lim EH, B Lim. 2012. Glycine decarboxylase activity drives non-small cell lung cancer tumor-initiating cells and tumorigenesis. *Cell* 148: 259-272.

Zid BM, Rogers AN, Katewa SD, Vargas MA, Kolipinski MC, Lu TA et al. 2009. 4E-BP extends lifespan upon dietary restriction by enhancing mitochondrial activity in *Drosophila*. *Cell* 139: 149-160.

Xie J, Bao M, Hu X, Koopman WJH, Huck WTS. 2021. Energy expenditure during cell spreading influences the cellular response to matrix stiffness. *Biomaterials* 267: 120494.

Exact genotype of *Drosophila* lines used in Figures:

Figure 1 and Figure S1

Figs. 1B-D: Control: *w*;⁻; +; *srpHemo-H2A::3xmCherry*, Mutant: *w*;⁻; *P{EP}CG9005^{BG02278}*; *srpHemo-H2A::3xmCherry*, Rescue: *w*;⁻; *P{EP}CG9005^{BG02278}*; *srpHemo-CG9005*, *srpHemo-H2A::3xmCherry*. **Fig. 1E:** Control: *w*;⁻; +; *srpHemo-H2A::3xmCherry*, mutant: *w*;⁻; *P{EP}CG9005^{BG02278}*; *srpHemo-H2A::3xmCherry*, Df1: *w*;⁻; *P{EP}CG9005^{BG02278}*/*Df(2R)ED2222*; *srpHemo-H2A::3xmCherry*, Df2: *w*;⁻; *P{EP}CG9005^{BG02278}*/*Df(2R)BSC259*; *srpHemo-H2A::3xmCherry*, rescue: *w*;⁻; *P{EP}CG9005^{BG02278}*; *srpHemo-CG9005*, *srpHemo-H2A::3xmCherry*. **Fig. 1F:** Control 1: *w* *P(w+)UAS-dicer/w*;⁻; *P{attP,y[+],w[3`]}/+*; *srpHemo-Gal4 UAS-GFP*, *UAS-Dicer2/w*;⁻; *CG9005 RNAi (v106589)/+*; *srpHemo-Gal4 UAS-GFP*, *UAS-H2A::RFP/+*, Control 2: *w* *P(w+)UAS-dicer/w*;⁻; +; *srpHemo-Gal4 UAS-GFP*, *UAS-Dicer2/w*;⁻; *CG9005 RNAi (v36080)/+*; *srpHemo-Gal4 UAS-GFP*, *UAS-H2A::RFP/+*, Control 3: *w* *P(w+)UAS-dicer/w*;⁻; *P{attP,y[+],w[3`]}/+*; *srpHemo-Gal4 UAS-GFP*, *UAS-Dicer2/w*;⁻; *CG9005 RNAi (v33362)/+*; *srpHemo-Gal4 UAS-GFP*, *UAS-H2A::RFP/+*. **Figs. 1G-M:** Control: *w*;⁻; +; *srpHemo-H2A::3xmCherry*, mutant: *w*;⁻; *P{EP}CG9005^{BG02278}*; *srpHemo-H2A::3xmCherry*. **Fig. S1B:** Control: *w*;⁻; +; *srpHemo-H2A::3xmCherry*, mutant: *w*;⁻; *P{EP}CG9005^{BG02278}*; *srpHemo-H2A::3xmCherry*, Df1 cross: *w*;⁻; *P{EP}CG9005^{BG02278}*/*Df(2R)ED2222*; *srpHemo-H2A::3xmCherry*, Df2 cross: *w*;⁻; *P{EP}CG9005^{BG02278}*/*Df(2R)BSC259*; *srpHemo-H2A::3xmCherry*, rescue: *w*;⁻; *P{EP}CG9005^{BG02278}*; *srpHemo-CG9005*, *srpHemo-H2A::3xmCherry*. **Figs. S1C,D:** Control: *w*;⁻; +; *srpHemo-H2A::3xmCherry*, mutant: *w*;⁻; *P{EP}CG9005^{BG02278}*; *srpHemo-H2A::3xmCherry*. **Figs. S1E,F:** Control 1: *w* *P(w+)UAS-dicer/w*;⁻; *P{attP,y[+],w[3`]}/+*; *srpHemo-Gal4 UAS-GFP*, *CG9005 RNAi 1: UAS-Dicer2/w*;⁻; *v106589/+*; *srpHemo-Gal4 UAS-GFP*, *UAS-H2A::RFP/+*, Control 2: *w* *P(w+)UAS-dicer/w*;⁻; +; *srpHemo-Gal4 UAS-GFP*, *CG9005 RNAi 2: UAS-Dicer2/w*;⁻; *v36080/+*; *srpHemo-Gal4 UAS-GFP*, *UAS-H2A::RFP/+*, Control 3: *w* *P(w+)UAS-dicer/w*;⁻; *P{attP,y[+],w[3`]}/+*; *srpHemo-Gal4 UAS-GFP*, *CG9005 RNAi 3: UAS-Dicer2/w*;⁻; *v33362/+*; *srpHemo-Gal4 UAS-GFP*, *UAS-*. **Fig. S1G:** Control 1: *w* *P(w+)UAS-dicer/w*;⁻; *P{attP,y[+],w[3`]}/+*; *srpHemo-Gal4 UAS-GFP*, *CG9005 RNAi 1: UAS-Dicer2/w*;⁻; *v106589/+*; *srpHemo-Gal4 UAS-GFP*, *UAS-H2A::RFP/+*. **Fig. S1H:** Control 2: *w* *P(w+)UAS-dicer/w*;⁻; +; *srpHemo-Gal4 UAS-GFP*, *CG9005 RNAi 2: UAS-Dicer2/w*;⁻; *v36080/+*; *srpHemo-Gal4 UAS-GFP*, *UAS-H2A::RFP/+*. **Fig. S1I:** Control 3: *w* *P(w+)UAS-dicer/w*;⁻; *P{attP,y[+],w[3`]}/+*; *srpHemo-Gal4 UAS-GFP*, *CG9005 RNAi 3: UAS-Dicer2/w*;⁻; *v33362/+*; *srpHemo-Gal4 UAS-GFP*, *UAS-*. **Figs. S1J-M:** Control: *w*;⁻; +; *srpHemo-H2A::3xmCherry*, mutant: *w*;⁻; *P{EP}CG9005^{BG02278}*; *srpHemo-H2A::3xmCherry*

Figure 2 and Figure S2

Fig. 2A: *w*;⁻; +; *UAS-atossa::FLAG::HA*, *srpHemo-Gal4*, *srpHemo-H2A::3xmCherry*. **Figs. 2C,D:** Control: *w*;⁻; +; *srpHemo-H2A::3xmCherry*, mutant: *w*;⁻; *atossa^{BG02278}*; *srpHemo-H2A::3xmCherry*, Rescue: *w*;⁻; *atossa^{BG02278}*; *srpHemo-atossa*, *srpHemo-H2A::3xmCherry*, Rescue: *w*;⁻; *atossa^{BG02278}*; *srpHemo-atossa^{DUF2410}*, *srpHemo-H2A::3xmCherry*, Rescue: *w*;⁻;

atossa^{BG02278}; *srpHemo-atossa*^{CherSeg-}, *srpHemo-H2A::3xmCherry*, Rescue: *w-*; *atossa*^{BG02278}; *srpHemo-atossa*^{DUF2410-/CherSeg-}, *srpHemo-H2A::3xmCherry*, Rescue: *w-*; *atossa*^{BG02278}; *srpHemo-atossa*^{TAD1-/TAD2-}, *srpHemo-H2A::3xmCherry*. **Figs. 2E,F:** Control: *w-*; +; *srpHemo-H2A::3xmCherry*, mutant: *w-*; *atossa*^{BG02278}; *srpHemo-H2A::3xmCherry*, Rescue: *w-*; *atossa*^{BG02278}; *srpHemo-FAM214A*, *srpHemo-H2A::3xmCherry*, Rescue: *w-*; *atossa*^{BG02278}; *srpHemo-FAM214B*, *srpHemo-H2A::3xmCherry*

Figure S2C: Rescue: *w-*; *atossa*^{BG02278}; *srpHemo-atossa*^{TAD1-}, *srpHemo-H2A::3xmCherry*, Rescue: *w-*; *atossa*^{BG02278}; *srpHemo-atossa*^{TAD2-}, *srpHemo-H2A::3xmCherry*. **Fig. S2D:** Control: *w-*; +; *srpHemo-H2A::3xmCherry*, mutant: *w-*; *atossa*^{BG02278}; *srpHemo-H2A::3xmCherry*, Rescue: *w-*; *atossa*^{BG02278}; *srpHemo-atossa*, *srpHemo-H2A::3xmCherry*, Rescue: *w-*; *atossa*^{BG02278}; *srpHemo-atossa*^{TAD1-}, *srpHemo-H2A::3xmCherry*, Rescue: *w-*; *atossa*^{BG02278}; *srpHemo-atossa*^{TAD2-}, *srpHemo-H2A::3xmCherry*. **Fig. S2E:** Control: *w-*; +; *srpHemo-H2A::3xmCherry*, mutant: *w-*; *atossa*^{BG02278}; *srpHemo-H2A::3xmCherry*, Rescue: *w-*; *atossa*^{BG02278}; *srpHemo-atossa*, *srpHemo-H2A::3xmCherry*, Rescue: *w-*; *atossa*^{BG02278}; *srpHemo-atossa*^{DUF2410-}, *srpHemo-H2A::3xmCherry*, Rescue: *w-*; *atoss*^{BG02278}; *srpHemo-atossa*^{CherSeg-}, *srpHemo-H2A::3xmCherry*, Rescue: *w-*; *atossa*^{BG02278}; *srpHemo-atossa*^{DUF2410-/CherSeg-}, *2srpHemo-H2A::3xmCherry*, Rescue: *w-*; *atossa*^{BG02278}; *srpHemo-atossa*^{TAD1-}, *srpHemo-H2A::3xmCherry*, Rescue: *w-*; *atossa*^{BG02278}; *srpHemo-atossa*^{TAD2-}, *srpHemo-H2A::3xmCherry*, Rescue: *w-*; *atossa*^{BG02278}; *srpHemo-atossa*^{TAD1-/2-}, *srpHemo-H2A::3xmCherry*. **Fig. S2F:** Control: *w-*; +; *srpHemo-H2A::3xmCherry*, mutant: *w-*; *atossa*^{BG02278}; *srpHemo-H2A::3xmCherry*, Rescue: *w-*; *atossa*^{BG02278}; *srpHemo-atossa*, *srpHemo-H2A::3xmCherry*, Rescue: *w-*; *atossa*^{BG02278}; *srpHemo-FAM214A*, *srpHemo-H2A::3xmCherry*, Rescue: *w-*; *atossa*^{BG02278}; *srpHemo-FAM214B*, *srpHemo-H2A::3xmCherry*

Figure 3 and Figure 3S

Fig. 3B: Control (for CG9253 RNAi): *w/y,w[1118]; P{attP,y[+],w[3']}*; *srpHemo-Gal4*, *srpHemo-H2A::3xmCherry/+*, CG9253 RNAi (porthos): *UAS-Dicer2/ w-*; *srpHemo-Gal4*, *srpHemo-H2A::3xmCherry/+*, Control 1 (for CG9331 RNAi 1): *w/y,w[1118]; P{attP,y[+],w[3']}*; *srpHemo-Gal4*, *srpHemo-H2A::3xmCherry/+*, CG9331 RNAi 1 (GR/HPR): *UAS-Dicer2/ w-*; *v44653/+*; *srpHemo-Gal4*, *srpHemo-H2A::3xm-Cherry/+*, Control 1 (for CG7144 RNAi 1): *w/y,w[1118]; P{attP,y[+],w[3']}*; *srpHemo-Gal4*, *srpHemo-H2A::3xmCherry/+*, CG7144 RNAi 1 (LKR/SDH): *UAS-Dicer2/ w-*; *v51346/+*; *srpHemo-Gal4*, *srpHemo-H2A::3xm-Cherry/+*

Fig. 3C: Control: *w/y,w[1118]; P{attP,y[+],w[3']}*; *srpHemo-Gal4*, *srpHemo-H2A::3xm-Cherry/+*, porthos RNAi (CG9253): *UAS-Dicer2/ w-*; *36589/+*; *srpHemo-Gal4*, *srpHemo-H2A::3xm-Cherry/+*. **Fig. 3D:** Control 1: *w/y,w[1118]; P{attP,y[+],w[3']}*; *srpHemo-Gal4*, *srpHemo-H2A::3xm-Cherry/+*, CG9331 RNAi 1 (GR/HPR): *UAS-Dicer2/ w-*; *v44653/+*; *srpHemo-Gal4*, *srpHemo-H2A::3xm-Cherry/+*, Control 2: *w/y,w[1118]; P{attP,y[+],w[3']}*; *srpHemo-Gal4*, *srpHemo-H2A::3xm-Cherry/+*, CG9331 RNAi 2 (GR/HPR): *UAS-Dicer2/ w-*; *v10780/+*; *srpHemo-Gal4*, *srpHemo-H2A::3xm-Cherry/+*, Control 3: *w/y,w[1118]; P{attP,y[+],w[3']}*; *srpHemo-Gal4*, *srpHemo-H2A::3xm-Cherry/+*, CG9331 RNAi 3 (GR/HPR):

UAS-Dicer2/ w-; 64652/+; srpHemo-Gal4, srpHemo-H2A::3xm-Cherry/+. **Fig. 3E:** Control 1: w/y,w[1118]; P{attP,y[+],w[3']}; srpHemo-Gal4, srpHemo-H2A::3xm-Cherry/+, CG7144 RNAi 1 (LKR/SDH): UAS-Dicer2/ w-; v51346/+; srpHemo-Gal4, srpHemo-H2A::3xm-Cherry/+, **Control 2:** w/y,w[1118]; P{attP,y[+],w[3']}; srpHemo-Gal4, srpHemo-H2A::3xm-Cherry/+, CG7144 RNAi 2 (LKR/SDH): UAS-Dicer2/ w-; v109650/+; srpHemo-Gal4, srpHemo-H2A::3xm-Cherry/+. **Figs. 3E-F:** Control: w-; +; srpHemo-H2A::3xmCherry, mutant: w-; atossa^{BG02278}; srpHemo-H2A::3xmCherry, Rescue: w-; atossa^{BG02278}; UAS-atossa::FLAG::HA, srpHemo-Gal4, srpHemo-H2A::3xmCherry, Rescue: w-; atossa^{BG02278}; UAS-grhpr::FLAG::HA, srpHemo-Gal4, srpHemo-H2A::3xmCherry, Rescue: w-; atossa^{BG02278}; UAS lkrsdh::FLAG::HA, srpHemo-Gal4, srpHemo-H2A::3xmCherry

Fig. S3F: Control 1: w/y,w[1118]; P{attP,y[+],w[3']}; srpHemo-Gal4, srpHemo-H2A::3xm-Cherry/+, CG2137 RNAi 1 (Gpo2): w-/y,w[1118]; v41234/+; srpHemo-Gal4, srpHemo-H2A::3xm-Cherry/+, Control 2: w/y,w[1118]; P{attP,y[+],w[3']}; srpHemo-Gal4, srpHemo-H2A::3xm-Cherry/+, CG2137 RNAi 2 (Gpo2): w-/y,w[1118]; 68145/+; srpHemo-Gal4, srpHemo-H2A::3xm-Cherry/+. **Fig. S3G:** Control 1: w/y,w[1118]; P{attP,y[+],w[3']}; srpHemo-Gal4, srpHemo-H2A::3xm-Cherry/+, CG11061 RNAi 1 (GM130): w-/y,w[1118]; v330284/+; srpHemo-Gal4 UAS-GFP, UAS-H2A::RFP/+, Control 2: w/y,w[1118]; P{attP,y[+],w[3']}; srpHemo-Gal4, srpHemo-H2A::3xm-Cherry/+, CG11061 RNAi 2 (GM130): w-/y,w[1118]; 64920/+; srpHemo-Gal4, srpHemo-H2A::3xm-Cherry/+. **Fig. S3H:** Control 1: w/y,w[1118]; P{attP,y[+],w[3']}; srpHemo-Gal4, srpHemo-H2A::3xm-Cherry/+, CG12505 RNAi 1 (Arc1): w-/y,w[1118]; v31123/+; srpHemo-Gal4, srpHemo-H2A::3xm-Cherry/+, CG12505 RNAi 2 (Arc1): w-/y,w[1118]; v109141/+; srpHemo-Gal4 UAS-GFP, UAS-H2A::RFP/+

Control 2: w/y,w[1118]; P{attP,y[+],w[3']}; srpHemo-Gal4, srpHemo-H2A::3xm-Cherry/+, CG12505 RNAi 3 (Arc1): w-/y,w[1118]; 25954/+; srpHemo-Gal4, srpHemo-H2A::3xm-Cherry/+. **Fig. S3I:** Control 1: w/y,w[1118]; P{attP,y[+],w[3']}; srpHemo-Gal4, srpHemo-H2A::3xm-Cherry/+, CG3752 RNAi 1 (Aldh): w-/y,w[1118]; 34989/+; srpHemo-Gal4, srpHemo-H2A::3xm-Cherry/+, Control 2: w/y,w[1118]; P{attP,y[+],w[3']}; srpHemo-Gal4, srpHemo-H2A::3xm-Cherry/+, CG3752 RNAi 2 (Aldh): w-/y,w[1118]; 68084/+; srpHemo-Gal4, srpHemo-H2A::3xm-Cherry/+. **Fig. S3J:** Control 1: w/y,w[1118]; P{attP,y[+],w[3']}; srpHemo-Gal4, srpHemo-H2A::3xm-Cherry/+, CG8780 RNAi 1 (Teyrha-meyrha): w-/y,w[1118]; 24067/+; srpHemo-Gal4, srpHemo-H2A::3xm-Cherry/+, Control 2: w/y,w[1118]; P{attP,y[+],w[3']}; srpHemo-Gal4, srpHemo-H2A::3xm-Cherry/+, CG8780 RNAi 2 (Teyrha-meyrha): w-/y,w[1118]; v28947/+; srpHemo-Gal4, srpHemo-H2A::3xm-Cherry/+. **Fig. S3K:** Control 1: w/y,w[1118]; P{attP,y[+],w[3']}; srpHemo-Gal4, srpHemo-H2A::3xm-Cherry/+, CG5005 RNAi 1 (HLH54F): w-/y,w[1118]; v13725/+; srpHemo-Gal4, srpHemo-H2A::3xm-Cherry/+, Control 2: w/y,w[1118]; P{attP,y[+],w[3']}; srpHemo-Gal4, srpHemo-H2A::3xm-Cherry/+, CG5005 RNAi 2 (HLH54F): w-/y,w[1118]; v103965/+; srpHemo-Gal4, srpHemo-H2A::3xm-Cherry/+, Control 3: w/y,w[1118]; P{attP,y[+],w[3']}; srpHemo-Gal4, srpHemo-H2A::3xm-Cherry/+, CG5005 RNAi 3 (HLH54F): w-/y,w[1118]; v28698/+; srpHemo-Gal4,

srpHemo-H2A::3xm-Cherry/+, CG5005 RNAi 4 (HLH54F): *w-/y,w[1118]*; *v65244/+*; *srpHemo-Gal4, srpHemo, H2A::3xm-Cherry/+*

Figure 4 and Figure 4S

Fig. 4A: *w-/+*; *UAS-porthos::FLAG::HA, srpHemo-Gal4, srpHemo::3xmCherry* . **Figs. 4B-H:** Control: *w/y,w[1118]*; *P{attP,y[+],w[3']}*; *srpHemo-Gal4, srpHemo-H2A::3xm-Cherry/+*, CG9253 (*porthos*) RNAi: *w-; v36589/+*; *srpHemo-Gal4, srpHemo-H2A::3xm-Cherry/+*. **Figs. 4I-J:** Control: *w-; +*; *srpHemo-H2A::3xmCherry*, mutant: *w-; atossa^{BG02278}*; *srpHemo-H2A::3xmCherry* , Rescue: *w-; atossa^{BG02278}*; *UAS-atossa::FLAG::HA, srpHemo-Gal4, srpHemo-H2A::3xmCherry* , Rescue: *w-; atossa^{BG02278}*; *UAS-porthos::FLAG::HA, srpHemo-Gal4, srpHemo-H2A::3xmCherry*

Figs. 4SC-H: Control: *w/y,w[1118]*; *P{attP,y[+],w[3']}*;/+; *srpHemo-Gal4, srpHemo-H2A::3xm-Cherry/+*, **CG9253** (*porthos*) RNAi: *w-; v36589/+*; *srpHemo-Gal4, srpHemo-H2A::3xm-Cherry/*

Figure 6 and Figure 6S

Fig. 6C-F: Control: *w-; +*; *srpHemo-Gal4, srpHemo-H2A::3xmCherry*, Dominant negative inhibitor of Complex V (CV-DN): *w-;UAS-CV DN*; *srpHemo-Gal4, srpHemo-H2A::3xmCherry*.

Figs. 6G-H: Control: *w-; P{attP,y[+],w[3']}*;/+; *srpHemo-Gal4, srpHemo-H2A::3xmCherry* , Complex III (Cyt-c1, CG4769) RNAi 1: *w-; RNAi (v109809)/+*; *srpHemo-Gal4, srpHemo-H2A::3xmCherry*, Complex III (UQCR-cp1, CG3731) RNAi 2: *w-; RNAi (v101350)/+*; *srpHemo-Gal4, srpHemo-H2A::3xmCherry*, Complex III (UQCR-cp2, CG4169) RNAi 3: *w-; RNAi (v100818)/+*; *srpHemo-Gal4, srpHemo -H2A::3xmCherry*, Complex V (ATP synthase F1F0, CG3612) RNAi: *w-; RNAi (v34664)/+*; *srpHemo-Gal4, srpHemo-H2A::3xmCherry*. **Fig. 6J:** Control: *+/+;srpHemo-Gal4, srpHemo-3xmCherry*, *atos* mutant: *w-; atossa^{BG02278}*; *srpHemo-Gal4, srpHemo-3xmCherry*, Control: *w/y,w[1118]*; *P{attP,y[+],w[3']}*;/+; *srpHemo-Gal4, srpHemo-3xmCherry/+*, CG9253 (*porthos*) RNAi: *w-; v36589/+*; *srpHemo-Gal4, srpHemo-3xmCherry/+*, Control: *w-; +*; *srpHemo-Gal4, srpHemo-3xmCherry*, CV-DN: *w-;UAS-CV DN*; *srpHemo-Gal4, srpHemo-3xmCherry*

Fig. 6SF: Control: *w-; P{attP,y[+],w[3']}*;/+; *srpHemo-Gal4, srpHemo-H2A::3xmCherry* , Complex III (Cyt-c1, CG4769) RNAi 1: *w-; RNAi (v109809)/+*; *srpHemo-Gal4, srpHemo-H2A::3xmCherry*, Complex III (UQCR-cp1, CG3731) RNAi 2: *w-; RNAi (v101350)/+*; *srpHemo-Gal4, srpHemo-H2A::3xmCherry*, Complex III (UQCR-cp2, CG4169) RNAi 3: *w-; RNAi (v100818)/+*; *srpHemo-Gal4, srpHemo -H2A::3xmCherry*, Complex V (ATP synthase F1F0, CG3612) RNAi: *w-; RNAi (v34664)/+*; *srpHemo-Gal4, srpHemo-H2A::3xmCherry*. **Figs. 6SG-H:** *+/+;srpHemo-Gal4, srpHemo-3xmCherry, atos* mutant: *w-; atossa^{BG02278}*; *srpHemo-Gal4, srpHemo-3xmCherry*, Control: *w/y,w[1118]*; *P{attP,y[+],w[3']}*;/+; *srpHemo-Gal4, srpHemo-3xmCherry/+*, CG9253 (*porthos*) RNAi: *w-; v36589/+*; *srpHemo-Gal4, srpHemo-3xmCherry/+*, Control: *w-; +*; *srpHemo-Gal4, srpHemo-3xmCherry*, CV-DN: *w-;UAS-CV DN*; *srpHemo-Gal4, srpHemo-3xmCherry*

Figures 7 and S7:

Figs. 7B-H, SB-I: Control: *w-; +; srpHemo-3xmCherry*, mutant: *w-; atossa^{BG02278}; srpHemo-3xmCherry*

Table 1. The enriched expression of FAM214A and FAM214B genes, the vertebrate orthologs of *Drosophila* Atossa, in vertebrate human immune cells.

Gene	Tissue/cell type	Description	Expression data	Source
FAM214A	Plasmacytoid dendritic cells (DCs)	Low cell type specificity	RNA Seq	The Human Protein Atlas https://www.proteinatlas.org/ENSG00000047346-FAM214A/blood
	Dendritic cells (DC.DC6.123+.Bl)	Human population Avg gene expression	Population RNA Seq	Immune Cell Atlas http://immunecellatlas.net/ICA_Skyline.php?gene=FAM214A&celltype=all&organ=Blood&datatype=rnaseq&scale=Local
	Plasma B cells (B.PC)	High expression, score 6859	RNA Seq	Immgen http://rstats.immgen.org/Skyline/skyline.html
	Regulatory T cells (Cd4+, Cd25+)	score 4.57	Microarray	BioGPS http://biogps.org/#goto=genereport&id=56204
FAM214B	Neutrophils	Cell type enhanced (neutrophil)	RNA Seq	The Human Protein Atlas https://www.proteinatlas.org/search/FAM214b
	Blood monocytes (Mo.16+.Bl, CD16+)	Human population Avg gene expression	Population RNA Seq	Immune Cell Atlas http://immunecellatlas.net/ICA_Skyline.php?gene=SLC10A2&celltype=all&organ=Blood&datatype=rnaseq&scale=Local
	Neutrophils Thio-induced peritoneal neutrophils (GN.Thio.PC)	High>800 High expression, score 802	RNA Seq	Immgen http://rstats.immgen.org/Skyline/skyline.html
	Neutrophils	score 4.81	Microarray	BioGPS http://biogps.org/#goto=genereport&id=80256

Table S1. Fly lines utilized in this paper.

Experimental models: organisms/Strains			
Designation	Source of reference	Identifiers	Additional information
<i>srpHemo-Gal4</i>	PMID: 15239955	Brückner et al., 2004	<i>D. melanogaster</i>
<i>srpHemo-3xmCherry</i>	PMID: 29321168	RRID:BDSC_78358 and 78359	<i>D. melanogaster</i> (Gyoergy et al., 2018)
<i>srpHemo-H2A::3xmCherry</i>	PMID: 29321168	RRID:BDSC_78360 and 78361	<i>D. melanogaster</i> (Gyoergy et al., 2018)
<i>CG9005</i> ^{BG02278}	Bloomington <i>Drosophila</i> Stock Center (BDSC),	RRID:BDSC_12768	
<i>Df(2R)ED2222</i>	BDSC		
<i>Df(2R)BSC259</i>	BDSC		
<i>UAS-CG9005 RNAi 1</i>	(VDRC), RRID	VDRC: v106589	
<i>UAS-CG9005 RNAi 2</i>	(VDRC), RRID	VDRC: v36080	
<i>UAS-CG9005 RNAi 3</i>	(BDSC), RRID:BDSC_33362	33362	
<i>srpHemo-HA::CG9005 (srpHemo-HA::atossa)</i>	this paper		CG9005 amplified from genome cloned into DSPL172 (PMID: 29321168)
<i>srpHemo-HA::atossa</i> ^{nl51-}	this paper		CG9005 amplified from genome cloned into DSPL172
<i>srpHemo-HA::atossa</i> ^{DUF2410-}	this paper		CG9005 amplified from genome cloned into DSPL172
<i>srpHemo-HA::atossa</i> ^{ChrSeg-}	this paper		CG9005 amplified from genome cloned into DSPL172
<i>srpHemo-HA::atossa</i> ^{DUF2410-/ChrSeg-}	this paper		CG9005 amplified from genome cloned into DSPL172
<i>srpHemo-HA::atossa</i> ^{TAD1-}	this paper		CG9005 amplified from genome cloned into DSPL172
<i>srpHemo-HA::atossa</i> ^{TAD2-}	this paper		CG9005 amplified from genome cloned into DSPL172 (PMID: 29321168)
<i>srpHemo-HA::atossa</i> ^{TAD1-/TAD2-}	this paper		CG9005 amplified from genome cloned into DSPL172
<i>srpHemo-FAM214A</i>	this paper		FAM214A amplified from dendritic cell cDNA library cloned into <i>srpHemo</i> plasmid (DSPL172)
<i>srpHemo-FAM214B</i>	this paper		FAM214B amplified from dendritic cell

			cDNA library cloned into <i>srpHemo</i> plasmid (DSPL172)
<i>UAS-HA::EGFP</i>	this paper		
<i>UASRpl30WTTOP-HA::EGFP</i>	this paper		
<i>UASRpl30mutTOP-HA::EGFP</i>	this paper		
<i>UAS-CG9253 RNAi (porthos)</i>	VDRC, RRID:	VDRC: v36589	
<i>UAS-CG9331 RNAi 1 (GRHPR)</i>	(VDRC), RRID:	VDRC: v44653	
<i>UAS-CG9331 RNAi 2 (GRHPR)</i>	BDSC, RRID:	BDSC: 64652	
<i>UAS-CG9331 RNAi 3 (GRHPR)</i>	(VDRC), RRID:	VDRC: v107680	
<i>UAS-CG7144 RNAi 1 (LKRS DH)</i>	(VDRC), RRID:	VDRC: v51346	
<i>UAS-CG7144 RNAi 2 (LKRS DH)</i>	(VDRC), RRID:	VDRC: v109650	
<i>UAS-CG2137 RNAi 1 (Gpo2)</i>	(VDRC), RRID:	VDRC: v1234	
<i>UAS-CG2137 RNAi 2 (Gpo2)</i>	BDSC, RRID:	BDSC: 68145	
<i>UAS-CG11061 RNAi (GM130)</i>	BDSC, RRID:	BDSC: 64920	
<i>UAS-CG11061 RNAi (GM130)</i>	(VDRC), RRID:	VDRC: v330284	
<i>UAS-CG12505 RNAi 1 (Arc1)</i>	(VDRC), RRID:	VDRC: v109141	
<i>UAS-CG12505 RNAi 2 (Arc1)</i>	(VDRC), RRID:	VDRC: v31123	
<i>UAS-CG12505 RNAi 3 (Arc1)</i>	BDSC, RRID:	BDSC: 25954	
<i>UAS-CG3752 RNAi 1 (Aldh)</i>	BDSC, RRID:	BDSC: 68084	
<i>UAS-CG3752 RNAi 2 (Aldh)</i>	BDSC, RRID:	BDSC: 34989	
<i>UAS-CG8780 RNAi 1 (Teyrha-meyrha)</i>	(VDRC), RRID:	VDRC: v28947	
<i>UAS-CG8780 RNAi 2 (Teyrha-meyrha)</i>	BDSC, RRID:	BDSC: 24067	
<i>UAS-CG5005 RNAi 1 (HLH54F)</i>	(VDRC), RRID:	VDRC: v13725	
<i>UAS-CG5005 RNAi 2 (HLH54F)</i>	(VDRC), RRID:	VDRC: v103965	
<i>UAS-CG5005 RNAi 3 (HLH54F)</i>	BDSC, RRID:	BDSC: 65244	
<i>UAS-CG5005 RNAi 4 (HLH54F)</i>	BDSC, RRID:	BDSC: 28698	
<i>y[-] v[-];attP40-pVALIUM22-UAS-ATPsyn Subunit C (CG1746) E121Q</i>	(VDRC), RRID:	Thomas Hurd, et al., 2016	

<i>UAS-CG4769 RNAi 1 (Cyt-c1)</i>	(VDRC), RRID:	VDRC: v109809	
<i>UAS-CG4169 RNAi 2 (UQCR-cp2)</i>	(VDRC), RRID:	VDRC: v100818	
<i>UAS-CG3731 RNAi 3 (UQCR-cp1)</i>	(VDRC), RRID:	VDRC: v101350	
<i>UAS-CG3612 RNAi (ATP synthase F1F0)</i>	(VDRC), RRID:	VDRC: v34664	

Table S2. The DNA plasmid constructs utilized in gene construction.

Recombinant DNA			
Designation	Source of reference	Identifiers	Additional information
<i>UAS-CG9005::FLAG::HA</i>	<i>Drosophila</i> Genomics Resource Center	DGRC: UFO03339 Flybase: FBgn0033638	atossa
<i>UAS-CG9253::FLAG::HA</i>	<i>Drosophila</i> Genomics Resource Center	DGRC: UFO12394 Flybase: FBgn0032919	porthos
<i>UAS-CG9331::FLAG::HA</i>	<i>Drosophila</i> Genomics Resource Center	DGRC: UFO02643 Flybase: FBgn0032889	Glyoxylate reductase (NADP(+)) Hydroxypyruvate reductase (GR/HPR)
<i>UAS-CG7144::FLAG::HA</i>	<i>Drosophila</i> Genomics Resource Center	DGRC: UFO05689 Flybase: FBgn0286198	Lysine reductase/saccharopine dehydrogenase (LKRS DH)
<i>pAC-sgRNA-Cas9</i>	Addgene	Addgene: 49330	49330 (DSPL 232)

Table S3. Oligonucleotides utilized in gene construction.

No.	Name	Sequence
1	FP-CG9005	TAGAAGCTTCTGCAAATGATACCGACAAGCGTCACC
2	RP-CG9005	GTGCCTAGGCGCGCCCTAAATCCTGCCGCGCT
3	FP-HACG9005	TAGAAGCTTCTGCAAATGTACCCATACGATGTTCCAGATTACGCTGCCGCC GCCATGATACCGACAAGCGTCACC
4	RP-HACG9005	GTGCCTAGGCGCGCCAGCGTAATCTGGAACATCGTATGGGTAGGCGGCGG CAATCCTGCCGCGCTCTC
5	infPCG9005_NotI BluS	ACCGCGGTGGCGGCCATGTACCCATACGATGTTCCAG

6	infRPCG9005_NotIBluS	CGAAGTTATGCGGCCCTAAATCCTGCCGCGCTC
7	FP-DUF2410·CG9005	TTGTGCGAGATTCGTTTGCCG
8	RP-DUF2410·CG9005	AACGGACGTCCTCCAAATTGAG
9	FP-ChrSeg·CG9005	AGTGCGCGACAGGAGAGC
10	RP- ChrSeg -CG9005	AGTCGCTTCATCTGCTCGG
13	FP-FAM214A-V13	ATGAAGCCAGACCGAGATGC
14	RP-FAM214A	TCAACATCTTGGTGAAAACCTGAG
15	infFP-FAM214A-V13	TAGAAGCTTCTGCAAATGAAGCCAGACCGAGATGC
16	infRP-FAM214A	GTGCCTAGGCGCGCCTCAACATCTTGGTGAAAACCTG
17	PF-FAM214B	GGCTTCATGCGCCACGTG
18	RP-FAM214B	CGATCAGGGCAAAGGTGAATAACG
19	infFP-FAM214B	TAGAAGCTTCTGCAAGGCTTCATGCGCCACGTG
20	infRP-FAM214B	GTGCCTAGGCGCGCCCGATCAGGGCAAAGGTGA
21	Insitu-CG9005 FP1	CCTCCTGGGCTCGGCTACTGC
22	Insitu-CG9005 RP1	GATAATACGACTCACTATAGGGTTGACGTTGGGAAAATT
23	Insitu-CG9005 RP2	GATAATACGACTCACTATAGGGTTTGCAAAGTTGTGCT
24	Insitu-CG9253 FP1	GGAAAGATCTCGGTCTCAATGAG
25	Insitu-CG9253 RP1	GATAATACGACTCACTATAGGGCCATCACCTCATCCTCC
26	sgRNA-F1-CG9005	TTCG GCAGTCGGATGTCCGTATGCAGG
27	sgRNA-R1-CG9005	AACGCATACGGACATCCGACTGC C
28	sgRNA-F2-CG9005	TTCGCAGTTCGTAGAAGTAAGAGACGG
29	sgRNA-R2-CG9005	AACTCTTACTTCTACGAACTG C
30	sgRNA-F3-CG9005	TTCGCGGCGGATTCTGTCCCACCCAGG
31	sgRNA-R3-CG9005	AACGGGTGGGACAGAATCCGCCG C
32	sgRNA-F1-CG9253	TTCGGATCCAACGTGAGGCCATTCCGG
33	sgRNA-R1-CG9253	AACGAATGGCCTCACGTTGGATC C
34	sgRNA-F2-CG9253	TTCGGGCCATTCCGGTCGCTTACAGG
35	sgRNA-R2-CG9253	AACGTAAGGCGACCGGAATGGCC C

36	sgRNA-F3-CG9253	TTCGCCCTCGTGGGGGTTAGCACGAGG
37	sgRNA-R3-CG9253	AACCGTGCTAACCCCCACGAGGG C
38	infNotI-TCHA-EGFPHA-FP	AACAGATCTGCGGCCGCATGTGTTGCCCGGGCTGCTGT
39	infNotI-TCHA-EGFP-RP	CCTCGAGCCGCGGCCGCTTAAGCGTAATCTGGCACATC
40	CG9005qPCR-FP1	TGTTACAGATTCTCGCCACCA
41	CG9005qPCR-RP1	TGAGGATTTGCCAGCTGTT
42	CG9005qPCR-FP2	GCACGCCTTATTTGTGCGAG
43	CG9005qPCR-RP2	CCCGCATGTCGTAGGGTATC
44	CG9005qPCR-FP3	TATGCGGCAGGGAGAAAAGTT
45	CG9005qPCR-RP3	GTGGTCTCTTCTGTCCACCG
46	CG9253qPCR-FP1	GCCTTACAGGGCAAGGATGT
47	CG9253qPCR-RP1	ATGCCAATCCCGCTACCAAG
48	CG9253qPCR-FP2	TCTAGGTAGCGAGGAGGAGC
49	CG9253qPCR-RP2	TGGCCTCACGTTGGATCTTC
50	CG9253qPCR-FP3	TTCGACCACGTGCTGCTATT
51	CG9253qPCR-RP3	TTGTAGCTGCGTCTGTTTCGT
52	RpL32 qPCR-FP	AGCATACAGGCCCAAGATCG
53	RpL32 qPCR-RP	TGTTGTGATACCTTGGGC
54	RpS20 qPCR-FP	ACGGTGCAAAGAACCAGAACT
55	RpS20 qPCR-RP	GGAGTCTTACGGGTGGTGATG
56	pAC-sgRNA-Cas9-U6F	TTTGATTCTAAAGGAAATTTGAAAA

Table S4: List of key resources used in this paper.

Antibodies			
Designation	Source of reference	Identifiers	Additional information
Chicken polyclonal anti-GFP	Aves Labs	Cat# GFP-1020, RRID:AB_10000240	
Rat monoclonal anti-HA	Roche	Roche Cat# 3F10, RRID: AB_2314622	
Mouse Lamin (lamin Dm0)	Drosophila Studies Hybridoma Bank (DSHB)	Cat#ADL1010	

Mouse Fibrillarlin	Rangan's lab		N/A	
Goat anti-Chicken IgY (H+L) Secondary Antibody, Alexa Fluor 488	Thermo Scientific	Fisher	Cat# A-11039, RRID: AB_2534096	
Alexa Fluor 488 goat anti-rat	Thermo Scientific	Fisher	Cat# A21212, RRID: AB_11180047	
Goat anti-Mouse IgG1 Secondary Antibody, Alexa Fluor 488 conjugate	Thermo Scientific	Fisher	Cat# A-21121, RRID: AB_2535764	
Goat anti-Mouse IgG2b Secondary Antibody, Alexa Fluor 633 conjugate	Thermo Scientific	Fisher	Cat# A-21146, RRID:AB_2535782	
Goat anti-Rabbit IgG (H+L) Secondary Antibody, Alexa Fluor 488 conjugate	Thermo Scientific	Fisher	Cat# R37116, RRID: AB_2556544	
Phalloidin 488	Thermo Scientific	Fisher	Cat# A12379, RRID:AB_2315147	
Phalloidin 633	Thermo Scientific	Fisher	Cat# 50-6559-05, RRID:AB_2574272	

Chemicals				
Vectashield mounting medium	Vector Laboratories, RRID:SCR_000821		VectorLabs: H-1000	
Vectashield Mounting medium with DAPI	Vector Laboratories, RRID:SCR_000821		VectorLabs: H-1200	
Beckman Coulter 9/16x3.5 PA tubes			Cat. #331372	

Critical Commercial Assays				
Infusion cloning kit	Clontech's European distributor		Cat# ?	
MEGAscript_ T7 Transcription Kit	Thermo Scientific	Fisher	Cat#AM1334	

MEGAscript_ T3 Transcription Kit	Thermo Fisher Scientific	Cat#AM1338	
Effectene Tranfection Reagent kit	Qiagen, Hilden, Germany		
DNeasy Blood & Tissue Kit	Qiagen, Hilden, Germany		
QIAGEN Rneasy Mini Kit	Qiagen, Hilden, Germany	Cat#74104	
Takyon™ No Rox SYBR MasterMix blue dTTP	Eurogentec, Liege, Belgium		
TURBO DNA-free Kit	Life Technologies	Cat# AM1907	
Agilent Seahorse XF Cell Mito Stress Test kit	Agilent Technologies, Inc., Santa Clara, CA, USA	Cat# 103015-100	
Agilent 6000 Pico kit	Agilent Technologies, Waldbronn, Germany	Cat#5067-1513	

Table S5. List of software tools, analytical packages, and laboratory devices utilized in this paper.

Software and Algorithms		
Designation	Source of reference	Identifiers
ImageJ/FIJI		http://fiji.sc/ RRID:SCR_002285)
Imaris	Bitplane	http://www.bitplane.com/Imaris/Imaris , RRID:SCR_007370
Matlab	Mathworks	https://www.mathworks.com/products/matlab.html , RRID:SCR_001622
FlowJo		https://www.flowjo.com/RRID:SCR_008520
LaVision ImSpector	LaVision BioTec	http://www.lavisionbiotec.com/ , RRID:SCR_015249
Proteome Discoverer 1.4		https://www.thermofisher.com/order/catalog/product/OPTON-30795 , RRID:SCR_014477
LightCycler 480 software (v. 1.5)	Roche Diagnostics	https://lifescience.roche.com/en_at/products/lightcycler14301-480-software-version-15.html
9 aaTAD Prediction Tool		https://www.med.muni.cz/9aaTAD/analysis.php#matches
Conserved Domain Architecture Retrieval Tool (CDART) program		https://www.ncbi.nlm.nih.gov/Structure/93exington/93exington.cgi
Conserved Domain Database (CDD)		https://www.ncbi.nlm.nih.gov/Structure/cdd/wrpsb.cgi
Prism	GraphPad	https://www.graphpad.com/scientific-software/prism/ RRID:SCR_002798
Flyrnai	sgRNA design	https://www.flyrnai.org/crispr/ http://tools.flycrispr.molbio.wisc.edu/targetFinder/
Infusion primer tool	Clontech website	http://bioinfo.clontech.com/infusion/convertPcrPrimersInit.do
HISAT2		https://ccb.jhu.edu/software/hisat2/index.shtml Kim et al., 2015
CAGE		
MEME Suite		http://meme-suite.org/doc/overview.html Bailey et al., 2009
Homer (v4.10.4)		http://homer.ucsd.edu/homer/

Others		
Designation	Source of reference	Identifiers
Nikon Eclipse Ti Inverted widefield Microscope	Nikon	https://www.nikoninstruments.com/en_EU/Products/Inverted-Microscopes/Eclipse-Ti-E
Zeiss LSM 800 Confocal Microscope	Zeiss	https://www.zeiss.com/microscopy/us/products/confocal-microscopes.html
LaVision 2-Photon Inverted Microscope	LaVision BioTec	http://www.lavisionbiotec.com/products/trim-scope-ii-1.html
YSI Stretch membranes	YSI	https://www.ysi.com/Accessory/id-066155/Membranes-10-Pack-Standard
LightCycler 480	Roche Diagnostics	Idaho Technology Inc., Salt Lake City, UT, USA.
FACS Aria III (BD) flow cytometer		
Leica SP8 FALCON inverted confocal	WLL, FALCON, Leica	https://www.leica-microsystems.com/products/confocal-microscopes/p/dive/
Beckman L7 ultracentrifuge	Beckman Coulter, Krefeld, Germany	

3. FUTURE DIRECTION

The research I have described in last chapter provoked many exciting questions. Here, I am discussing some of them, including some supplemental projects that I have already conducted in the lab and topics that would be intriguing to investigate in future.

3.1. More investigation on Atossa's molecular function(s)

Atossa (CG9005) regulates the initiation of tissue invasion of macrophages. As RNA sequencing data reveals, Atossa enhances the RNA levels of target genes, mainly helicase Porthos and metabolic enzymes, including GR/HPR and LKR/SDH. Each of these targets is also required in immune cells for tissue infiltration (Chapter 3, Figures 3, & 4). The absence of Atossa leads to higher RNA levels of a set of genes, which themselves showed a stimulating effect on macrophage migration, possibly through compensatory mechanisms.

1. Is Atossa a transcription factor (TF) or indirect binding partner of TFs?

Nuclear Atossa is predicted to contain two 9 amino acid transactivation domains (9aaTADs), including 9aaTAD 1 (172 ELVSLAIND 180) and 9aaTAD2 (1148 GTVQATLLN 1156) (<https://www.med.muni.cz/9aaTAD/analysis.php#matches>). 9aaTADs are universally recognized by the transcriptional machinery in eukaryotes (Raj et al., 2017, Piskacek et al., 2016). These conserved domains have been found in well-characterized transcription activators/suppressors, including p53 (Lemon and Tjian, 2000; Raj et al., 2017), *Drosophila* Yorkie and YAP transcriptional co-activator (Zhang et al., 2012), and the forkhead box (FOX) transcription factor family (Ma et al., 2005; Laissue, 2019), which are the conserved regulators of histone modification, chromatin remodeling, tissue growth, cell proliferation, migratory behavior, and tumorigenesis (Lemon and Tjian, 2000; Raj et al., 2017). Our results showed that deletion of Atossa's conserved TADs blocked its function in macrophages, indicating their functional importance for the tissue invasion of immune cells (Chapter 3, Figure 2).

It still needs to be determined if Atossa exerts its stimulating effect on macrophage invasion, directly or indirectly, through the recruitment and transcriptional activation or suppression of transcriptional regulators. The first step would be to perform a comprehensive and/or detailed analysis of DNA binding sites to identify genes directly targeted by Atossa's TADs using ChIP seq and ChIPchip analyses, and examine if these are the same targets as in our RNA sequencing result.

2. How does Atossa control the eventual level of transcripts?

Gene regulation is an exquisitely complex and multifaceted process that operates at all stages of gene expression, ranging from pre-transcriptional chromatin remodeling to the post-translational modification of proteins. RNA concentration is mediated not only by the transcription rate, but also by posttranscriptional regulation, including mRNA stability and degradation. Furthermore, mRNA stability control is independent of transcriptional

initiation, which is influenced by chromatin states (Maekawa et al., 2015). Therefore, a dynamic equilibrium between mRNA transcription and RNA decay determines the final mRNA levels. RNA-degradation mechanisms allow rapid up or downregulation of gene expression in response to environmental changes (Yamada et al., 2018; Blumberg et al., 2019)

Our RNA sequencing results can only indicate that *Atossa* enhances the eventual transcript levels of candidates. As mentioned before, mRNA abundance does not necessarily correlate with their transcription rates. Therefore, it is possible that *Atossa*, besides potential effects on chromatin modification or transcription, may have post-transcriptional regulatory effects, for instance on mRNA half-lives or mRNA halting (Maekawa et al., 2015; Blumberg et al., 2019). As a proposed assay, integration of CHIP-seq, RNA-seq and RNA half-life data would be a fascinating strategy to identify genes that may undergo post-transcriptional regulation.

3. Do *Atossa* and its metabolic enzyme, LKR/SDH, have any possible impact on epigenetic regulation in immune cells?

Epigenetics describes heritable traits, like chromatin remodeling, that arise without changes in DNA sequence. Metabolic reprogramming has a significant impact on the epigenetic remodeling of immune cells, either through epigenetic modification enzymes or by providing key metabolites as substrates or inhibitors of these enzymes. α -Ketoglutarate (α -KG), an important intermediate of the Krebs cycle, epigenetically affects immune cells through modulation of α -KG-dependent Histone demethylases (Lio and Huang, 2020; Britt, et al., 2020). *Atossa* might have various regulatory effects with consequences that extend beyond changes in ATP levels. The level of α -KG and other Krebs cycle intermediates were significantly changed in *atossa* mutant embryos, suggesting that *Atossa* might maintain a balance in their cellular production and consumption (Chapter 3, Figure 7) and thus alter epigenetic modifications, including histone demethylation. Besides a catalytic role in lysine catabolism, which is important for histone modifications, *Atossa*'s metabolic enzyme target, dLKR/SDH, binds to ecdysone-regulated hormone receptor (Ecr/USP) as a nuclear cofactor and inhibits histone modification by Arginine methyltransferase CARMER (Cakouros, et al., 2008).

Therefore, it will be an interesting challenge to explore the potential direct and indirect effects of *Atossa*, and dLKR/SDH, on the global epigenetic landscapes of macrophages, for instance DNA and histone modifications, which could ultimately modulate their invasive properties at a specific time window, e.g. when macrophages initiate tissue invasion.

3.2. More exploration on Porthos' mechanism of function(s)

1. How does *Porthos* affect the translational efficiency of 5'TOPL mRNAs?

Atossa's target, *Porthos*, drives immune cell invasion mainly by activating the translational capacity of a specific subset of mRNAs, containing a terminal oligopyrimidine sequence, called the 5'TOPL motif (Chapter 3, Figure 5). In our case, many of the 5'TOPL mRNAs encode proteins involved in cellular energy production and metabolism as well as a few ribosomal proteins. Interestingly, *Porthos* 5'TOPL mRNAs were not identified as transcriptional targets of Atossa. Although the depletion of *porthos* mainly leads to a lower translation level of 5'TOPL mRNAs, it does not explain how almost only the translation of specific mRNAs is selectively altered.

Our data show that *Porthos* enhances the translational efficiency of mitochondrial genes, including specific mitochondrial ETC subunits, which supports the importance of upregulation of mitochondrial energy production for cell invasion. Macrophages, as well as S2 cells, preferably obtain their emerging energy demands by activating oxidative phosphorylation (Chapter 3, Figure 6). We can anticipate that this special metabolic state towards mitochondrial OXPHOS is preprogrammed in macrophages prior to germband entry, so that it guarantees sufficient energy for their long-term invasion across the energy demanding constraint tissues. It would be intriguing to know if macrophages exert a distinct metabolic adaptation in other tissues or in response to different signals.

2. Does *Porthos* regulate translation efficiency of its target mRNAs through a global or tissue-specific mechanism?

Our collaborators, Martin et al. (unpublished, 2020), have discovered that three uncharacterized *Drosophila* RNA helicases, named Aramis, Athos, and *Porthos*, are required for proper germline stem cell (GSC) differentiation *in vivo*. They have investigated the helicase Aramis in more detail. They observed that Aramis regulates the proper translation of 5'UTR TOPL mRNAs, which mostly include ribosomal proteins as well as, Novel Nucleolar protein 1 (Non1), a negative regulator of P53. It is proposed that Aramis promotes cell cycle progression via Non1-mediated repression of p53 as well as enhanced ribosome levels.

I have only found *Porthos*, not the two other helicases, among Atossa's transcriptional targets. Interestingly, downregulation of either Aramis or Athos by RNAi-expressing in macrophages leads to a similar defect in germband invasion (Figure 1). My data suggest that two other helicases are regulated in a different way at least in macrophages. We should test if these helicases, despite a potentially distinct upstream regulation, display their triggering impact on macrophage invasion through parallel or shared downstream pathways.

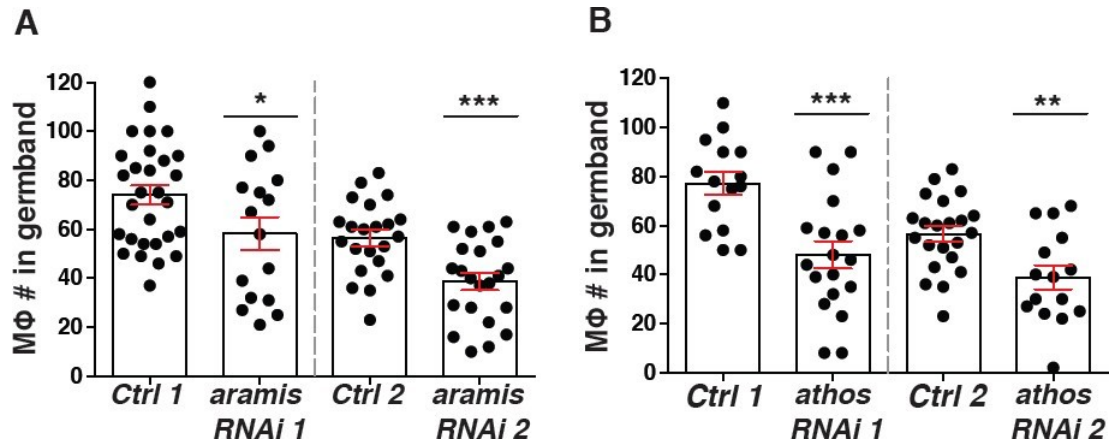


Figure 1: RNA helicases Aramis and Athos enhance germband tissue invasion of macrophages. Quantification of Stage 12 embryos indicates that fewer macrophages have moved into the germband upon the expression in macrophages of either of (A) two different RNAis against *aramis* (CG5589) or (B) two different RNAis against *athos* (CG4901), arguing that these helicase are required in macrophages for their tissue invasion. Control 1 n=29, *aramis* RNAi 1 (BL32334) n=16, p=0.03, Control 2 n=22, *aramis* RNAi 2 (VDRC 108642) n=22, p=0.006. Control 1 n=15, *athos* RNAi 1 (VDRC 51346) n=19, p=0.005, Control 2 n=22, *athos* RNAi 2 (VDRC 109650) n=15, p=0.003.

While Aramis' target mRNAs in the ovary mostly consist of ribosomal proteins and a negative regulator of p53, among Porthos' target mRNAs in macrophages we found only three ribosomal proteins, while a sizable portion are involved in mitochondrial and metabolic functions. Yet in the ovary and in macrophages knockdown of either helicases produces the same phenotype, lack of differentiation for the ovary, and lack of invasion in macrophages. Does Porthos regulate the same 5'TOPL mRNA targets in other tissues such as the germline? Interestingly, mitochondrial complex V, ATP synthase (Teixeira et al., 2015), a Porthos 5'TOPL mRNA target, are both required for proper GSC differentiation in the *Drosophila* ovary. Aramis' negative regulation of p53 promotes cell division in the ovary, however my data shows that increasing cell division suppresses macrophage invasion (Figure 2) arguing for a difference in Aramis' targets in different tissues. To begin to address this question one could conduct polysome profiling data on all three helicases in the germline and in S2 cells and check if there is any overlap among their polysome targets.

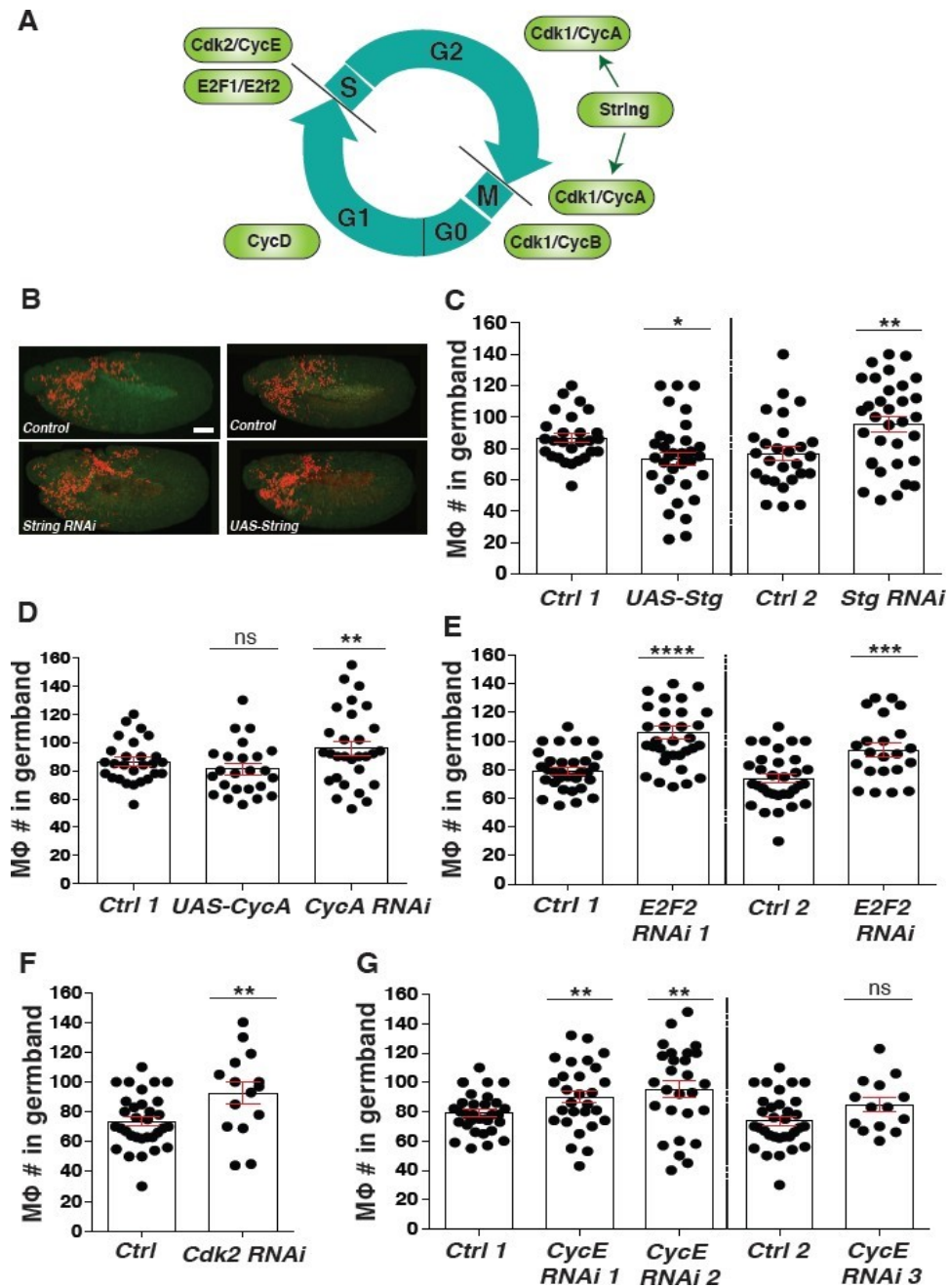


Figure 2: Increase of proliferation of macrophages attenuates their tissue invasion, while suppressing their cell division promotes tissue invasion. (A) Cell cycle and the check point regulators (B) Representative confocal images of Stage 12 embryos from Control, *srpHemo>string* RNAi (VDRC 330033), and *srpHemo>UASstring* (BL34958) expressing in macrophages. Macrophages (red) are visualized by *srpHemo-H2A::3xmCherry* expression. (C) Quantification in fixed early Stage 12 embryos shows that expression of *srpHemo>UASstring* (CG14228) in macrophages results in a significant decrease in the number of macrophages within the germband compared to the control. Whereas expression of *string* RNAi in macrophages significantly increased the number of macrophages within this tissue. Control 1 n=, *UAS-String* (BL34958) n=34, p=0.02; Control 2 n=27, *String* RNAi (VDRC 330033) n=33, p=0.006. (D) Quantification in fixed early Stage 12 embryos shows that expression of *srpHemo>cycA* RNAi in macrophages results in a significant decrease in the number of macrophages within the germband compared to the control. However, expression of *srpHemo>UAScycA* (CG5940) in macrophages didn't significantly change the number of macrophages within this tissue. Control 1 n=32; *UAS-String* (BL34958) n=24, p=0.02; *String* RNAi (VDRC 330033) n=29, p=0.6. (E-F) Quantification of Stage 12 embryos indicates that higher number of macrophages have moved into the germband upon the expression in macrophages of either of (F) two different RNAis against *E2F2* (CG) or (G) an RNAi against *Cdk2* (CG). Control 1 n=32, *E2F2* RNAi 1 (VDRC 45473) n=34, p<0.0001, Control 2 n=27, *E2F2* RNAi 2 (VDRC 100990) n=22, p=0.0005. Control n=32, *Cdk2* RNAi (VDRC 107680) n=15, p=0.007. (G) Quantification in fixed early Stage 12 embryos shows that expression of two independent RNAis against *CycE* (CG) in macrophages results in a significant increase in the number of macrophages within the germband compared to the control, while the third RNAi has a trend to increase macrophages moved into in this tissue. Control 1 n=32, *CycE* RNAi 1 (VDRC 47941) n=18, p=0.02, *CycE* RNAi 2 (VDRC 47942) n=27, p=0.007; Control 2 n=27, *CylE* RNAi 3 (VDRC 110204) n=14, p=0.06.

3. Does Porthos enhance the translational efficiency of 5'TOPL mRNAs independently or via the dTOR pathway?

We confirmed that Porthos, by enhancing 5'TOPL mRNA translation, regulates the translation of mitochondrial proteins and affects OXPHOS, although the precise mechanism by which Porthos acts has yet to be elucidated.

The 5'TOP sequence is a potent translational regulator that sensitizes the translation of the respective transcripts to metabolic conditions (Xie et al., 2021). Most 5'TOP mRNAs are ribosomal proteins and translational initiation factors, while recently some mitochondrial-related mRNAs have been also identified.

The mechanistic target of rapamycin (mTOR) is an evolutionarily conserved crucial signaling pathway controlling cellular metabolism. mTOR consists of two complexes, mTORC1 and mTORC2. The mTORC1 controls anabolic metabolism, including lipid, glutamine, and glucose metabolism, while it inhibits catabolic processes, namely, autophagy. mTORC2 influences cell survival, cytoskeletal organization, lipogenesis, and gluconeogenesis (Sarbasov et al., 2004).

In *Drosophila* it was shown that various mitochondrial genes possess a 5'pyrimidine-rich translational element (5'PRTE), which are important for enhanced TOR-mediated mRNA translation. dPRTE resembles the mammalian 5'TOP and the PRTE elements, which are also enriched within the 5'UTRs of mTOR-responsive mammalian mRNAs (Xie et al., 2021). Generally, many mTOR responsive genes have either a 5'TOP, 5'TOP-like or a PRTE, and many of them are associated with protein synthesis, metabolism, mitochondrial function and energy production as well as invasion (Hsieh et al., 2012; Thoreen et al., 2012). Interestingly, we observed an overlap between a number of Porthos 5'TOPL mRNAs (including subunits of mitochondrial complexes III and V, and mitochondrial transporter and ribosomal proteins) with mitochondrial-related mRNA targets shown in another study to have their translation controlled in a TOR-dependent manner in *Drosophila* (Zid et al., 2009). Such a similarity is intriguing, in a way to see if there is any possible commonality or link between Porthos and dTOR pathway on the regulation of 5'TOPL mRNAs, which are involved in energy maintenance? Or does the dTOR pathway have any, even an independent, regulatory function in the protein synthetic capacity of macrophages, required for their migration?

4. Does Porthos enhance translational efficiency of 5'TOPL mRNAs in a Larp-dependent manner?

Martin et al. showed *Drosophila* Larp protein binds 5'TOPL sequences, including Non1 and RpL30 TOPL sequences, to regulate their translational occupancy. Similar to mentioned RNA helicases, deletion of Larp in *Drosophila* ovaries also causes defects in the germline, indicating a germline-specific function. Nevertheless, a clear link between the helicase Aramis and Larp in the ribosome biogenesis of 5'TOPL mRNAs is still missing.

La-related proteins 1 (LARP1) is an evolutionarily conserved RNA binding protein that interacts with active eIF4F complex and mTORC1, as well as PABP and RNA and directly

regulates stability and translation of 5'TOP mRNAs (Tcherkezian et al., 2014). LARP1 regulates translation and stability of target mRNAs through their 5'TOP motif (Fonseca et al., 2015; Lahr et al., 2015; Aoki et al., 2013) and cap recognition. Mechanistically, LARP1 has a high affinity toward 5'TOP mRNAs, which selectively prevents the interaction of 5'TOP mRNAs with eIF4G/eIF4E by binding competition. Activated mTORC1 blocks the inhibitory function of LARP1 on translation (Lahr et al., 2017; Fonseca et al., 2015; Jin et al., 2020). It should be further clarified: (1) Is *Larp* also a translation regulator of 5'TOPL mRNAs in macrophages? If so (2) do helicase *Porthos* and *Larp* act together or in parallel to display their effect in our system?

5. What are the roles of other Porthos TOPL mRNA targets?

Besides TOPL mRNAs with mitochondrial and metabolic functions, we also found other categories of Porthos 5'TOPL mRNAs that are predicted to participate in Redox reactions, gene regulation, transcription, cytoplasmic protein translation and degradation, immune responses, and signal transduction. It would be interesting to see if these TOPL mRNAs are the primary or indirect targets of Porthos. Apparently many of these mRNAs require ATP for their function, suggesting that their translation capacity could be a response to the cellular ATP level, that itself may be tuned by the translation of TOPL mRNAs that encode for mitochondrial ETC. A possible experiment to evaluate this idea is to diminish ATP generation, either by genetic depletion or biochemical inhibition, and perform Polysome profiling assay, to compare any possible common transcripts to the ones we have already found for Porthos.

6. What would be the role of other mitochondrial aspects in macrophage migration?

Porthos triggers mitochondrial ATP production by enhancing the translational efficiency of mRNAs encoding mitochondrial ETC components, including subunits of complexes I, II, III, and V. Besides ETC components, Porthos has other mitochondrial-related TOPL mRNA targets, which are involved in mitochondrial structural integrity, crista formation, transport and translation.

The orchestration of metabolic programming of cell migration is modulated by a balance in mitochondrial dynamics, the fusion (fragmentation) and fission (elongation), and mitochondrial biogenesis as well as its subcellular distribution (Seo et al., 2018; Denisenko et al., 2019). For instance, migrating lymphocytes (T cells), which mainly rely on oxidative phosphorylation, increase mitochondrial fission and relocate this organelle via microtubules towards the rear end of uropod for proper polarization and migration (Campello et al., 2006; Seo et al., 2018). In contrast, in cancer cells mitochondrial dynamics promotes mitochondrial fission and their redistribution to the leading edge, with the help of the cortical cytoskeleton, to provide an efficient “regional” energy source to induce the lamellipodia formation and cell invasion (Morlino et al., 2014; Zhao et al., 2013; Schuler et al., 2017; LeBleu et al., 2014; Porporato et al., 2018, Rivadeneira et al., 2015).

This raises the question if *Porthos* also impacts other mitochondrial aspects, such as mitochondrial biogenesis and dynamics (fusion and fission), morphology and subcellular distribution, or if these features can generally have a determining role in developmental macrophage invasion, even independent of *Porthos* control.

3.3. Functional conservation of Atossa and Porthos

Are Atossa's mammalian orthologs, mFAM214A and B, functioning in immune cells through the same way as of flies?

Atossa's mammalian orthologs, mFAM214A and B, are also highly enriched in vertebrate immune cells and contain the same 9aaTADs and other conserved motifs. They can to a large extent rescue the tissue invasion of *Drosophila* macrophages (Chapter 3, Figure 2), substituting for the function of Atossa in its absence.

These data are inspiring, leading us to propose that our results from flies can help produce more insights into mammals. Do mFAM214A and B also regulate cell infiltration of immune cells in higher organisms? If so, do they turn on a similar metabolic rewiring? If the mammalian orthologs exert similar functionality in immune cells, they could potentially become fascinating targets for the prevention or treatment of immuno-metabolic disorders or even metastasis.

Is Porthos' effect on mRNA translation conserved?

RNA helicases from the DEAD-box family generally participate in many processes, such as RNA transcription, RNA processing, export, and degradation. The mammalian ortholog of *Drosophila* Porthos, the DEAD-box RNA helicase DDX47, and its yeast homolog, Rrp3a, participate in RNA metabolism, pre-rRNA processing, and ribosome biogenesis (Sekiguchi et al., 2006).

Further studies are required to uncover the exact mechanism by which Porthos' effect on ribosomal assembly alters the translation of a specific subset of mRNAs and assess if its role is conserved in other organisms. Porthos is highly conserved throughout vertebrates and though its orthologs are enriched in immune cells, are also expressed in many tissues. This supports the idea that this helicase family affects a possible broader range of functions, extending beyond immune cell invasion in more complex organisms.

Cell migration is essential for organism homeostasis, immunity, and metastasis emergence. Metabolic adaption has a powerful role in defining the fate and functions of immune cells, mainly performed by their migration across complex tissue contexts to reach their destinations. Macrophages are professional phagocytic immune cells. They play essential roles in the resolution of inflammation and pathogens as a fast response. They also dynamically participate in long-term processes such as tissue hemostasis and remodeling, and wound healing. Supposedly, for different tasks they might require distinct metabolic adaptations to meet their energy demands (Caputa et al. 2019; Riera-Domigo et al., 2020; Buck et al., 2017). In developmental tissue invasion of *Drosophila* macrophages, energetic reliance of leading cells upon mitochondrial respiration may reflect a preference

for more efficient ATP generation to sustain the energy for a long-term invasion, rather than the fast but less efficient aerobic glycolytic program. One could speculate that such metabolic shift we found at this developmental stage has a functional advantage for immune cells. Regarding that stimulation of cell division in embryonic macrophages, hinders their tissue invasion, it might suggest that such metabolic rewiring is critical to invasive characteristics, which occurs following the downregulation of cell proliferation program. Understanding how metabolic programs fine-tune cellular metabolic capacities, required for a proper cell invasion in challenging constrained microenvironments, will help to emerge novel immunotherapeutic approaches. Particularly, co-targeting distinct metabolic platforms of invading cells may be an attractive therapeutic approach for a diverse range of pathological conditions, from autoimmune diseases to cancer.

Exact genotype of *Drosophila* lines used in “Future direction” section

Figure 1. Fig. 1A: Control 1: *w/y,w[1118]; P{attP,y[+],w[3']}/+*; *srpHemo-Gal4, srpHemo-H2A::3xm-Cherry/+*. CG5589 RNAi 1 (*BL32334, aramis*): *CG5589 RNAi (BL32334)/+*; *srpHemo-Gal4, srpHemo-H2A::3xmCherry/+*. Control 2: *w-; P{attP,y[+],w[3']}/+*; *srpHemo-Gal4, srpHemo-H2A::3xmCherry/+*. CG5589 RNAi 2 (*v108642, aramis*): *CG5589 RNAi (v108642)/+*; *srpHemo-Gal4, srpHemo-H2A::3xmCherry/+*. **Fig. 1B:** Control 1: *w/y,w[1118]; P{attP,y[+],w[3']}/+*; *srpHemo-Gal4, srpHemo-H2A::3xm-Cherry/+*. CG4901 RNAi 1 (*v51346, athos*): *CG4901 RNAi 1 (v51346)/+*; *srpHemo-Gal4, srpHemo-H2A::3xmCherry/+*. Control 2: *w-; P{attP,y[+],w[3']}/+*; *srpHemo-Gal4, srpHemo-H2A::3xmCherry/+*. CG4901 RNAi 2 (*v109650, athos*): *CG4901 RNAi (v109650)/+*; *srpHemo-Gal4, srpHemo-H2A::3xmCherry/+*

Figure 2. Figs. 2B,C: Control 1: *w-; +; srpHemo-H2A::3xmCherry/+*. *UAS-String (4778)*: *UAS-stg/w-; srpHemo-Gal4, srpHemo-H2A::3xmCherry/+*. Control 2: *w-; P{attP,y[+],w[3']}/+*; *srpHemo-Gal4, srpHemo-H2A::3xmCherry/+*. CG1395 RNAi (*v330033, String*): *CG1395 RNAi (v330033)/+*; *srpHemo-Gal4, srpHemo-H2A::3xmCherry/+*. **Fig. 2D:** Control: *w-; +; srpHemo-H2A::3xmCherry/+*. *UAS-CycA (83154)*: *UAS-CycA/w-; srpHemo-Gal4, srpHemo-H2A::3xmCherry/+*. CG5940 RNAi (*v32421, CycA*): *CG5940 RNAi (v32421)/+*; *srpHemo-Gal4, srpHemo H2A::3xmCherry/+*. **Fig. 2E:** Control 1: *w-; +; srpHemo-H2A::3xmCherry/+*. CG1071 RNAi 1 (*v100990, E2F2*): *CG1071 RNAi (v100990)/+*; *srpHemo-Gal4, srpHemo-H2A::3xmCherry/+*. Control 2: *w-; P{attP,y[+],w[3']}/+*; *srpHemo-Gal4, srpHemo-H2A::3xmCherry/+*. CG1071 RNAi 2 (*v45743, E2F2*): *CG1071 RNAi (v45743)/+*; *srpHemo-Gal4, srpHemo-H2A::3xmCherry/+*. **Fig. 2F:** Control: *w-; P{attP,y[+],w[3']}/+*; *srpHemo-Gal4, srpHemo-H2A::3xmCherry/+*. CG10498 RNAi (*v104959, Cdk2*): *CG10498 RNAi (v104959)/+*; *srpHemo-Gal4, srpHemo-H2A::3xmCherry/+*. **Fig. 2G:** Control: *w-; P{attP,y[+],w[3']}/+*; *srpHemo-Gal4, srpHemo-H2A::3xmCherry/+*. CG3938 RNAi 1 (*v47941, CycE*): *CG3938 RNAi (v47941)/+*; *srpHemo-Gal4, srpHemo-H2A::3xmCherry/+*. CG3938 RNAi 2 (*v47942, CycE*): *CG3938 RNAi (v47942)/+*; *srpHemo-Gal4, srpHemo-H2A::3xmCherry/+*. Control 2: *w-; P{attP,y[+],w[3']}/+*; *srpHemo-Gal4, srpHemo-H2A::3xmCherry/+*. CG3938 RNAi 3 (*v110204, CycE*): *CG3938 RNAi (v110204)/+*; *srpHemo-Gal4, srpHemo-H2A::3xmCherry/+*

Table 1. Fly lines utilized in “Future direction” section.

Designation	Source of reference	Identifiers	Additional information
<i>UAS-CG14228 RNAi 1 (Merlin)</i>	BDSC, RRID:	BDSC: 34958	<i>D. melanogaster</i>
<i>UAS-CG14228 RNAi 2 (Merlin)</i>	BDSC, RRID:	BDSC: 28007	<i>D. melanogaster</i>
Mer3	BDSC, RRID:	BDSC: 9103	<i>D. melanogaster</i>
Mer4	BDSC, RRID:	BDSC: 9104	<i>D. melanogaster</i>
<i>UAS-CG6944 RNAi 1 (LamDm0)</i>	VDRC, RRID:	VDRC: v45636	<i>D. melanogaster</i>
<i>UAS-CG6944 RNAi 2 (LamDm0)</i>	VDRC, RRID:	VDRC: v45635	<i>D. melanogaster</i>
<i>UAS-CG6944 RNAi 3 (LamDm0)</i>	VDRC, RRID:	VDRC: v107419	<i>D. melanogaster</i>
<i>UAS-CG6944-GFP (LamDm0)</i> [y[1] w[*]; P{w[+mC]=UAS-Lam.GFP}3-3]	BDSC, RRID:	BDSC: 7376	<i>D. melanogaster</i>
<i>UAS-CG1395 RNAi 1 (String)</i>	VDRC, RRID:	VDRC: v330033	<i>D. melanogaster</i>
<i>UAS-CG1395 (String)</i>	VDRC, RRID:	4778	<i>D. melanogaster</i>
<i>UAS-CG5940 (CycA)</i>	BDSC, RRID:	83154	<i>D. melanogaster</i>
<i>UAS-CG5940 RNAi 1 (CycA)</i>	VDRC, RRID:	VDRC: V32421	<i>D. melanogaster</i>
<i>UAS-CG1395 RNAi 1 (String)</i>	VDRC, RRID:	VDRC: v45743	<i>D. melanogaster</i>
<i>UAS-CG RNAi 2 (String)</i>	VDRC, RRID:	VDRC: v100990	<i>D. melanogaster</i>
<i>UAS-CG10498 RNAi (Cdk2)</i>	VDRC, RRID:	VDRC: v104959	<i>D. melanogaster</i>
<i>UAS-CG3938 RNAi 1 (CycE)</i>	VDRC, RRID:	VDRC: v47941	<i>D. melanogaster</i>
<i>UAS-CG3938 RNAi 2 (CycE)</i>	VDRC, RRID:	VDRC: v47942	<i>D. melanogaster</i>
<i>UAS-CG3938 RNAi 3 (CycE)</i>	VDRC, RRID:	VDRC: v110204	<i>D. melanogaster</i>
<i>UAS-CG1071 RNAi 1 (E2F2)</i>	VDRC, RRID:	VDRC: v100990	<i>D. melanogaster</i>
<i>UAS-CG1071 RNAi 2 (E2F2)</i>	VDRC, RRID:	VDRC: v45743	<i>D. melanogaster</i>
<i>UAS-CG5589 RNAi 1 (aramis)</i>	BDSC, RRID:	BDSC: BL32334	<i>D. melanogaster</i>
<i>UAS-CG5589 RNAi 2 (aramis)</i>	VDRC, RRID:	VDRC: v108642	<i>D. melanogaster</i>
<i>UAS-CG4901 RNAi 1 (athos)</i>	VDRC, RRID:	VDRC: v51346	<i>D. melanogaster</i>
<i>UAS-CG4901 RNAi 2 (athos)</i>	VDRC, RRID:	VDRC: v109650	<i>D. melanogaster</i>

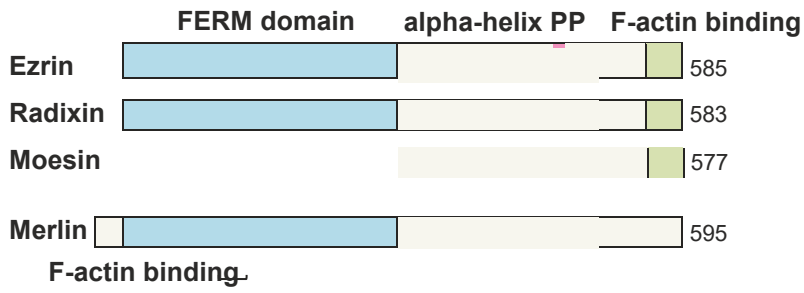
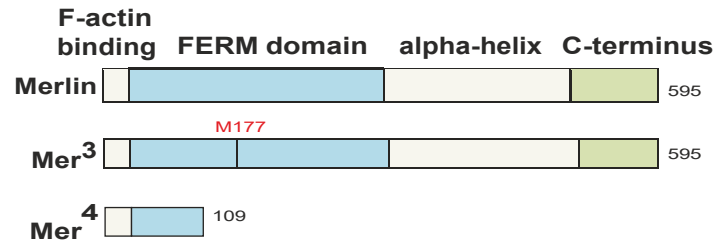
4. SIDE PROJECTS

4.1 The effect of the tumor suppressor Merlin, a putative CG9005 (Atossa) interacting protein, on tissue invasion of *Drosophila* macrophages

In the beginning of my PhD project, I was searching for the potential interactors of CG9005 to figure out more about its function in macrophage invasion. To obtain some hints regarding its function, I took advantage of published data from a two-hybrid assay (Giot et al., 2003), in which I found a tumor suppressor protein, named Merlin or NF2, as a first interacting partner in the list.

Neurofibromatosis-2 (NF2) homologue in *Drosophila*, also called Merlin (Mer), has shown both structural and functional similarity to human tumor suppressor NF2 in regulating cell proliferation and apoptosis (McCartney et al., 2000). Mutation of human NF2 causes the tumor syndrome neurofibromatosis type 2, a disease characterized by benign tumors of the central nervous system, particularly schwannomas and meningiomas (Evans et al., 1992). Merlin shares significant sequence identity with ERM proteins, including Ezrin, Radixin, and Moesin, which via their C-termini link the cytoskeleton to membrane proteins. In contrast to ERM proteins, Merlin does not bear a C-terminal spectrin-actin binding domain, so probably it might interact with actin through its FERM domain (Figure 1.A). Loss of Merlin function in mammalian cell culture appears to destabilize adherens junctions and results in loss of contact-dependent inhibition of proliferation. In fly tissues and cells, Merlin physically interacts with a Protein 4.1 superfamily member in *Drosophila*, named Expanded through a conserved N-terminal region of its C-terminal domain to regulate cell proliferation and differentiation, and apoptosis, specifically via Wingless signaling as well as Decapentaplegic-mediated differentiation events (McCartney et al., 2000; Pellock et al., 2007).

To analyze the independent effect of the downregulation of this gene on tissue invasion, I tested 2 different RNAi lines and counted the number of macrophages entering the extended germband in early stage 12 embryos (up to a germband retraction of 40%). I observed a strong reduction in number of macrophages penetrating into the germband tissue for both RNAi lines, compared to the control embryos (Figure 1.B,C). Beside RNAi expression assay, I assessed the effect of two merlin mutants: a viable allele, named *Mer3*, which has a missense mutation of Met177 to Isoleucine, and a lethal mutant named *Mer4*, having a substitution of Gln170 to a stop codon, which encodes a truncated protein (Figure 1.A') (Lajeunesse et al., 1998). Similarly, both *merlin* mutants caused a significant decrease in macrophage invasion into the germband tissue (Figure 1.D). These results argue that Merlin is specifically required in macrophages for their germband invasion. Moreover, to test if *merlin* downregulation or mutation has any potential effect on general migration, I counted macrophages moving along the inner vnc route in late Stage 12 embryos (Figure 1.E,F). However, I didn't observe any significant difference between the RNAis and the control, suggesting that the general migratory steps maintain normal. Also the total number of macrophages didn't change significantly in RNAi expressing embryos (Figure 1.G). Based on the results from fixed embryos, I could conclude that Merlin is specifically required in macrophages to promote their tissue invasion.

A**A'****B**

Stg 12

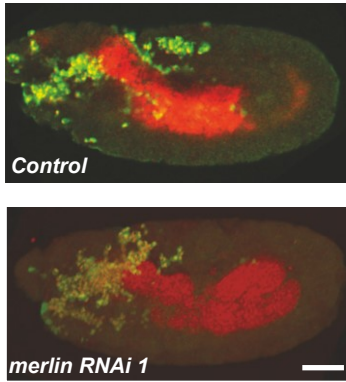
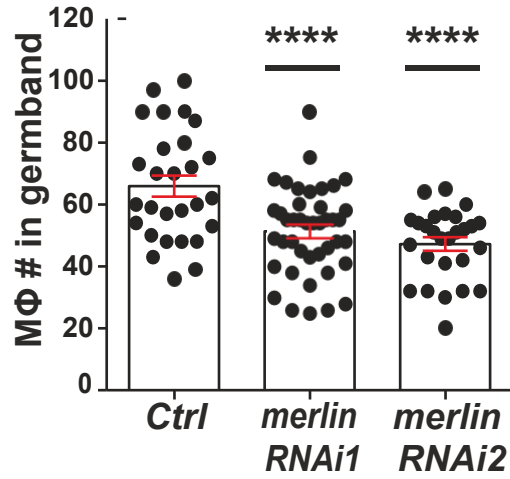
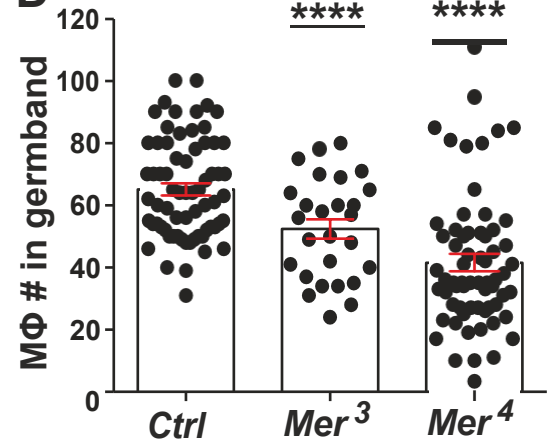
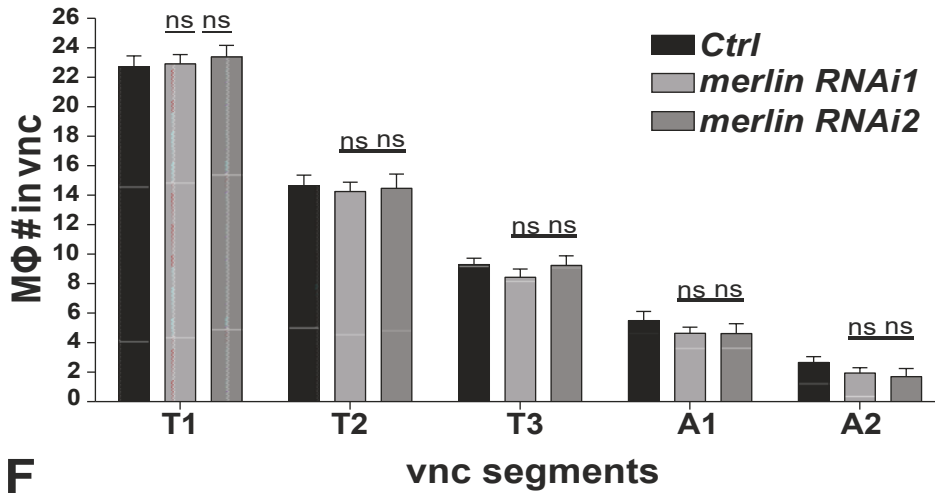
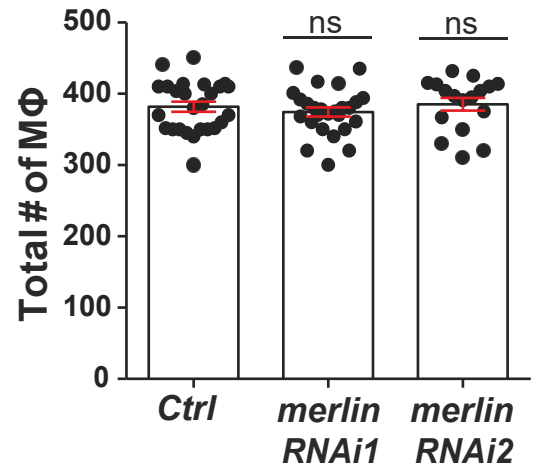
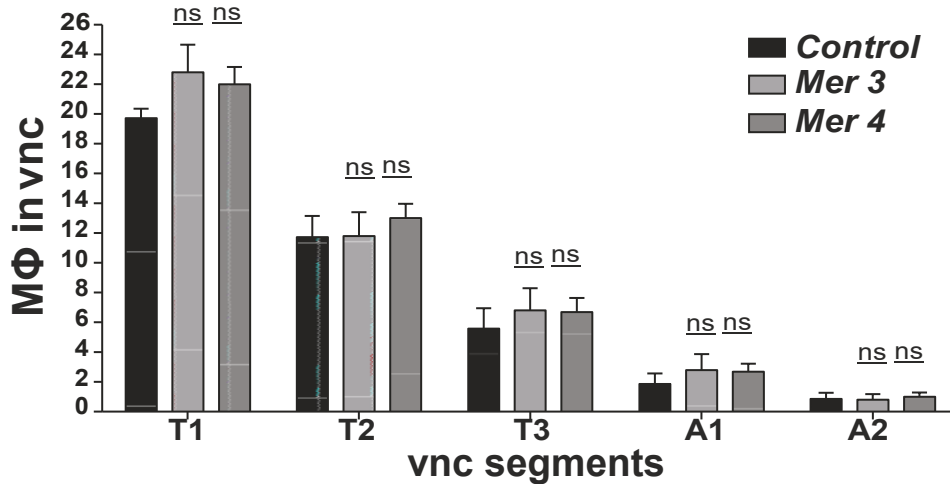
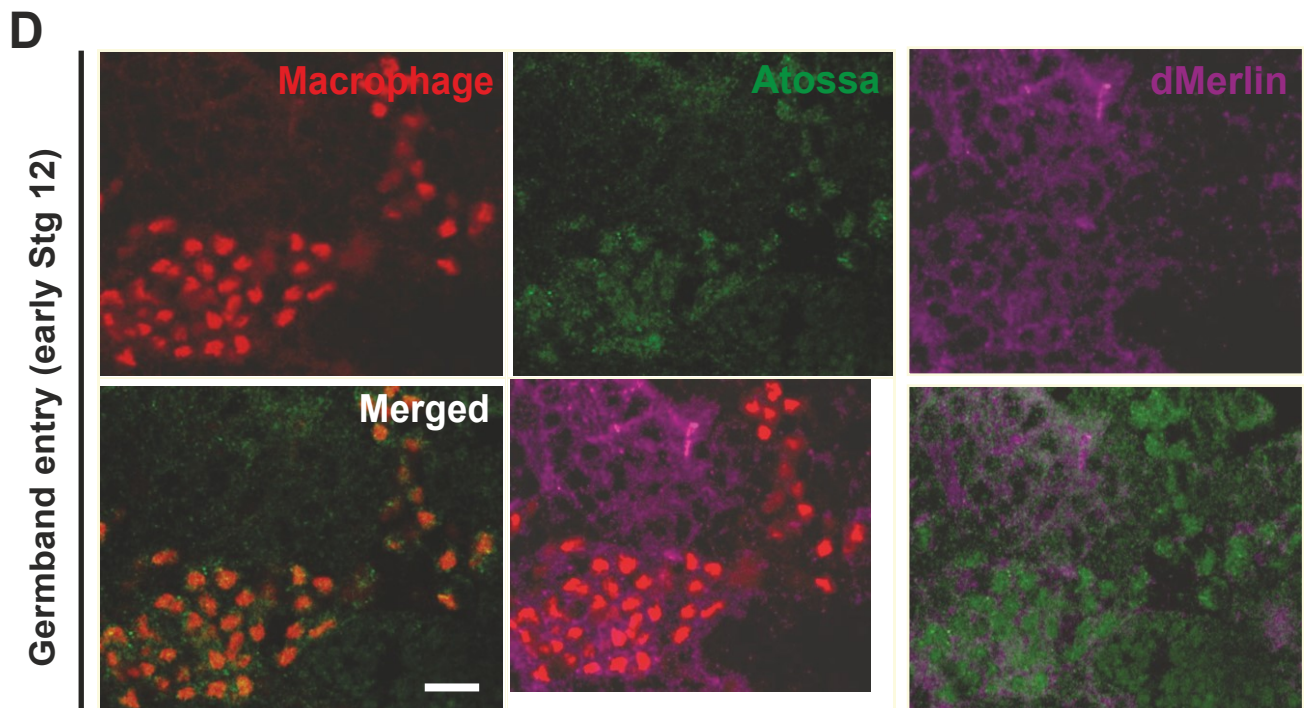
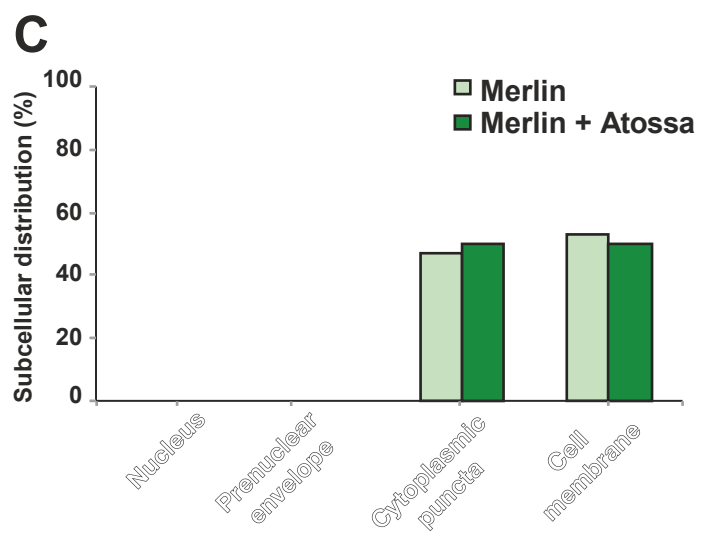
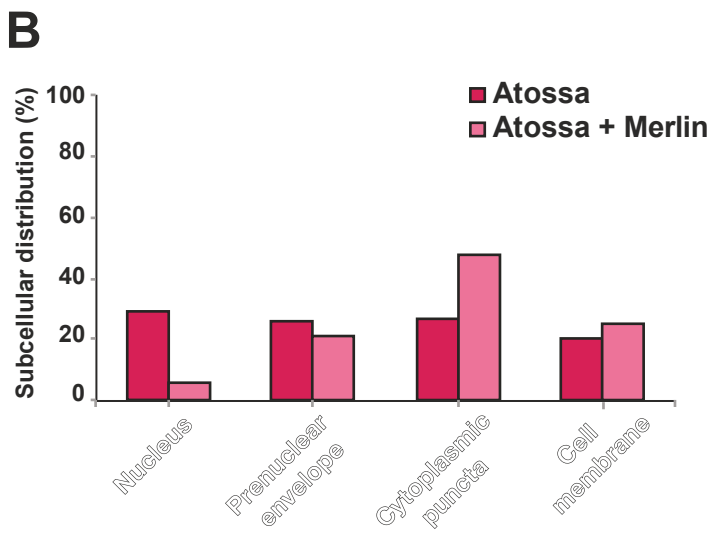
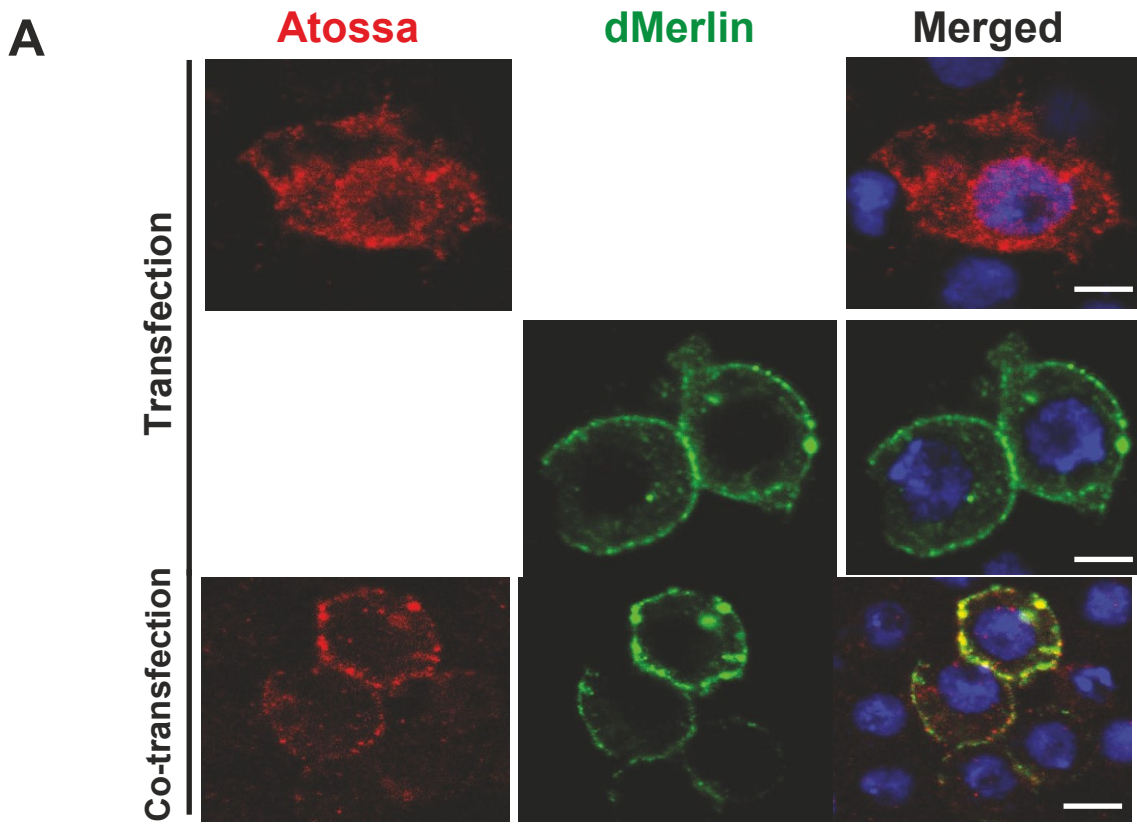
**C****D****E****G****F**

Figure 1: Tumor suppressor Merlin is specifically required in macrophages to trigger their invasion into the germband. (A) Merlin shares significant sequence identity with ERM proteins, including Ezrin, Radixin, and Moesin, which via their C-termini link the cytoskeleton to membrane proteins. However, Merlin lacks a C-terminal actin-binding domain. **(A')** The primary protein structure of Merlin and its two mutants, Mer 3 and Mer4. **(B)** Representative confocal images of early Stage 12 embryos from the control, and line expressing RNAi (1) against Merlin in macrophages (red). *srpHemo::RFPnls,UAS::GFP* labels macrophages. **(C,D)** Quantification of Stage 12 embryos indicates that fewer macrophages have moved into the germband upon the expression in macrophages of either of **(C)** two different RNAis against *merlin* or **(D)** two different *merlin* mutants, *Mer3* and *Mer4*, arguing that Merlin is required in macrophages for tissue invasion, control n=28, *merlin* RNAi 1 (BL-34958) n=42, p=0.0003; *merlin* RNAi 2 (BL-28007) n=27, p=0.0001; control n=68, *Mer3* (BL-9103) n=27, p=0.0008; *Mer4* (BL-9104) n=65, p<0.0001. **(E,F)** Macrophage quantification in ventral nerve cord (vnc) segments reveals no significant difference in macrophage migration along this route between **(E)** two *merlin* RNAis (RNAi 1 n=33, p=0.46; RNAi 2 n=13, p>0.99) and **(F)** control embryos (n=20) and also two *merlin* mutants (*Mer3* n=5, p=0.; *Mer4* n=13, p>0.1) and their control embryos (n=7). **(G)** Quantification of the total macrophage number shows no significant change between the control (n=26) and two merlin RNAis (RNAi 1 n=26, p=; RNAi 2 n=17, p>0.99). Scale bar: 50 μ m in (B).

As a next step, I assessed the cellular distribution of Merlin, *in vitro* and *in vivo*, to see if Merlin is really interacting with CG9005 (Atossa), as claimed by data from yeast two-hybrid assay. I overexpressed the tagged forms of Atossa and Merlin under *srpGal4* driver in macrophage-like cells, also called S2R+ cells. I observed that Atossa was localized in the nucleus and prenuclear region, in some cytoplasmic particles as well as close to the cell membrane (Figure 2.A). The tagged form of Merlin was localized both at the plasma membrane and in clusters or cytoplasmic particles (Figure 2.A). Functionally, such subcellular distribution of Merlin is critical for its tumor-suppression activity (LaJeunesse et al., 1998; McCartney and Fehon, 1996). When both Atossa and Merlin were coexpressed, I saw a shift in Atossa's localization from nucleus towards more cytoplasmic puncta in the presence of Merlin (Figure 2.B), whereas there was no change in Merlin's subcellular distribution in the presence of Atossa (Figure 2.C). Similar to *in vitro* finding, *in vivo* immunostaining of embryos showed that endogenous Merlin, visualised by an anti-Merlin antibody, also forms particles near the plasma membrane as well as in the cytoplasm in macrophages (Figure 2.D) (LaJeunesse et al., 1998; McCartney and Fehon, 1996), while the tagged form of Atossa was mainly found in the nucleus of macrophages. Surprisingly, I didn't see any clear colocalization for Atossa and Merlin in macrophages *in vivo* (Figure 2.D). One interpretation would be that Merlin and Atossa localize differently and thus act independently in macrophages or the observed *in vitro* colocalization could be an artifact and nonspecific interactions, possibly due to higher loads of overexpressed proteins. Given the *in vivo* localization data, I concluded that Merlin, though being important for macrophage germband invasion, would affect immune cell migration through a distinct and independent mechanism than Atossa in fly embryos.

Figure 2: Merlin localizes into the cell membrane in macrophages without interacting with nuclear Atossa (CG9005). (A) S2R+ cells were transfected with tagged forms of Atossa and Merlin. HA tagged Atossa (red) and myc-tagged Merlin (green) were visualized with antibodies, and the nucleus with DAPI (blue). These constructs were expressed under control of the *srpHemoGal4* promoter. **(B)** Quantification of subcellular distributions showed that Atossa is mainly found in the nucleus, prenuclear regions, in cytoplasmic particles and close the cell membrane, while it altered its localization more outside of the nucleus in the presence of Merlin (n>30), **(C)** whereas Merlin is seen both at the cell membrane and in clusters in the cytoplasm and didn't show any shift in its localization when coexpressed with Atossa (n>30). **(D)** *in vivo* localization assay in embryos revealed that the HA-tagged Atossa is mainly found in the nucleus, whereas endogenous Merlin is localized at the cell membrane and in cytoplasmic puncta, and these two protein didn't show any colocalisation in macrophages. Scale bars: 5 μ m in (A) and 10 μ m in (D).



4.2 How does the alteration in nuclear Lamin levels affect the tissue invasion of macrophages?

Atossa is a nuclear protein in *Drosophila* macrophages, so I was wondering if this nuclear factor could directly or indirectly affect the nuclear properties, such as chromatin remodeling, nuclear stiffness or shape. Therefore, I first assessed if the macrophage nucleus impedes normal tissue invasion by altering levels of the *Drosophila* Lamin gene (*LamDm0*), which is relevant to the vertebrate lamin B2 (Muñoz-Alarcón et al., 2007) and is found to affect nuclear stiffness and deformability (Wintner et al., 2020; Zwerger et al., 2013).

When I knocked down Lamin expression via three independent RNAis (Figure 3. A',B) or overexpressed (Figure 3. A'',C) in macrophages, I didn't observe any differences in tissue invasion of macrophages into the germband, compared to their control embryos (Figure 3. A-C).

These results indicate that the stiffness of the macrophage nucleus, here controlled by nuclear intermediate filament Lamin, is not a rate limiting parameter for macrophages to invade along the narrow path between the ectoderm and mesoderm tissues. Moreover, it could be interpreted that generally the Lamin expression is not highly crucial for immune cell invasion (Andrés & González, 2009).

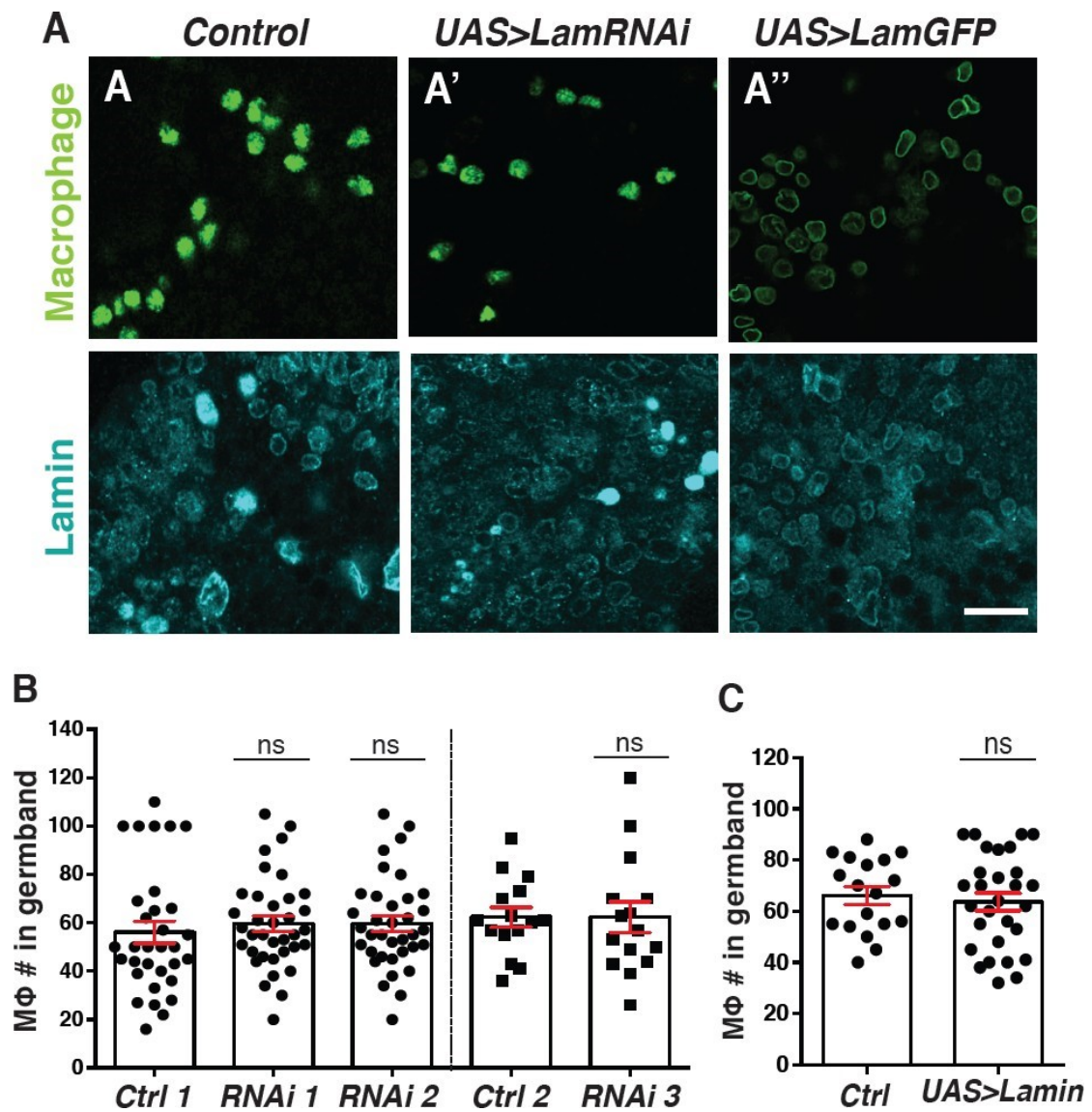


Figure 3: Alteration of nuclear stiffness by either overexpressing or downregulation of Lamin in macrophages doesn't affect their germband invasion. (A-A'') Confocal images of St 12 embryos of the control (A), or those expressing RNAi against Lamin (A') and its overexpression (A'') in macrophages. *srpHemo-GAL4* used as driver. **(B)** Downregulating the *lamin* expression in macrophages by expressing three different RNAis, which can enhance nuclear deformability, did not alter macrophages numbers in the germband tissue, compared to the controls. **(C)** Overexpression of Lamin in macrophages, which can increase the nuclear stiffness, also didn't affect their numbers in the germband, arguing that Lamin is dispensible for macrophage tissue invasion. Control 1 n= 33, *LamDm0* RNAi 1 n=32, p=0.59, and *LamDm0* RNAi 2 n= 34, p>0.99. Control 2 n= 15, *LamDm0* RNAi 3 n= 15, p>0.99. Control n= 18, *UAS>LamDm0* n=29, p=0.64.

REFERENCES

Acín-Pérez R, Bayona-Bafaluy MP, Fernández-Silva P, Moreno-Loshuertos R, Pérez-Martos A, Bruno C, Moraes CT, Enríquez JA. 2004. Respiratory complex III is required to maintain complex I in mammalian mitochondria. *Mol Cell*. 13(6):805-15. doi: 10.1016/s1097-2765(04)00124-8. PMID: 15053874; PMCID: PMC3164363.

Acín-Pérez R, Bayona-Bafaluy MP, Fernández-Silva P, Moreno-Loshuertos R, Pérez-Martos A, Bruno C, Moraes CT, Enríquez JA. 2004. Respiratory complex III is required to maintain complex I in mammalian mitochondria. *Molecular Cell* 13: 805–815.

Agostini M, Romeo F, Inoue S, Niklison-Chirou MV, Elia AJ, Dinsdale D, Morone N, Knight RA, Mak TW, Melino G. 2016. Metabolic reprogramming during neuronal differentiation. *Cell Death and Differentiation* 23: 1502-1514.

Albert V, Hall MN. 2015. mTOR signaling in cellular and organismal energetics. *Current Opinion in Cell Biology* 33:55-66.

Ayyaz A, Li H, Jasper H. 2015. Haemocytes control stem cell activity in the *Drosophila* intestine. *Nat Cell Biol*. 17(6):736-48. doi: 10.1038/ncb3174. Epub 2015 May 25. PMID: 26005834; PMCID: PMC4449816.

Banerjee U, Girard JR, Goins LM, Spratford CM. 2019. *Drosophila* as a genetic model for hematopoiesis. *Genetics*, 211: 367–417.

Barry NP, Bretscher MS. 2010. Dictyostelium amoebae and neutrophils can swim. *Proc. Natl. Acad. Sci*. 107: 11376–11380.

Beauchamp EM, Platanias LC. 2013. The evolution of the TOR pathway and its role in cancer. *Oncogene* 32: 3923-3932.

Benelli D, Cialfi S, Pinzaglia M, Talora C, Londei P. 2012. The translation factor eIF6 is a Notch-Dependent regulator of cell migration and invasion. *PLOS ONE* 2: e32047.

Benseñor LB, Barlan K, Rice SE, Fehon RG, Gelfand VI. 2010. Microtubule-mediated transport of the tumor-suppressor protein Merlin and its mutants *Proceedings of the National Academy of Sciences*, 107 (16): 7311-7316; DOI:10.1073/pnas.0907389107

Bernier LP, York EM, Kamyabi A, Choi HB, Weilinger NL, MacVicar BA. 2020. Microglial metabolic flexibility supports immune surveillance of the brain parenchyma. *Nature Communications* 11: 1559.

Berre M, Lautenschlaeger F, Maiuri P, Callan-Jones A, Heuzé M, Takaki T, Voituriez R, Piel M. Confinement and low adhesion induce fast amoeboid migration of slow mesenchymal cells. *Cell*. 2015, 12;160(4):659-672. doi: 10.1016/j.cell.2015.01.007. PMID: 25679760.

Bjedov I, Toivonen JM, Kerr F, Slack C, Jacobson J, Foley A, Partridge L. 2010. Mechanisms of life span extension by Rapamycin in the fruit fly *Drosophila melanogaster*. *Cell Metabolism* 11: 35-46.

Blumberg A, Zhao Y, Huang YF, Dukler N, Rice EJ, Krumholz K, Danko CG, Siepel A. 2019. Characterizing RNA stability genome-wide through combined analysis of PRO-seq and RNA-seq data. *bioRxiv*.

Britt EC, John SV, Locasale JW, Fan J. 2020. Metabolic regulation of epigenetic remodeling in immune cells. *Current Opinion in Biotechnology* 63:111-117.

Brückner K, Kockel L, Duchek P, Luque CM, Rørth P, Perrimon N. 2004. The PDGF/VEGF receptor controls blood cell survival in *Drosophila*. *Dev. Cell* 7: 73–84. <https://doi.org/10.1016/j.devcel.2004.06.007>.

- Buchon, N., Silverman, N. & Cherry, S. Immunity in *Drosophila melanogaster*-from microbial recognition to whole-organism physiology. *Nature Rev. Immunol.* 14, 796–810 (2014).
- Buck MD, Sowell RT, Kaech SM, Pearce EL. 2017. Metabolic instruction of immunity. *Cell* 169: 570-586.
- Bunt, S., Hooley, C., Hu, N., Scahill, C., Weavers, H., and Skaer, H. 2010. Hemocyte-eecreted Type IV collagen enhances BMP signaling to guide renal tubule morphogenesis in *Drosophila*. *Dev. Cell* 19:296-306.
- Caino MC, Chae YC, Vaira V, Ferrero S, Nosotti M, Martin NM, Weeraratna A, O’Connell M, Jernigan D, Fatatis A, et al. 2013. Metabolic stress control of cytoskeletal dynamics and metastasis. *J Clin Invest.* 123: 2907–2920.
- Cakouros D, Mills K, Denton D, Paterson A, Daish T, Kumar S. 2008. dLKR/SDH regulates hormone-mediated histone arginine methylation and transcription of cell death genes, *J. Cell Biol.* 182: 48-495.
- Campello S, Lacalle RA, Bettella M, Manes S, Scorrano L, Viola A. 2006. Orchestration of lymphocyte chemotaxis by mitochondrial dynamics. *J Exp Med* 203:2879-2886. doi:10.10 84/jem.20061877
- Caputa G, Castoldi A, Pearce EJ. 2019. Metabolic adaptations of tissue-resident immune cells. *Nature Immunology* 20: 793-801.
- Carmona-Fontaine C, Matthews HK, Kuriyama S, Moreno M, Dunn GA, Parsons M, Stern CD, Mayor R. 2008. Contact inhibition of locomotion in vivo controls neural crest directional migration. *Nature.* 456(7224): 957-961. doi: 10.1038/nature07441. Epub 2008 Dec 10. PMID: 19078960; PMCID: PMC2635562.
- Carvalho GB, Drago I, Hoxhaa S, Yamadaa R, Mahnevac O, Brucea KD, Obandoa AS, Contia B, Ja WW. 2017. The 4E-BP growth pathway regulates the effect of ambient temperature on *Drosophila* metabolism and lifespan. *PNAS.* 114 (36): 9737-9742.
- Cherry JD, Olschowka JA, O'Banion MK .2014. Neuroinflammation and M2 microglia: the good, the bad, and the inflamed. *J Neuroinflammation* 11: 98. doi: 10.1186/1742-2094-11-98
- Commander R, Wei C, Sharma A, Mouw JK, Burton LJ, Summerbell E, Mahboubi D, RJ Peterson, Konen J, Zhou W, Du Y, Fu H, Shanmugam M, Marcus AI. 2020. Subpopulation targeting of pyruvate dehydrogenase and GLUT1 decouples metabolic heterogeneity during collective cancer cell invasion. *Nat. Commun.* 11:1.
- Cox N, Crozet L, Holtman IR, Loyher PL, Lazarov T, Mass E, Stanley ER, Glass CK, Geissmann F. 2020. Resident macrophages establish and control lipid stores via PDGFcc production. *bioRxiv.* doi: <https://doi.org/10.1101/2020.06.15.152397>.
- Damm, EW, Winklbauer R. 2011. PDGF-A controls mesoderm cell orientation and radial intercalation during *Xenopus* gastrulation. *Development* 138: 565–575.
- Dang CV . 2012. Links between metabolism and cancer. *Genes Dev.* 26: 877–890.
- Davies LC, Rice Danie CM, McVicar W, Weiss JM. 2019. Diversity and environmental adaptation of phagocytic cell metabolism. *J Leukoc Biol.* 105: 37-48.
- David NB, Sapède D, Saint-Etienne L, et al.: Molecular basis of cell migration in the fish lateral line: role of the chemokine receptor CXCR4 and of its ligand, SDF1. *Proc Natl Acad Sci U S A.* 2002; 99(25): 16297–302.
- Dawson CA, Pal B, Vaillant F, Gandolfo LC, Liu Z, Bleriot C, Ginhoux F, Smyth GK, Lindeman GJ, Mueller SN, AC Rios, Visvader JE. 2020. Tissue-resident ductal macrophages survey the mammary epithelium and facilitate tissue remodeling. *Nature Cell Biology, VOL 22* 546, , 546-558.
- Davidson AJ, Wood W. 2020. Macrophages use distinct actin regulators to switch engulfment strategies and ensure phagocytic plasticity in vivo. *Cell Reports* 31: 107692.

Denisenko TV, Gorbunova AS, Zhivotovsky B. 2019. Mitochondrial Involvement in Migration, Invasion and Metastasis. *Frontiers in Cell and Developmental Biology*. 7: 355.

Di Liegro CM, Schiera G, Di Liegro I. 2014. Regulation of mRNA transport, localization and translation in the nervous system of mammals. *Int J Mol Med* 33: 747-762.

Diz-Muñoz A, Krieg M, Bergert M, Ibarlucea-Benitez I, Muller DJ, Paluch E, Heisenberg CP. 2010. Control of directed cell migration in vivo by membrane-to-cortex attachment. *PLoS Biol*. 8(11):e1000544. doi: 10.1371/journal.pbio.1000544. PMID: 21151339; PMCID: PMC2994655.

Diz-Muñoz A, Thurley K, Chintamen S, Altschuler SJ, Wu LF, Fletcher DA, Weiner OD. 2016. Membrane Tension Acts Through PLD2 and mTORC2 to Limit Actin Network Assembly During Neutrophil Migration. *PLoS Biol*. 14(6):e1002474. doi: 10.1371/journal.pbio.1002474. PMID: 27280401; PMCID: PMC4900667.

Donà E, Barry JD, Valentin G, Quirin C, Khmelinskii A, Kunze A, Durdu S, Newton LR, Fernandez-Minan A, Huber W, Knop M, Gilmour D. 2013. Directional tissue migration through a self-generated chemokine gradient. *Nature*.: 503(7475):285-9. doi: 10.1038/nature12635. Epub 2013 Sep 25. PMID: 24067609.

Eales KL, Hollinshead KER, Tennant DA. 2016. Hypoxia and metabolic adaptation of cancer cells. *Oncogenesis* 5: e190; doi:10.1038/oncsis.2015.50.

Eming SA, Wynn TA, Martin P. 2017. Inflammation and metabolism in tissue repair and regeneration. *Science* 356: 1026–103.

Etienne-Manneville S. 2008. Polarity proteins in migration and invasion. *Oncogene* 27: 6970-6980.

Evans DG, Huson SM, Donnai D, Neary W, Blair V, Teare D, Newton V, Strachan T, Ramsden R, Harris R. 1992. A genetic study of type 2 neurofibromatosis in the United Kingdom. I. Prevalence, mutation rate, fitness, and confirmation of maternal transmission effect on severity. *J Med Genet*. 29(12):841–846.

Evans IR, Wood W. 2011. *Drosophila* embryonic hemocytes. *Current Biology* 21(5): R173– R174. <https://doi.org/10.1016/j.cub.2011.01.061>.

Fonseca BD, Zakaria C, Jia JJ, Graber TE, Svitkin Y, Tahmasebi S, Healy D, Hoang HD, Jensen JM, Diao IT, Lussier A, Dajadian C, Padmanabhan N, Wang W, Matta-Camacho E, Hearnden J, Smith EM, Tsukumo Y, Yanagiya A, Morita M, Petroulakis E, González JL, Hernández G, Alain T, Damgaard CK. 2015. La-related protein 1 (LARP1) represses terminal oligopyrimidine (TOP) mRNA translation downstream of mTOR complex 1 (mTORC1). *J Biol Chem*. 290(26): 15996-6020. doi: 10.1074/jbc.M114.621730. Epub May 4. PMID: 25940091; PMCID: PMC4481205.

Franc NC, Dimarcq JL, Lagueux M, Hoffmann J, Ezekowitz RA. 1996. Croquemort, a novel *Drosophila* hemocyte/macrophage receptor that recognizes apoptotic cells. *Immunity* 4:431–443.

Franz A, Wood W, Martin P. 2018. Fat body cells are motile and actively migrate to wounds to drive repair and prevent infection. *Developmental Cell* 44: 460-470.

Friedl P, Alexander S. 2011. Cancer invasion and the microenvironment: plasticity and reciprocity. *Cell*. 147(5):992-1009. doi: 10.1016/j.cell.2011.11.016. PMID: 22118458.

Friedl P, Locker J, Sahai E, Segall JE. 2012. Classifying collective cancer cell invasion. *Nature Cell Biology* 14(8): 777–783. <https://doi.org/10.1038/ncb2548>.

Friedl P, Bocker EB. 2000. The biology of cell locomotion within three-dimensional extracellular matrix. *Cellular and Molecular Life Sciences* 57: 41–64. <https://doi.org/10.1007/s000180050498>.

Friedl P, Weigelin B. 2008. Interstitial leukocyte migration and immune function. *9 nature immunology*.

Friedl P, Wolf K. 2009. Proteolytic interstitial cell migration: a five-step process. *Cancer Metastasis Rev* 28:129–135.

Gaggioli C, Hooper S, Hidalgo-Carcedo C, Grosse R, Marshall JF, Harrington K, Sahai E. 2007. Fibroblast-led collective invasion of carcinoma cells with differing roles for RhoGTPases in leading and following cells. *Nat Cell Biol.* 9(12):1392-400. doi: 10.1038/ncb1658. Epub Nov 25. PMID: 18037882.

Bottom of Form

Gandin, V., Masvidal, L., Hulea, L., Gravel, S.P., Cargnello, M., McLaughlan, S., Cai, Y., Balanathan, P., Morita, M., Rajakumar, A., Furic, L., Pollak, M., Porco Jr., J.A., St-Pierre, J., Pelletier, J., Larsson, O., Topisirovic, I., 2016. nanoCAGE reveals 5' UTR features that define specific modes of translation of functionally related mTOR-sensitive mRNAs. *Genome Res.* 26 (5), 636-648.

Galvan-Peña S, O'Neill LA. 2014. Metabolic reprogramming in macrophage polarization. *Front Immunol* 5: 420.. 00420. <https://doi.org/10.3389/fimmu.2014.00420>

Gavilan HS, Kulikaukas RM, Gutmann DH, Fehon RG. 2014. in vivo functional analysis of the human NF2 Tumor suppressor gene in *Drosophila*. *PLoS ONE* 9(3): e90853. <https://doi.org/10.1371/journal.pone.0090853>

Giot L, Bader JS, Brouwer C, Chaudhuri A, Kuang B, Li Y, Hao YL, Ooi CE, Godwin B, Vitols E, Vijayadamodar G, Pochart P, Machineni H, Welsh M, Kong Y, Zerhusen B, Malcolm R, Varrone Z, Collis A, Minto M, Burgess S, McDaniel L, Stimpson E, Spriggs F, Williams J, Neurath K, Ioime N, Agee M, Voss E, Furtak K, Renzulli R, Aanensen N, Carrolla S, Bickelhaupt E, Lazovatsky Y, DaSilva A, Zhong J, Stanyon CA, Finley RL, White KP, Braverman M, Jarvie T, Gold S, Leach M, Knight J, Shimkets RA, McKenna MP, Chant J, Rothberg JM. 2003. A protein interaction map of *Drosophila melanogaster*. *Science* 302:1727-36. doi:10.1126/science.1090289

Gold KS, Brückner K. 2015. Macrophages and cellular immunity in *Drosophila melanogaster*. *Semin Immunol.* 27(6): 357-368. doi: 10.1016/j.smim.2016.03.010. Epub 2016 Apr 23. PMID: 27117654; PMCID: PMC5012540.

Guillou A, Troha Wang KH, Franc NC, Buchon N. 2016. The *Drosophila* CD36 homologue croquemort is required to maintain immune and Gut homeostasis during development and aging. *PLoS Pathog.* 12: e1005961.

Haas P, Gilmpur D. 2006. Chemokine signaling mediates self-organizing tissue migration in the zebrafish lateral line. *Developmental Cell* 10: 673-680.

Hava D, Forster U, Matsuda M, Cui S, Link BA, Eichhorst J, Wiesner B, Chitnis A, Abdelilah-Seyfried S. 2009. Apical membrane maturation and cellular rosette formation during morphogenesis of the zebrafish lateral line. *J Cell Sci.* 122(Pt 5):687-95.

doi: 10.1242/jcs.032102. Epub 2009 Feb 10. PMID: 19208766; PMCID: PMC3188803.

Hawkins RJ, Poincloux R, Bnichou O, Piel M, Chavrier P, Voituriez R. 2011. Spontaneous contractility-mediated cortical flow generates cell migration in threedimensional environments. *Biophysical Journal,* 101(5): 1041–1045.

Hershey JWB, Sonenberg N , Mathews MB. 2012. Principles of translational control: an overview. *Cold Spring Harb. Perspect. Biol.* 4 (12), Article a01152.

Hinnebusch AG, Ivanov IP, Sonenberg N. 2016. Translational control by 5'-untranslated regions of eukaryotic mRNAs. *Science* 352: 1413-1413.

Hoang-Minh LB, Siebzehnrübl FA, Yang C, Suzuki-Hatano S, Dajac K, Loche T, Andrews N, Massari, MS, Patel J, Amin K, et al. 2018. Infiltrative and drug-resistant slow-cycling cells support metabolic heterogeneity in glioblastoma. *EMBO J.* 37, e98772.

Hoch RV, Soriano P. 2003. Roles of PDGF in animal development. *Development* 130:4769–4784.

Hsieh AC, Liu Y, Edlind MP, Ingolia NT, Janes MR, Sher A, Shi EY, Stumpf CR, Christensen C, Bonham MJ, Wang S, Ren P, Martin M, Jessen K, Feldman ME, Weissman JS, Shokat KM, Rommel C, Ruggero D. 2012. The translational landscape of mTOR signalling steers cancer initiation and metastasis. *Nature* 485: 55–61. doi: 10.1038/nature10912

Ilina O, Peter Friedl P. 2009. Mechanisms of collective cell migration at a glance. *Journal of Cell Science* 122: 3203-3208; doi: 10.1242/jcs.036525,

Jin H, Xu W, Rahman R, Na D, Fieldsend A, Song W, Liu S, Li C, Rosbash M. 2020. TRIBE editing reveals specific mRNA targets of eIF4E-BP in *Drosophila* and in mammals. *Sci. Adv.* 6: eabb8771.

Jose C, Bellance N, Rossignol R. 2011. Choosing between glycolysis and oxidative phosphorylation: A tumor's dilemma? *Biochimica et Biophysica Acta* 1807: 552–561.

Kay RR, Langridge P, Traynor D, Hoeller O. 2008. Changing directions in the study of chemotaxis. *Nat Rev Mol Cell Biol.* 9(6):455-63. doi: 10.1038/nrm2419. PMID: 18500256.

Kenney JW, Moore CE, Wang X, Proud CG. 2014. Eukaryotic elongation factor 2 kinase, an unusual enzyme with multiple roles. *Adv. Biol. Regul.* 55:15-20.

Kim J, De Berardinis RJ. 2019. Mechanisms and implications of metabolic heterogeneity in cancer. *Cell Metabolism* 30: 434-446.

Kurosaka S, Kashina A. 2008. Cell biology of embryonic migration. *Birth Defects Res C: Embryo Today* 84: 102-122.

Ladoux B, Mège RM, Trepas X. 2016. Front-rear polarization by mechanical cues: from single cells to tissues. *Trends Cell Biol.* 26(6):420-433. doi: 10.1016/j.tcb.2016.02.002. Epub 2016 Feb 23. PMID: 26920934; PMCID: PMC5421599.

Lahr RM, Fonseca BD, Ciotti GE, Al-Ashtal HA, Jia JJ, Niklaus MR, Blagden SP, Alain T, Berman AJ. 2017. La-related protein 1 (LARP1) binds the mRNA cap, blocking eIF4F assembly on TOP mRNAs. *Elife* 6:e24146.

LaJeunesse DR, McCartney BM, Fehon RG. 1998. Structural analysis of *Drosophila* merlin reveals functional domains important for growth control and subcellular localization. *J Cell Biol* 141:1589-1599.

Lämmermann T, Bader BL, Monkley SJ, Worbs T, Wedlich-Söldner R, Hirsch K, Keller M, Förster R, Critchley DR, Fässler R, Sixt M. 2008. Rapid leukocyte migration by integrin-independent flowing and squeezing. *Nature.* 453(7191): 51-55. doi: 10.1038/nature06887. PMID: 18451854.

Lämmermann T, Sixt M. 2009. Mechanical modes of 'amoeboid' cell migration. *Curr Opin Cell Biol.* 21(5): 636-644.

Lauro C, Limatola C. 2020. Metabolic reprogramming of microglia in the regulation of the innate inflammatory response. *Frontiers in Immunology* 11: 493.

Laissue P. 2019. The forkhead-box family of transcription factors: key molecular players in colorectal cancer pathogenesis. *Molecular Cancer* 18:5.

LeBleu VS, O'Connell JT, Gonzalez Herrera KN, Wikman H, Pantel K, Haigis MC, de Carvalho FM, Damascena A, Domingos Chinen LT, Rocha RM, Asara JM, Kalluri R. 2014. PGC-1 α mediates mitochondrial biogenesis

and oxidative phosphorylation in cancer cells to promote metastasis. *Nat Cell Biol.* 16(10): 992-1003, 1-15. doi: 10.1038/ncb3039.

Lee LJ, Papadopoli D, Jewer M, del Rincon S, Topisirovic I, Lawrence MG, Postovit LM. 2020. Cancer Plasticity: The Role of mRNA Translation. *Trends in Cancer.*

Lehuédé C, Dupuy F, Rabinovitch R, Jones RG, Siegel PM. 2016. Metabolic plasticity as a determinant of tumor growth and metastasis. *Cancer Res.* 76(18): 5201-5208. doi: 10.1158/0008-5472.CAN-16-0266. Epub 2016 Sep 1. PMID: 27587539

Leibovitch M, Topisirovic I. 2018. Dysregulation of mRNA translation and energy metabolism in cancer. *Advances in Biological Regulation* 67: 30–39.

Lemaitre B, Hoffmann J. 2007. The Host Defense of *Drosophila melanogaster*. *Annual Review of Immunology* 25(1): 697–743.

Lemon B, Tjian R. 2000. Orchestrated response: A symphony of transcription factors for gene control. *Genes Dev* 14: 2551–2569.

Leone RD, Powell JD. 2020. Metabolism of immune cells in cancer. *Nature Reviews Cancer.* *Nature* 20: 516-531.

Li Y, Yao L, Mori Y, Sun SX. 2019. On the energy efficiency of cell migration in diverse physical environments. *PNAS* 116 (48) 23894-23900.

Liao G, Mingle L, Van De Water L, Liu G. 2015. Control of cell migration through mRNA localization and local translation. *WIREs RNA* 6:1-15.

Lio CWJ, Huang SCC. *Circles of Life: linking metabolic and epigenetic cycles to immunity.* 2020. John Wiley & Sons Ltd, *Immunology* 161: 165-174.

Liu L, Parent CA. 2011. TOR kinase complexes and cell migration. *J. Cell Biol.* 194: 815-824.

Ma, R. Y. et al. Raf/MEK/MAPK signaling stimulates the nuclear translocation and transactivating activity of FOXM1c. *J. Cell Sci.* 118, 795–806 (2005).

Macintyre AN, Gerriets VA, Nichols AG, Michalek RD, Rudolph MC, Deoliveira D, Anderson SM, Abel ED, Chen BJ, Hale LP, Rathmell JC. 2014. The glucose transporter Glut1 is selectively essential for CD4 T cell activation and effector function. *Cell Metab.* 20(1):61-72. doi: 10.1016/j.cmet.2014.05.004. Epub 2014 Jun 12. PMID: 24930970; PMCID: PMC4079750.

Maekawa S, Imamachi N, Irie T, H Tani, Matsumoto K, Mizutani R, Imamura K, Kakeda M, Yada T, Sugano S, Suzuki Y, Akimitsu N. 2015. Analysis of RNA decay factor mediated RNA stability contributions on RNA abundance. *BMC Genomics* 16:154.

Mafezzini C, Calvo-Garrido J, Wredenberg A, Freyer C. 2020. Metabolic regulation of neurodiferentiation in the adult brain. *Cellular and Molecular Life Sciences* 77: 2483-2496.

Mantovani A, Biswas SK, Galdiero MR, Sica A, Massimo Locati M. 2013. Macrophage plasticity and polarization in tissue repair and remodeling. *Journal of Pathology J Pathol* 229: 176-185.

Martínez-Reyes I, Chandel NS. 2020. Mitochondrial TCA cycle metabolites control physiology and disease. *Nature Communications* 11:102.

Matsubayashi Y, Louani A, Dragu A, Sa´ nchez-Sa´ nchez BJ, Serna-Morales E, Yolland L, Gyoergy A, Vizcay G, Fleck RA, Heddleston JM, Chew TL, Siekhaus DE, Stramer BM. 2017. A moving source of matrix components

is essential for de novo basement membrane formation. *Current Biology* 27:3526–3534. DOI: <https://doi.org/10.1016/j.cub.2017.10.001>, PMID: 29129537

Mayor R, Etienne-Manneville S. 2016. The front and rear of collective cell migration. *Nat Rev Mol Cell Biol.* 17(2):97-109. doi: 10.1038/nrm.2015.14. Epub 2016 Jan 4. PMID: 26726037.

Mayor R, Theveneau E. 2013. The neural crest. *Development* 140: 2247–2251 10.1242/dev.091751

McCartney BM and Fehon RG. 1996. Distinct cellular and subcellular patterns of expression imply distinct functions for the *Drosophila* homologues of moesin and the neurofibromatosis 2 tumor suppressor, merlin. *J. Cell Biol.* 133: 843-852.

McCartney BM, Kulikauskas RM, LaJeunesse DR, Fehon RG. 2000. The neurofibromatosis-2 homologue, Merlin, and the tumor suppressor expanded function together in *Drosophila* to regulate cell proliferation and differentiation. *Development.* 127(6):1315-24. PMID: 10683183.

Meyuhas O, Kahan T. 2015. The race to decipher the top secrets of TOP mRNAs. *Biochimica Et Biophysica Acta.* 1849:801–811. doi: 10.1016/j.bbagr.2014.08.015

Montell DJ. 2008. Morphogenetic Cell Movements: diversity from modular mechanical properties. *Science,* 322: 1502-1505.

Montell DJ, Yoon WH, Starz-Gaiano M. 2012. Group choreography: mechanisms orchestrating the collective movement of border cells. *Nat Rev Mol Cell Biol* 13: 631–645.

Morita M, Gravel SP, Chénard V, Sikström K, Zheng L, Alain T, Gandin V, Avizonis D, Arguello M, Zakaria C, McLaughlan S, Nouet Y, Pause A, Pollak M, Gottlieb E, Larsson O, St-Pierre J, Topisirovic I, Sonenberg N. 2013. mTORC1 controls mitochondrial activity and biogenesis through 4E-BP-dependent translational regulation. *Cell Metab.* 18(5):698-711. doi: 10.1016/j.cmet.2013.10.001. PMID: 24206664.

Morita M, Gravel SP, Hulea L, Larsson O, Pollak M, St-Pierre J, Topisirovic I. 2015. mTOR coordinates protein synthesis, mitochondrial activity and proliferation. *Cell Cycle* 4: 473–480.

Morlino G, Barreiro O, Baixauli F, Robles-Valero J, González-Granado JM, Villa-Bellosta R, Cuenca J, Sánchez-Sorzano CO, Veiga E, MartínCofreces NB, Sánchez-Madrid F. 2014. Miro-1 links mitochondria and microtubule Dynein motors to control lymphocyte migration and polarity. *Mol Cell Biol* 34: 1412–1426.

Muller WA. 2013. Getting leukocytes to the site of inflammation. *Vet. Pathol.* 50:7–22. doi:10.1177/0300985812469883.

Nagai T, Ishikawa T, Minami Y, Nishita M. 2020. Tactics of cancer invasion: solitary and collective invasion. *J. Biochem.* 167(4):347–355 doi:10.1093/jb/mvaa003.

Nikolaou S, Machesky LM. 2020. The stressful tumour environment drives plasticity of cell migration programs, contributing to metastasis. *J Pathol* 250: 612-623.

Nourshargh S, Hordijk PL, Sixt M. 2010. Breaching multiple barriers: leukocyte motility through venular walls and the interstitium. *Nat Rev Mol Cell Biol.* 11(5):366-78. doi: 10.1038/nrm2889. PMID: 20414258.

Nourshargh S, Alon R. 2014. Immune cell invasion and function leukocyte migration into inflamed tissues. *Immunity* 41: 694-707.

Odegaard JI, Chawla A. 2013. Pleiotropic actions of insulin resistance and inflammation in metabolic homeostasis. *Science.* 339: 172–177.

- Olofsson B, Page DT. 2005. Condensation of the central nervous system in embryonic *Drosophila* is inhibited by blocking hemocyte migration or neural activity. *Dev Biol* 279:233–243. doi:10.1016/j.ydbio.2004.12.020.
- O'Neill LAJ, Pearce EJ. 2016. Immunometabolism governs dendritic cell and macrophage function. *The Journal of Experimental Medicine*. 1: 15-23.
- Orihuela R, McPherson CA, Harry GJ. 2016. Microglial M1/M2 polarization and metabolic states. *British Journal of Pharmacology* 173: 649-665.
- Ostojić J, Panozzo C, Lasserre JP, Nouet C, Courtin F, Blancard C, di Rago JP, Dujardin G. 2013. The energetic state of mitochondria modulates complex III biogenesis through the ATP-dependent activity of Bcs1. *Cell Metab*. 18(4):567-77. doi: 10.1016/j.cmet.2013.08.017. Epub 2013 Sep 19. PMID: 24055101.
- Ostuni R, Kratochvill F, Murray PJ, Natoli G. 2015. Macrophages and cancer: from mechanisms to therapeutic implications. *Trends Immunol*. 36: 229–239.
- Paluch EK, Raz E. 2013. The role and regulation of blebs in cell migration. *Curr Opin Cell Biol* 25: 582–590.
- Parsons JT, Horwitz AR, Schwartz MA. 2010. Cell adhesion: integrating cytoskeletal dynamics and cellular tension. *Nature Rev. Mol. Cell Biol*. 11: 633–643.
- Parsons B, Foley E. 2016. Cellular immune defenses of *Drosophila melanogaster*. *Developmental and Comparative Immunology* 58: 95-101.
- Pellock BJ, Buff E, White K, Hariharan IK. 2007. The *Drosophila* tumor suppressors Expanded and Merlin differentially regulate cell cycle exit, apoptosis, and Wingless signaling. *Dev Bio*. 304: 102–115.
- Perkins LA, Holderbaum L, Tao R, Hu Y, Sopko R, McCall K, Yang-Zhou D, Flockhart I, Binari R, Shim HS, Miller A, Housden A, Foos M, Randkelv S, Kelley C, Namgyal P, Villalta C, Liu LP, Jiang X, Huan-Huan Q, Wang X, Fujiyama A, Toyoda A, Ayers K, Blum A, Czech B, Neumuller R, Yan D, Cavallaro A, Hibbard K, Hall D, Cooley L, Hannon GJ, Lehmann R, Parks A, Mohr SE, Ueda R, Kondo S, Ni JQ, Perrimon N. 2015. The Transgenic RNAi project at Harvard medical school: resources and validation. *Genetics*. 201(3):843-52. doi: 10.1534/genetics.115.180208. Epub 2015 Aug 28. PMID: 26320097; PMCID: PMC4649654.
- Phung B, Ciesla M, Sanna A, Guzzi N, Beneventi G, Thi Ngoc PC, Lauss M, Cabrita R, Cordero E, Bosch A, Rosengren F, Haikkinen J, Griewank K, Paschen A, K Harbst, H Olsson, C Ingvar, Carneiro A, Tsao H, Schadendorf D, Pietras K, Bellodi C, Joñsson G. 2019. The X-Linked DDX3X RNA helicase dictates translation reprogramming and metastasis in melanoma. *Cell Reports* 27: 3573-3586.
- Piskacek M, Havelka M, Rezacova M, Knight A. 2016. The 9aaTAD Transactivation Domains: From Gal4 to p53. *PLoS ONE* 11: e0162842. PMID:27618436.
- Pocha SM, Montell DJ. 2014. Cellular and molecular mechanisms of single and collective cell migrations in *Drosophila*: themes and variations. *Annu Rev Genet*. 48:295-318. doi: 10.1146/annurev-genet-120213-092218. PMID: 25421599.
- Popper H, Kenner L, Haigh JJ, Kepp O, Rak M, Cai K, Kroemer G, Penninger JM. 2019. AIF-regulated oxidative phosphorylation supports lung cancer development. *Cell Research* 29: 579-591.
- Porporato PE, Filigheddu N, Pedro JMB, Kroemer G, Galluzzi L. 2018. Mitochondrial metabolism and cancer. *Cell Res*. 28(3):265-280. doi: 10.1038/cr.2017.155. Epub 2017 Dec 8. PMID: 29219147; PMCID: PMC5835768.
- Prasad M, Wang X, He L, Montell DJ. 2011. Border cell migration: a model system for live imaging and genetic analysis of collective cell movement. *Methods Mol Biol*. 769:277-286. doi: 10.1007/978-1-61779-207-6_19. PMID: 21748683; PMCID: PMC4006199.

Raj N, Attardi LD. 2017. The transactivation domains of the p53 protein. *Cold Spring Harb Perspect Med* 7. doi:10.1101/cshperspect.a026047

Ratheesh A, Belyaeva V, Siekhaus DE. 2015. *Drosophila* immune cell migration and adhesion during embryonic development and larval immune responses. *Curr. Opin. Cell Biol.* 36: 71–79.

Ratheesh A, Biebl J, Vesela J, Smutny M, Papusheva E, Krens SFG, Kaufmann W, Gyoergy A, Casano AM, Siekhaus DE. 2018. *Drosophila* TNF modulates tissue tension in the embryo to facilitate macrophage invasive migration. *Dev Cell.* 45(3): 331-346.e7. doi: 10.1016/j.devcel.2018.04.002. PMID: 29738712.

Remmerie A, Scott CL. 2018. Macrophages and lipid metabolism. *Cellular immunology* 330: 27-42. doi: 10.1016/j.cellimm.2018.01.020. Epub 2018 Feb 2. PMID: 29429624; PMCID: PMC6108423

Reversat A, Merrin J, Hauschild R, deVries I, Piel M, Callan-Jones A, Voituriez R, Sixt M. 2020. Adhesion-free cell migration by topography-based force transduction. *Nature* 582(7813): 582-585. doi: 10.1038/s41586-020-2283-z. Epub 2020 May 13. PMID: 32581372.

Riahi R, Sun J, Wang S, Long M, Zhang DD, Wong PK. 2015. Notch1-Dll4 signalling and mechanical force regulate leader cell formation during collective cell migration. *Nat Commun.* 6:6556. doi: 10.1038/ncomms7556. PMID: 25766473; PMCID: PMC4380165.

Richardson BE, Beckett K, Nowak SJ, Baylies MK. 2007. SCAR/WAVE and Arp2/3 are crucial for cytoskeletal remodeling at the site of myoblast fusion. *Development.* D134(24): 4357-467. doi: 10.1242/dev.010678. Epub 2007 Nov 14. PMID: 18003739; PMCID: PMC2880884.

Ridley AJ, Schwartz MA, Burridge K, Firtel RA, Ginsberg MH, Borisy G, Parsons JT, Horwitz AR. 2003. Cell migration: integrating signals from front to back. *Science.* 302(5651): 1704-9. doi: 10.1126/science.1092053. PMID: 14657486.

Riera-Domingo C, Audigé A, Granja S, Cheng WC, Ho PC, Baltazar F, Stockmann C, Mazzone M. 2020. Immunity, hypoxia, and metabolism- the ménage a trois of cancer: implications for immunotherapy. *Physiol Rev* 100: 1–102.

Rivadeneira DB, Caino MC, Seo JH, Angelin A, Wallace DC, Languino LR, Altieri DC. 2015. Survivin promotes oxidative phosphorylation, subcellular mitochondrial repositioning, and tumor cell invasion. *Sci Signal.* 8(389):ra80. doi: 10.1126/scisignal.aab1624. PMID: 26268608; PMCID: PMC4539531.

Robida-Stubbs S, Glover-Cutter K, Lamming DW, Mizunuma M, Narasimhan SD, Neumann-Haefelin E, Sabatini DM, Blackwell TK. 2012. TOR signaling and Rapamycin influence longevity by regulating SKN-1/Nrf and DAF-16/FoxO. *Cell Metabolism* 15: 713-724.

Roux P, Topisirovic I. 2018. Signaling pathways involved in the regulation of mRNA translation. *Molecular and Cellular Biology* 38 (12): e00070-18.

Rodriguez-Prados JC, Traves PG, Cuenca J, et al. 2010. Substrate fate in activated macrophages: a comparison between innate, classic, and alternative activation. *J Immunol.* 185: 605–614.

Sánchez-Sánchez BJ, Urbano JM, Comber K, Dragu A, Wood W, Stramer B, Martín-Bermudo MD. 2017. *Drosophila* embryonic Hemocytes produce laminins to strengthen migratory Response. *Cell Rep* 21:1461–1470. doi:10.1016/j.celrep.2017.10.047.

Sarbassov DD, Ali SM, Kim DH, Guertin DA, Latek RR, Erdjument-Bromage H, Tempst P, Sabatini DM. 2004. Rictor, a novel binding partner of mTOR, defines a rapamycin-insensitive and raptor-independent pathway that regulates the cytoskeleton. *Current biology* 14: 1296–1302.

- Saxton RA, Sabatini DM. mTOR Signaling in Growth, Metabolism, and Disease. *Cell*. 2017 Mar 9;168(6):960-976. doi: 10.1016/j.cell.2017.02.004.
- Scarpa E, Mayor R. 2016. Collective cell migration in development. *The Journal of cell biology* 212: 143-55.
- Schmidt S, Friedl P. 2010. Interstitial cell migration: Integrin-dependent and alternative adhesion mechanisms. *Cell and Tissue Research* 339: 83–92.
- Schuler MH, Lewandowska A, Di Caprio G, Skillern W, Upadhyayul S, Kirchhausen T, Shawa JM, Cunniff B. 2017. Miro1-mediated mitochondrial positioning shapes intracellular energy gradients required for cell migration. *Molecular Biology of the Cell* 28(16): 2159–2169.
- Sekiguchi T, Hayano T, Yanagida M, Takahashi N, Nishimoto T. 2006. NOP132 is required for proper nucleolus localization of DEAD-box RNA helicase DDX47. *Nucleic Acids Research* 16: 4593-4608.
- Seo BJ, Yoon SH, Do JT. 2018. Mitochondrial dynamics in stem cells and differentiation. *Int. J. Mol. Sci.* 19: 3893. doi:10.3390/ijms19123893.
- Siekhaus D, Haesemeyer, M Moffitt O, Lehmann R. 2010. RhoL controls invasion and Rap1 localization during immune cell transmigration in *Drosophila*. *Nature Cell Biology*, 12 (6), 605– 610. <https://doi.org/10.1038/ncb2063>.
- Simkin JE, Zhang D, Rollo BN, Newgreen DF. 2013. Retinoic acid upregulates ret and induces chain migration and population expansion in vagal neural crest cells to colonise the embryonic gut. *PLoS One* 8(5):e64077. doi: 10.1371/journal.pone.0064077. PMID: 23717535; PMCID: PMC3661488.
- Smith PM, Fox JL, Winge DR. 2012. Biogenesis of the cytochrome bc1 complex and role of assembly factors. *Biochim Biophys Acta*. 1817(2): 276-286.
- Song J, Pfanner N, Becker T. 2018. Assembling the mitochondrial ATP synthase. *Proc Natl Acad Sci* 20: 2850–2852
- Spriggs KA, Bushell M, Willis AE. 2010. Translational regulation of gene expression during conditions of cell stress. *Molecular Cell* 40: 228-237.
- Stienstra R, Netea-Maier RT, Riksen NP, Joosten LAB, Netea MG. 2017. Specific and Complex reprogramming of cellular metabolism in myeloid cells during innate immune responses. *Cell Metab*. 26(1): 142-156. doi: 10.1016/j.cmet.2017.06.001. PMID: 28683282.
- Stuelten CH, Parent CA, Montell DJ. 2018. Cell motility in cancer invasion and metastasis: insights from simple model organisms. *Nat Rev Cancer*. 18(5): 296-312. doi: 10.1038/nrc.2018.15. Epub 2018 Mar 16. PMID: 29546880; PMCID: PMC6790333.
- Suffoletto K, Jetta D, Hua SZ. 2018. E-cadherin mediated lateral interactions between neighbor cells necessary for collective migration. *Journal of Biomechanics*, 71, 159-166.
- O’Sullivan D, Sanin DE, Pearce EJ, Pearce EL. 2019. Metabolic interventions in the immune response to cancer *Nature Reviews, Immunology* 19: 324-335.
- Tanabe S, Yamashita T. 2018. The role of immune cells in brain development and neurodevelopmental diseases. *Int. Immunol.* 30: 437-444.
- Tcherkezian J, Cargnello M, Romeo Y, Huttlin EL, Lavoie G, Gygi SP, Roux PP. 2014. Proteomic analysis of cap-dependent translation identifies LARP1 as a key regulator of 5'TOP mRNA translation. *Genes Dev*. 28(4):357-71. doi: 10.1101/gad.231407.113. PMID: 24532714; PMCID: PMC3937514.

- Tepass U, Fessler LI, Aziz A, Hartenstein V. 1994. Embryonic origin of hemocytes and their relationship to cell death in *Drosophila*. *Development* 120: 1829-1837.
- Theveneau E, Linker C. 2017. Leaders in collective migration: are front cells really endowed with a particular set of skills? *F1000Res*. 6: 1899.
- Theveneau E, Mayor R. 2013. Collective cell migration of epithelial and mesenchymal cells. *Cell. Mol. Life Sci*. 70:3481–3492. 10.1007/s00018-012-1251-7
- Thion MS, Ginhoux F, Garel S. 2018. Microglia and early brain development: an intimate journey. *Science* 362: 185–189.
- Thoreen CC, Chantranupong L, Keys HR, Wang T, Gray NS, Sabatini DM. 2012. A unifying model for mTORC1-mediated regulation of mRNA translation. *Nature* 485: 109–113.
- Thuma L, Carter D, Weavers H, Martin P. 2018. *Drosophila* immune cells extravasate from vessels to wounds using Tre1 GPCR and Rho signaling. *J. Cell Biol.*. Vol. 217 No. 9 3045–3056.
- Teixeira FK, Sanchez CG, Hurd TR, Seifert JRK, Czech B., Preall J.B., Hannon G. J, Lehmann R. 2015. ATP synthase promotes germ cell differentiation independent of oxidative phosphorylation. *Nature Cell Biology* 17: 689–696. DOI: 10.1038/ncb3165.
- Tiku V, Tan MW, Dikic I. 2020. Mitochondrial functions in infection and immunity. *Trends in Cell Biology*, Vol. 30, No. 4.
- Trepat X, Chen Z, Jacobson K. 2012. Cell migration. *Compr. Physiol*. 2369-2392.
- Valoskova K, Biebl J, Roblek M, Emtenani S, Gyoergy A, Misova M, Ratheesh A, Reis-Rodrigues P, Shkarina K, Larsen ISB, Vakhrushev SY, Clausen H, Siekhaus DE. 2019. A conserved major facilitator superfamily member orchestrates a subset of O-glycosylation to aid macrophage tissue invasion. *eLife*. 8. pii: e41801.
- van der Blik AM, Sedensky MM, Morgan PG. 2017. Cell biology of the mitochondrion. *Genetics* 207: 843–71. 10.1534/genetics.117.300262.
- Van Horssen R, Janssen E, Peters W, Van de Pasch L, Te Lindert MM, Van Dommelen MMT, Linssen PC, Ten Hagen TLM, Franssen JAM, Wieringa B. 2009. Modulation of cell motility by spatial repositioning of enzymatic ATP/ADP exchange capacity. *J Biol Chem*. 284:1620–1627.
- Vitorino P, Meyer T. 2008. Modular control of endothelial sheet migration. *Genes & Development* 22: 3268-3281.
- Walker MA, Volpi S, Sims KB, Walter JE Traggiai, E. 2014. Powering the immune system: mitochondria in immune function and deficiency. *Journal of Immunology Research* 1-8.
- Warburg O, Wind F, Negelein E. 1927. The metabolism of tumors in the body. *J Gen Physiol*. 8(6):519-30. doi: 10.1085/jgp.8.6.519. PMID: 19872213; PMCID: PMC2140820.
- Watanabe N, Mitchison TJ. 2002. Single-molecule speckle analysis of actin filament turnover in lamellipodia. *Science* 295(5557):1083-1086. doi: 10.1126/science.1067470. PMID: 11834838.
- Weavers, H., I.R. Evans, P. Martin, and W. Wood. 2016. Corpse engulfment generates a molecular memory that primes the macrophage inflammatory response. *Cell* 165:1658–1671. <https://doi.org/10.1016/j.cell.2016.04.049>
- Williams MJ. 2007. *Drosophila* hemopoiesis and cellular immunity. *J Immunol*. 178:4711-4716.

- Wilson CA, Tsuchida MA, Allen GM, Barnhart EL, Applegate KT, Yam PT, Ji L, Keren K, Danuser G, Theriot JA. 2010. Myosin II contributes to cell-scale actin network treadmilling through network disassembly. *Nature* 465(7296): 373-377. doi: 10.1038/nature08994. PMID: 20485438; PMCID: PMC3662466.
- Wilson K, Lewalle A, Fritzsche M, Thorogate R, Duke T, Charras G. 2013. Mechanisms of leading edge protrusion in interstitial migration. *Nature Communications* 4: 1–12. <https://doi.org/10.1038/ncomms3896>
- Wintner O, Hirsch-Attas, N, Schlossberg, M, Brofman F, Friedman R, Kupervaser M, Kitsberg D, Buxboim A. 2020. A unified linear viscoelastic model of the cell nucleus defines the mechanical contributions of lamins and chromatin. *Advanced Science*, 7 (8). <https://doi.org/10.1002/advs.201901222>.
- Witkiewicz AK, Whitaker-Menezes D, Dasgupta A, NJ Philp, Lin Z, Gandara R, Sneddon S, Martinez-Outschoorn UE, Sotgia F, Lisanti MP. 2012. Using the “reverse Warburg effect” to identify high-risk breast cancer patients: Stromal MCT4 predicts poor clinical outcome in triple-negative breast cancers. *Cell Cycle* 11: 1108–1117.
- Wood W, Martin P. 2017. Macrophage functions in tissue patterning and disease: new insights from the fly. *Dev. Cell*. 40: 221–233.
- Woodcock KJ, Kierdorf K, Pouchelon CA, Vivancos V, Dionne MS, Geissmann F. 2015. Macrophage-derived upd3 cytokine causes impaired glucose homeostasis and reduced lifespan in *Drosophila* fed a lipid-rich diet. *Immunity* 42(1): 133-144.
- Worbs T, Hammerschmidt SI, Förster R. 2017. Dendritic cell migration in health and disease. *Nat Rev Immunol*. 17(1): 30-48. doi: 10.1038/nri.2016.116. Epub 2016 Nov 28. PMID: 27890914.
- Wu J, Jiang J, Chen B, Wang K, Tang Y, Liang X. 2021. Plasticity of cancer cell invasion: Patterns and mechanisms. *Translational Oncology* 14: 100899.
- Xie J, Bao M, Hu X, Koopman WJH, Huck WTS. 2021. Energy expenditure during cell spreading influences the cellular response to matrix stiffness. *Biomaterials* 267: 120494.
- Yamada T, Nagahama M, Akimitsu N. 2018. Interplay between transcription and RNA degradation, gene expression and regulation in mammalian cells-transcription from general aspects. London: InTech.
- Zanotelli MR, Goldblatta ZE, Millera JP, F Bordeleaub, Lia J, VanderBurgha JA, Lampia MC, Kinga MR, Reinhart-Kinga A. 2018. Regulation of ATP utilization during metastatic cell migration by collagen architecture. *Molecular Biology of the Cell*: 29.
- Zanotelli MR, Rahman-Zaman A, Vander Burgh JA, Taufalele PV, Jain A, Erickson D, Bordeleau F, Reinhart-King CA. 2019. Energetic costs regulated by cell mechanics and confinement are predictive of migration path during decision-making. *Nat. Commun* 10: 4185.
- Zhao J, Zhang J, Yu M, Xie Y, Huang Y, Wolff DW, Abel PW, Tu Y. 2013. Mitochondrial dynamics regulates migration and invasion of breast cancer cells. *Oncogene* 32: 4814-4824.
- Zhang X, Fryknäs M, Hernlund E, Fayad W, De Milito A, Olofsson MH, Gogvadze V, Dang L, Pålman S, Schughart LA, Rickardson L, D'Arcy P, Gullbo J, Nygren P, Larsson R, Linder S. 2014. Induction of mitochondrial dysfunction as a strategy for targeting tumour cells in metabolically compromised microenvironments. *Nat Commun*. 5:3295. doi: 10.1038/ncomms4295. PMID: 24548894; PMCID: PMC3929804.
- Zhang J, Goliwas KF, Wang W, Taufalele PV, Bordeleau F, Reinhart-King CA. 2019. Energetic regulation of coordinated leader-follower dynamics during collective invasion of breast cancer cells. *Proc. Natl. Acad. Sci. USA* 116: 7867–7872.

Zid BM, Rogers AN, Katewa SD, Vargas MA, Kolipinski MC, Lu TA, Benzer S, Kapahi P. 2009. 4E-BP extends lifespan upon dietary restriction by enhancing mitochondrial activity in *Drosophila*. *Cell* 139(1):149-60. doi: 10.1016/j.cell.2009.07.034. PMID: 19804760; PMCID: PMC2759400.

Zou Z, Tao T, Li H, Zhu X. 2020. mTOR signaling pathway and mTOR inhibitors in cancer: progress and challenges. *Cell Biosci.* 10:31. 10.1186/s13578-020-00396-1.

Zwenger M, Jaalouk DE, Lombardi ML, Isermann P, Mauermann M, Dialynas G, Herrmann H, Wallrath LL, Lammerding J. 2013. Myopathic lamin mutations impair nuclear stability in cells and tissue and disrupt nucleo-cytoskeletal coupling. *Human Molecular Genetics*, 22(12). <https://doi.org/10.109>